Summer 2001

Optimal Aeroelastic Vehicle Sensor Placement for Root Migration Flight Control Applications

Abdul Ghafoor Al-Shenhabi
Old Dominion University

OPTIMAL AEROELASTIC VEHICLE SENSOR PLACEMENT FOR ROOT MIGRATION FLIGHT CONTROL APPLICATIONS

by

Abdul Ghafoor Al-Shehabi
B.Sc. November, 1986, Aleppo University, Syria
M.Sc. December, 1995, Cairo University, Egypt

A Dissertation Submitted to the Faculty of
Old Dominion University in Partial Fulfillment of the
Requirements for the Degree of

DOCTOR OF PHILOSOPHY
AEROSPACE ENGINEERING
OLD DOMINION UNIVERSITY
August 2001

Approved by:

Brett A. Newman (Director)

Donald L. Kunz (Member)

Oscar R. González (Member)

ABSTRACT

OPTIMAL AEROELASTIC VEHICLE SENSOR PLACEMENT FOR ROOT MIGRATION FLIGHT CONTROL APPLICATIONS

Abdul Ghafoor Al-Shehabi
Old Dominion University, August 2001
Director: Dr. Brett Newman

An important step in control design for elastic systems is the determination of the number and location of control system components, namely sensors. The number and placement of sensors can be critical to the robust functioning of active control systems, especially when the system of interest is a large high-speed aeroelastic vehicle. The position of the sensors affects not only system stability, but also the performance of the closed-loop system. In this dissertation, a new approach for sensor placement in the integrated rigid and vibrational control of flexible aircraft structures is developed. Traditional rigid-body augmentation objectives are addressed indirectly through input-output pair and compensation selection. Aeroelastic control suppression objectives are addressed directly through sensor placement. A nonlinear programming problem is posed to minimize a cost function with specified constraints, where the cost function terms are multiplied by appropriate weighting factors. Cost function criteria are based on complex frequency domain geometric pole-zero structures in order to gain stabilize or phase stabilize the aeroelastic modes. Specifically, these criteria are based on dipole magnitude and complementary departure angle. In turn, the control design approach utilizes one of the classical methods known as Evans root migration to exploit the pole-zero structures resulting from sensor placement. Desirable complementary departure angles can lead to

significant aeroelastic damping improvement as loop gain is increased, while favorable dipole magnitudes can virtually eliminate the effects of aeroelastics in a feedback loop. Appropriate constraints include minimum phase aeroelastic zeros to avoid common problems associated with right-half plane zeros. To achieve desirable flight control system characteristics via optimal sensor locations, different kinds of blending filters for multiple sensors are investigated. Static filters, as well as dynamic filters with fixed or variable parameters and fixed or variable compensator parameters, are considered. For every cost function, there are several local minima indicating many distributions of the sensors are available. By evaluating the cost for each minimum, the global optimum can then be found.

This dissertation is dedicated to my sons

Abdul, Tarek, Mazen and Feras.

ACKNOWLEDGMENTS

I would like to express my sincere thanks to my advisor, Dr. Brett Newman, for his guidance throughout this research project. His vast knowledge and innovative ideas guided the project from its inception. I extend many, many thanks to my committee members for their patience and assistance in preparing this dissertation.

I am truly blessed to have a wonderful supportive family; they have all been a constant source of love and encouragement. I am very thankful to my wife Farial for her patience, her support, and for building a true family. My deepest thanks to my father and my mother who have inspired me through my life.

TABLE OF CONTENTS

Chapter Page

LIST OF TABLES

LIST OF FIGURES

FIGURE Page

FIGURE Page

FIGURE Page

FIGURE Page

FIGURE Page

CHAPTER 1

INTRODUCTION

1.1 Problem Motivation

Commercial flight studies[1,2] indicate the existence of potential markets for a long range, high-speed, high capacity vehicle to link global centers of business activity. International cooperation and/or competition on such a vehicle is currently underway. This class of vehicle must be environmentally friendly and economically efficient if it is to be a viable concept. Utilization of new but affordable technologies such as advanced materials, boundary layer augmentation, multi-cycle engines, active control, and synthetic vision are key to the economic success of this second generation supersonic transport.[3,4]

The high speeds of this vehicle, coupled with the use of lightweight composite materials for the primary structure and overall minimal structural mass, will make the vehicle highly flexible with many low frequency structural modes. Such design characteristics will lead to significant interactions between the rigid-body and structural dynamics. These interactions occur through cause and effect inertial, structural and aerodynamic mechanisms between structural deflections and rigid-body motions, and *vice versa*. This interaction is further aggravated by the use of a high-bandwidth/high-authority flight control system. Such a flight control system may incorporate stability augmentation logic to stabilize possibly multi-axis relaxed stability characteristics, or to

---

The journal model for this work is the Journal of Guidance, Control, and Dynamics.

increase damping levels in key motions such as the short period and dutch-roll modes, as well as command augmentation logic to reshape the motion responses for desired handling qualities. Additionally, the flight control system may incorporate structural mode control system strategies to dampen vibrational motions. Traditionally, independent control systems have been used to augment the rigid-body and structural dynamics. In the high-speed transport arena, the highly coupled motions will not allow this design freedom. Therefore, control of rigid-body and aeroelastic motions, and their interactions, must be considered with an integrated control strategy.

An important step in the design of flight control systems for high-speed, highly flexible vehicles is feedback sensor placement. From a traditional rigid-body stability augmentation perspective, sensor signals containing key information appropriate for augmenting oscillatory pitch and yaw motions are sought. Further, these feedback signals should not be contaminated with high frequency structural vibration content, which may destabilize the control loop or drive the actuator excessively. On the other hand, from a pure structural mode control perspective, sensor signals that facilitate considerable leverage on mode damping are sought. These signals should avoid passing rigid-body rotational motion content to circumvent unwanted excitation of the structural dynamics during desired overall rotational motions and to avoid impacting the characteristics of these rigid-body motions. With an integrated flight control system, the sensor signal should be optimized for both rigid-body and aeroelastic content, appropriate for the control objectives. On an even more fundamental level, feedback sensor signal content must be consistent with the design objective. If the sensor does not provide useful

information, then no amount of gain adjustment or filtering on this signal will lead to acceptable closed-loop results.

The importance of optimal sensor placement for aeroelastic vehicle flight control applications is thus underscored. One approach to systematic and efficient optimal sensor placement, as opposed to manual placement strategies, is application of theoretical and applied optimization concepts. A critical step in such methodologies is identification of relevant objective functions with applicable constraints that have direct bearing on the control design strategy. This dissertation focuses on such optimal sensor placement strategies. The objectives of this dissertation include the following: 1) formulation of candidate sensor placement criteria tailored for application to conventional-based root migration flight control design techniques, 2) application of theoretic principles and numeric algorithms for the minimization of such criteria for optimal sensor placement, and 3) utilization of these optimal sensor locations in flight control design.

1.2 Literature Survey and Problem Definition

One critical issue in flight control system design for elastic vehicles is determination of the number and location of actuation and sensory components. The primary function of these components is to implement feedback control strategies. Actuators and sensors also play a key role in reliability monitoring and fault detection systems and for real-time model identification systems. In high-speed atmospheric flight applications, minimal drag objectives and design architecture cost constraints fix the number of aerodynamic control surfaces or actuators to a small number. Further, these control input devices are typically constrained to lie near the aft region of the vehicle and

on the trailing edge of lifting surfaces. On the other hand, a large number of sensors, and a wide range of feasible locations for these sensors, are available since these components, for the most part, are internally or flush mounted elements and are relatively cheap from an architectural perspective. This dissertation will focus exclusively on sensor placement problems, although review of both sensor and actuator placement literature provides a broad foundation to draw upon.

Traditional approaches for manually distributing flight control feedback sensors and actuators throughout the interior and exterior regions of a flight vehicle are based on linear transfer function or state space models of the relevant dynamics. Such analytically based approaches provide key insight into desirable sensor locations and further reveal the mechanisms that lead to these desirable locations and associated characteristics. In the case of vehicles whose characteristics can be sufficiently modeled as a rigid system, placement of accelerometer sensors to approximate angle of attack or side slip angle feedback is a well-known classic problem.[5] Recall that an accelerometer senses pure translational motion, as well as effective translational motion arising from rotational motion acting through a moment arm separating the sensor and vehicle mass center. The acceleration feedback signal best approximates the aerodynamic angle feedback signal when the accelerometer is located at the center of rotation. At this special point, translational and rotational motions precisely cancel. References 5-6 document acceleration transfer function dependencies on sensor location.

For true acceleration command systems, the accelerometer location can lead to undesirable response reversal if not properly positioned relative to the mass center.[7] Reference 7 discusses such behavior and implies that, at least for small agile vehicles, the

accelerometer sensor should be located well in front of the mass center, near the cockpit. Reference 8 discusses how the accelerometer sensor location in a blended pitch rate-normal acceleration control system can desensitize the closed-loop behavior to flight condition changes. Theoretically, for a rigid aircraft, dynamic characteristics are invariant to rate gyro sensor location, since all points on the vehicle possess the same angular rate. However, Reference 7 and 9 indicate that care must also be given to rate gyro sensor placement due to the pick up of localized structural vibrations that can degrade or even destabilize the associated control loop.

Sensor placement for vehicle characteristics that require flexible body or aeroelastic descriptions is a considerably more difficult problem. In this situation, accelerometers are sensitive to not only the rigid-body translational and rotational motions, but also to translational structural deflections. Under such situations, the accelerometer output signal is proportional to the second temporal derivative of the dominant generalized structural deflection coordinate where the proportionality constant is the characteristic deflection mode shape value at the sensor mounting location. In the case of a rate gyro instrument, the sensor is excited by rotational structural deflections. Here, the rate gyro output is proportional to generalized structural deflection rate. The proportionality constant is the mode slope value at the sensor location. Note that the deflection mode shape and mode slope values depend on location within the vehicle. This feature brings an entirely new dimension and difficulty to the sensor placement problem. Such difficulties are a central part of the dissertation research.

References 10-18 illustrate the difficulties and various techniques associated with manual sensor/actuator placement and control system design for flexible flight vehicles

based on transfer function analysis. In References 10-12, approximate factored transfer functions in symbolic form are derived in terms of basic vehicle parameters for various flexible configurations including a high-speed bank to turn missile, subsonic transport, and supersonic fighter. Basic parameters describing inertial, aerodynamic, structural, and design properties include stability and control derivatives, modal vibration damping, frequency and mode shape coefficients, sensor and actuator locations, and flight condition variables. Various analytical and numerical sensitivity studies are conducted with these transfer functions. For the sensor placement focus in this dissertation, such transfer functions reveal how sensor location affects open-loop airframe numerator factors associated with short period, dutch-roll, and 1^{st} fuselage or wing bending modes, for example. Recall the numerator polynomial roots or zeros, relative to the poles, are important in determining the contribution of each mode to the overall motion in the input-output channel of interest. Zeros associated with rigid-body dynamics can influence vehicle handling qualities and time response behaviors in many different ways including apparent overshoot, drop back, time delay, and even response reversal in extreme cases. Note that many flying quality metrics explicitly depend on transfer function zeros.[19] Aeroelastic pole-zero combinations, when located close to the imaginary axis, can significantly impact the response characteristics with high frequency residual contamination, undesirable aeroelastic-to-aeroelastic or aeroelastic-to-rigid modal phasing, and response reversal. [20-22]

In References 13-18, consideration is given to loop closure around the sensor dependent flexible vehicle transfer functions. Basic stability augmentation loops, such as pitch and yaw dampers, are investigated. As discussed above, sensor location influences

the numerator roots which, in turn, influences closed-loop pole augmentation. For example, with a root locus or root migration based design technique, the zeros have a strong influence on the closed-loop pole migration paths. Zeros influence the initial migration direction, the migration path while transitioning between the initial and terminal points, and the terminal points themselves. Aeroelastic pole-zero factors, or dipoles, are especially critical in these loop closures. Depending upon specific control objectives, sensor locations are sought, which yield tight dipole structure (near pole-zero elimination), or a dipole with proper direction (desirable pole-zero orientation). Destabilizing dipole orientations, or loose dipole structures with one right-half and one left-half plane real axis zero, are to be avoided. Further, the sensor locations should not significantly degrade the rigid-body augmentation features. For a system with only one or two significant aeroelastic modes, References 13-18 develop correlation between mode shape/slope values at the sensor location and the resulting numerator loop closure features. With this understanding, flight control engineers have *a priori* knowledge on where to place sensors so that when math models are generated and loops are closed, the resulting dynamics are as expected, the design iteration effort is lessened, and the key tradeoffs are clearly evident.

An important paradigm discovered in the actuator and sensor placement discipline for elastic systems is documented in References 15-16 and 23-28. This paradigm is often referred to as a "collocated actuator and sensor." For an undamped elastic body such as an idealized spacecraft model, placement of an actuator and sensor at the same location will result in a guaranteed transfer function pole-zero structure that is highly desirable for feedback control. The resulting transfer function will have alternating or interlaced poles

and zeros along the imaginary axis. The significance of actuator and sensor collocation is that all rigid-body and all vibrational modes can be simultaneously stabilized and damped with a single negative rate feedback signal. Root locus formulas can be used to show that for co-location, angles of departure and angles of arrival are *±180 deg* indicating superior augmented damping behavior. To exploit this paradigm, the actuator and sensor must be compatible in the sense that both instruments are translational derives or rotational devices, but not mixed. In other words, a force actuator and rate gyro sensor, or a torque actuator and accelerometer sensor, will not theoretically guarantee the desired transfer properties. Reference 27 gives an application of this technique to the Solar Electric Propulsion spacecraft. Unfortunately for atmospheric vehicle applications, aerodynamic stiffness and damping violate the necessary assumptions of an *in vacuo* environment. Nevertheless, References 15-16 document significant success with this technique as applied to the XB-70 aircraft. The vehicle of interest in the dissertation research significantly violates necessary assumptions required for a simple collocated actuator-sensor solution strategy.

The techniques described in References 10-12 are primarily based on *ad hoc* procedures, and calculations were considered well before the availability of high-performance desktop computing. References 29-31 revisited these techniques with updated tools and concepts. These references reformulated the procedure for obtaining symbolic transfer function factors with a sound theoretical framework and applied modern computers and software in the calculations. The improved technique has been used to develop analytical relationships for transfer function poles and zeros of a fourth order, large high-speed flexible airframe in terms of basic parameters such as stability

and control derivatives, modal vibration parameters, and sensor location. Relatively simple and accurate analytical expressions conducive to obtaining insight into the vehicle physics have been obtained. For example, an analytical expression for the right-half plane zero associated with the 1^{st} fuselage bending mode in the elevator to cockpit pitch rate dynamics mathematically reveals the competing effects of rigid and elastic pitch as a function of sensor location or mode slope.[30] These competing pitch mechanisms ultimately determine the zero location. Such information is highly relevant for manual sensor placement tasks. Other literature in this area that provides applicable knowledge useful for actuator/sensor placement activities in open-loop and closed-loop scenarios includes References 32-39.

With the exception of Reference 14 and 17, the flexible vehicle models studied in References 10-18 and 29-39 either have rigid-flexible bandwidth separation of 8 to 10 rad/s and above, or the number of significant low frequency flexible modes below 30 rad/s is on the order of 4 or less. Such characteristics are not the case for design models approximating current high-speed transport configurations of interest.[40] These current models are considerably more modally dense and flexible (approximately 8 significant modes below *30 rad/s* and rigid-elastic frequency separation of *5-7 rad/s*). Such characteristics present a significantly more difficult control and sensor placement challenge, which is the primary focus of this dissertation research.

References 41-45 document conventional based control development activities for these newer high-speed transport configurations. Primary control objectives are to artificially supply the stability inherently lacking in the airframe, augment key pilot/passenger centered responses leading to crisp well damped behavior, and suppress

aeroelastic motion in all responses, all with minimal use of architecture. Considerable effort is devoted to achieving these objectives with a predefined single input control structure (i.e., the elevator). Thus, a critical task in the development work dealt with identifying desirable regions for feedback sensors, which result in favorable transfer functions for loop closure consistent with the design objectives. Reference 45 is particularly important in motivating the dissertation research topic and is discussed further.

A modified version of the numerical model from Reference 17 provides the basis for the vehicle model utilized in Reference 45. The dynamic model includes 40 state variables accounting for rigid longitudinal relaxed stability motion and 18 lightly damped symmetric aeroelastic modes. Based on advantages associated with the so called "superaugmented pitch loop" architecture,[46,47] rate gyro based feedback signals are exclusively considered. By manual inspection of the characteristic deflection shapes as a function of fuselage centerline position for all 18 modes, candidate sensor locations with projected transfer characteristics beneficial to control are highlighted for further detail investigation. In this inspection process, fuselage stations corresponding to near zero mode slope, or finite mode slope that is in-phase with the rigid pitch motion, simultaneously for many modes, are sought. Such locations tend to yield favorable aeroelastic dipole structures and rigid-body characteristics. After a few necessary, manual sensor placement iterations on the complete model with all aerodynamic coupling terms present, the process yields transfer functions with the approximate desired features.

Unfortunately, serious conflicts exist between several key aeroelastic modes. Sensor locations desirable for some aeroelastic dipoles and the rigid-body mode are

undesirable for other modes, and *vice versa*. The ultimate conclusion in Reference 45 is that for high-speed transports with high levels of instability and flexibility, a single-surface/single-sensor control architecture is not feasible for meeting the design objectives. These results motivated investigation of a blended sensor architecture. Two rate gyro signals are blended in such a way to preserve the desirable signal content of both, while simultaneously eliminating the undesirable signal content. Blending filter logic and associated parameters increase the problem dimensionality. Based on problem insight, simple blending logic is selected and improved transfer characteristics for loop closure result. However, the improvements still were lacking in certain respects. Thus, References 41 and 43 also considered formal optimization as a means to conduct efficient, automatic blended sensor placement. Some further improvements are demonstrated, but limited resources prevented a thorough investigation of the subject. Optimal, auto sensor placement strategies and techniques per References 41, 43, and 45 are primary to this dissertation research subject.

This dissertation will investigate and explore a methodology and strategy for optimal placement of feedback sensors to be utilized in conjunction with conventional root migration flight control design techniques applied to flexible atmospheric flight vehicles.[48-51] All numerical sensor placement calculations in this dissertation are conducted with a large, high-speed aeroelastic transport dynamic model. This numerical model is identical to that used in References 41, 43, and 45. This vehicle is characterized as highly flexible and modally dense with very little frequency separation between rigid-body and structural dynamics and many important low frequency structural modes, with significant aeroelastic contributions existing in all vehicle motions. With such

characteristics, the transfer function numerator roots for loop closure will be highly dependent on sensor mounting location, thus fostering a rich and challenging sensor placement problem. Significant aerodynamic coupling also rules out the potential for collocated actuator-sensor placement solutions due to violation of the necessary assumptions.

This dissertation will take the perspective that sensor placement and loop closure efforts should remain, for the most part, separate design steps in the overall closed-loop synthesis procedure. Such a two step strategy may ultimately limit the achievable closed-loop stability and performance to some extent. However, such partitioning is initially prudent when considering optimization-based methodologies, which tend to exploit unknown and often undesirable regions of the solution space. Further, releasing the sensor placement step to an optimizer while retaining the loop closure step for the engineer provides an attractive balance between automatic and manual functions. Even under this perspective, a few exploratory investigations involving coupled sensor placement and loop closure optimization are considered in this body of research. The conventional Evans root migration technique is exclusively considered in this dissertation for designing the closed-loop systems. At this time, production flight control systems are still primarily designed with conventional techniques for multiple reasons, and the dissertation is consistent with this trend. The reader should not interpret this to mean conventional control design techniques are superior to contemporary techniques, rather the reader should understand the selected design technique is amply sufficient for the dissertation focus. The dissertation research also exclusively considers angular rate feedback control architectures because of their effectiveness in this application. In other

words, only rate gyro sensor placement is addressed in this research effort, accelerometer sensors are not considered.

A key focus of the dissertation research involves formulating and identifying sensor placement criteria and objective functionals for optimization, which are tightly coupled to important closed-loop dynamic characteristics and the chosen control design technique that can leverage these characteristics effectively. Therefore, objective functions based on open-loop transfer function pole-zero geometric features in the complex frequency plane are of great importance to this dissertation. Various sensor placement criteria based on rigid-body mode and aeroelastic dipole root structures are investigated. In particular for aeroelastic dipoles, gain, phase, and mixed gain-phase, stabilization criteria are addressed. Appropriate constraint functions such as restrictions against nonminimum phase numerator roots or off-body sensor locations are also utilized. Primary decision variables for optimization include multi-sensor locations, while blending filter and control compensation parameters are secondary decision variables used in a limited fashion. The sensor placement research problem is formulated and posed within the rigorous framework of parameter optimization theory. Numerical search algorithms utilized in the dissertation research are based on low order, reduced convergence rate, gradient methods. These algorithms provide a stable and reliable solution at the expense of higher computational burdens. Higher order, multi-strategy algorithms available in commercial engineering software applications were considered, but ultimately were found to be unworkable for this complex application. The optimization problem is computationally intensive, requiring implicit gradient construction and generation of a high dimensional root locus solution involving

polynomial factoring and root sorting for each independent hyper-direction and at each iteration step.

Although engineering judgment and manual analysis are quite often used to determine favorable locations for flight control actuators and sensors (as discussed in Reference 45), there have been numerous attempts (other than in References 41 and 43) to develop systematic means for identifying optimal locations in non-flight control aerospace applications. A literature search for various actuator and sensor placement methods yielded a large number of publications from widely different engineering applications. For example, Reference 52 contains over 50 internal references on the subject matter alone. Some of the major applications include large flexible spacecraft vibration control,[53-63] aircraft panel and lifting surface flutter control,[64-68] vehicle exterior flow control,[69-74] mechanical structural control,[75-91] model identification/fault detection,[92-102] and interior cabin structural acoustic control.[103-109]

These existing techniques appearing in the literature for optimal auto sensor placement are related to the dissertation topic, but in many instances are not directly applicable. Majority of reported studies has focused on either

- Open-loop criteria such as controllability, observability, and transmission zeros,
- Closed-loop criteria such as quadratic metrics inherently tied to contemporary design,
- Unconstrained flexible space vehicles or constrained elastic terrestrial systems, or
- Vibrating structural or fluidic systems not strongly tied to free vehicle motion.

These studies often lack key aspects of the dissertation research topic. For example, state space controllablity and observability metrics, and contemporary design quadratic performance metrics, are not easily traceable to individual transfer function aeroelastic

dipole structures, and often do not capture critical phasing information. As another example, seldom will sufficient control bandwidth exist to relocate closed-loop poles near the transmission zeros. Unconstrained space vehicles and constrained terrestrial systems are undamped structures that do not have airflow pressure as the single most important load influencing the motion. Finally, pure vibrating systems lack the complexities associated with integrated flight control involving tightly coupled rigid motions and structural dynamics. A brief review of a few selected past works in these areas, and their contrast to the dissertation research, is given next.

In Reference 53, criteria for determining the optimal actuator and sensor locations is based on open-loop controllability and observability levels associated with a variably located actuator-sensor pair. The application is pure vibrational control of flexible space structures. The vehicle dynamics are modeled as a linear, vector second-order dynamical system. Based on this model structure, the controllable and observable subspaces, and their intersection subspace, are defined. An initial objective function based on the degree or size of the intersection subspace is considered. Actuator and sensor locations corresponding to large values for the objective function will yield a large number of states that can be broadly affected through feedback. A second, refined objective function based on the weighted projection of selected structural modes into the controllable-observable intersection subspace is introduced. Controllability and observability grammians are used to weigh the projection of these selected modes. Actuator and sensor locations corresponding to large values for this refined objective function will yield selected modes that can be efficiently augmented with feedback. The proposed search technique evaluates a given set of actuator-sensor positions for determining the best

locations, rather than finding the best actuator-sensor locations given a continuous region of feasible positions. The proposed technique is highly attractive but does not fit well to the dissetation research. The underlying objective in Reference 53 is maximum controllability-observability. Such a characteristic, while generally a desirable feature for any control scheme, oversimplifies the control problem. Formulating relationships between high levels of controllability-observability and desirable pole-zero structures, and in particular the phase relastionship between aeroelastic-to-aeroelastic and aeroelastic-to-rigid coupling, is difficult. Additionally, such objectives ignore rigid motion control objectives. Finally, most control design techniques do not directly utilize these measures.

Reference 54 also develops a method to place the sensors and actuators for active control of flexible space structures. Two placement metrics are considered for the optimization. The metrics are chosen such that, when optimized, the transmission zeros of the open-loop system are relocated farther to the left of the imaginary axis. The metrics are constructed around the real part of the system's transmission zeros. A nonlinear programming problem is posed to minimize the metrics. Sensor and actuator locations that yield transmission zeros deep within the left-half plane are desirable because the closed-loop poles migrate towards these locations for a high overall multivariable gain value. This proposed technique is highly attractive and is the most relevant work (other than References 41, 43, and 45) to the dissertation topic. However, this technique is also lacking in certain respects. Seldom is sufficient gain available to relocate the closed-loop poles to the transmission zeros. Further, individual input-output responses are not easily tailored with an overall system approach. Nevertheless, utilization of the concepts from

Reference 54 to relocate selected zeros to more favorable locations in individual channels benefits the dissertation research.

Reference 56 presents an algorithm that solves the problem of selecting a limited number of sensor and actuator locations from a given set to best achieve closed-loop output specifications with minimal input actuator power. The application is again for large space structures. Since the solution to this kind of problem requires a specific closed-loop control law structure, a technique for closed-loop control that is readily adjusted to meet the output specification with minimal power usage, and which allows assessment of sensor and actuator configurations in achieving these requirements, is needed. A Linear Quadratic Gaussian (LQG) controller is thus selected. This controller is extremely powerful with high utility for attacking the sensor-actuator selection problem. The algorithm involves no gradient or costly calculation beyond the LQG controller and can be used to adjust weight matrices to achieve the output specifications with minimal power. The effectiveness of each sensor and actuator is assessed through their contribution to the closed-loop LQG cost functional. Sensors and actuators with small effectiveness are eliminated. Appealing as this procedure is, some difficulties are encountered when applied to the dissertation research topic. LQG and other contemporary design methods based on cost function minimization, although quite suitable for regulation and vibration suppression, are not well suited for aeroelastic flight control where tailoring of the transient response due to commands, or shaping closed-loop pole-zero features in specific channels, is often required. Further, algorithm cost functions are not tightly coupled to the complex frequency domain design objectives.

Recasting the standard LQG regulation framework into a model following or model tracking framework may circumvent some of these difficulties, however.

Finally in Reference 64, the effectiveness of individual piezoceramic actuators, or groups of actuators, in terms of their contribution to joint controllability and observability levels, is investigated and examined from a flutter control design perspective. Joint controllablity and obsevability is quantified by the Hankel singular values. For given sets of candidate actuators, selection methodology is based on determining the relative effectiveness of these candidate actuators by decomposing this metric as a sum of contributions from each actuator. The goal of this strategy is to maximize the weighted Hankel singular value metric across the candidate actuators. The degree of participation of individual structural modes in the flutter control problem is used to weight the actuator selection metric. By decomposing the placement metric into contributions from individual actuators, *a priori* specification of the number of actuators is not required. In fact, by inspection of the decomposition, the optimum number of actuators can be determined. This approach is highly attractive for avoiding computational burdens associated with other methods involving combinational or optimizational searches. However, for the dissertation research topic, controllability, observability, and singular values are not easily traceable to detail transfer function pole-zero structures. Also, the Reference 64 technique is applied to a constrained lifting surface, which ignores the difficulties associated with dynamics and control of unconstrained flexible lifting surfaces or bodies.

1.3 Contributions of the Research

A new systematic methodology and strategy to determine optimal feedback sensor positions for a highly flexible atmospheric vehicle is developed. Overall control objectives are to supply artificial stability to the airframe, tailor key handling and ride quality responses, and to suppress aeroelastic motions. These first two objectives are considered indirectly, while the aeroelastic suppression objective is treated directly through sensor placement. Gain and phase stabilization placement criteria are utilized to achieve this later objective *via* Evans control design. This methodology and strategy is implemented with a numerical optimization software tool and demonstrated on an example large high-speed elastic airframe model. The theoretical formulation and numerical application has resulted in a new and systematic process which takes an initial flight control system with given augmentation characteristics and transforms this into a new system with improved augmentation characteristics by relocating the feedback sensors to more desirable locations. This contribution is significant and has practical application to important problems.

1.4 Dissertation Outline

Chapter 2 is a preliminary chapter that contains development of the equations of motion for non-rigid or aeroelastic vehicles and an associated numerical model used throughout the dissertation, as well as the flight control design strategy based on conventional theory. In particular, the Evans root locus or root migration technique is given attention, with particular emphasis directed towards key features to be considered in optimal sensor placement objective functionals. The importance of sensor location on

the resulting vehicle dynamics and flight control design effort are underscored and manual sensor placement results are reviewed and expanded. In Chapter 3, the theoretical framework for parameter optimization is laid out. The steepest descent or gradient method is explained for optimal numerical solutions. Attention is given to unconstrained, equality constrained, and inequality constrained problems. Various sensor placement objective functions with relevant constraints that have direct bearing on the control design strategy and objectives are defined.

The main body of the dissertation revolves around Chapters 4, 5, and 6, each dedicated to a class of objective functions used for optimally locating feedback sensors. In Chapter 4, objective functions based on dipole magnitude are investigated using two sensors. Such criteria are useful for gain stabilization of aeroelastic modes. Static and dynamic blending filters with fixed or variable parameters are investigated. In Chapter 5, objective functions based on complementary departure angle are investigated using two sensors. This class of criteria is used to stabilize the phase of aeroelastic modes. Fixed and variable static, and fixed and variable dynamic sensor blend filters are considered. In Chapter 6, both the dipole magnitude and complementary departure angle are used together to form a new class of objective functions. Criteria of this type allow for a mixed gain-phase stabilization control strategy. Two sensors are again considered with fixed and variable static and dynamic blend filtering. Additional cases with a variable compensation parameter are also investigated. A summary of these optimal sensor placement strategies is shown in Table 1.1. Finally, in Chapter 7, conclusions and recommendations are outlined.

Table 1.1 Summary of Optimal Sensor Placement Strategies

Cost Strategy / Blending/Compesating	Gain Stabilization $w_i\mu_i$	Phase Stabilization $w_i\phi_i$	Gain-Phase Stabilization $w_{\mu_i}\mu_i$, $w_{\phi_i}\phi_i$
Fixed Static Blending $h_1(s) = 1$ $h_2(s) = 1$ Fixed Compensating $k(s)=k_k(s+z_k)/s$	Section 4.2 x_{s1}, x_{s2} z_k=1 rad/s	Section 5.2 x_{s1}, x_{s2} z_k=2 rad/s	Section 6.2 x_{s1}, x_{s2} z_k=1 rad/s z_k=2 rad/s
Variable Static Blending $h_1(s)= c_1$ $h_2(s)= 1$ Fixed Compensating $k(s)=k_k(s+z_k)/s$	Section 4.3 x_{s1}, x_{s2}, c_1 z_k=1 rad/s	Section 5.3 x_{s1}, x_{s2}, c_1 z_k=2 rad/s	Section 6.3 x_{s1}, x_{s2}, c_1 z_k=1 rad/s z_k=2 rad/s
Fixed Dynamic Blending $h_1(s) = 1\frac{3}{s+3}$ $h_2(s) = 7\frac{s}{s+3}$ Fixed Compensating $k(s)=k_k(s+z_k)/s$	Section 4.4 x_{s1}, x_{s2} z_k=1 rad/s	Section 5.4 x_{s1}, x_{s2} z_k=2 rad/s	Section 6.4 x_{s1}, x_{s2} z_k=1 rad/s z_k=2 rad/s
Variable Dynamic Blending $h_1(s) = 1\frac{a}{s+a}$ $h_2(s) = 2a\frac{s}{s+a}$ Fixed Compensating $k(s)=k_k(s+z_k)/s$	Section 4.5 x_{s1}, x_{s2}, a z_k=1 rad/s	Section 5.5 x_{s1}, x_{s2}, a z_k=2 rad/s	Section 6.5 x_{s1}, x_{s2}, a z_k=1 rad/s z_k=2 rad/s
Variable Compensating $k(s)=k_k(s+z_k)/s$ Fixed Static Blending $h_1(s) = 1$ $h_2(s) = 1$ or Fixed Dynamic Blending $h_1(s) = 1\frac{3}{s+3}$ $h_2(s) = 7\frac{s}{s+3}$			Section 6.6 x_{s1}, x_{s2}, z_k

CHAPTER 2

MODELING, CONTROL, AND MANUAL SENSOR PLACEMENT

2.1 Introduction

This chapter deals with development of aeroelastic vehicle dynamics, flight control design for such dynamics, and manual sensor placement, which impacts both the vehicle dynamics and control system characteristics. Mathematical descriptions of aeroelastic dynamics are described and incorporated into traditional nonlinear aircraft equations of motion. A linearized model describing symmetric motion with numerical data is provided. Unacceptable dynamic characteristics are noted and motivate the need for feedback augmentation. Control of these dynamics is considered using a conventional method, namely the Evans root locus or root migration technique. Emphasis is given to the control objectives and how to leverage these objectives with the chosen design technique. The operation of an aircraft flight control system is greatly influenced by feedback sensor locations. The position of the sensors affect not only the stability of the closed-loop system, but also the attainable system performance. Selecting the number and the location of sensors is a very important design step, especially when the system of interest is a large aeroelastic vehicle. Manual sensor placement to facilitate desirable characteristics is also investigated.

2.2 Aeroelastic Vehicle Modeling

The current design and mission requirements for commercial and military high-speed transport aircraft are such that the resulting configurations require the use of thin lifting surfaces, long slender fuselages, low mass fraction structures, and high design stress levels. In turn, these features have resulted in aircraft that are structurally light and flexible. Such aircraft can exhibit large values of displacement, rate, and acceleration resulting from structural deformations, in addition to the components of displacement, rate, and acceleration arising from rigid-body motion of the aircraft. Such transients may occur as a result of aircraft maneuvers, which have been commanded by the pilot, or as a result of the aircraft's passage through turbulent air. When the amplitude of the elastic response is such that it compares with that of rigid-body motion, there can be an interchange between the rigid-body energy and the elastic energy to the detriment of the flying qualities of the aircraft. In addition, aircraft motion of this kind can result in a reduction of the structural life of the airframe due to large amplitude, high frequency cyclic loading.

When significant aeroelastic effects occur, they must be taken into account in the dynamic model. In these situations, it becomes necessary to augment the aircraft rigid-body equations of motion with a set of vibrational equations associated with the bending and torsional modes of the overall airframe. These bending and torsional modes are the normal modes in traditional vibration theory. For a continuous structural model, an infinite number of vibrational modes theoretically exist. When using finite element methods to model the structure, a finite but large number of vibration modes result.

Usually only a small set of significant modes are retained for the flight dynamics model. Conventional notation orders these modes with increasing natural frequency.

References 110-116 outline procedures for generating such models based on fundamental governing principles. Figure 2.1 illustrates the modeling framework. In this figure, *XYZ* and *xyz* denote inertial and body reference frames, respectively. Note the body frame is attached to the vehicle mass center, which does not correspond to any fixed mass particle within the vehicle. The "rigid" motion of the vehicle is described by the translational velocity vector $\vec{V}$, the translational position vector $\vec{R}$, the angular velocity vector $\vec{\Omega}$, and the angular positions Ψ, Θ and Φ (Euler angles). These variables track the complete motion of the body frame with respect to inertial space. The "flexible" motion of the vehicle, or the motion of the mass particles relative to the body frame, are described by the translational position vector $\vec{r}$. This vector is split into the constant equilibrium position vector $\vec{p}$ and the time dependent deformation position vector $\vec{q}$, which is defined with respect to the static equilibrium deformation shape. This deformation vector can be further decomposed into a summation of products involving the mode shape vectors $\vec{\phi}_i$ and generalized structural deflection coordinates ξ_i. By applying fundamental mechanics principles to a small infinitesimal mass *dm*, multiplying the governing expressions by both rigid and structural mode shapes, and integrating over the total vehicle mass, a set of governing expressions for the vehicle motion can be generated.

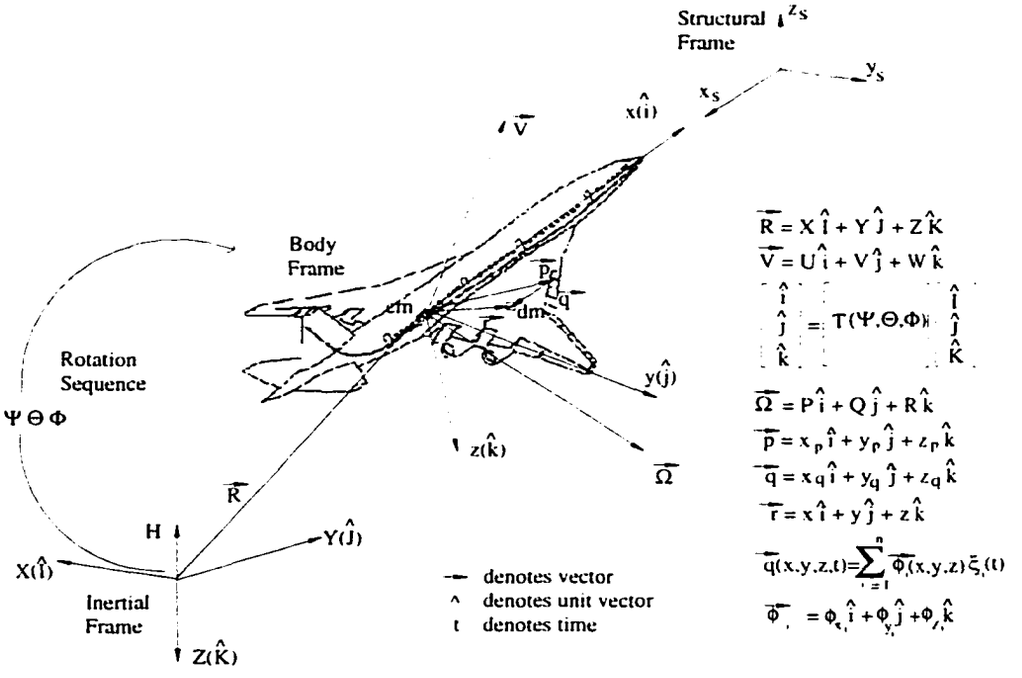

Figure 2.1 Aeroelastic Modeling Framework

The complete set of equations of motion are derived by Waszak in Reference 113, and are given in Equation (2.1). In the Waszak derivation, the structural deformation is considered small, the elastic deformation and rate are nearly collinear so their cross product is negligible, and the inertia tensor is assumed constant. Note inertial and structural coupling have been neglected in Equation (2.1).[116] Nevertheless, this dissertation is using Equation (2.1) as the basis for the vehicle dynamic model. Equation (2.1) contains three translational kinetic equations and three rotational kinetic equations that describe the "rigid" motion of an arbitrary aircraft in the body reference coordinate system and a set of *n* kinetic equations that describe the "flexible" motion relative to the body axes. Additionally, there are six translational and rotational kinematic equations for the rigid motion. In Equation (2.1), dynamic variables include translational velocity components *U*, *V* and *W*; rotational velocity components *P*, *Q* and *R*; translational

position components X, Y and H $(-Z)$; rotational position components Φ, Θ and Ψ; and generalized structural deflection ξ_i for the i^{th} aeroelastic mode. Aerodynamic and propulsive forces and moments for the kinetic equations include Q_X, Q_Y, Q_H, Q_Φ, Q_Θ, Q_Ψ and Q_{ξ_i}. Additional parameters of interest in Equation (2.1) include total mass m, inertia moment I_{ij}, gravity g, modal mass m_i, structural damping ζ_i, structural natural frequency ω_i, and number of aeroelastic modes n.

$$m[\dot{U} - RV + QW + g\sin\Theta] = Q_X$$

$$m[\dot{V} + RU - PW - g\sin\Phi\cos\Theta] = Q_Y$$

$$m[\dot{W} - QU + PV - g\cos\Phi\cos\Theta] = Q_H$$

$$I_{xx}\dot{P} - (I_{xy}\dot{Q} + I_{xz}\dot{R}) + (I_{zz} - I_{yy})QR + (I_{xy}R - I_{xz}Q)P + I_{yz}(R^2 - Q^2) = Q_\Phi$$

$$I_{yy}\dot{Q} - (I_{xy}\dot{P} + I_{yz}\dot{R}) + (I_{xx} - I_{zz})PR + (I_{yz}P - I_{xy}R)Q + I_{xz}(P^2 - R^2) = Q_\Theta$$

$$I_{zz}\dot{R} - (I_{xz}\dot{P} + I_{yz}\dot{Q}) + (I_{yy} - I_{xx})PQ + (I_{xz}Q - I_{yz}P)R + I_{xy}(Q^2 - P^2) = Q_\Psi$$

$$P = \dot{\Phi} - \dot{\Psi}\sin\Theta$$

$$Q = \dot{\Theta}\cos\Phi + \dot{\Psi}\cos\Theta\sin\Phi$$

$$R = \dot{\Psi}\cos\Theta\cos\Phi - \dot{\Theta}\sin\Phi$$

$$\dot{X} = U\cos\Theta\cos\Psi + V(-\cos\Phi\sin\Psi + \sin\Phi\sin\Theta\cos\Psi) + W(\sin\Phi\sin\Psi + \cos\Phi\sin\Theta\cos\Psi)$$

$$\dot{Y} = U\cos\Theta\sin\Psi + V(\cos\Phi\cos\Psi + \sin\Phi\sin\Theta\cos\Psi) + W(-\sin\Phi\cos\Psi + \cos\Phi\sin\Theta\sin\Psi)$$

$$\dot{H} = U\sin\Theta - V\sin\Phi\cos\Theta - W\cos\Phi\cos\Theta$$

$$\ddot{\xi}_i + 2\zeta_i\omega_i\dot{\xi}_i + \omega_i^2\xi_i = \left(\frac{1}{m_i}\right)Q_{\xi_i}$$

$$i = 1, 2, \ldots\ldots n \qquad (2.1)$$

Underlying assumptions in the development of Equation (2.1) include a flat Earth and constant gravity model, a single body vehicle with no internal motion due to spinning rotors or fluid slosh and neglection of inertia changes due to control surface movement, a constant mass vehicle, and small structural deformation. Under these assumptions, note the governing expressions in Equation (2.1) appear to be a direct union of traditional rigid-body equations of motion and traditional vibrational equations of motion. In particular, there is no direct inertial or structural coupling present in Equation (2.1). Significant rigid-flexible coupling will exist, however, in the aerodynamic and propulsive load terms. In Equation (2.1), also note the structural dynamics description has already been transformed from physical coordinates to generalized or modal coordinates.

Equation (2.2) shows a typical expansion of aerodynamic forces and moments in terms of nondimensional aerodynamic coefficients. In these expressions, α denotes angle of attack, β denotes side slip angle, Δ_j denotes the j^{th} control surface deflection, n_Δ denotes the number of control inputs, ρ denotes atmospheric density, V_T denotes total velocity, S denotes reference area, c denotes reference chord, b denotes reference span, C_{ij} denotes aerodynamic coefficient, and T_i denotes a propulsive load. These forces and moments completely describe the coupling which exists between the rigid-body and elastic degrees of freedom. For example, a structural deflection ξ_j can lead to a pitch moment Q_Θ due to the aerodynamic coefficient $C_{M_{\xi_j}}$. Likewise, a pitch rate Q can lead to a generalized or modal structural load Q_{ξ_i} due the aerodynamic coefficient $C_{\xi_{iQ}}$.

$$Q_X = \frac{\rho V_T^2 S}{2}(C_{X_0} + C_{X_\alpha}\alpha + C_{X_\beta}\beta + \sum_{j=1}^{n_\Delta} C_{X_{\Delta_j}}\Delta_j + \sum_{j=1}^{n} C_{X_{\xi_j}}\xi_j) + \frac{\rho V_T Sc}{4}(C_{X_P}P + C_{X_Q}Q + C_{X_R}R + \sum_{j=1}^{n} C_{X_{\dot{\xi}_j}}\dot{\xi}_j) + T_X$$

$$Q_Y = \frac{\rho V_T^2 S}{2}(C_{Y_0} + C_{Y_\alpha}\alpha + C_{Y_\beta}\beta + \sum_{j=1}^{n_\Delta} C_{Y_{\Delta_j}}\Delta_j + \sum_{j=1}^{n} C_{Y_{\xi_j}}\xi_j) + \frac{\rho V_T Sb}{4}(C_{Y_P}P + C_{Y_Q}Q + C_{Y_R}R + \sum_{j=1}^{n} C_{Y_{\dot{\xi}_j}}\dot{\xi}_j) + T_Y$$

$$Q_H = \frac{\rho V_T^2 S}{2}(C_{H_0} + C_{H_\alpha}\alpha + C_{H_\beta}\beta + \sum_{j=1}^{n_\Delta} C_{H_{\Delta_j}}\Delta_j + \sum_{j=1}^{n} C_{H_{\xi_j}}\xi_j) + \frac{\rho V_T Sc}{4}(C_{H_P}P + C_{H_Q}Q + C_{H_R}R + \sum_{j=1}^{n} C_{H_{\dot{\xi}_j}}\dot{\xi}_j) + T_H$$

$$Q_\Phi = \frac{\rho V_T^2 Sb}{2}(C_{L_0} + C_{L_\alpha}\alpha + C_{L_\beta}\beta + \sum_{j=1}^{n_\Delta} C_{L_{\Delta_j}}\Delta_j + \sum_{j=1}^{n} C_{L_{\xi_j}}\xi_j) + \frac{\rho V_T Sb^2}{4}(C_{L_P}P + C_{L_Q}Q + C_{L_R}R + \sum_{j=1}^{n} C_{L_{\dot{\xi}_j}}\dot{\xi}_j) + T_\Phi$$

$$Q_\Theta = \frac{\rho V_T^2 Sc}{2}(C_{M_0} + C_{M_\alpha}\alpha + C_{M_\beta}\beta + \sum_{j=1}^{n_\Delta} C_{M_{\Delta_j}}\Delta_j + \sum_{j=1}^{n} C_{M_{\xi_j}}\xi_j) + \frac{\rho V_T Sc^2}{4}(C_{M_P}P + C_{M_Q}Q + C_{M_R}R + \sum_{j=1}^{n} C_{M_{\dot{\xi}_j}}\dot{\xi}_j) + T_\Theta$$

$$Q_\Psi = \frac{\rho V_T^2 Sb}{2}(C_{N_0} + C_{N_\alpha}\alpha + C_{N_\beta}\beta + \sum_{j=1}^{n_\Delta} C_{N_{\Delta_j}}\Delta_j + \sum_{j=1}^{n} C_{N_{\xi_j}}\xi_j) + \frac{\rho V_T Sb^2}{4}(C_{N_P}P + C_{N_Q}Q + C_{N_R}R + \sum_{j=1}^{n} C_{N_{\dot{\xi}_j}}\dot{\xi}_j) + T_\Psi$$

$$Q_{\xi_i} = \frac{\rho V_T^2 Sc}{2}(C_{\xi_0} + C_{\xi_\alpha}\alpha + C_{\xi_\beta}\beta + \sum_{j=1}^{n_\Delta} C_{\xi_{\Delta_j}}\Delta_j + \sum_{j=1}^{n} C_{\xi_{\xi_j}}\xi_j) + \frac{\rho V_T Sc^2}{4}(C_{\xi_P}P + C_{\xi_Q}Q + C_{\xi_R}R + \sum_{j=1}^{n} C_{\xi_{\dot{\xi}_j}}\dot{\xi}_j) + T_\xi \tag{2.2}$$

Analysis of aeroelastic vehicle dynamics often requires information pertaining to the translational acceleration and rotational velocity at various points throughout the airframe. Starting with the former, the translational acceleration of infinitesimal mass *dm* in Figure 2.1 is

$$\vec{A} = \frac{d^2}{dt^2}(\vec{R} + \vec{r}) \tag{2.3}$$

where $d(\cdot)/dt$ denotes a derivative in the inertial frame. Upon expanding Equation (2.3) with basic principles, the acceleration becomes

$$\vec{A} = \frac{\partial}{\partial t}(\vec{V} + \frac{d\vec{r}}{dt}) + \vec{\Omega}\times(\vec{V} + \frac{d\vec{r}}{dt}) \tag{2.4}$$

where $\partial(\cdot)/\partial t$ denotes a derivative in the body frame. Further expansion of Equation (2.4) yields

$$\vec{A} = \frac{\partial \vec{V}}{\partial t} + \vec{\Omega}\times\vec{V} + \frac{\partial^2 \vec{q}}{\partial t^2} + 2\vec{\Omega}\times\frac{\partial \vec{q}}{\partial t} + \frac{\partial \vec{\Omega}}{\partial t}\times(\vec{p} + \vec{q}) + \vec{\Omega}\times(\vec{\Omega}\times(\vec{p} + \vec{q})) \tag{2.5}$$

If the body frame components of $\vec{A}$ are denoted as

$$\vec{A} = A_x \hat{i} + A_y \hat{j} + A_z \hat{k} \tag{2.6}$$

then expressions for the component accelerations are

$$\begin{aligned}
A_x &= \dot{U} + QW - RV + \ddot{x}_q + 2(Q\dot{z}_q - R\dot{y}_q) + \dot{Q}(z_p + z_q) - \dot{R}(y_p + y_q) - (Q^2 + R^2)(x_p + x_q) + PQ(y_p + y_q) + PR(z_p + z_q) \\
A_y &= \dot{V} + RU - PW + \ddot{y}_q + 2(R\dot{x}_q - P\dot{z}_q) + \dot{R}(x_p + x_q) - \dot{P}(z_p + z_q) - (P^2 + R^2)(y_p + y_q) + PQ(x_p + x_q) + RQ(z_p + z_q) \\
A_z &= \dot{W} + PV - QU + \ddot{z}_q + 2(P\dot{y}_q - Q\dot{x}_q) + \dot{P}(y_p + y_q) - \dot{Q}(x_p + x_q) - (P^2 + Q^2)(z_p + z_q) + PR(x_p + x_q) + QR(y_p + y_q)
\end{aligned} \tag{2.7}$$

where

$$\begin{aligned}
x_q &= \sum_{i=1}^{n} \phi_{x_i} \xi_i \\
y_q &= \sum_{i=1}^{n} \phi_{y_i} \xi_i \\
z_q &= \sum_{i=1}^{n} \phi_{z_i} \xi_i
\end{aligned} \tag{2.8}$$

Note these acceleration expressions are dependent on the measurement location explicitly through x, y and z and implicitly through $\phi_{x_i}(x, y, z)$, $\phi_{y_i}(x, y, z)$, and $\phi_{z_i}(x, y, z)$.

In similar fashion, expressions for the rotational velocity depend on the measurement location but only implicitly through deflection shape. Considering a general deformation state for the infinitesimal mass *dm* in Figure 2.1, the rotational velocity is

$$\vec{\Omega}' = \vec{\Omega} + \frac{\partial}{\partial t}(curl(\vec{q})) \tag{2.9}$$

This general expression accounts for significant modal deflection in all three body axes. If the body frame components of $\vec{\Omega}'$ are denoted as

$$\vec{\Omega}' = P'\hat{i} + Q'\hat{j} + R'\hat{k} \tag{2.10}$$

then the expressions for the component velocities are

$$P' = P + \sum_{i=1}^{n} \left(\frac{\partial \phi_{z_i}}{\partial y} - \frac{\partial \phi_{y_i}}{\partial z}\right)\dot{\xi}_i$$

$$Q' = Q + \sum_{i=1}^{n} \left(\frac{\partial \phi_{x_i}}{\partial z} - \frac{\partial \phi_{z_i}}{\partial x}\right)\dot{\xi}_i$$

$$R' = R + \sum_{i=1}^{n} \left(\frac{\partial \phi_{y_i}}{\partial x} - \frac{\partial \phi_{x_i}}{\partial y}\right)\dot{\xi}_i \tag{2.11}$$

Equations (2.7) and (2.11) describe auxiliary equations for extracting additional information from the complete model.

Equations (2.1), (2.7) and (2.11) are typically recast into first order state space form to facilitate their solution. For example, consider the equation of motion for the i^{th} aeroelastic mode in Equation (2.1). This equation is a second order differenential equation which can be represented by two first order, differential equations. If one introduces the notation x_1 and x_2 for the generalized deflection and rate, or

$$x_1 = \xi_i$$

$$x_2 = \dot{\xi}_i = \dot{x}_1 \tag{2.12}$$

then the i^{th} aeroelastic mode equation of motion can be represented in state space form as

$$\dot{x}_1 = x_2$$

$$\dot{x}_2 = -2\zeta_i \omega_i x_2 - \omega_i^2 x_1 + \left(\frac{1}{m_i}\right) Q_{\xi_i} \tag{2.13}$$

Reformulating the governing equations for U, V and W is accomplished by simple division and rearrangement. Equations for P, Q and R and Φ, Θ and Ψ are more involved. These equations are coupled at the first derivative level and must be simultaneously

manipulated to achieve the state space form. Equations for X, Y and H are already in state space form. After this process, the nonlinear state space model can be represented as

$$\begin{aligned} \dot{X}(t) &= f(X(t), U(t)) \\ Y(t) &= g(X(t), U(t)) \end{aligned} \tag{2.14}$$

where

$$\begin{aligned} X &= [U\ V\ W\ P\ Q\ R\ X\ Y\ H\ \Phi\ \Theta\ \Psi\ \dot{\xi}_1 \cdots \dot{\xi}_n \xi_1 \cdots \xi_n]^T \\ U &= [\Delta_1 \cdots \Delta_{n_\Delta}]^T \\ Y &= [A_{x_1} \cdots A_{x_{n_A}} A_{y_1} \cdots A_{y_{n_A}} A_{z_1} \cdots A_{z_{n_A}} P_1' \cdots P_{n_\Omega}' Q_1' \cdots Q_{n_\Omega}' R_1' \cdots R_{n_\Omega}']^T \end{aligned} \tag{2.15}$$

Elements of the vectors X, U and Y denote the state variables, inputs and outputs, respectively. Also, the functions f and g denote the nonlinear structure of the aircraft motion equations. Finally, n_A and n_Ω denote the number of translational acceleration and angular velocity output sets, respectively.

To perform synthesis of conventional control systems for an aircraft, linear equations are required. Various linearization techniques including numerical and analytical approaches are available for generating linear models. Two main reasons for using an analytical approach exist. First, linear stability and control derivatives can be estimated well before nonlinear aerodynamic data becomes available. The analytical model provides a framework for these early models. Second, the symbolic small perturbation equations provide a great deal of insight into the relative importance of the various stability and control derivatives under different flight conditions and into their effect on the stability and performance of the aircraft motion. Analytical linearization using a small perturbation approach first considers all variables to be given by the addition of a reference value and a perturbation value. The reference values correspond to

an equilibrium solution of the nonlinear equations. After substituting these expanded values into the nonlinear equations, canceling the reference solution, and neglecting the nonlinear terms, the linear model is obtained. To illustrate this method, the governing equation for U in Equation (2.1) will be explicitly linearized.

The governing equation for U is

$$\dot{U} = RV - QW - g \sin \Theta + Q_X / m \tag{2.16}$$

The equilibrium solution to this equation is denoted by subscript "0", or

$$\dot{U}_0 = R_0 V_0 - Q_0 W_0 - g \sin \Theta_0 + Q_{X_0} / m \tag{2.17}$$

Returning to Equation (2.16), consider each variable as consisting of a reference value plus a perturbation value, or

$$\dot{U}_0 + \dot{u} = (R_0 + r)(V_0 + v) - (Q_0 + q)(W_0 + w) - g \sin(\Theta_0 + \theta) + (Q_{X_0} + q_x)/m \tag{2.18}$$

Expanding this equation yields

$$\dot{U}_0 + \dot{u} = (R_0 V_0 + R_0 v + V_0 r + rv) - (Q_0 W_0 + Q_0 w + W_0 q + qw) - g(\sin\Theta_0 \cos\theta + \cos\Theta_0 \sin\theta) + (Q_{X_0} + q_x)/m \tag{2.19}$$

For small perturbation values, ignore multiplication terms involving perturbation values and consider the small angle approximations

$$\begin{aligned} \sin \theta &\approx \theta \\ \cos \theta &\approx 1 \end{aligned} \tag{2.20}$$

This process results in

$$\dot{U}_0 + \dot{u} = (R_0 V_0 - Q_0 W_0 - g \sin\Theta_0 + Q_{X_0} / m) + (R_0 v + V_0 r - Q_0 w - W_0 q - g \cos\Theta_0 \theta + q_X / m) \tag{2.21}$$

After canceling the reference solution, Equation (2.21) thus reduces to the following linear form:

$$\dot{u} = R_0 v + V_0 r - Q_0 w - W_0 q - g \cos\Theta_0 \theta + q_X / m \tag{2.22}$$

Note the lower case notation represents perturbation values, while upper case notation denotes the full values. Similar steps are applied to the other equations.

After this process, the linear state space model can be represented as

$$\begin{aligned} \dot{x}(t) &= Ax(t) + Bu(t) \\ y(t) &= Cx(t) + Du(t) \end{aligned} \tag{2.23}$$

where

$$\begin{aligned} x &= [u\ v\ w\ p\ q\ r\ x\ y\ h\ \phi\ \theta\ \psi\ \dot{\xi}_1 \cdots \dot{\xi}_n \xi_1 \cdots \xi_n]^T \\ u &= [\delta_1 \cdots \delta_{n_\Delta}]^T \\ y &= [a_{x_1} \cdots a_{x_{n_A}} a_{y_1} \cdots a_{y_{n_A}} a_{z_1} \cdots a_{z_{n_A}} p'_1 \cdots p'_{n_\Omega} q'_1 \cdots q'_{n_\Omega} r'_1 \cdots r'_{n_\Omega}]^T \end{aligned} \tag{2.24}$$

The elements of vectors x, u and y are also termed the state variables, inputs and outputs, respectively. Additionally, A is the state dynamics matrix, B is the input driving matrix, C is the output sensing matrix, and D is the direct feed through matrix.

The linear model at this stage is very general, encompassing many features. For the dissertation research, a specialized model is considered. The equilibrium solution corresponds to a wing-level, level rectilinear flight condition. Only longitudinal or symmetric motion will be considered, and the vehicle is assumed to exhibit strictly symmetric aerodynamic, structural, and propulsive behavior. Translational kinematics states are of no interest here and will be neglected. Structural deformations in the x axis are negligible and dropped. The number of aeroelastic modes retained in the simplified model is *18*. A single input corresponding to elevator deflection is considered ($n_\Delta=1$), and no acceleration output variables are considered ($n_A=0$). The output variable consists entirely of angular velocity signals corresponding to points along the fuselage centerline.

Under these conditions, the state and output equations represented by Equation (2.23) become

$$\dot{u} = X_u u + X_w w + (-W + X_q) q - g\cos\Theta\theta + \sum_{j=1}^{18} X_{\dot{\xi}_j} \dot{\xi}_j + \sum_{j=1}^{18} X_{\xi_j} \xi_j + X_{\delta_E} \delta_E$$

$$\dot{w} = Z_u u + Z_w w + (U + Z_q) q - g\sin\Theta\theta + \sum_{j=1}^{18} Z_{\dot{\xi}_j} \dot{\xi}_j + \sum_{j=1}^{18} Z_{\xi_j} \xi_j + Z_{\delta_E} \delta_E$$

$$\dot{q} = M_u u + M_w w + M_q q + \sum_{j=1}^{18} M_{\dot{\xi}_j} \dot{\xi}_j + \sum_{j=1}^{18} M_{\xi_j} \xi_j + M_{\delta_E} \delta_E$$

$$\dot{\theta} = q \tag{2.25}$$

$$\frac{\partial \dot{\xi}_i}{\partial t} = F_{i_u} u + F_{i_w} w + F_{i_q} q + \sum_{\substack{j=1 \\ j \neq i}}^{18} F_{i_{\dot{\xi}_j}} \dot{\xi}_j + (F_{i_{\dot{\xi}_i}} - 2\zeta_i \omega_i) \dot{\xi}_i + \sum_{\substack{j=1 \\ j \neq i}}^{18} F_{i_{\xi_j}} \xi_j + (F_{i_{\xi_i}} - \omega_i^2) \xi_i + F_{i_{\delta_E}} \delta_E$$

$$\frac{\partial \xi_i}{\partial t} = \dot{\xi}_i \qquad (i = 1, 2, \ldots 18)$$

$$q_i' = q - \sum_{j=1}^{18} \frac{\partial \phi_{z_j}}{\partial x} \dot{\xi}_j \qquad (i = 1, 2, \ldots\ldots n_\Omega)$$

Here the state, input and output vectors are

$$\begin{aligned} x &= [u \;\; w \;\; q \;\; \theta \;\; \dot{\xi}_1 \cdots \dot{\xi}_{18} \xi_1 \cdots \xi_{18}]^T \\ u &= [\delta_E]^T \\ y &= [q_1' \cdots q_{n_\Omega}']^T \end{aligned} \tag{2.26}$$

In Equation (2.25), the parameters Z_j, M_j, F_{ij} with $j = u,\ w,\ q,\ \dot{\xi}_j, \xi_j, \delta_E$ are dimensional stability and control derivatives having their origin in the aerodynamic coefficients in Equation (2.2). Also, in Equation (2.25), the terms $\frac{\partial \phi_{z_j}}{\partial x}$ are referred to as mode slopes and will be denoted by ϕ_j'.

The control design technique considered in this dissertation lies in the complex frequency domain. To convert the linear state space model in Equation (2.23) from the time domain to the frequency domain, application of Laplace transform theory is

considered. At a fundamental level, the Laplace transform replaces differential equations with algebraic equations, which are more amenable to dynamic analysis and control design. Application of the transform to Equation (2.23) yields

$$y(s) = G(s)u(s) \tag{2.27}$$

where

$$G(s) = C(sI - A)^{-1}B + D \tag{2.28}$$

$G(s)$ denotes the transfer function matrix and s represents complex frequency. The relationship between the i^{th} output y_i and the j^{th} input u_j is

$$y_i(s) = g_{ij}(s)u_j(s) = \frac{k_{g_{ij}} n_{g_{ij}}(s)}{d_g(s)} u_j(s) \tag{2.29}$$

where $g_{ij}(s)$ is the ij element of $G(s)$ with numerator and denominator polynomials k_{gij} $n_{g_{ij}}(s)$ and $d_g(s)$.

2.3 Numerical Model

Reference 17 contains numerical data consistent with the linear model structure given in Equation (2.25). A modified version of this data is documented in the Appendix for utilization in this dissertation. This data corresponds to a large high-speed transport whose three-view drawing is given in Figure A.1. The vehicle is characterized by a slender fuselage and cranked arrow wing with a conventional tail. The data corresponds to an ascent condition at weight *730,000 lbf*, *Mach 0.6* and altitude *6,500 ft*. The original model from Reference 17 is awkward in that coupling existed at the $\dot{u}$, $\dot{w}$, $\dot{q}$, $\ddot{\xi}_i$, $\ddot{\delta}_E$ level. Elimination of this coupling by algebraic manipulation of the governing equations was first implemented. Second, Reference 17 indicated a discrepancy in the imbedded

actuator model. To eliminate validity concerns, the supplied actuator dynamics were residualized out of the model. Finally, the stability derivative M_w was adjusted to bring the static margin from a value of *7.3* % stable to *10* % unstable. With the listed modifications, the numerical data corresponds precisely to the model in Equation (2.25) and represents behavior exhibited by current high-speed transport configurations under study. The numerical model in the Appendix is identical to that used in Reference 45.

The original mode shape data from Reference 17 is of a graphical nature, i.e., plots of fuselage centerline mode shape deflection vs. fuselage centerline station number. This information was converted to a numerical format by utilization of a graphics tablet input device with computer interface. Mode shape plots of this raw data were judged to be excessively rough for direct use in sensor placement studies. Therefore, polynomial curve fits to the raw data have been generated. Mode shape plots generated from the polynomial functions compare closely with the original information from Reference 17. The polynomial fits provide a significant capability and benefit, that being a smooth and continuous transfer function behavior during optimal sensor placement studies. The model in the Appendix is of such form that sensors can be placed anywhere along the fuselage centerline, and the corresponding model characteristics are easily generated. High order polynomials with *16*-digit precision are used in the fits. Readers are warned that truncation of the 16 digit information can lead to inaccurate mode shape representations. The results in Reference 45 utilized the full *16*-digit information but unfortunately only documented truncated mode shape information (*4* digits). The Appendix documents the full *16* digit information.

Figure 2.2 shows the aeroelastic mode shape data that will be critical during optimal sensor placement and control system development. In this figure, x_s and z_s denote the structural axes indicated in Figure 2.1. In Figure 2.2, the nose and the tail of the vehicle are at $x_s=120$ *in* and $x_s=3,640$ *in*, respectively. The vehicle mass center is located at $x_s=2,364$ *in*, although not associated with any specific mass particle. These modes represent free-free fuselage bending modes. Note the 1^{st} and 3^{rd} modes are similar to the first two modes of a free-free vibrating beam, but the 2^{nd} mode appears similar to a cantilevered beam bending mode. At a given value of x_s, note that the corresponding mode slope ϕ_j' directly influences the measured pitch rate signal (see Equation (2.25)).

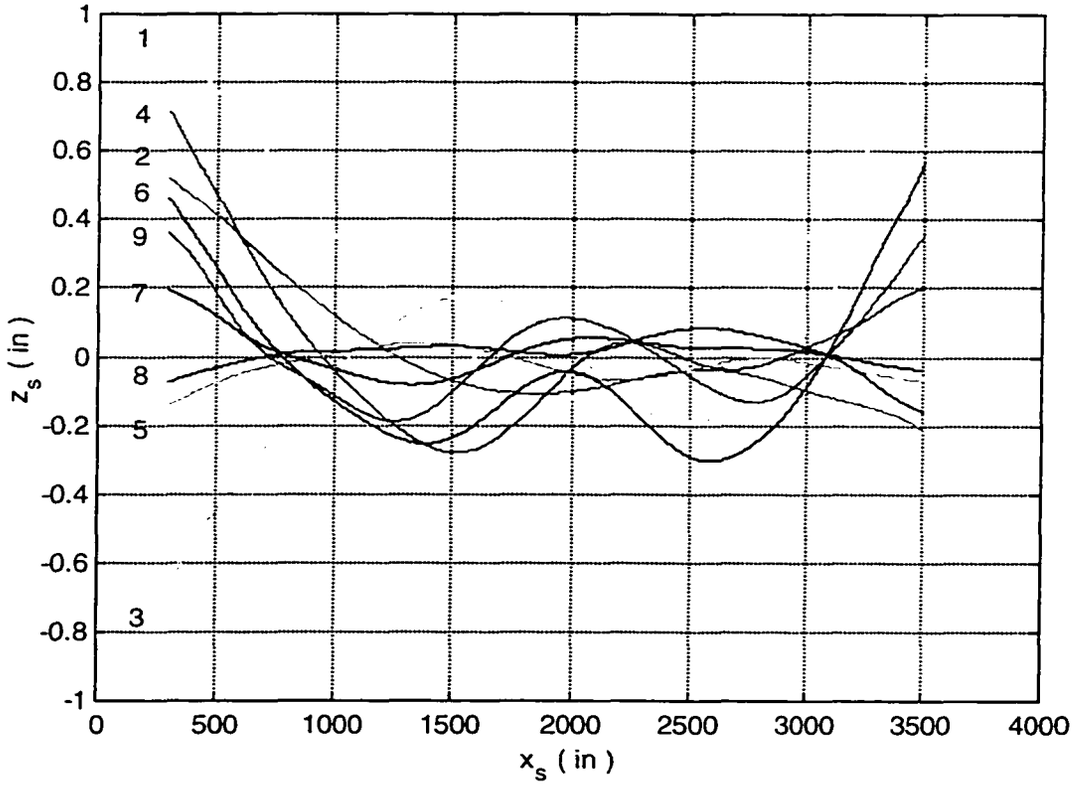

Figure 2.2a Aeroelastic Mode Shapes $1^{st} - 9^{th}$

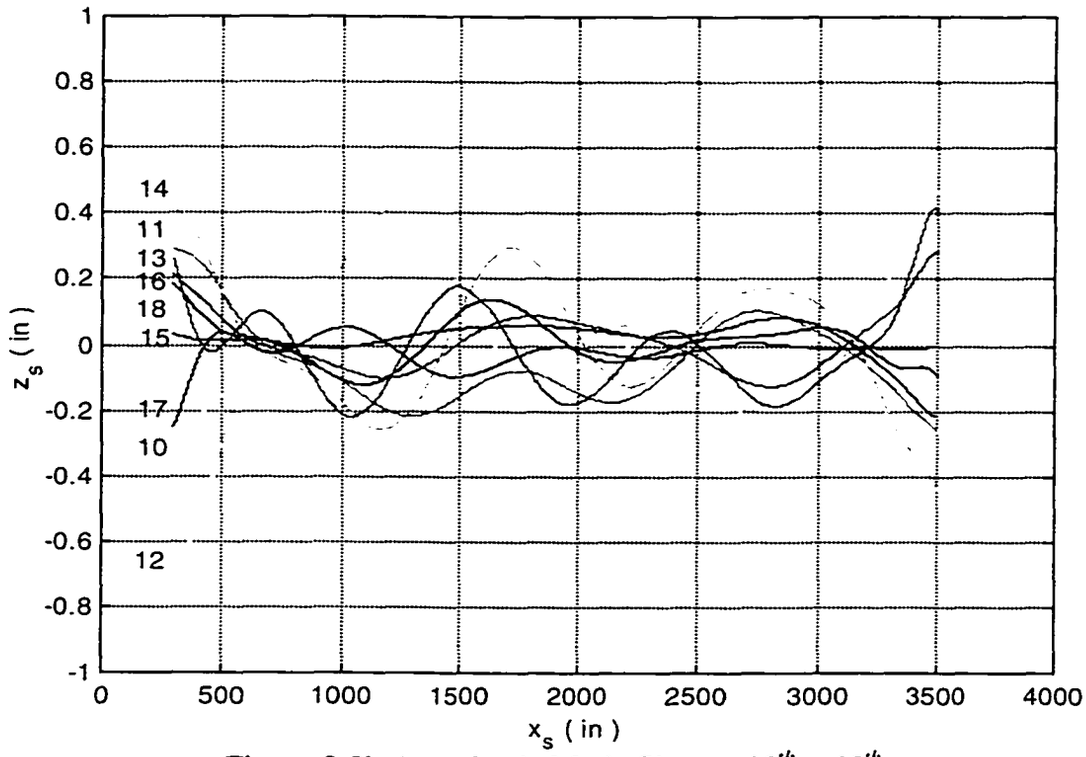

Figure 2.2b Aeroelastic Mode Shapes 10^{th} – 18^{th}

Table 2.1 lists the vehicle transfer function poles and zeros for two rate gyro sensors located near the mass center (x_s = *2,364 in*) and near the cockpit (x_s = *470 in*), both excited by the elevator. Further, Figures 2.3 and 2.4 show this same information graphically in a pole-zero plot. Examination of the vehicle poles in Table 2.1 and Figure 2.3-2.4 reveals a slow and fast rigid-body mode consisting of real roots at *s=+0.10 rad/s* and *s=-1.2 rad/s*. Note the slow mode is unstable. An additional mid frequency, moderately damped rigid-body mode referred to as the mid period mode, exists. This root structure is common for relaxed stability airframes. Another key denominator feature to note from Table 2.1 and Figure 2.3-2.4 is the 1^{st} aeroelastic mode (*s = -0.48±6.6i rad/s*) encroachment upon the rigid-body modes. The frequency separation is on the order of *5*

rad/s ($1/\tau_f = 1.2 rad/s$ vs. $\omega_{f_1} = 6.6 rad/s$). Also note the low damping values associated with all aeroelastic modes. For example, the 1^{st} mode damping ratio is $\zeta_{f_1} = 0.072$.

Table 2.1 Pitch Rate to Elevator Transfer Function Roots

Pole Location (rad/s)	Zero Location (rad/s)		Description
	$x_s = 470$ in Near Cockpit	$x_s = 2{,}364$ in Near Mass Center	
0.1024	0.0000	0.0000	Slow Mode, Pitch "Rate"
-0.1347±0.1093i	-0.0077	-0.0080	Mid Period Mode, $1/\tau_{\theta 1}$
-1.2131	-0.9375	-0.8211	Fast Mode, $1/\tau_{\theta 2}$
-0.4810±6.6284i	5.6026, -6.3884	-0.2403±4.5713i	1st Aeroelastic Mode
-1.9880±11.5569i	-2.3033 ± 11.7474i	-2.1131±11.5688i	2nd Aeroelastic Mode
-1.4348±14.7947i	-0.8283±16.7504i	-1.1452±16.3948i	3rd Aeroelastic Mode
-0.2287±16.4596i	-0.4480±23.7592i	-0.2708±16.9802i	4th Aeroelastic Mode
-0.6288±23.3865i	-0.2041±27.4501i	-0.5570±23.5419i	5th Aeroelastic Mode
-0.6680±26.0989i	-0.7510±30.2251i	-25.0609, 25.9264	6th Aeroelastic Mode
-1.9759±28.6077i	-3.2524±29.1919i	-0.5456±26.8727i	7th Aeroelastic Mode
-0.5698±30.2615i	-0.9781±32.9799i	-2.1659±28.6276i	8th Aeroelastic Mode
-0.7014±32.1397i	-11.8388±19.9198i	-0.6405±30.3500i	9th Aeroelastic Mode
-2.1891±34.0659i	-0.9128±35.6675i	-0.5182±32.6955i	10th Aeroelastic Mode

-0.9040±35.6531i	11.5102±19.2991i	-2.4196±34.8419i	11th Aeroelastic Mode
-1.0334±37.6964i	1.7893±40.1607i	-0.7639±35.6178i	12th Aeroelastic Mode
-2.0190±40.0829i	-4.0517±40.4330i	-0.9334±39.1756i	13th Aeroelastic Mode
-0.9878±42.3940i	-0.7905±43.0678i	-0.9681±41.7515i	14th Aeroelastic Mode
-1.1154±44.0400i	-0.8519±44.4465i	-1.2387±43.8843i	15th Aeroelastic Mode
-0.9673±45.2972i	-0.7497±47.0483i	-1.0067±44.9968i	16th Aeroelastic Mode
-2.7348±46.5602i	-2.8929±47.2543i	-2.7105±46.3199i	17th Aeroelastic Mode
-1.0438±47.2865i	-55.2341, 65.5153	-0.8922±47.4450i	18th Aeroelastic Mode

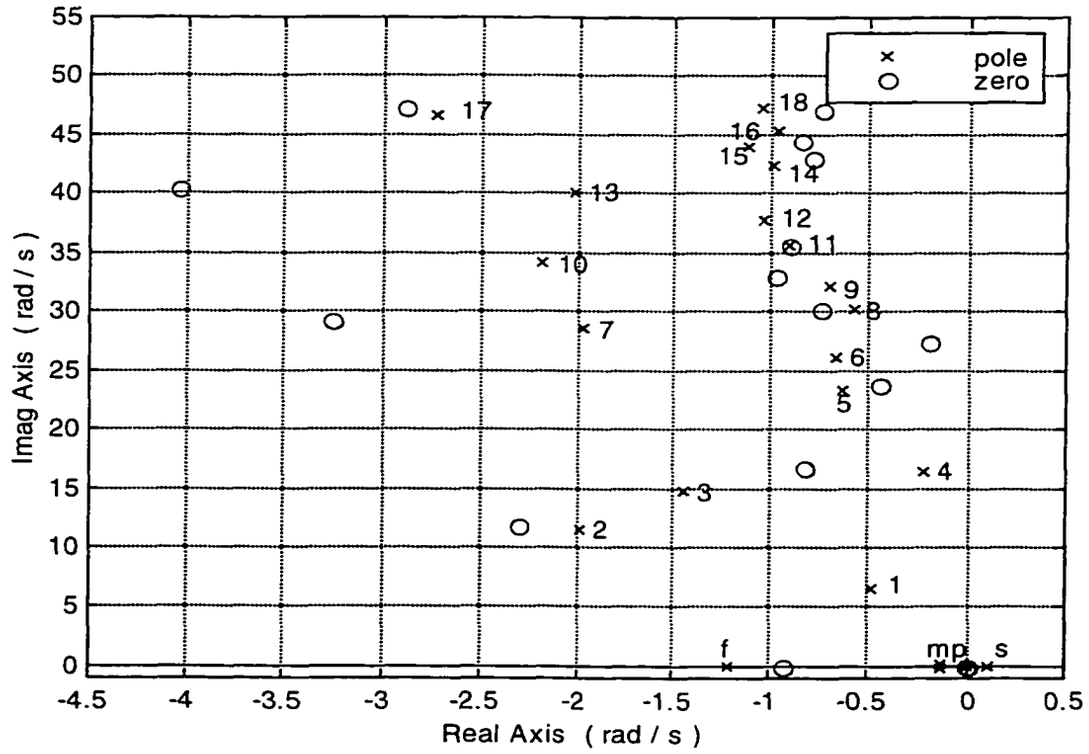

Figure 2.3 Pole-Zero Locations for x_s=*470 in*

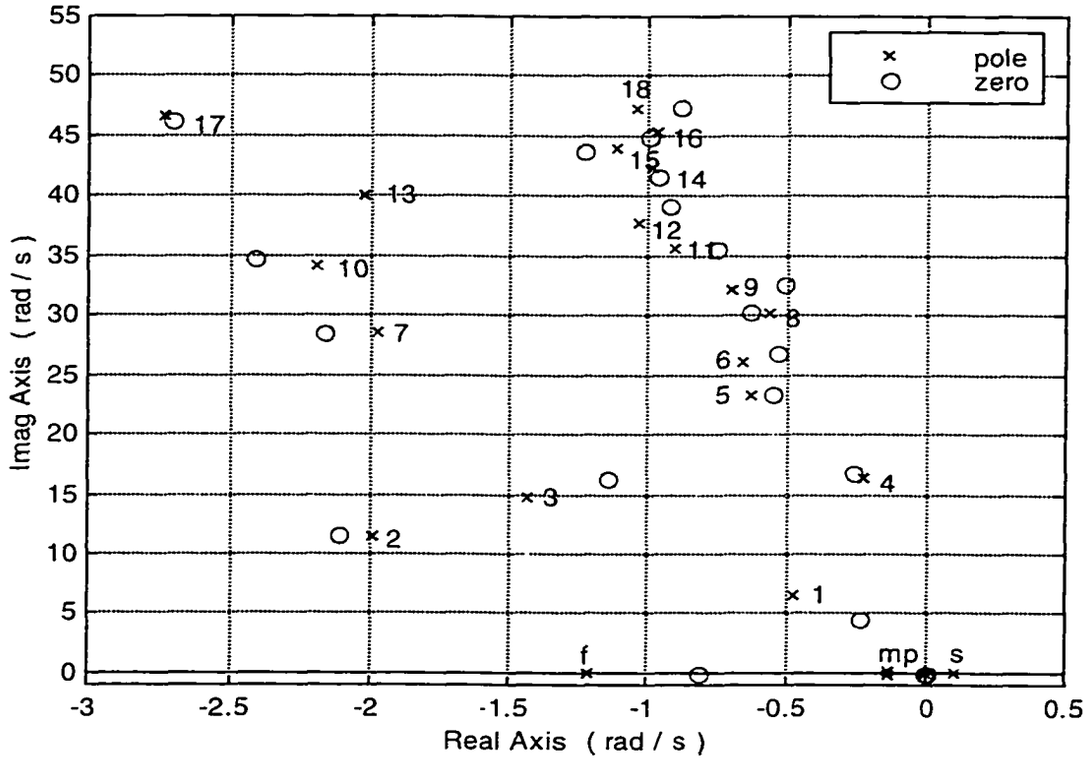

Figure 2.4 Pole-Zero Locations for x_s=*2,364 in*

Figures 2.5 and 2.6 show the q_i'/δ_E frequency responses for x_s=*470 in* and x_s=*2,364 in*. Observe the limited frequency separation between the fast rigid and 1^{st} aeroelastic modes near *1* and *6 rad/s*. Low aeroelastic mode damping is also evidenced in Figures 2.5-2.6 by the many sharp peaks in the magnitude responses. The presence of these large peaks indicate significant aeroelastic participation in, and contamination of, the pitch rate signals. This information is also observable from Table 2.1. For example, the mass center numerator roots *s=-0.24±4.6i rad/s* do not sufficiently "cover" the 1^{st} aeroelastic poles *at s=-0.48±6.6i rad/s*, which corresponds to the large valley and peak near *6 rad/s* in Figure 2.6. Finally, observe the phase roll off in the cockpit sensor

frequency response near *6 rad/s*. This phase loss is a direct result of the absence of a complex numerator root for the 1^{st} aeroelastic mode (see Table 2.1 for x_s=*470 in*). In fact, the corresponding zeros are real with *s=+5.6 rad/s* and *s=-6.4 rad/s*. Note one of these roots is the strongly nonminimum phase. This contrasting numerator information illustrates the point that sensor location strongly influences the resulting dynamics.

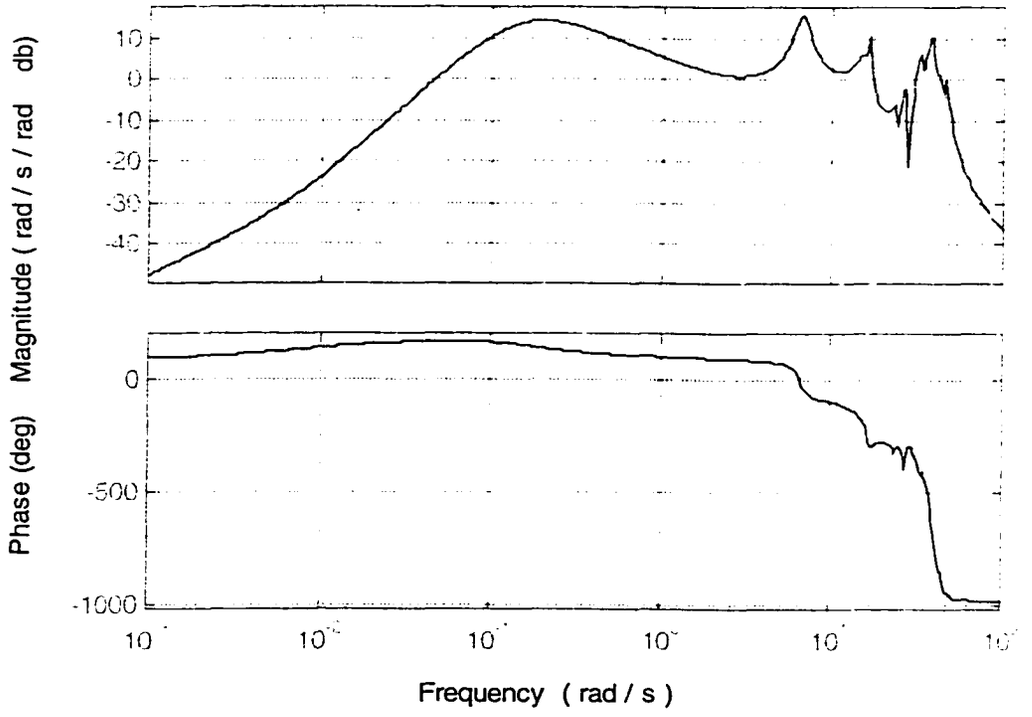

Figure 2.5 Frequency Response for x_s=*470 in*

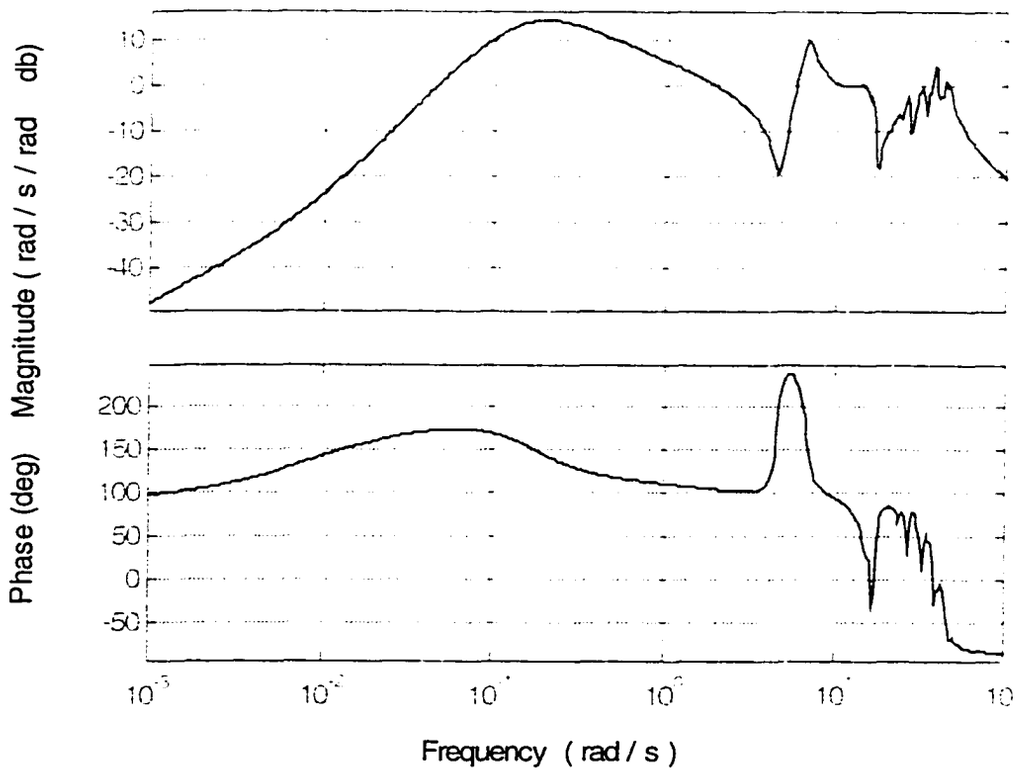

Figure 2.6 Frequency Response for x_s=*2,364 in*

Figures 2.7 and 2.8 show the corresponding time responses for a nose up *0.01 rad* elevator step command. For a moderately flexible vehicle, a rate gyro sensor placed near the mass center will typically yield an acceptable response. In this case, the response in Figure 2.8 is unsatisfactory due to the unstable airframe divergence and oscillatory aeroelastic motions. Also note the initial short duration response reversal due to the right-half plane zero at *s=+25.9 rad/s* (see Table 2.1). Matters are even worse for x_s=*470 in.* Due to the extreme levels of flexibility in the vehicle structure and the location of the crew station relative to the input device, the cockpit pitch rate response in Figure 2.7 exhibits a harsh high frequency vibration environment with strong response reversal. This

nonminimum phase characteristic can be traced directly to the *s=+5.6 rad/s* zero in Table 2.1. In summary, the airframe dynamics are unacceptable for manual control by the pilot, and flight control augmentation is necessary.

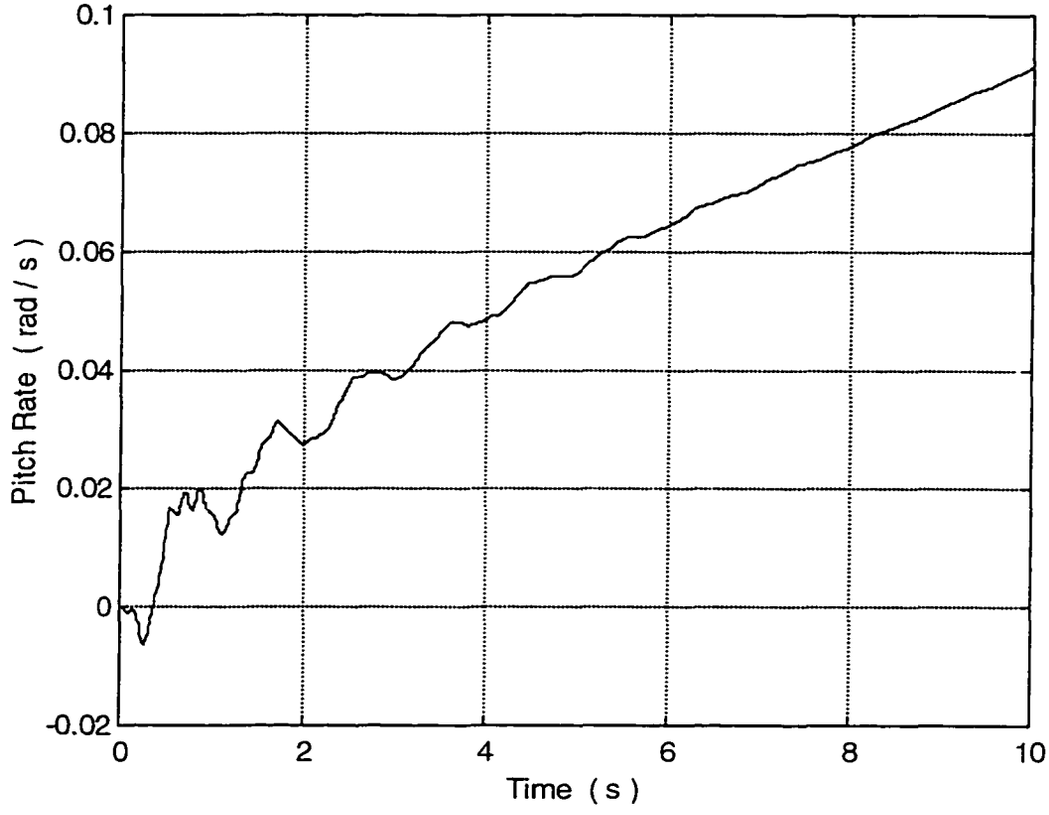

Figure 2.7 Step Response for x_s=*470 in*

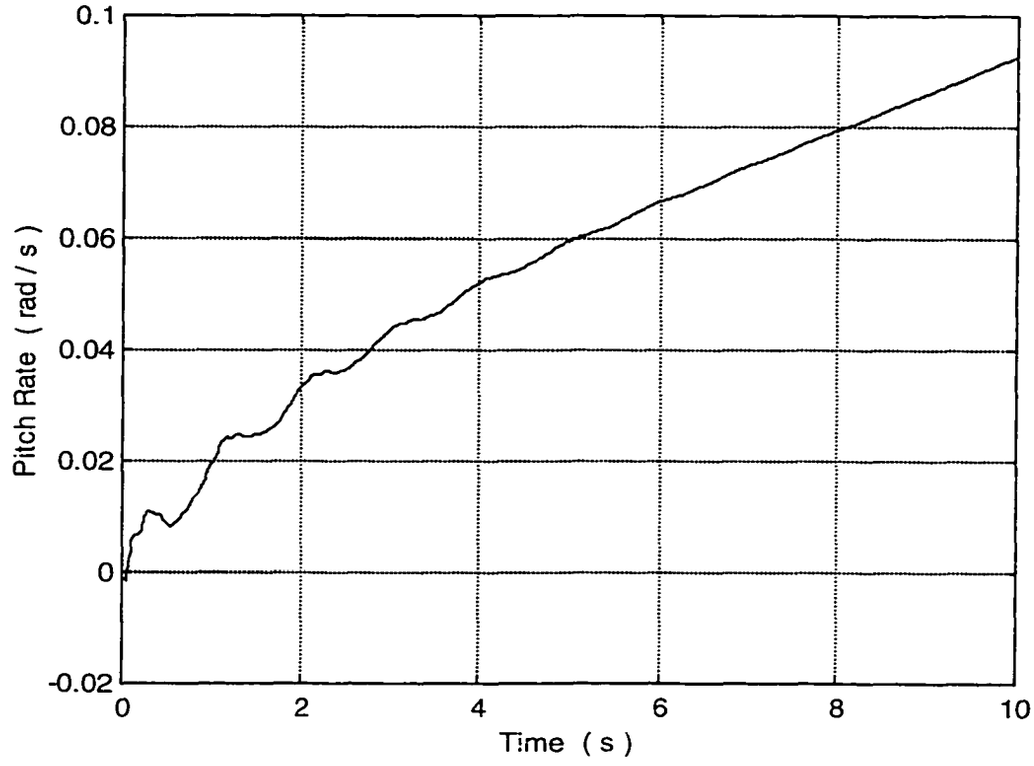

Figure 2.8 Step Response for x_c=*2,364 in*

2.4 Aeroelastic Flight Control

At this time, production flight control systems are still primarily designed with conventional techniques. Widely available and highly attractive contemporary techniques developed over the last quarter century are being considered for such applications, yet conventional techniques still hold a prominent position in the practice of flight control. Several important factors contribute to this longevity. Conventional methods are based on direct, explicit, and often graphical frameworks that link the relevant closed-loop features to the design freedoms. These attributes foster insight and confidence in the control law's stabilization and/or augmentation of the vehicle. The role each feedback loop plays in

leveraging specific plant modes, or the effect of individual compensation parameters on key closed-loop traits, is transparent. Such methods yield low order, minimal architecture solutions that are amenable to modification during test and development. As with any design method, conventional techniques also have weaknesses, the major ones being an inability to fully address multivariable systems and parametric uncertainty.

Based on these observations, the Evans root migration technique is selected for aeroelastic flight control development in this dissertation. Even with this design technique, a precursory step is to identify suitable feedback sensor locations. For if the vehicle transfer dynamics are not suitable, then no amount of gain adjustment or filter equalization with the Evans technique will yield satisfactory results. Optimal sensor placement is the primary dissertation focus, but before considering that topic, familiarization with the design technique and the desired objectives must be briefly reviewed.

Consider a *2x1* system (see Equation (2.27)) whose dynamics are to be augmented with feedback, such as an aircraft with inherent deficiencies, or

$$\begin{bmatrix} y_1(s) \\ y_2(s) \end{bmatrix} = \begin{bmatrix} g_{11}(s) \\ g_{21}(s) \end{bmatrix} u(s) \tag{2.30}$$

In this development, the output signals are generic. However, in the high-speed transport application, y_1 and y_2 could represent pitch rate measurements from two gyro sensors, while u may represent elevator deflection. Suppose the y_1 to u loop is closed with forward path compensation. The feedback control law is

$$u(s) = k(s)(y_{1_c}(s) - y_1(s)) \tag{2.31}$$

where $k(s)$ denotes the compensator transfer function and y_{1c} is the command signal entering the loop. Figure 2.9 shows the corresponding block diagram. The compensator $k(s)$ is further expressed with numerator and denominator polynomials $k_k n_k(s)$ and $d_k(s)$, where $n_k(s)$ is monic. The purpose of this loop might be to augment damping or quicken the response of important modes or to stabilize inherent airframe instabilities, for example. Substituting Equation (2.31) into Equation (2.30) yields the closed-loop system, or

$$\begin{aligned} y_1(s) &= \frac{k(s)g_{11}(s)}{1+k(s)g_{11}(s)}\, y_{1c}(s) \\ y_2(s) &= \frac{k(s)g_{21}(s)}{1+k(s)g_{11}(s)}\, y_{1c}(s) \end{aligned} \tag{2.32}$$

In Equation (2.32), note the denominator polynomial is strongly influenced by the feedback, while the original numerator polynomials are preserved and combined with compensation numerator terms.

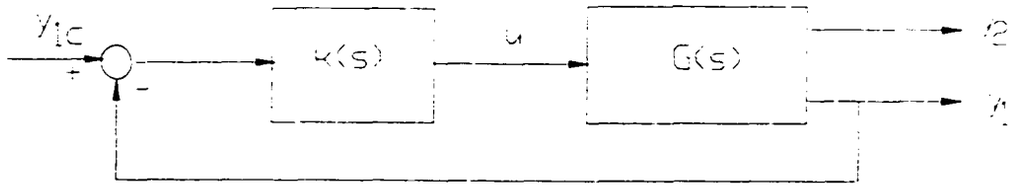

Figure 2.9 Closed-Loop System with One Feedback

For a given plant ($k_{g_{11}} n_{g_{11}}(s), d_g(s)$) and compensation ($n_k(s)$, $d_k(s)$), the Evans root locus technique is used to relocate the closed-loop denominator roots for various values of k_k.[117,118] The characteristic equation from Equation (2.32) can be written as

$$1 + k(s) g_{11}(s) = 0 \tag{2.33}$$

The root locus method provides a graphical means of evaluating the roots of Equation (2.33) as k_k varies. To develop a few key design guidelines for this method, Equation (2.33) is rewritten as a magnitude and phase condition, or

$$| k(s) g_{11}(s) | = 1 \tag{2.34}$$

$$\angle k(s) g_{11}(s) = 180^{\circ} \pm 360^{\circ} r \tag{2.35}$$

where r denotes any integer. If the combined plant-compensator polynomials are factored as

$$\begin{aligned} n_k(s) n_{g_{11}}(s) &= (s + z_1)(s + z_2) \cdots (s + z_{m'}) \\ d_k(s) d_g(s) &= (s + p_1)(s + p_2) \cdots (s + p_{n'}) \end{aligned} \tag{2.36}$$

then the magnitude and phase conditions become

$$| k_k | = \frac{\prod_{i=1}^{n'} | s + p_i |}{| k_{g_{11}} | \prod_{i=1}^{m'} | s + z_i |} \tag{2.37}$$

$$\angle k_k + \angle k_{g_{11}} + \sum_{i=1}^{m'} \angle s + z_i - \sum_{i=1}^{n'} \angle s + p_i = 180^{\circ} \pm 360^{\circ} r \tag{2.38}$$

In Equations (2.37)-(2.38), n' and m' denote the number of poles and zeros in the combined plant-compensator or open-loop system. Any point in the Laplace plane that satisfies the above two conditions is a possible closed-loop pole location for some value of k_k.

From Equation (2.37), note that for a value of s equal to one of the poles ($s=-p_i$), the gain k_k is null ($|k_k|=0$). On the other hand, for a value of s equal to one of the zeros ($s=-z_i$), or an infinite value ($|s|=\infty$) for $n' > m'$, the gain k_k is infinite ($|k_k|=\infty$). Therefore, the first guideline is the closed-loop pole migration paths initiate at the open-loop poles for $|k_k|=0$ and terminate at the open-loop zeros, or at infinity, for $|k_k|=\infty$. Figure 2.10 illustrates this guideline. As the compensator gain is increased, the closed-loop poles will move away from the open-loop poles and towards the open-loop zeros. This guideline is a fundamental rule that is useful when trying to shape the migration paths with either filter equalization or sensor placement.

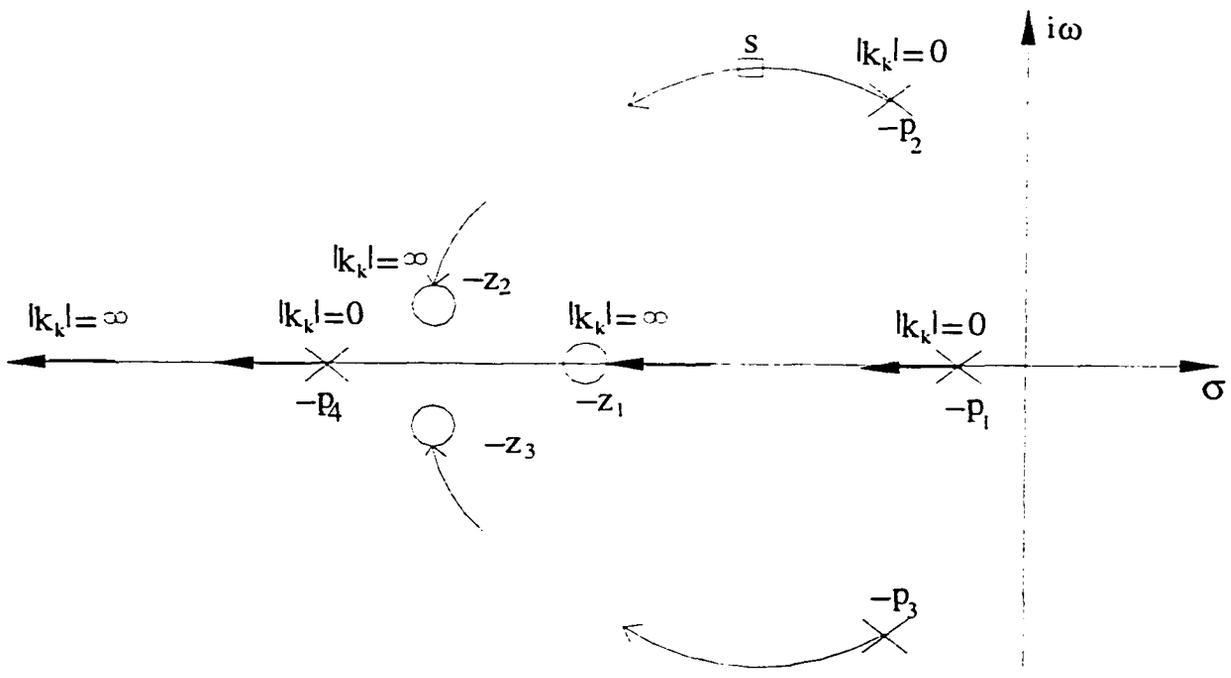

Figure 2.10 Guideline for Initial and Terminal Points

In Equation (2.38), consider the stabilizing case when k_k is chosen to have the same sign as $k_{g_{11}}$. To satisfy the right-hand side of this expression, the left-hand side must lead to an integer multiple of 180 deg. For a given value of s on the real axis ($s=\sigma$), Equation (2.38) requires the total phase from the polynomial factor terms to also equal an integer multiple of 180 deg. The only condition leading to this equality is when an odd number of poles and zeros lie to the right of the s value location. Due to symmetry about the real axis, when counting the number of open-loop poles and zeros to the right of the s point, one only needs to consider poles and zeros on the real axis. Therefore, a second guideline is the closed-loop pole migration path will lie on the real axis only in the region where they are to the left of an odd number of open-loop poles and zeros. Figure 2.11 illustrates this guideline. This guideline is another fundamental and well known rule that is useful when designing the closed-loop system with this technique.

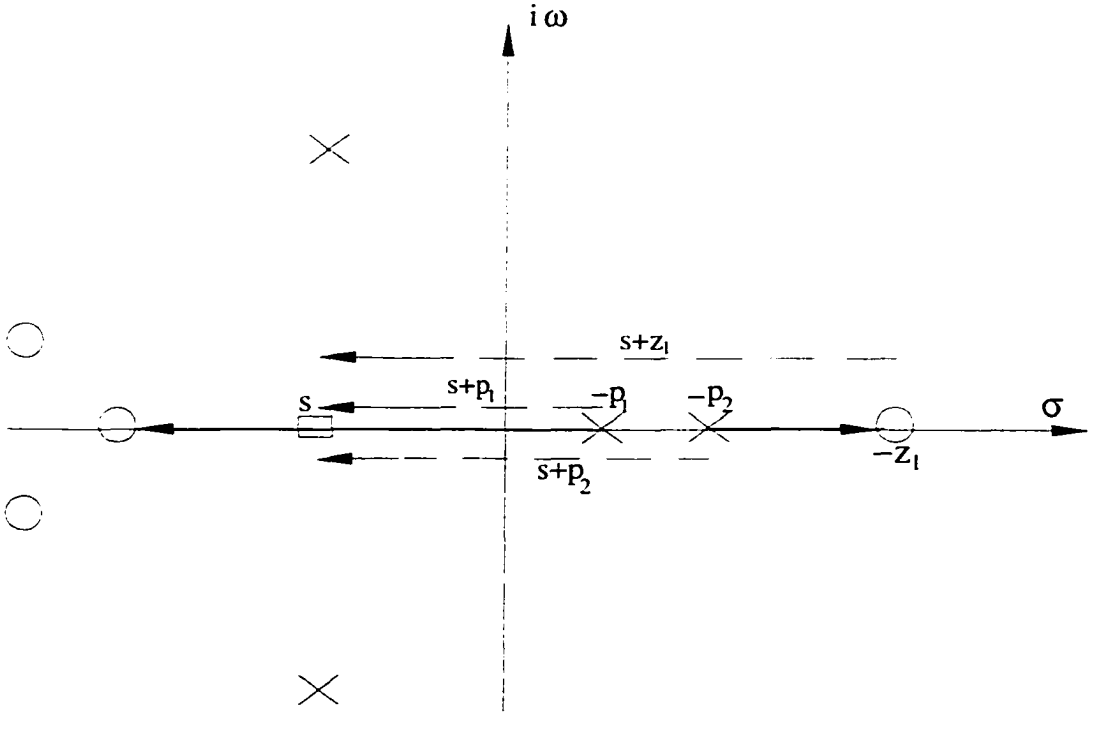

2.11 Guideline for Real Axis Segments

Reconsider Equation (2.38) again with k_k and $k_{g_{11}}$ having the same sign. Now consider a value of s located very close to the j^{th} open-loop complex pole ($s=-p_j+\varepsilon$, $|\varepsilon| \to 0$ along the migration path). The angle of departure is defined as the angle between the real axis and the tangent line to the migration path at the initial point corresponding to $|k_k|=0$. Mathematically, this angle is defined as

$$\theta_{d_j} = \lim_{\substack{|\varepsilon| \to 0 \\ along\ \ line}} \angle (s + p_j) \Big|_{s=-p_j+\varepsilon} \tag{2.39}$$

and with Equation (2.38), an expression for this departure angle is

$$\theta_{dj} = \sum_{i=1}^{m'} \angle (s + z_i) \Big|_{s=-p_j} - \sum_{\substack{i=1 \\ i \neq j}}^{n'} \angle (s + p_i) \Big|_{s=-p_j} + 180^{\circ} \pm 360^{\circ} r \tag{2.40}$$

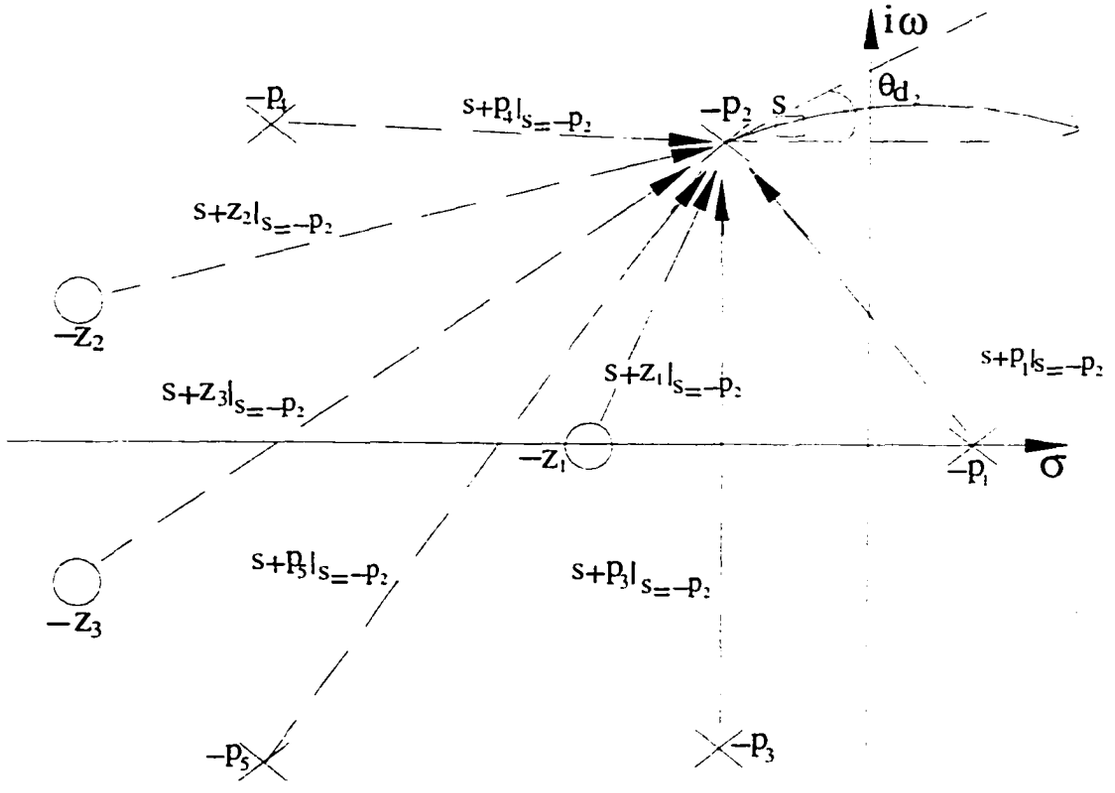

Figure 2.12 Guideline for Departure Angles

Therefore, a third and final guideline is the closed-loop pole migration path initially departs from the open-loop complex pole location with an angle governed by Equation (2.40). Note this departure angle is completely determined by the open-loop root locations. Figure 2.12 illustrates this guideline. This guideline is also a fundamental rule that is useful in Evans control design. There are many other guidelines developed in References 117-118, but these highlighted results are particularly useful here.

General objectives of the flight control system are to supply artificial stability, which is inherently lacking in the bare airframe, to reshape key pilot or passenger centered responses to satisfy handling and ride requirements, and to suppress aeroelastic motions in all responses. Specifically, the control system should stabilize the unstable slow mode in Table 2.1 and should do so in a manner which leads to conventional response types with appropriate behavior. Simultaneously, the control system must stabilize and suppress the aeroelastic modes in Figures 2.3-2.4 by either gain stabilization (approximate mode cancellation) or phase stabilization (increased damping) strategies. Note that gain stabilization here in an Evans context has a slightly different connotation than in a Bode sense (e.g., attenuation or $|k(i\omega)g_{11}(i\omega)| << 1$).

First, consider the low frequency, rigid airframe stabilization and handling-ride quality objectives. Careful examination of the low frequency pole-zero root structure in Table 2.1, coupled with Evans design rules mentioned previously, reveals that a proportional plus integral feedback of pith rate, or

$$k(s) = \frac{k_k (s + z_k)}{s} \tag{2.41}$$

results in 1) stabilization and suppression of the unstable slow mode by driving it into the $1/\tau_{\theta 1}$ zero, 2) suppression of the stable fast mode by driving it into the $1/\tau_{\theta 2}$ zero, and 3) augmentation of the mid period mode by relocating it to a more desirable region in the complex frequency plane. Figure 2.13 illustrates these key features of the control loop. For sufficient control gain k_k, the slow and fast modes are essentially eliminated from the dynamics, and the mid period mode is converted into the dominant oscillatory pitch mode with desirable damping and frequency. As this latter root migration path wraps around the compensator zero $-z_k$, the pitch mode damping and frequency can be easily and directly tailored with parameters k_k and z_k. Note the open-loop system is not rigorously Type *1* because the pitch "rate" zero precisely cancels the integral action in Equation (2.41). However, the augmented slow mode will lie close to the origin, and the closed-loop system will thus behave similar to a pitch rate command system over the initial duration of interest. This response type is consistent with the short period approximation. This control architecture has been referred to as a "superaugmented pitch loop" and is highly attractive.[45-47] Alternative feedback signals can be used to stabilize this type of airframe,[7] but these possibilities are not considered here.

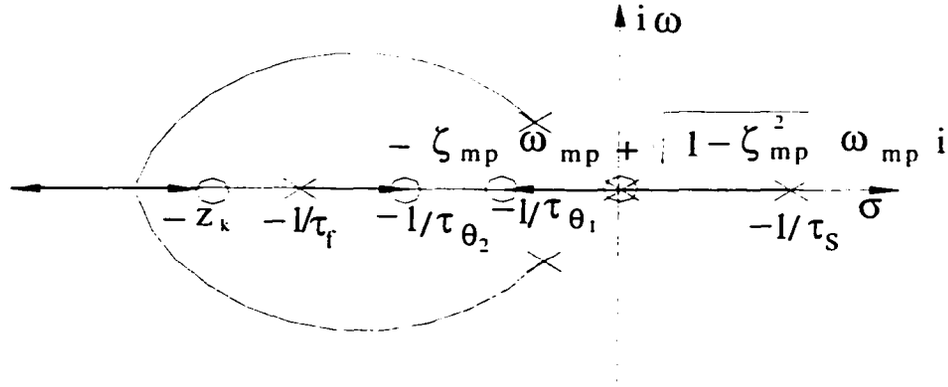

Figure 2.13 Low Frequency Augmentation

Now consider the high frequency, flexible airframe stabilization and suppression objectives. Close examination of the high frequency pole-zero structure in Table 2.1 or Figures 2.3-2.4 reveals that in most cases a lightly damped flexible mode lying near the imaginary axis is accompanied by an associated zero. Typically, the zero lies near the pole, but in some cases the zero can be far removed from the pole. This lightly damped pole-zero pair is commonly referred to as a dipole, and the location of the zero, relative to the pole, is critical for influencing closed-loop behavior. Using the Evans design guidelines developed previously, Figure 2.14 illustrates the various closed-loop possibilities. If the zero is very close to the pole (i.e., a tight dipole structure), the root migration path is constrained to lie within a small region near the dipole. In this situation, the aeroelastic mode is gain stabilized and the mode is essentially removed from the corresponding closed-loop input-output channel. Of course, for a different input-output

channel, the mode may not be similarly suppressed. The pole-zero separation (dipole magnitude) is critical here.

In contrast, if the zero is distanced from the pole (i.e., a loose dipole structure), the root migration path can be significantly displaced from the initial point, allowing the potential for increased damping. The pole-zero orientation (dipole phase), and thus the angle of departure, is critical here. Using Equation (2.40) in the pitch control loop, favorable departure angles (e.g., $\theta_{d_i} \approx 180\ deg$) occur when the zero lies below the pole. This condition is referred to as phase stabilization. If the zero lies above the pole, a potentially disastrous condition can occur where the mode is destabilized or made less stable (e.g., $\theta_{d_i} \approx 0\ deg$). In extreme cases, the zero can even lie on the real axis, with minimum phase conditions being acceptable and nonminimum phase conditions being totally unacceptable. With this suppression logic, all input-output channels will see the increased damping. However, increased damping may actually lead to a degraded time response, due to the closed-loop dipole being more loose than its open-loop counterpart. Control of highly flexible vehicles typically boils down to a careful balance of aeroelastic gain and phase stabilization while augmenting the rigid dynamics.

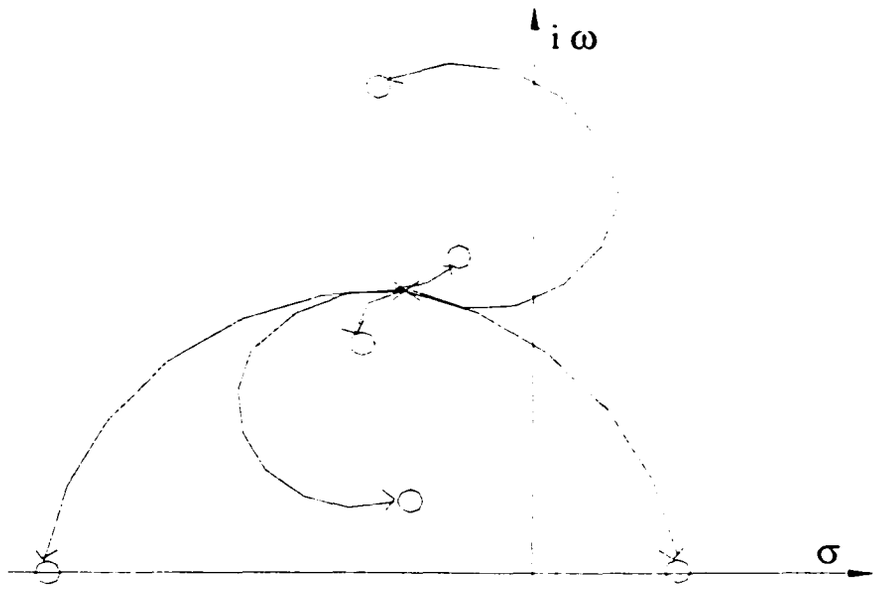

Figure 2.14 High Frequency Augmentation

As an example control design, consider closing the pitch rate loop with a sensor located near the mass center (x_s=*2.364 in*). The compensator root parameter is chosen as z_k=*2 rad/s*. Figure 2.15 shows the corresponding Evans root migration plot. In the low frequency, rigid dynamics region, note the similarities between Figures 2.15 and 2.13. The real axis modes are stabilized and suppressed, while the complex mode is transformed into a dominant pitch mode with desirable frequency and damping levels. These desirable low frequency traits are directly traceable to the selected feedback signal type and the compensation filter structure. In particular, the contribution of q in Equation (2.25) to q_i' and proportional plus integral structure in Equation (2.41) are key. In the high frequency, flexible dynamics region, note the similarities between Figures 2.15 and 2.14. Aeroelastic mode *1* is phase stabilized with potential for significant damping increase. However, the closed-loop dipole would be more loose than the open-loop

dipole, possibly leading to a worse condition. Aeroelastic mode *5* is gain stabilized and effectively removed from the input-output channel. However, the damping is unaltered and the implications of this may appear in other channels. Mode *4* is destabilized and unacceptable. Also note mode *12* most likely has an associated nonminimum phase real axis zero (see Table 2.1), again leading to an undesirable augmentation behavior. Overall, the augmentation features portrayed in Figure 2.15 are undesirable and/or unacceptable (due to the high frequency problems). These objectionable high frequency traits are influenced and affected primarily by the $\phi_j'(x)\,\ddot{\xi}_j(t)$ contribution terms in Equation (2.25). Further, the mode slope terms are a direct function of sensor location (see Figure 2.2). Thus, feedback of pitch rate measured near the mass center is not appropriate, and a more careful placement of the gyro sensor is required.

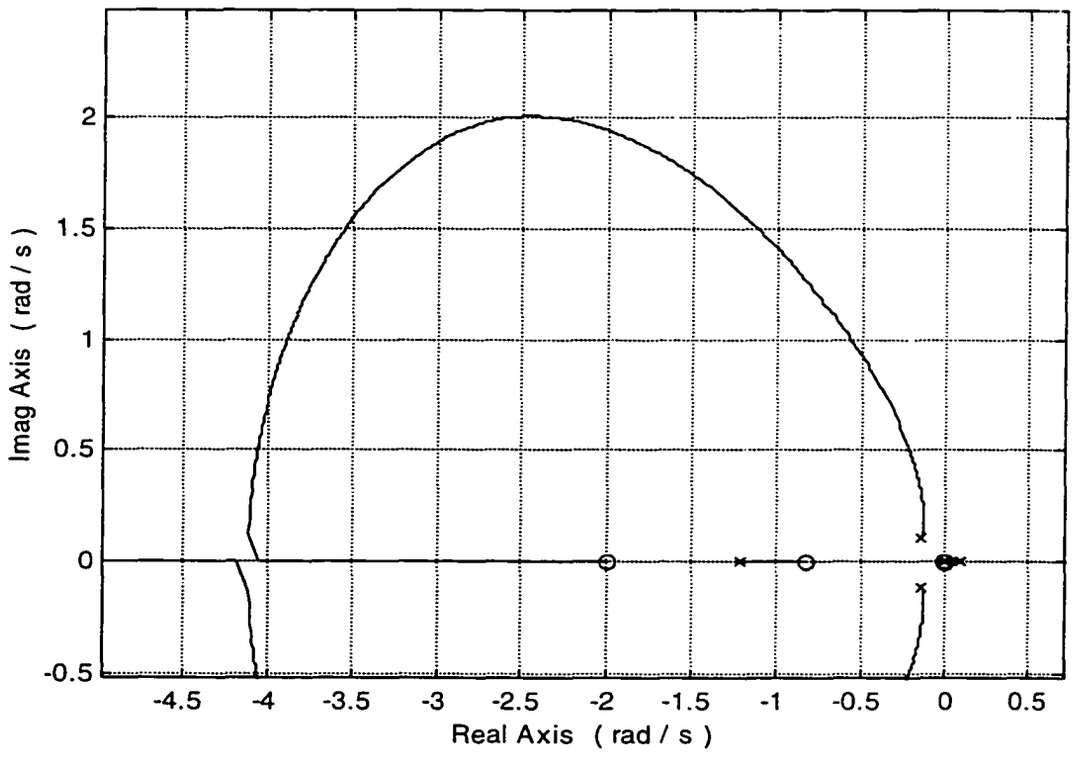

Figure 2.15a Root Locus Plot for x_s=*2,364 in*

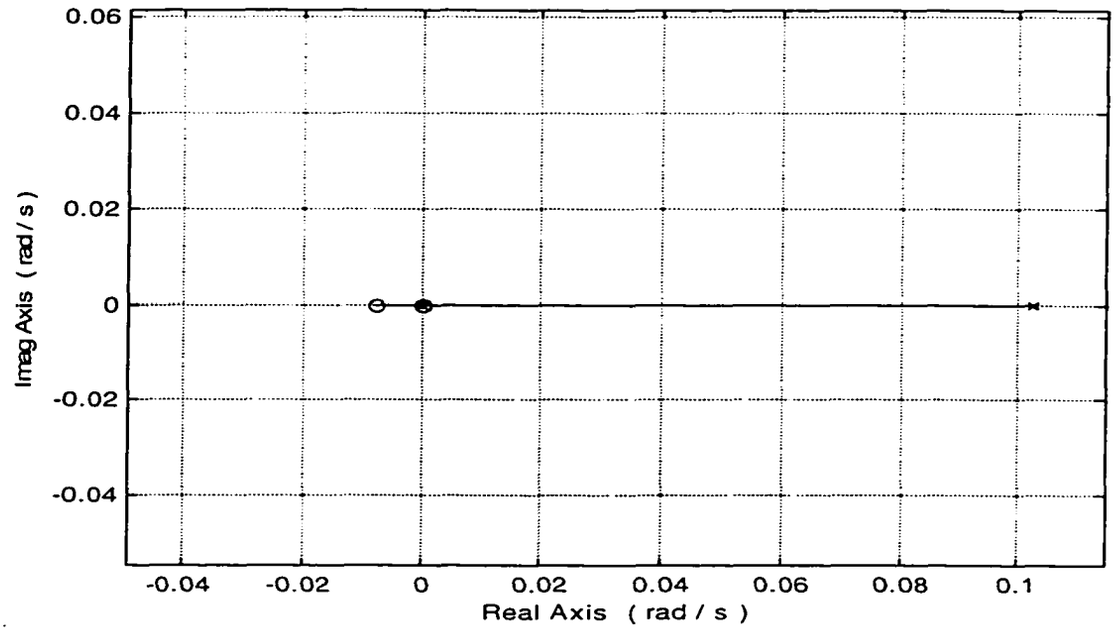

Figure 2.15b Root Locus Plot for x_s=2,364 *in*

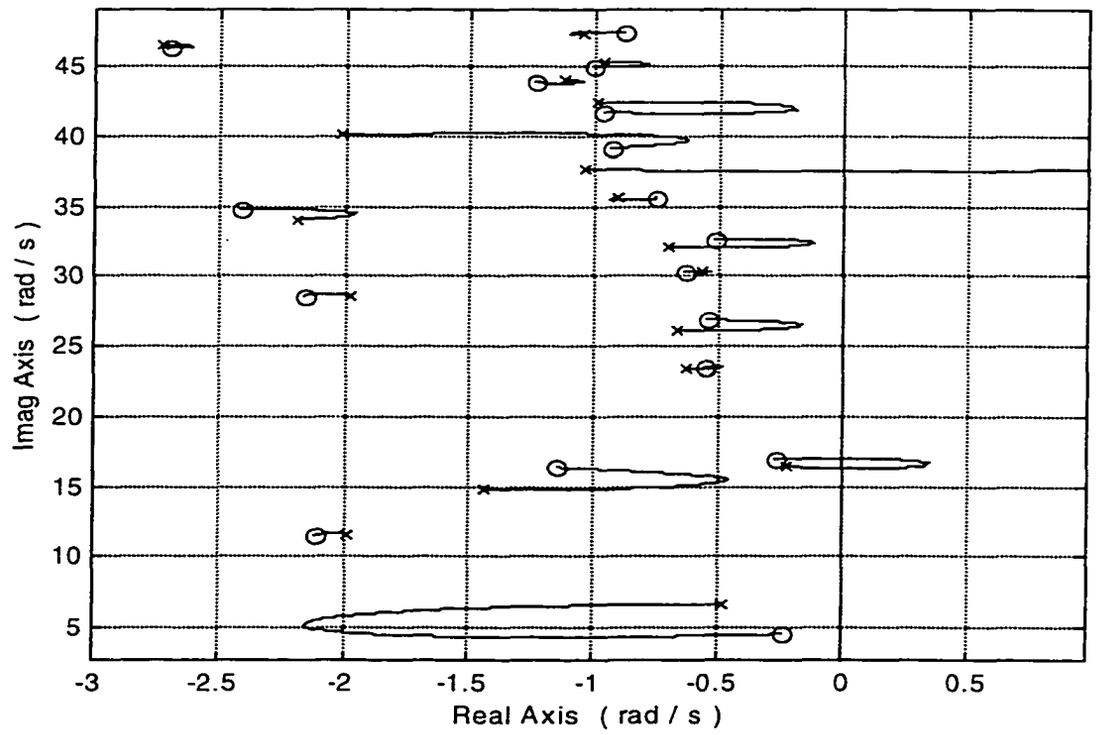

Figure 2.15c Root Locus Plot for x_s=2,364 *in*

2.5 Manual Sensor Placement

Obtaining desirable features in the Evans plot for the large high-speed, highly flexible transport application is largely dependent on feedback sensor location, and in particular the mode slopes at the sensor mounting location (see Equation (2.25)). These slope values determine the aeroelastic content and characteristics in the feedback signal. Tailoring this signal content by manual sensor placement is "standard" practice. Such strategy is based on understanding and/or correlation between the mode slope characteristics at the sensor location (Figure 2.2) and the resulting transfer function dipole structures (Figure 2.15). The sensor is located to increase or decrease the effects from signal contamination on the feedback system. Aeroelastic contamination is minimized to reduce coupling and instability tendencies (gain stabilization), while it is maximized to actively control structural modes (phase stabilization).

To simplify the discussion, consider the mode shape schematic given in Figure 2.16, which shows only the rigid-body, 1^{st} aeroelastic, and 3^{rd} aeroelastic mode deflections from the full set in Figure 2.2. Figure 2.16 can be thought of as the initial time dependent deflection state immediately following a nose down elevator input. Note the rigid-body motion response is a nose down rotation. The upwards tail force deforms the fuselage such that modes *1* and 3 undergo tail up deflections leading to a mode 1 nose up rotation and a mode *3* nose down rotation. Suppose a sensor could be theoretically placed on the mass center (position 0). In this case, all mode slope values are zero ($\phi_j' = 0$), and the measured pitch rate becomes the "rigid" pitch state q ($q_0' = q$, see Equation (2.25)). Assuming no aerodynamic coupling between the rigid and structural motion, it can be easily shown that the aeroelastic dipoles become maximally tight with the pole and zero

precisely canceling. With aerodynamic coupling, the signal q itself contains some aeroelastic content, and the dipoles are consequently perturbed. Exact pole-zero cancellation will not occur. However, the dipoles remain relatively tight since the coupling path is an indirect mechanism. References 42 and 44 fully document these observations. If the design objective is gain stabilization, then placing the sensor at the mass center is the theoretical optimum situation.[45]

Now suppose the sensor in Figure 2.16 is located at position 1. At this location, the mode slope *1* is nearly zero ($\phi_1' \approx 0$), and mode slope *3* is significantly nonzero and negative ($\phi_3' << 0$). Equation (2.25) implies that the mode *1* content in the signal q_1' is negligible, while the mode *3* content is significant and is out-of-phase with the rigid content (i.e., $+q$ and $-\phi_3' \dot{\xi}_3$ are of different sign). Consequently, the mode *1* dipole will be tight, while the mode *3* dipole will have an undesirable orientation with the zero located significantly above the pole. The direct pick-up of the $-\phi_3' \dot{\xi}_3$ term by the sensor in Equation (2.25) is a direct mechanism, consequently, the dipole is significantly altered. If the design objective is gain stabilization, then sensor position *1* is beneficial for mode *1*, but a serious problem occurs with mode *3* (phase destabilization).

To resolve this problem, suppose the sensor is relocated to position *2*. Here, $\phi_3' = 0$ and $\phi_1' >> 0$. The term $-\phi_3' \dot{\xi}_3$ will be negligible in Equation (2.25) and the mode *3* dipole will be tight (gain stabilization). Additionally, the $-\phi_1' \dot{\xi}_1$ term will be significant and in-phase with the q term in Equation (2.25). The mode *1* dipole will have the zero located well below the pole leading to a phase stabilization condition. This closed-loop behavior may or may not be acceptable depending on the specific design objectives.

Based on the mode shapes indicated in Figure 2.16, significant trades between the mode *1* and *3* dipole structures for various sensor locations exist. With many modes such as in Figure 2.2, the manual sensor placement task is extremely challenging with many constraints from conflicting modes.

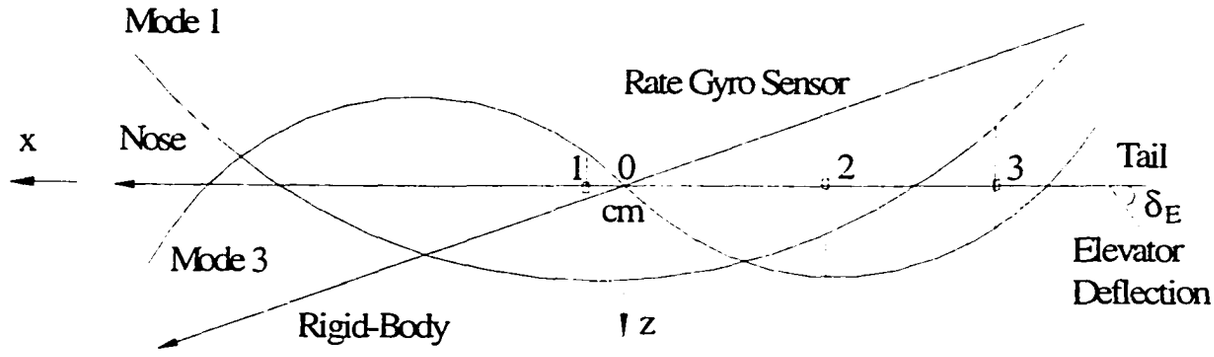

Figure 2.16 Initial Deflection State for Elevator Down Input

Now suppose the design objective is to phase stabilize most or all aeroelastic modes. The only region where both mode *1* and mode *3* have in-phase motion with the rigid motion is near the vehicle tail (position 3). For a sensor placed in this region, $\phi_1' >> 0$, $\phi_3' >> 0$ and the terms $-\phi_1' \dot{\xi}_1$ and $-\phi_3' \dot{\xi}_3$ are initially sign consistent with $+q$ in Equation (2.25). Each dipole should have its zero oriented below the pole (phase stabilization) allowing for augmentation of aeroelastic damping. This sensor placement corresponds to a "collocated actuator-sensor" solution. As stated previously, significant damping augmentation is synonymous with loose closed-loop dipole structure, and the resulting response behavior may be objectable. Further, if the aerodynamic coupling mechanisms are strong enough, the indirect mechanisms may alter the dipole structures from that stated above.

To demonstrate some of these issues with the full vehicle model, consider a phase stabilization objective for all aeroelastic modes. Inspection of Figure 2.2 with all *18* modes present suggests a gyro placed at x_s=*3.340 in* (e.g., elevator hinge line station) will result in $\phi_j' >> 0$ for all j except j=*16* and *17* where $\phi_j' \approx 0$. Note this interpretation requires reflection about the zero line of some of the mode shapes to be consistent with an assumed elevator down or tail up load. Figure 2.17 shows the corresponding Evans plot for this sensor location and for z_k=*2 rad/s*. Most every aeroelastic pole is phase stabilized, with a few being gain stabilized. The near *180 deg* departure angles are highly desirable for damping augmentation. However, the closed-loop dipoles would be significantly loose. Further note this all out phase stabilization objective has opened up the mode 1 dipole to an extent where the rigid-body mid period mode and aeroelastic mode1 migration paths couple. The rigid pitch mode migrates towards the fundamental aeroelastic mode zero, while aeroelastic mode *1* migrates towards the compensator zero at *–2 rad/s*. This feature limits the amount of all important rigid pitch damping that can be achieved. Unfortunately, sliding the sensor location forward destabilizes certain aeroelastic modes before the low frequency characteristics in Figure 2.17 are restored back to Figure 2.13.

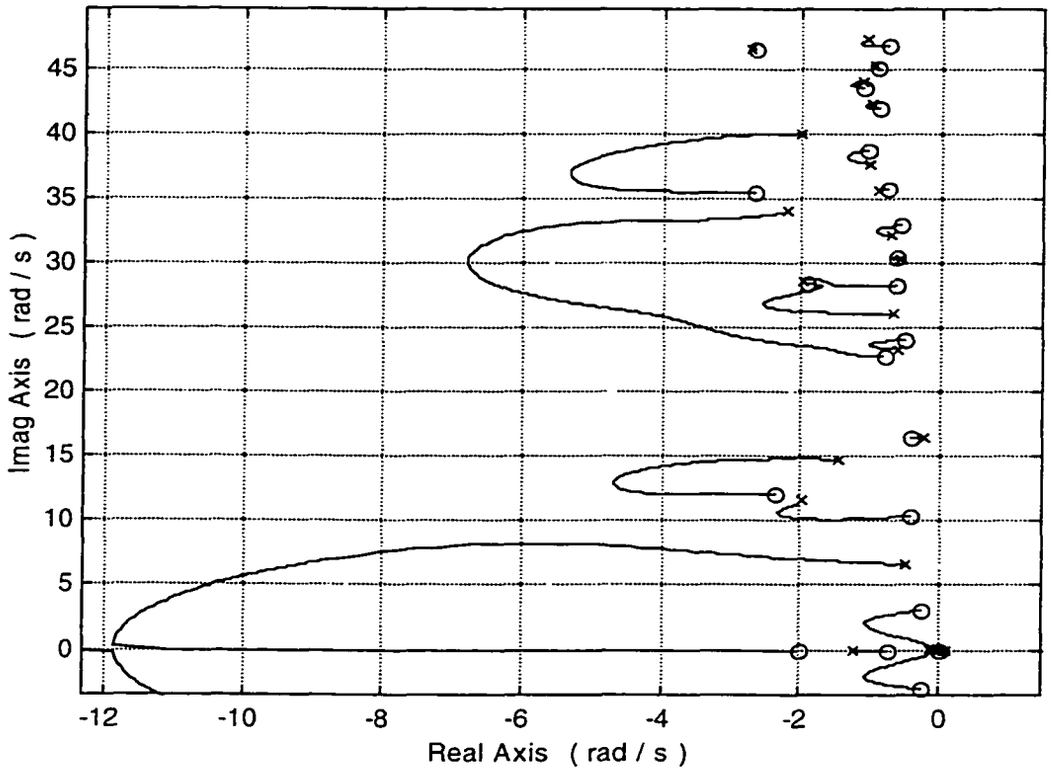

Figure 2.17 Root Locus Plot for x_s=*3,340 in*

Now consider a gain stabilization objective for all aeroelastic modes. Inspection of Figure 2.2 shows a region near x_s=*2,000 in* slightly ahead of the mass center where several (but not all) modes correspond to $\phi_j' \approx 0$, especially mode *1*. Figure 2.18 shows the corresponding Evans plot for x_s=*2,000 in* and z_k=*2 rad/s*. In Figure 2.18, observe the desirable rigid body pitch augmentation features. Additionally, note the first aeroelastic mode is approximately cancelled by its associated zero (gain stabilization). However, both the *3rd* and the *13th* modes are particularly objectionable, showing instability as the loop gain increases. This destabilization is consistent with Figure 2.2 where $\phi_3' << 0$.

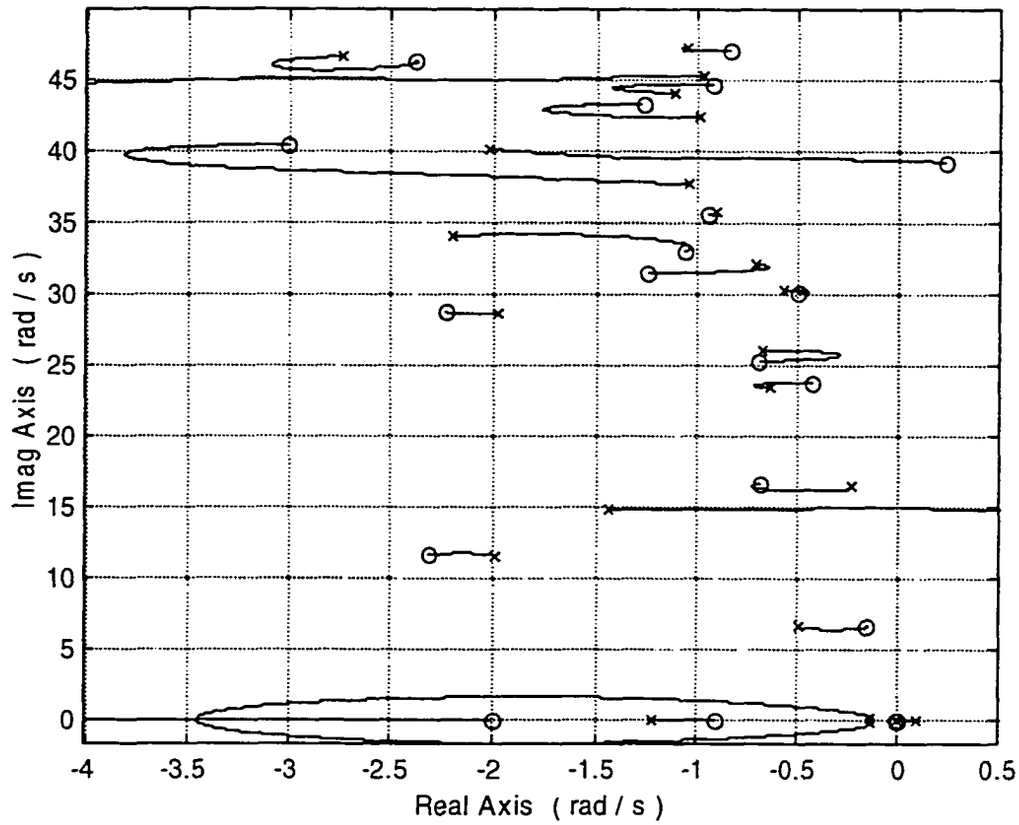

Figure 2.18 Root Locus Plot for x_s=*2,000 in*

Examination of Figure 2.2 also reveals a region near x_s=*2,500 in* slightly aft of the mass center where many modes have zero mode slope, including mode 3. Figure 2.19 shows the corresponding Evans plot for x_s=*2,500 in* and z_k=*2 rad/s*. Note in Figure 2.19 that many modes between *10 rad/s* and *30 rad/s* are gain stabilized. However, at even higher frequency, several aeroelastic modes are destabilized. Finally, note that desired rigid body pitch augmentation has broken down restricting the upper limit of achievable pitch damping.

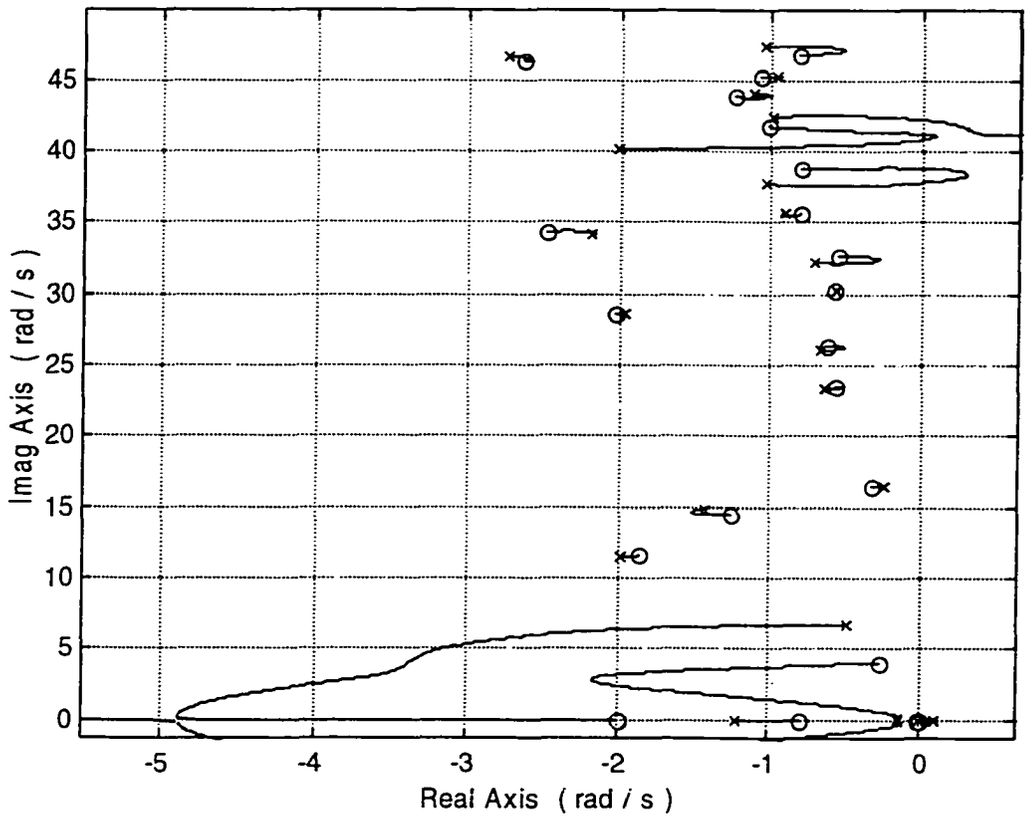

Figure 2.19 Root Locus Plot for x_s=*2,500 in*

To summarize the gain stabilization objectives, the forward sensor offers the capability to add significant damping to the rigid pitch mode, while simultaneously suppressing mode *1*. However, mode *3* is destabilized. On the other hand, the aft sensor achieves suppression of many modes, including mode 3, but at the expense of limited pitch damping. Further, although the damping of mode *1* could be greatly increased, the closed-loop dipole will be excessively loose. The conclusion is that a single sensor architecture (see Figure 2.9) is not feasible for meeting the gain stabilization objective. A similar conclusion can be said about the phase stabilization results.

Additional design freedom is achieved by considering a two sensor architecture, as shown in Figure 2.20. The strategy here (gain stabilization, for example) is to blend the desirable features of both fore and aft sensor signals and to avoid the undesirable features. Two rate gyro signals $y_1 = q_1'$, $y_2 = q_2'$ will be blended into the single feedback signal $\hat{y}$, as shown in Figure 2.20, where $h_1(s)$ and $h_2(s)$ denote blending filter transfer functions. In this situation, the feedback control law is

$$u(s) = k(s)(\hat{y}_c(s) - \hat{y}(s)) = k(s)(\hat{y}_c(s) - h_1(s)y_1(s) - h_2(s)y_2(s)) \qquad (2.42)$$

Substitution of Equation (2.42) into Equation (2.30) and providing allowance for the composite signal $\hat{y}$ yields the closed-loop system

$$\begin{aligned} y_1(s) &= \frac{k(s)g_{11}(s)}{1 + k(s)(h_1(s)g_{11}(s) + h_2(s)g_{21}(s))}\hat{y}_c(s) \\ y_2(s) &= \frac{k(s)g_{21}(s)}{1 + k(s)(h_1(s)g_{11}(s) + h_2(s)g_{21}(s))}\hat{y}_c(s) \\ \hat{y}(s) &= \frac{k(s)(h_1(s)g_{11}(s) + h_2(s)g_{21}(s))}{1 + k(s)(h_1(s)g_{11}(s) + h_2(s)g_{21}(s))}\hat{y}_c(s) \end{aligned} \qquad (2.43)$$

Note here the denominator polynomial is influenced by both feedbacks and both blending filters. Within the closed-loop pole migration framework, the zeros can now be tailored by blending the two feedback signals. However, note the $\hat{y}$ signal does not correspond to any single pitch rate signal obtained from the airframe.

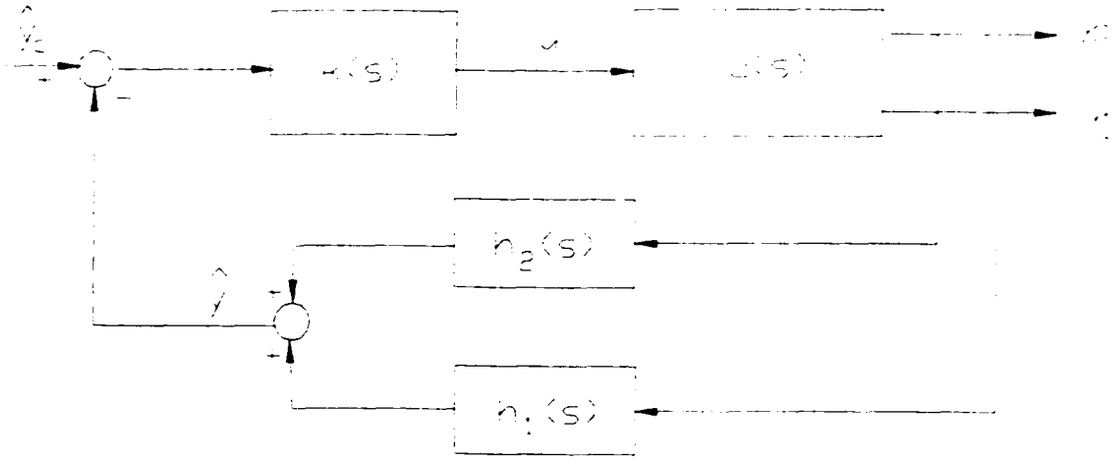

Figure 2.20 Closed-Loop System with Two Feedbacks

For the forward sensor (x_{s1}=*2,000 in*), desirable low frequency characteristics below *10 rad/s* are observed, while above this frequency undesirable behavior is present (see Figure 2.18). Note the opposite trend with the aft sensor (x_{s2}=*2,500 in*), undesirable features reside below *10 rad/s*, while desirable characteristics are present above *10 rad/s* until *30 rad/s* is reached (see Figure 2.19). Therefore, low pass filtering of the forward sensor with cut off at *7 rad/s* will be used to preserve low frequency characteristics, while above *7 rad/s* but below *31 rad/s* band pass filtering of the aft sensor with break frequency at *7 rad/s* and *31 rad/s* will be used to preserve mid frequency characteristics. Attenuation of all feedback signals above *31 rad/s* is enforced. Characteristics of both the low pass $h_1(s)$ and band pass $h_2(s)$ filtering are shown in Figure 2.21.

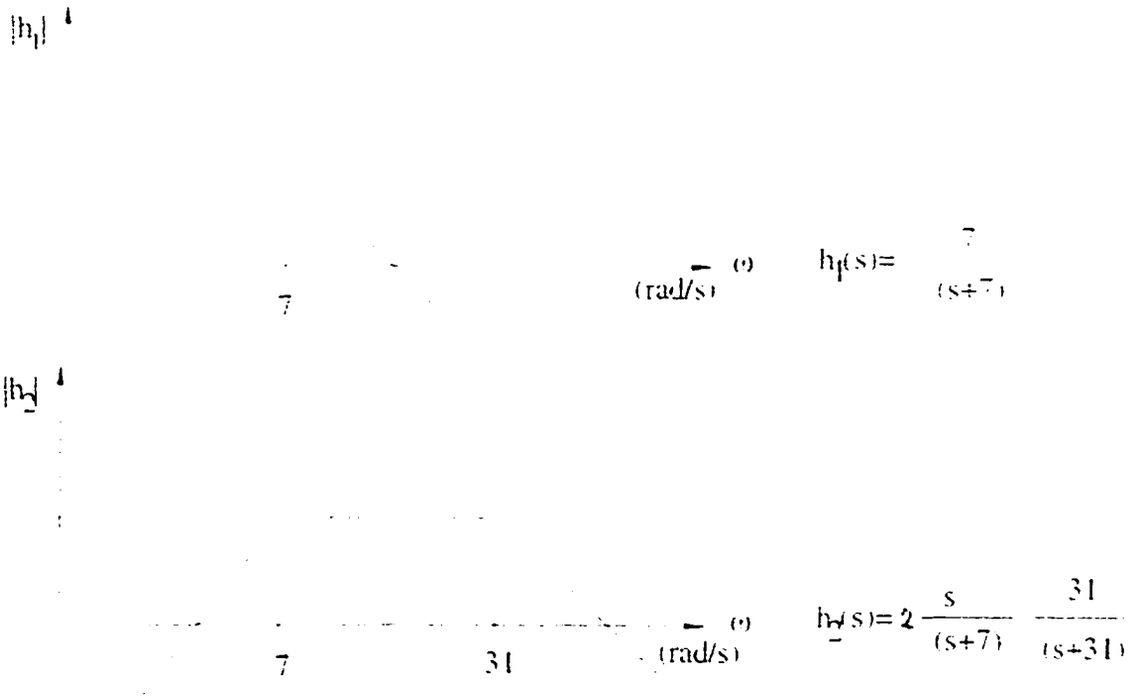

Figure 2.21 Low Pass Filter and Band Pass Filter Characteristics

Figure 2.22 shows the Evans plot for the blended sensor arrangement with x_s=*2,000 in* and *2,500 in* and the blend filters in Figure 2.21. The compensator parameter z_k is again *2 rad/s*. The root locus behavior shown in Figure 2.22 correlates with the blend strategy. For frequencies below *7 rad/s*, the closed-loop dynamics correlate with the fore design in Figure 2.18. A conventional, well damped rigid-body pitch mode is present, but mode *1* is slightly less gain stabilized. Note, however, the new zero appearing near *–2 rad/s* and the *1st* aeroelastic mode zeros pushed slightly to nonminimum phase. In spite of this, the low frequency characteristics appear desirable. For frequencies in the band between *7 rad/s* and *31 rad/s*, the closed-loop dynamics match the aft design in Figure 2.19. The dipole structures, in general, are tight. The *3rd* aeroelastic dipole structure could use further improvement, but is certainly more desirable when compared with the *3rd*

aeroelastic characteristics in Figure 2.18. Note the hard aeroelastic instabilities lying beyond *31 rad/s*, which are inherent in the *2,500 in* rate gyro signal.

Overall, the blended sensor strategy for gain stabilization captures the desirable features of both the fore and aft designs and looks promising. Note a similar manual blending strategy for the phase stabilization objective could be considered but is not pursued here. The blending filter parameters make the manual placement procedure less tractable. Utilization of even more sensors would exasperate this trend. Thus, to fully exploit multi-sensor blending, development of an optimal, auto sensor placement procedure is warranted.

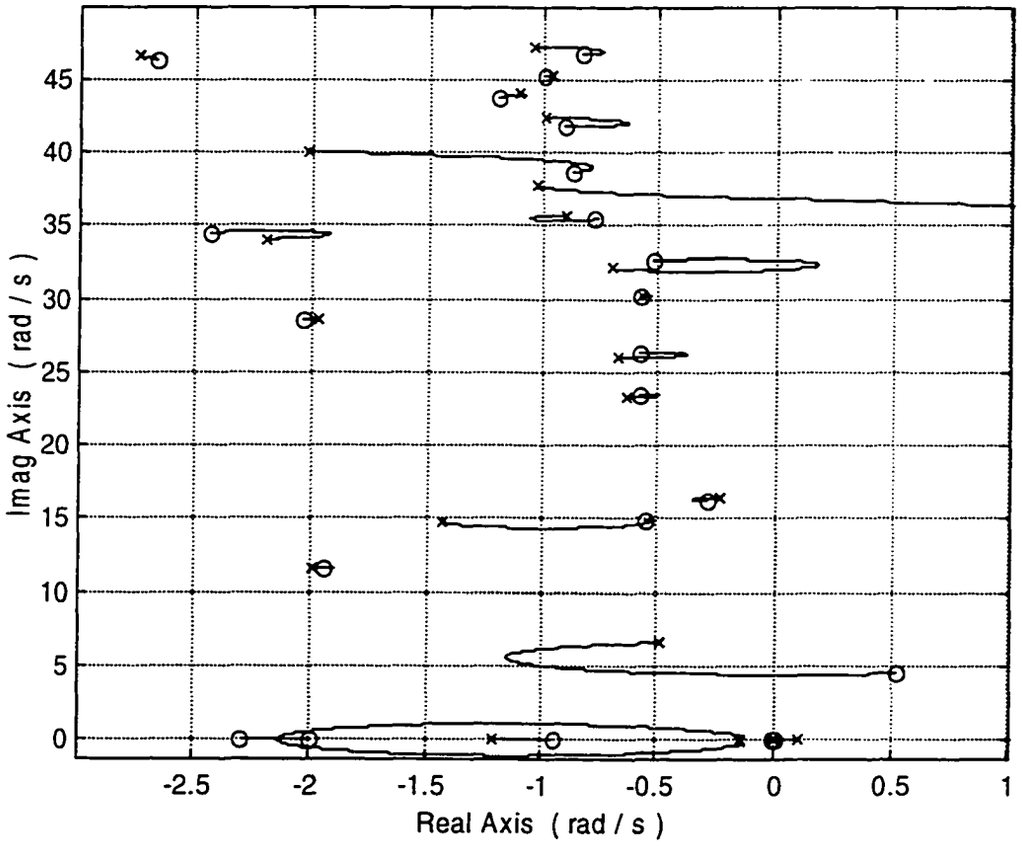

Figure 2.22 Root Locus Plot for x_{s1}=*2,000 in* and x_{s2}=*2,500 in*

CHAPTER 3

PARAMETER OPTIMIZATION CONCEPTS

3.1 Introduction

This chapter deals with the development of parameter optimization concepts including theoretic principles and numeric algorithms to be used in optimal sensor placement efforts. In this chapter, various classes of optimization problems will be presented and reviewed. The simplest class of problems that have no constraints on the independent variables will be introduced first. This problem class is called unconstrained optimization. Optimization problems having constraints on the parameter values, commonly referred to as constrained optimization, will be introduced as well. Both equality and inequality constraint cases are considered. Emphasis is given to the necessary and/or sufficient conditions for optimality. A numerical technique called the gradient descent method will be presented for finding the optimal placement of flight control sensors. This computational search method will be used in the dissertation research. This chapter also focuses on the formulation of candidate sensor placement criteria tailored for use in the conventional-based root migration flight control design of highly elastic vehicles. Attention is given to criteria based on root locus concepts such as departure angle and dipole structure. Additionally, constraint conditions on the independent variables and/or system properties are addressed. The main condition is to enforce minimum phase behavior for the open-loop transfer function.

3.2 Unconstrained Optimization

Suppose an engineer is faced with the design task for a system having complex nonlinear dependence on many variables requiring specification. Placement of multiple feedback sensors within a highly elastic flight vehicle is a prime example. Complete understanding of relationships between the design variables and the resulting system characteristics may be lacking and/or difficult to formulate due to high dimensionality and nonlinear interdependencies. Critical system characteristics may drive the need for not just a feasible selection of numerical values, but rather the "best" selection which provides the "highest" benefit. In many cases, these variables cannot be freely chosen but must satisfy various restrictions and requirements. In addition to selecting the design variable values, the engineer must also formulate a meaningful metric to assess the benefit. A design task of this flavor is well suited to parameter optimization concepts.[119-122]

Application of optimization techniques and tools to large, complex, and multi-dimensional science and engineering problems is an effective and efficient solution strategy. Design and research in the areas of flight vehicle dynamics and control, and many other areas, are beginning to employ such tools and concepts routinely. The applications have in turn furthered vigorous development of computational techniques and engendered new directions of research. Practical implementation of these theoretic principles with various numerical methods of high computational complexity is now possible with the availability of high-speed, large-memory digital computers.

The mechanics of most parameter optimization problems can be described as follows: find the combination of independent variable values which optimize a stipulated quantity, possibly subject to some restrictions on the variable values. The quantity to be optimized (maximized or minimized) is termed the objective function. The variables that may be changed in the quest for the optimum condition are called decision parameters, and the restrictions on allowable parameter values are known as constraint functions. For a minimization problem, the objective function is commonly referred to as the cost function, while for maximization problems, the benefit function is considered. In this dissertation, parameter optimization techniques are classified according to the type of applicable constraints being enforced. These categories include no constraints, equality constraints, and inequality constraints. In the following discussion, concepts from Reference 119 are heavily used.

First consider unconstrained optimization. Unconstrained optimization principles address the conditions required for finding local minimums of multivariate functions whose arguments are continuous and on which no restrictions are imposed. This problem type is the simplest class of parameter optimization problems. Solution techniques for this class of problems involve finding values of the decision parameters that minimize the cost function, which is a function of these parameters. The principal objective here is to identify the necessary and/or sufficient conditions for optimality. Techniques for numerically achieving these conditions are considered later.

Let u_i for $i = 1, 2, \ldots n$ denote the i^{th} scalar decision parameter out of a total set containing n parameters, or

$$\begin{aligned} u_i &= i^{th}\ decision\ parameter \\ i &= 1, 2, \cdots n \end{aligned} \tag{3.1}$$

In most problems, identifying the decision parameter set is obvious, but in some cases identification may require some effort. The decision parameters must form an independent set. In the aeroelastic vehicle sensor placement focus, decision parameters are primarily sensor locations (x *or* x_s) and possibly blending filter and control compensation parameters ($h_1(s)$, $h_2(s)$, $k(s)$) described in Chapter 2. The decision parameters can be collected into a decision vector u, or

$$u = [u_1 \; u_2 \; \cdots u_n]^T \tag{3.2}$$

Also let J be the scalar cost function which depends on the decision parameters, or

$$J(u_1, \; u_2, \; \cdots \; u_n) = J(u) = \; cost \; function \tag{3.3}$$

Formulating and identifying relevant and practical cost functions that have direct bearing on the overall design objectives is a critical step requiring considerable effort. This process should be well thought out and based on problem insight and familiarization, if possible. With respect to aeroelastic vehicle sensor placement interests for Evans-based root migration control design strategies, the cost function will be based on the key rigid-body and aeroelastic pole-zero geometric structures discussed previously in Chapter 2.

Suppose the cost function J is a continuous function of u through second order partial derivatives. In this case, the Taylor series expansion for dJ can be expressed as

$$dJ(u) = \frac{\partial J(u)}{\partial u} du + \frac{1}{2} du^T \frac{\partial^2 J(u)}{\partial u^2} du + \cdots \tag{3.4}$$

where the partial derivatives in Equation (3.4) are evaluated at some expansion point. From elementary principles of calculus and Equation (3.4), necessary conditions for a local minimum are

Condition 1:
$$\frac{\partial J(u)}{\partial u} = 0 \tag{3.5}$$

where

$$\frac{\partial J(u)}{\partial u} = [\frac{\partial J(u)}{\partial u_1} \quad \frac{\partial J(u)}{\partial u_2} \quad \cdots \frac{\partial J(u)}{\partial u_n} \quad] = 0 \tag{3.6}$$

Condition 2:

$$\frac{\partial^2 J(u)}{\partial u^2} \geq 0 \tag{3.7}$$

where

$$\frac{\partial^2 J(u)}{\partial u^2} = \begin{bmatrix} \frac{\partial^2 J(u)}{\partial u_1 \partial u_1} & \frac{\partial^2 J(u)}{\partial u_1 \partial u_2} & \cdots & \frac{\partial^2 J(u)}{\partial u_1 \partial u_n} \\ \frac{\partial^2 J(u)}{\partial u_2 \partial u_1} & \frac{\partial^2 J(u)}{\partial u_2 \partial u_2} & \cdots & \frac{\partial^2 J(u)}{\partial u_2 \partial u_n} \\ \vdots & \vdots & \ddots & \vdots \\ \frac{\partial^2 J(u)}{\partial u_n \partial u_1} & \frac{\partial^2 J(u)}{\partial u_n \partial u_2} & \cdots & \frac{\partial^2 J(u)}{\partial u_n \partial u_n} \end{bmatrix} \tag{3.8}$$

Condition 1 says the gradient of the cost function with respect to the decision parameters must equal zero. Each first order partial derivative or slope corresponding to individual decision parameters must have a zero value. In this situation, Equation (3.4) implies the tangent to the cost function hyper-surface is level, suggesting an extremity has been reached. Points satisfying *Condition 1* are called stationary points and are feasible candidates for a local minimum. This condition, however, does not distinguish between maxima and minima. *Condition 2* can be used to resolve this distinction. *Condition 2* says the Jacobian of the cost function with respect to the decision parameters must be positive semi-definite. Each quadratic form involving the second order partial derivatives (or equivalently, the curvatures) must have a nonnegative value. An equivalent condition requires the eigenvalues of the Jacobian matrix to be nonnegative. In this situation, Equation (3.4) implies small changes in u will lead to nonnegative changes in J, thus

ruling out the maximum case. Figure 3.1 illustrates these basic concepts for one dimension.

Equations (3.5) and (3.7) are necessary conditions. If a candidate decision vector does not satisfy these conditions, then it is not a minimum. If a candidate decision vector satisfies these conditions, then no rigorous conclusion can be made, although the candidate vector is a strong contender for being a minima. In Equation (3.7), the objectionable condition is $\partial^2 J / \partial u^2 = 0$. A stationary point with $\partial^2 J / \partial u^2 = 0$ is called a singular point. In these cases, additional information (i.e., third order derivative $\partial^3 J / \partial u^3$) is needed to establish whether the point is a true minimum. Sufficient conditions for a local minimum are *Condition 1* and

Condition 3:
$$\frac{\partial^2 J(u)}{\partial u^2} > 0 \tag{3.9}$$

Condition 3 says the cost function to decision parameter Jacobian is positive definite (or has positive eigenvalues). If a candidate decision vector satisfies *Condition 1* and *3*, then it is indisputably a minima, and such points are referred to as minimum points.

The aeroelastic vehicle sensor placement problem has certain constraints imposed on the decision parameters and other system properties, and thus does not precisely fit the problem structure outlined in this section. Therefore, the next section addresses equality constrained optimization. The topics in this section do, however, lay the foundation for these more advanced topics. As a final comment, numerical generation of candidate decision vectors that satisfy *Conditions 1, 2, or 3* are not considered until Section 3.5.

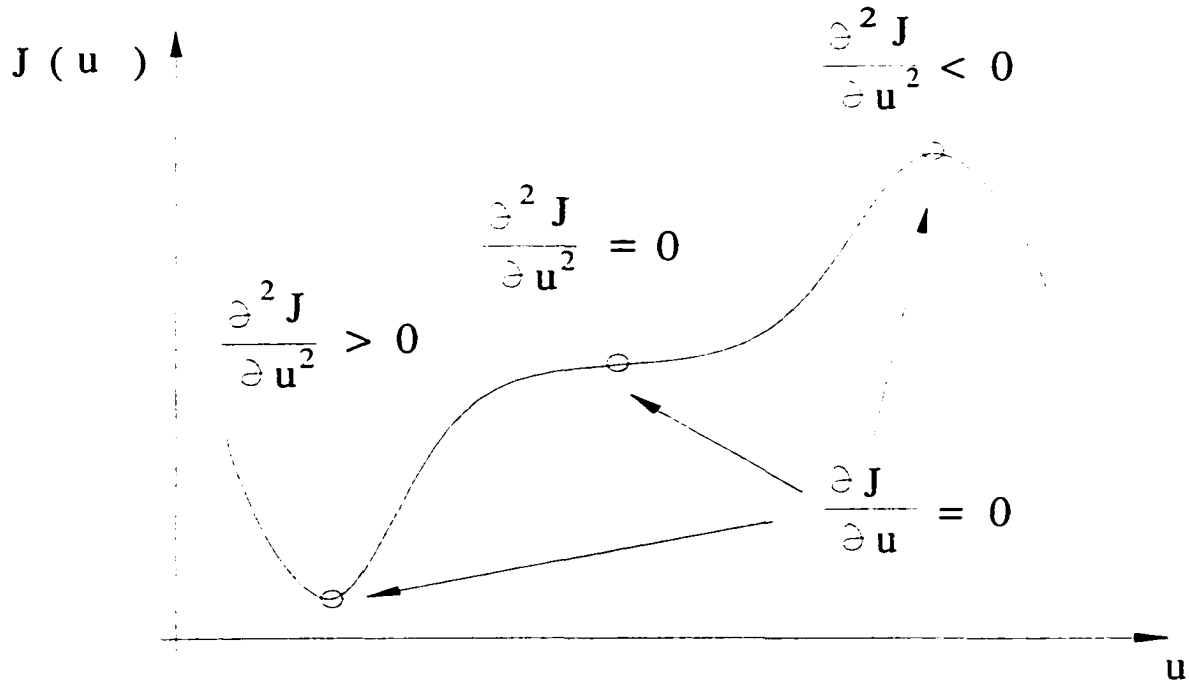

Figure 3.1 Unconstrained Optimality Conditions for One Dimension

3.3 Equality Constrained Optimization

Theoretic principles for constrained optimization problems are more challenging than their unconstrained counterparts. This class of problem involves finding values of the decision parameters $u_1, u_2, \ldots u_n$ that minimize cost function J, which is dependent on the decision parameters and on state parameters $x_1, x_2, \ldots x_m$, *or*

$$J(x_1, x_2, \ldots x_m, u_1, u_2, \ldots u_n) = \textit{cost function} \qquad (3.10)$$

In Equation (3.10), n and m are the number of decision and state parameters, respectively. The state and decision parameters are required to also satisfy equality constraint functions F_i of the form

$$0 = F_i(x_1, x_2, \ldots x_m, u_1, u_2, \ldots u_n) = i^{th} \textit{ constraint function} \qquad (3.11)$$

$$i = 1,2, \ldots m$$

Equality constraint functions can be real physical constraints such as geometric/kinematic conditions or governing models from first principles. These types of constraints are easily identified in most problems. Equality constraint functions can also be stipulations by the engineer to illicit some desired behavior from the system. These types of constraints, which are effective but not overly restrictive, are more difficult to formulate. Identification of the state parameters can also be challenging at times.

To write the problem in compact form, state, decision, and constraint vectors can be written as

$$x = [x_1 \ x_2 \ldots\ldots\ldots\ldots x_m]^T \tag{3.12}$$

$$u = [u_1 \ u_2 \ldots\ldots\ldots\ldots u_n]^T \tag{3.13}$$

$$F = [F_1 \ F_2 \ldots\ldots\ldots\ldots F_m]^T \tag{3.14}$$

In compact form, the cost and constraint functions can thus be written as $J(x,u)$ and $F(x,u)$, respectively. The problem now is to find the decision vectors u that minimize cost J where simultaneously the state vector x is determined from the decision vector through the constraint $F=0$. The equality constraints thus add a new level of difficulty to the optimization problem. A first order necessary condition for the solution of this optimization problem is the gradient of the cost function with respect to the decision parameters, subject to the equality constraints, must equal zero, or

Condition 4:
$$\frac{\partial J(x,u)}{\partial u}\Big|_{F(x,u)=0} = 0 \tag{3.15}$$

To develop this condition and to uncover the notational meaning in Equation (3.15), consider the differential Taylor series expansion for J and F through first order.

$$dJ = \frac{\partial J}{\partial x}dx + \frac{\partial J}{\partial u}du = J_x dx + J_u du \tag{3.16}$$

$$dF = \frac{\partial F}{\partial x}dx + \frac{\partial F}{\partial u}du = F_x dx + F_u du \tag{3.17}$$

Also consider the special points where $dJ = 0$ for an arbitrary change in du while holding $dF = 0$. Inserting $dF = 0$ into Equation (3.17) and solving for dx yields

$$dx = -F_x^{-1} F_u du \tag{3.18}$$

Substituting for dx in Equation (3.16) yields

$$dJ = (J_u - J_x F_x^{-1} F_u)du \tag{3.19}$$

If dJ must equal zero for any du, it is necessary for the row matrix coefficient of du in Equation (3.19) to equal zero. This necessary condition is precisely Equation (3.15), or

$$\frac{\partial J(x,u)}{\partial u}\Big|_{F(x,u)=0} = J_u' = J_u - J_x F_x^{-1} F_u = 0 \tag{3.20}$$

Note J_u is the partial derivative of J with respect to u holding x constant, while J_u' is the partial derivative of J with respect to u holding F constant at zero. Points satisfying *Condition 4* are called stationary points and are feasible candidates for a local minimum. As before, the first order condition does not clarify between maxima and minima.

To resolve this dilemma, reconsider the cost function Taylor series expansion in Equation (3.16), but now expanded through second order derivatives, or

$$dJ = \begin{bmatrix} J_x & J_u \end{bmatrix}\begin{bmatrix} dx \\ du \end{bmatrix} + \frac{1}{2}\begin{bmatrix} dx^T & du^T \end{bmatrix}\begin{bmatrix} J_{xx} & J_{xu} \\ J_{ux} & J_{uu} \end{bmatrix}\begin{bmatrix} dx \\ du \end{bmatrix} + \cdots \tag{3.21}$$

where J_{xx}, J_{xu}, J_{ux} and J_{uu} are the second order partial derivatives of the cost function with respect to x and u as similarly defined in Equation (3.8). The constraint function expansion in Equation (3.17) is also recalled. From this expression at $dF=0$, the

differential state vector must still satisfy Equation (3.18). Substitution for dx from Equation (3.18) in Equation (3.21) yields

$$dJ = \begin{bmatrix} J_x & J_u \end{bmatrix} \begin{bmatrix} -F_x^{-1} F_u du \\ du \end{bmatrix} + \frac{1}{2} \begin{bmatrix} (-F_x^{-1} F_u du)^T & du^T \end{bmatrix} \begin{bmatrix} J_{xx} & J_{xu} \\ J_{ux} & J_{uu} \end{bmatrix} \begin{bmatrix} -F_x^{-1} F_u du \\ du \end{bmatrix} + \cdots \quad (3.22)$$

$$dJ = (J_u - J_x F_x^{-1} F_u) du + \frac{1}{2} du^T (J_{uu} - J_{ux} F_x^{-1} F_u - F_u^T F_x^{-1^T} J_{xu} + F_u^T F_x^{-1^T} J_{xx} F_x^{-1} F_u) du + \cdots \quad (3.23)$$

Define the second partial derivative of J with respect to u holding F constant at zero as

$$\frac{\partial^2 J(x,u)}{\partial u^2} \Big|_{F(x,u)=0} = J'_{uu} = J_{uu} - J_{ux} F_x^{-1} F_u - F_u^T F_x^{-1^T} J_{xu} + F_u^T F_x^{-1^T} J_{xx} F_x^{-1} F_u \quad (3.24)$$

Thus, Equation (3.24) yields a second order necessary condition for the solution of the optimization problem. The Jacobian of the cost function with respect to the decision parameters, subject to the equality constraints, must be positive semi-definite, or

Condition 5:
$$\frac{\partial^2 J(x,u)}{\partial u^2} \Big|_{F(x,u)=0} \geq 0 \quad (3.25)$$

The objectionable condition occurs again when the Jacobian is identically zero. Thus, sufficient conditions for a local minimum are *Condition 4* and

Condition 6:
$$\frac{\partial^2 J(x,u)}{\partial u^2} \Big|_{F(x,u)=0} > 0 \quad (3.26)$$

Another perspective for approaching the equality constrained optimization problem is the Adjoint Method using Lagrange Multipliers. This procedure is distinct from that just discussed, however, the procedure leads to the same conditions for optimality. This procedure is a popular and powerful approach that streamlines the solution steps and may offer additional insight and computational advantages.

In this approach, the equality constraints in Equation (3.11) will be attached or adjoined to the cost function by a set of undetermined multiplier coefficients λ_1, λ_2,.....λ_m as follows.

$$H(x,u,\lambda_1,\lambda_2,\cdots\lambda_m) = J(x,u) + \sum_{i=1}^{m} \lambda_i F_i(x,u) \tag{3.27}$$

$$H(x,u,\lambda) = J(x,u) + \lambda^T F(x,u) \tag{3.28}$$

In Equation (3.27), the scalar coefficients λ_i are called Lagrange multipliers, and the Lagrange multiplier vector λ is thus defined as

$$\lambda = [\lambda_1 \quad \lambda_2 \quad \cdots \quad \lambda_m]^T \tag{3.29}$$

It is important to note that λ is independent of x and u. In Equation (3.27)-(3.28), H represents a modified cost, but ultimately if constraints are enforced *(F=0)*, then H is equivalent to J.

To determine first order conditions for optimality, consider the Taylor series expansion for dH through first order.

$$dH = \frac{\partial H}{\partial x}dx + \frac{\partial H}{\partial u}du + \frac{\partial H}{\partial \lambda}d\lambda = H_x dx + H_u du + H_\lambda d\lambda \tag{3.30}$$

Note that H_λ in Equation (3.30) is always zero from the specified structure in Equation (3.28), or

$$H_\lambda = F^T(=0) \tag{3.31}$$

Thus, the third term in Equation (3.30) disappears leaving only the dx and du terms. With x being determined from $F=0$ for a given u, dx cannot change independently from du. Direct accounting for this dependency in Equation (3.30) is cumbersome. Therefore, with the free parameters, specify λ such that H_x is always zero, or

$$H_x = J_x + \lambda^T F_x = 0 \tag{3.32}$$

$$\lambda^T = -J_x F_x^{-1} \qquad (= -J_F) \tag{3.33}$$

Now the first term in Equation (3.30) disappears leaving only the *du* term.

With this only remaining term, the condition for optimality is

$$H_u = J_u + \lambda^T F_u = 0 \tag{3.34}$$

Equations (3.31), (3.32) and (3.34) imply the gradient of the modified cost with respect to the decision parameters, subject to the constraints and a specific choice for the Lagrange multipliers, must equal zero. After collecting these results, the first order necessary condition for the solution of the equality constrained optimization problem is

Condition 7:

$$H_\lambda = 0 \tag{3.35}$$

$$H_x = 0 \tag{3.36}$$

$$H_u = 0 \tag{3.37}$$

Condition 7 is equivalent to *Condition 4* with Equation (3.11).

To determine second order conditions for optimality, reconsider the modified cost function Taylor series expansion in Equation (3.30) through second order, or

$$dH = \begin{bmatrix} H_x & H_u & H_\lambda \end{bmatrix} \begin{bmatrix} dx \\ du \\ d\lambda \end{bmatrix} + \frac{1}{2} \begin{bmatrix} dx^T & du^T & d\lambda^T \end{bmatrix} \begin{bmatrix} H_{xx} & H_{xu} & H_{x\lambda} \\ H_{ux} & H_{uu} & H_{u\lambda} \\ H_{\lambda x} & H_{\lambda u} & H_{\lambda\lambda} \end{bmatrix} \begin{bmatrix} dx \\ du \\ d\lambda \end{bmatrix} + \cdots \tag{3.38}$$

The main question here is the value of $d\lambda$. Consider the differential of Equation (3.28).

$$dH = dJ + \lambda^T dF + F^T d\lambda \tag{3.39}$$

If the equality constraints are enforced ($F^T=0$), note Equation (3.39) implies that $d\lambda$ can be chosen arbitrarily. Here, $d\lambda$ will be specified as zero. This conclusion is consistent with Equation (3.33) where if F is held constant, then λ is also required to be constant.

With $dF=0$, the differential state vector must still satisfy Equation (3.18). Substitution for dx and $d\lambda$ in Equation (3.38) thus yields

$$dH = \begin{bmatrix} H_x & H_u & H_\lambda \end{bmatrix} \begin{bmatrix} -F_x^{-1}F_u\,du \\ du \\ 0 \end{bmatrix} + \frac{1}{2}\begin{bmatrix} (-F_x^{-1}F_u\,du)^T & du^T & 0 \end{bmatrix} \begin{bmatrix} H_{xx} & H_{xu} & H_{x\lambda} \\ H_{ux} & H_{uu} & H_{u\lambda} \\ H_{\lambda x} & H_{\lambda u} & H_{\lambda\lambda} \end{bmatrix} \begin{bmatrix} -F_x^{-1}F_u\,du \\ du \\ 0 \end{bmatrix} + \cdots$$

$$= (H_u - H_x F_x^{-1}F_u)du + \frac{1}{2}du^T(H_{uu} - H_{ux}F_x^{-1}F_u - F_u^T F_x^{-1^T}H_{xu} + F_u^T F_x^{-1^T}H_{xx}F_x^{-1}F_u)du + \cdots \quad (3.40)$$

Define the second partial derivative of H with respect to u holding F constant at zero as

$$H'_{uu} = H_{uu} - H_{ux}F_x^{-1}F_u - F_u^T F_x^{-1^T}H_{xu} + F_u^T F_x^{-1^T}H_{xx}F_x^{-1}F_u \quad (3.41)$$

Thus, a second order necessary condition for the solution of the optimization problem is the Jacobian of the cost function with respect to the decision parameters, subject to the equality constraints, must be positive semi-definite, or

Condition 8: $$H'_{uu} \geq 0 \quad (3.42)$$

The objectionable condition occurs again when the Jacobian is identically zero. Thus, sufficient conditions for a local minimum are *Condition 7* and

Condition 9: $$H'_{uu} > 0 \quad (3.43)$$

Conditions 7 and *9* are equivalent to *Conditions 4* and *6*, respectively.

The constraints imposed on the decision parameters and other system properties in the aeroelastic vehicle sensor placement problem are of an inequality form. Thus, the dissertation research problem does not exactly fit the problem structure of this section. Consequently, the next section addresses inequality constrained optimization problems.

3.4 Inequality Constrained Optimization

Inequality constrained optimization problems are of an advanced nature, however, their theoretical development relies heavily upon previously considered topics. Most applied engineering optimization problems, including the dissertation research, lie within this category. In this problem class, the constraint relationships are of an inequality form, rather than the equality case. Suppose the decision and state parameters are combined into a signal set of generic parameters $y_1, y_2, \ldots\ldots y_p$ where p denotes the number of parameters. Introduce the generic parameter vector y as

$$y = [\, y_1 \;\; y_2 \ldots\ldots y_p]^T \tag{3.44}$$

The optimization problem involves finding the parameters y that minimize cost function J

$$J(y) = cost\,function \tag{3.45}$$

subject to the inequality constraints F

$$0 \geq F(y) = constraint\,function \tag{3.46}$$

$$F = [\, F_1 \;\; F_2 \ldots\ldots F_q]^T \tag{3.47}$$

In general, y and F are vectors of a different dimension. Equation (3.46) adds yet another level of difficulty to the optimization problem.

For a one dimensional problem, Figure 3.2 illustrates the three possible cases for a local minimum point. In *case 1*, the constraint is inactive ($F<0$), and the situation is identical to that discussed in Section 3.2. The necessary and sufficient conditions for a minimum can be found there, where the reader is reminded of the first order condition $\partial J/\partial y = 0$. In *case 2*, the constraint is active ($F=0$). Consider the differential Taylor series expansion about these minimum points for J and F through first order, or

$$dJ = \frac{\partial J}{\partial y} dy \tag{3.48}$$

$$dF = \frac{\partial F}{\partial y} dy \tag{3.49}$$

Admissible values for dy must satisfy

$$\frac{\partial F}{\partial y} dy \leq 0 \tag{3.50}$$

while the minimality condition requires that

$$\frac{\partial J}{\partial y} dy \geq 0 \tag{3.51}$$

Equations (3.50) and (3.51) imply that $\partial J / \partial y$ and $\partial F / \partial y$ must have different sign or $\text{sgn}(\partial J / \partial y) = -\text{sgn}(\partial F / \partial y)$. *Case 3* is a special situation where the unconstrained minimum point and the equality constraint are coincident. This case can be considered as in *case 1* assuming the minimum is approached from the admissible region. The *case 1, 2* and *3* conditions for optimality can be combined into the signal statement

$$\frac{\partial J}{\partial y} + \lambda \frac{\partial F}{\partial y} = 0 \qquad \text{where} \qquad \begin{array}{l} \lambda = 0 \ \textit{if} \ \dfrac{\partial J}{\partial y} = 0 \ \textit{and} \ F \leq 0 \\ \lambda > 0 \ \textit{if} \ \dfrac{\partial J}{\partial y} \neq 0 \ \textit{and} \ F = 0 \end{array} \tag{3.52}$$

In Equation (3.52), λ denotes a scalar Lagrange multiplier with more restrictions (nonnegativeness) than in Section 3.3.

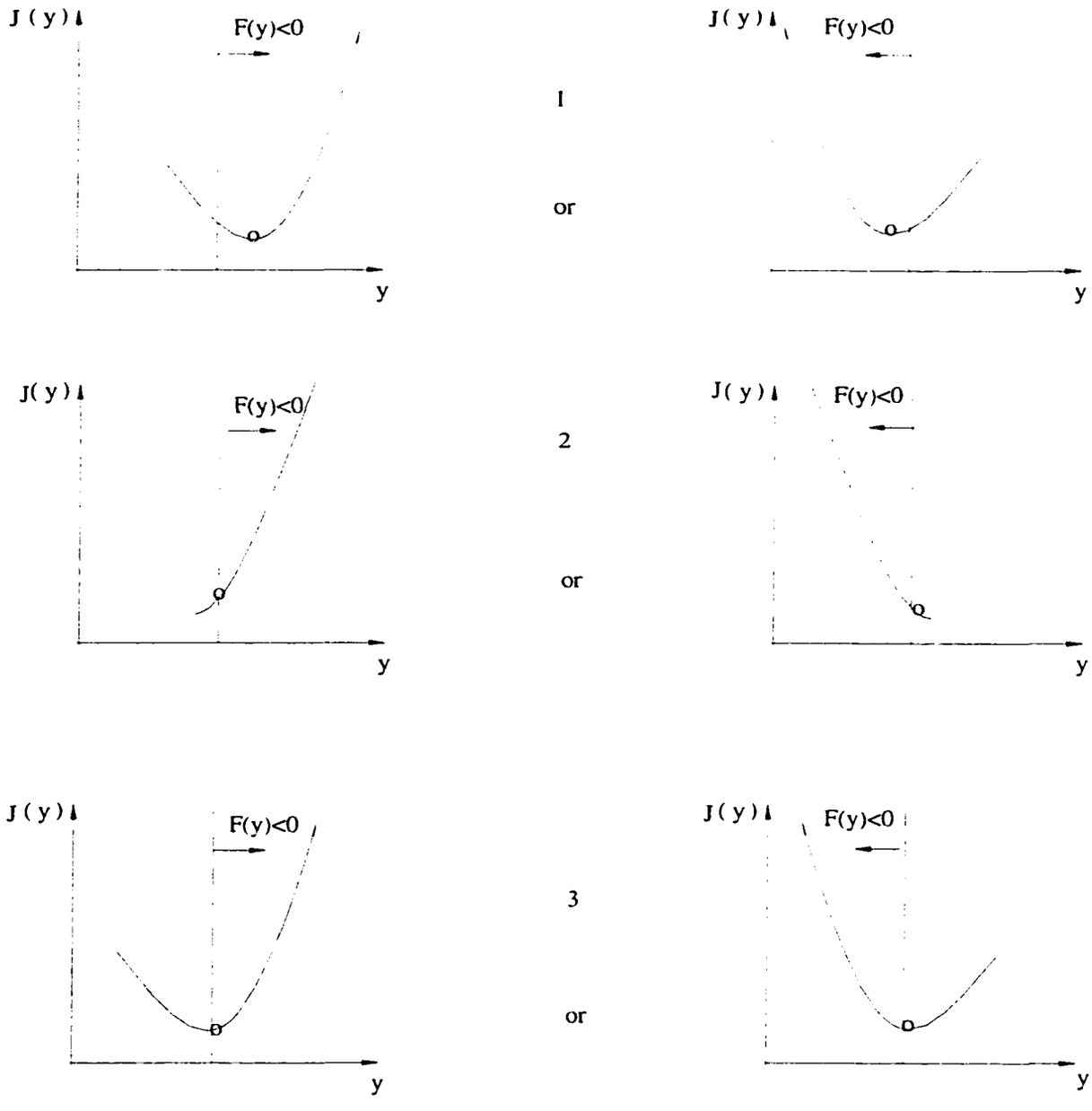

Figure 3.2 Inequality Constrained Optimality Cases for One Dimension

In the general case when y and F are vectors, the first order necessary condition for optimality in Equation (3.52) is still applicable after generalization to

$$\frac{\partial J}{\partial y}+\lambda^T\frac{\partial F}{\partial y}=0 \qquad \text{where} \qquad \begin{array}{l}\lambda = 0 \ \text{if} \ \partial J/\partial y = 0 \ \text{and} \ F \le 0 \\ \lambda_i > 0 \ \text{if} \ \partial J/\partial y \ne 0 \ \text{and} \ F_i = 0 \\ \lambda_i = 0 \ \text{if} \ \partial J/\partial y \ne 0 \ \text{and} \ F_i < 0 \\ \text{for} \ i = 1,2,.....q\end{array} \tag{3.53}$$

Equation (3.53) mathematically implies that $\partial J/\partial y$ must be a linear combination of the vectors $\partial F_i/\partial y$, in a negative sense. Geometrically, this result means the gradient of the cost with respect to the parameters must point in a direction such that a decrease in cost can only occur under constraint violation. The conditions given in Equation (3.53) do not include the Kuhn-Tucker constraint qualification conditions which are needed for rare and uncommon minima points.[119]

The structure in Equation (3.53) is similar to that in Equations (3.32) and (3.34) motivating consideration of an adjoint procedure. Thus, adjoining Equation (3.46) to Equation (3.45) with Lagrange multipliers yields

$$H(y) = J(y) + \lambda^T F(y) \tag{3.54}$$

In this format, a first order necessary condition for the solution of the inequality constrained optimization problem is

Condition 10:

$$\begin{array}{l}H_\lambda \le 0 \\ H_y = 0\end{array} \quad \text{with} \quad \begin{array}{l}\lambda = 0 \ \text{if} \ \partial J/\partial y = 0 \ \text{and} \ F \le 0 \\ \lambda_i > 0 \ \text{if} \ \partial J/\partial y \ne 0 \ \text{and} \ F_i = 0 \\ \lambda_i = 0 \ \text{if} \ \partial J/\partial y \ne 0 \ \text{and} \ F_i < 0 \\ \text{for} \ i = 1,2,.....q\end{array} \tag{3.55}$$

Condition 10 is essentially equivalent to *Condition 7* when the inactive constraints are discarded. To show this, suppose that m of the constraints are active. The maximum number of constraints that can be independently active is p, or $m \le p$. Discard the q-m

inactive constraints and rename the remaining active constraints as F. Select m elements of y and denote them as state parameters x. The remaining elements (n=p-m) of y are denoted as decision parameters u. In this situation, $H_\lambda = 0$, $H_y = 0$ implies $H_x = 0$ and $H_u = 0$, and each $\lambda_i > 0$. *Condition 10* is thus equivalent to *Condition 7* with the added requirement that the Lagrange multipliers are positive.

With this link to Section 3.3, the second order necessary condition for the solution to the optmization problem is *Condition 8* in Equation (3.42). In addition, sufficient conditions for a local minimum under the inequality constraints are *Condition 10* (or *7*) and *Condition 9* (see Equation (3.43)). This theoretical foundation can now be applied to the sensor placement problem in this dissertation. To actually compute the optimal solution, a numerical algorithm is discussed next.

3.5 Numerical Solution Strategy

In principle, computing parameter sets that satisfy optimality conditions in Section 3.4 is straightforward. In practice, however, implementing numerical search algorithms in a software format that computes optimal parameter sets both reliably and efficiently is challenging and requires a separate combination of skills distinct from theoretic development skills. This challenge is especially true for the complex elastic aircraft dissertation application, which is computationally intensive, requiring implicit gradient construction and generation of high dimensional root locus structures involving polynomial factoring and root sorting for each independent hyper-direction in the parameter space and at each iteration step. The initial strategy was to utilize commercially available software routines for optimization such as Reference 123.

Commercial software routines based on an advanced sequential quadratic programming algorithm were tested but ultimately were found to be unworkable for the dissertation research. In simple terms, the algorithm would never converge. Based on this experience, a decision was made to manually script and implement a low order, reduced convergence rate, gradient method. This strategy provides a stable and reliable solution at the expense of increased computational effort.

A first order gradient search strategy is the simplest of all methods. An alternative name for the gradient method is the method of steepest descent. This strategy is used to find a local minimum or maximum of the objective function J subject to the inequality constraints F. The strategy is based ultimately on the simple fact that J decreases when migrating in the parameter space along a heading that is aligned opposite to the directional derivative or gradient vector. In addition, the parameter step cannot violate any constraints imposed on the system, or if the constraints are initially violated, the parameter step must bring the solution closer to a condition satisfying the constraints. This strategy forms the basis for many direct methods used in unconstrained and constrained optimization. Although these methods often are slow to converge, they are by far the most widely applied strategy because of their simplicity and reliability. The gradient method is iterative, proceeding from an initial approximation for the parameter vector y_1 to successive points y_2, y_3.....*etc.*, until some stopping criteria related to the optimality conditions from Section 3.4 are satisfied. When using the gradient method, the following basic questions immediately arise:

- What direction should the parameter vector be stepped in?
- What magnitude should the parameter vector be stepped in?

A generic algorithm structure is given in Figure 3.3. The algorithm strategy is broken down into two parts focusing on 1) constraint satisfaction and 2) cost minimization with constraint. The algorithm starts with specification of the initial parameter vector y based on problem familiarization and manual optimization results. Constraint function vector F is then evaluated and tested for compliance. If the constraints are violated, the parameter vector y is stepped in a direction to bring the constraints closer to satisfaction. Only when the constraints are rigorously satisfied, does the algorithm strategy move on to cost minimization objectives. In this part, the gradients of the cost function J and constraint function F with respect to parameter vector y are computed, and from this the Lagrange multiplier vector λ is computed. The augmented cost function gradient H_y is then computed and tested for stationarity. If a stationary condition is not achieved, the parameter vector y is stepped in a direction to reduce the cost without violating the constraints. Numerically, the constraints may be slightly violated so the algorithm returns to the initial part to make small corrections to y if necessary. This process continues until a stationary condition is reached.

In the constraint satisfaction strategy noted in Figure 3.3, stepping y can be based on the condition

$$\mathcal{F}_y \Delta y \le 0 \tag{3.56}$$

where $\mathcal{F}$ denotes a vector containing the subset of constraint functions within F that are violated, and Δy denotes the parameter increment vector. Suppose there are two constraint violations ($2 \le q$) and three parameters ($p=3$). Equation (3.56) reduces to

$$\begin{aligned} \frac{\partial \mathcal{F}_1}{\partial y_1}\Delta y_1 + \frac{\partial \mathcal{F}_1}{\partial y_2}\Delta y_2 + \frac{\partial \mathcal{F}_1}{\partial y_3}\Delta y_3 \le 0 \\ \frac{\partial \mathcal{F}_2}{\partial y_1}\Delta y_1 + \frac{\partial \mathcal{F}_2}{\partial y_2}\Delta y_2 + \frac{\partial \mathcal{F}_2}{\partial y_3}\Delta y_3 \le 0 \end{aligned} \tag{3.57}$$

This set of equations is under constrained and can be reformulated as

$$\begin{bmatrix} \frac{\partial \bar{f}_1}{\partial y_1} & \frac{\partial \bar{f}_1}{\partial y_2} \\ \frac{\partial \bar{f}_2}{\partial y_1} & \frac{\partial \bar{f}_2}{\partial y_2} \end{bmatrix} \begin{bmatrix} \Delta y_1 \\ \Delta y_2 \end{bmatrix} \leq \begin{bmatrix} -\frac{\partial \bar{f}_1}{\partial y_3} \\ -\frac{\partial \bar{f}_2}{\partial y_3} \end{bmatrix} \Delta y_3 \tag{3.58}$$

Increments Δy_1 and Δy_2 can be solved for after specifying Δy_3. The parameter update law is then

$$y_{new} = y_{old} + \Delta y \tag{3.59}$$

with $F(y_{new})$ being closer to satisfaction than $F(y_{old})$. This procedure is continued until $F(y) \leq 0$.

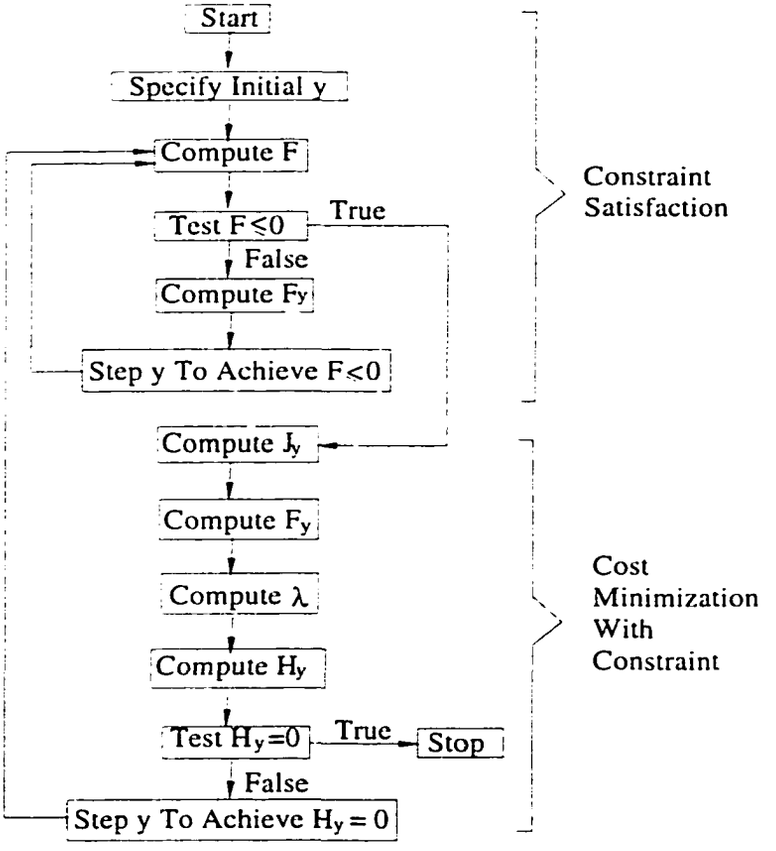

Figure 3.3 Numerical Algorithm for Inequality Constraint Optimization with Direct Lagrange Multiplier Strategy

Now suppose there are three constraint violations ($3 \leq q$) and two parameters ($p=2$). Equation (3.56) reduces to

$$\begin{aligned}
\frac{\partial \bar{F}_1}{\partial y_1}\Delta y_1 + \frac{\partial \bar{F}_1}{\partial y_2}\Delta y_2 &\le 0 \\
\frac{\partial \bar{F}_2}{\partial y_1}\Delta y_1 + \frac{\partial \bar{F}_2}{\partial y_2}\Delta y_2 &\le 0 \\
\frac{\partial \bar{F}_3}{\partial y_1}\Delta y_1 + \frac{\partial \bar{F}_3}{\partial y_2}\Delta y_2 &\le 0
\end{aligned} \tag{3.60}$$

This set of equations is over constrained and no exact solution for the increment is available. An approximate solution strategy is to artificially insert nonzero values c_i into the right-hand side of Equation (3.60), or

$$\begin{bmatrix}
\frac{\partial \bar{F}_1}{\partial y_1} & \frac{\partial \bar{F}_1}{\partial y_2} \\
\frac{\partial \bar{F}_2}{\partial y_1} & \frac{\partial \bar{F}_2}{\partial y_2} \\
\frac{\partial \bar{F}_3}{\partial y_1} & \frac{\partial \bar{F}_3}{\partial y_2}
\end{bmatrix}
\begin{bmatrix} \Delta y_1 \\ \Delta y_2 \end{bmatrix} \le
\begin{bmatrix} c_1 \\ c_2 \\ c_3 \end{bmatrix} \tag{3.61}$$

Equation (3.61) can then be "solved" by a least squares procedure. The parameter update law in Equation (3.59) is again used, and the process is repeated until $F(y) \le 0$. In this latter case, no guarantees are in place to ensure success. In addition, the problem may be overly constrained where some $F_i(y) > 0$ for all y. Additional strategy or problem reformulation may be required in these situations.

Now focus on the cost minimization with constraint strategy shown in Figure 3.3. The gradients J_y and F_y are computed first. These computations can be based on explicit closed-form expressions for J_y and F_y, if available, or they can be based on finite differencing. If the problem allows, the Lagrange multiplier vector λ can be computed directly as

$$\begin{aligned}
\lambda_i &= -J_{F_i} \ \ if \ \ F_i = 0 \\
\lambda_i &= 0 \ \ if \ \ F_i < 0
\end{aligned} \tag{3.62}$$

$$for \ \ i = 1, 2, \ldots\ldots q$$

To implement this direct method, the constraint F must be explicitly accessible for numerical manipulation. The nonzero λ_i in Equation (3.62) will most commonly be computed from a finite differencing scheme. With this information, H_y is computed and the parameter vector y is again updated, as in Equation (3.59). Here, Δy is based on the strategy

$$\Delta y = -k \frac{H_y^T}{|H_y|} \tag{3.63}$$

Equation (3.63) indicates the step direction is opposite to the modified cost gradient. This direction provides the largest reduction of H (or reduction of J without violating $F \leq 0$). Normalization by $|H_y|$ yields a unit direction, thus leaving the scaling parameter k to control the step magnitude. Parameter k can be either a scalar (uniform step magnitude) or diagonal matrix (nonuniform step magnitude) and typically must be reduced in value as the search proceeds in order to balance convergence rate with solution precision.

To further illustrate the algorithm strategy given in Figure 3.3, consider the geometry in Figure 3.4 for two parameters ($p=2$) and one constraint ($q=1$). If the current parameter solution violates the constraint (*point 1*), the step Δy will be computed similar to the strategy in Equation (3.58) and can be along the $-F_y$ vector. Repeated iterations will ultimately lead to a parameter solution that over satisfies the constraints (*point 2*). At this point, the constraints are inactive and $\lambda=0$ (see Equation (3.62)). The step Δy will be along the $-J_y$ vector ($H_y=J_y$). Repeated iterations will ultimately lead to a parameter solution that just satisfies the constraint (*point 3*). At this point, the constraint is active and $\lambda \neq 0$ (see Equation (3.62)). Geometrically, the vector λF_y is the negative projection of J_y onto F_y, or

$$\lambda F_1 = -(J_2 \cdot \frac{F_2}{|F_2|})\frac{F_1}{|F_1|} = -\frac{|J_1|}{|F_1|}\cos\theta \; F_2 \tag{3.64}$$

where θ is the angle between J_2 and F_2. Thus, Lagrange multiplier λ is precisely the negative change in J due to F_1 and Equation (3.64) matches Equation (3.62). For minimization; θ must satisfy $\pi/2 \le \theta \le \pi \; rad$, which leads to the conclusion that $\lambda>0$. Note how this precise value of λ results in H_2 being tangent to the constraint curve. The step Δy will thus be in a direction which provides the largest reduction of J without violating $F \le 0$. Depending on the constraint shape (convex or concave), the algorithm may require a return to the constraint satisfaction strategy for a small correction to y. Repeated iterations will ultimately lead to the optimum condition shown in Figure 3.5 where J_2 and F_2 are parallel and point in opposite directions. This condition corresponds to *case 2* in Figure 3.2. In principle, with more constraints and more parameters, the numerical algorithm is identical to that just discussed, but visualization is more difficult or intractable. After convergence, the second order condition should always be checked to rule out any saddle point solutions.

In some problems, the constraint relations do not permit a direct computation for the Lagrange multipliers as described in Figure 3.3 and Equation (3.62). In such problems, an alternate algorithm structure is required, such as given in Figure 3.6. The algorithm strategy is again split into two parts with the constraint satisfaction part being identical to that in Figure 3.3. The difference lies in the cost minimization with constraint section. After entering this section of the algorithm, the constraints are sorted into active constraints F_a and inactive constraints F_{ia}, or

$$F = \begin{bmatrix} F_a^T & F_{ia}^T \end{bmatrix}^T \tag{3.65}$$

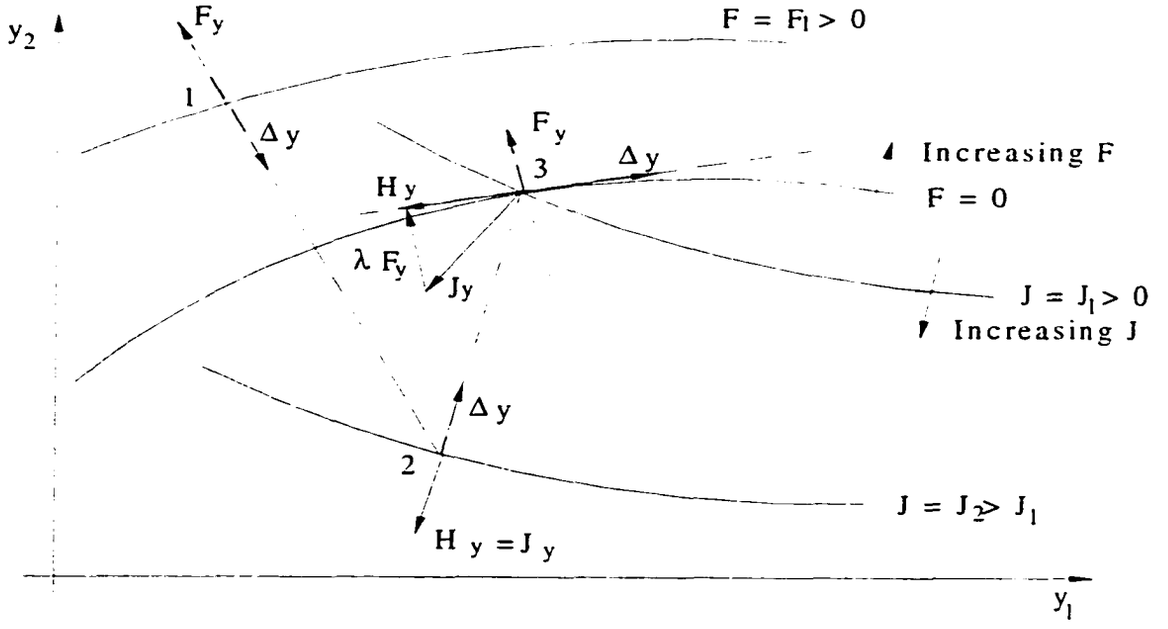

Figure 3.4 Illustration of Numerical Algorithm with Direct Strategy

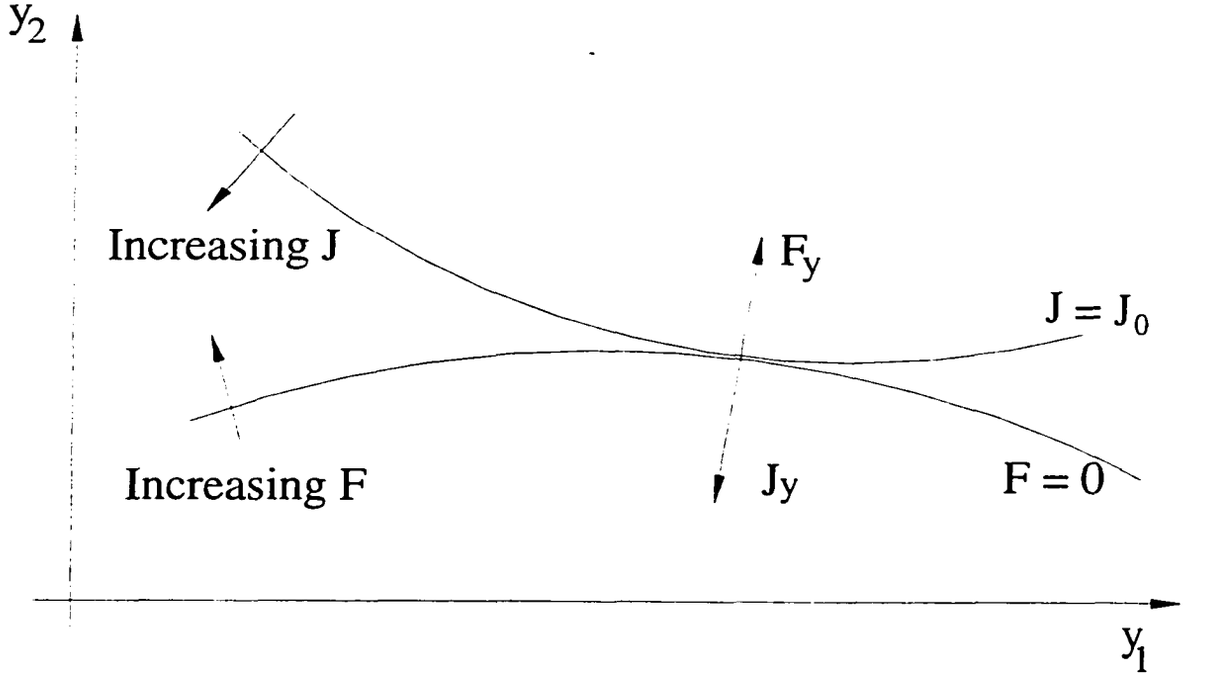

Figure 3.5 Optimum Solution Condition

In a similar fashion, sort the system parameters into state parameters x and decision parameters u

$$y = \begin{bmatrix} x^T & u^T \end{bmatrix}^T \tag{3.66}$$

To achieve this sorting, suppose that m of the constraints are active (recall $m \leq p$). Select m of the elements of y and denote them as x. The remaining $n=p-m$ elements are denoted as u. Hence, the sorting in Equation (3.66) results. Sorting of y is arbitrary, but ultimately must yield positive Lagrange multipliers (for F_a). Figure 3.6 indicates that if the Lagrange multipliers are nonpositive, then the algorithm returns to the y sorting process. One sorting set is always guaranteed to exist that leads to positive Lagrange multipliers.

After this sorting, gradients J_x, J_u and F_{ax} are computed. The augmented cost function H in Equation (3.54) and its gradient H_y thus become

$$H = J + \begin{bmatrix} \lambda_a^T & \lambda_{ia}^T \end{bmatrix} \begin{bmatrix} F_a \\ F_{ia} \end{bmatrix} \tag{3.67}$$

$$\begin{aligned} H_y &= \begin{bmatrix} J_x & J_u \end{bmatrix} + \begin{bmatrix} \lambda_a^T & \lambda_{ia}^T \end{bmatrix} \begin{bmatrix} F_{a_x} & F_{a_u} \\ F_{ia_x} & F_{ia_u} \end{bmatrix} \\ &= \begin{bmatrix} J_x + \lambda_a^T F_{a_x} + \lambda_{ia}^T F_{ia_x} & J_u + \lambda_a^T F_{a_u} + \lambda_{ia}^T F_{ia_u} \end{bmatrix} \end{aligned} \tag{3.68}$$

Next, Lagrange multipliers associated with the inactive constraints (λ_{ia}) are set to zero and the active Lagrange multipliers (λ_a) are computed indirectly, or

$$\begin{aligned} \lambda_{ia}^T &= 0 \\ \lambda_a^T &= -J_x F_{ax}^{-1} \end{aligned} \tag{3.69}$$

Gradient H_y thus becomes

$$H_y = \begin{bmatrix} 0 & J_u + \lambda_a^T F_{a_u} \end{bmatrix} = \begin{bmatrix} H_x & H_u \end{bmatrix} \tag{3.70}$$

where $H_x=0$. Finally, H_u is tested for stationarity. If a stationary condition is not achieved, the decision parameter vector u is stepped in a direction to better achieve stationarity, or

$$u_{new} = u_{old} + \Delta u \tag{3.71}$$

The increment decision vector is computed similar to the strategy given in Equation (3.63), or

$$\Delta y = \begin{bmatrix} 0 & -k\dfrac{H_u^T}{|H_u|} \end{bmatrix} = [\Delta x \quad \Delta u] \tag{3.72}$$

Note the state parameter vector x is held constant during this step.

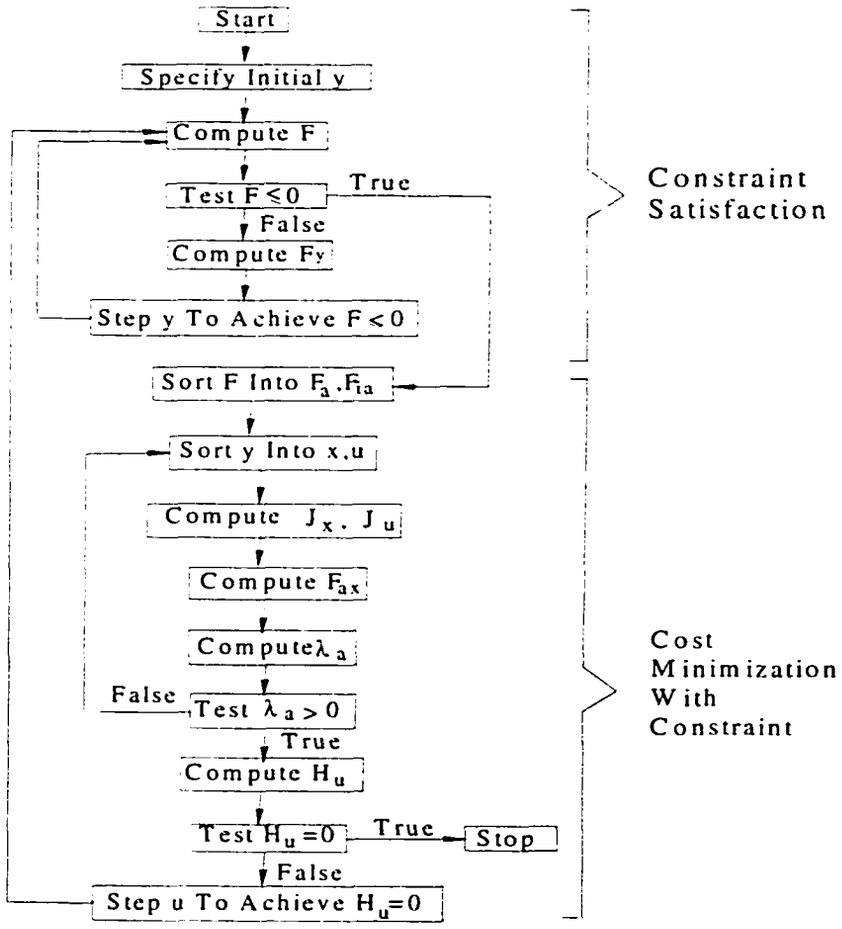

Figure 3.6 Numerical Algorithm for Inequality Constraint Optimization with Indirect Lagrange Multiplier Strategy

To further describe the arbitrariness of the y sorting process, reconsider *point 3* in Figure 3.4 redrawn in Figure 3.7. Here $p=2$ and $q=m=1$. Suppose y_1 is selected as the state parameter ($x=y_1$) and y_2 is selected as the decision parameter ($u=y_2$), as shown in Figure 3.7a. Because $F_{ay1}=F_{ax}$ and $J_{y1}=J_x$ are both negative, the active Lagrange multiplier will be negative ($\lambda_a<0$, see Equation (3.69)). Theoretic principles are violated here, and stepping the decision parameter in either direction would violate the constraint or increase the cost. Another sorting of y is required. Sorting of y must be $x=y_2$ and $u=y_1$, as shown in Figure 3.7b. Here, $F_{ay2}=F_{ax}$ and $J_{y2}=J_x$ have opposite signs leading to $\lambda_a>0$. Further, the decision parameter can be stepped into a region that does not violate the constraint and thus, the cost is reduced.

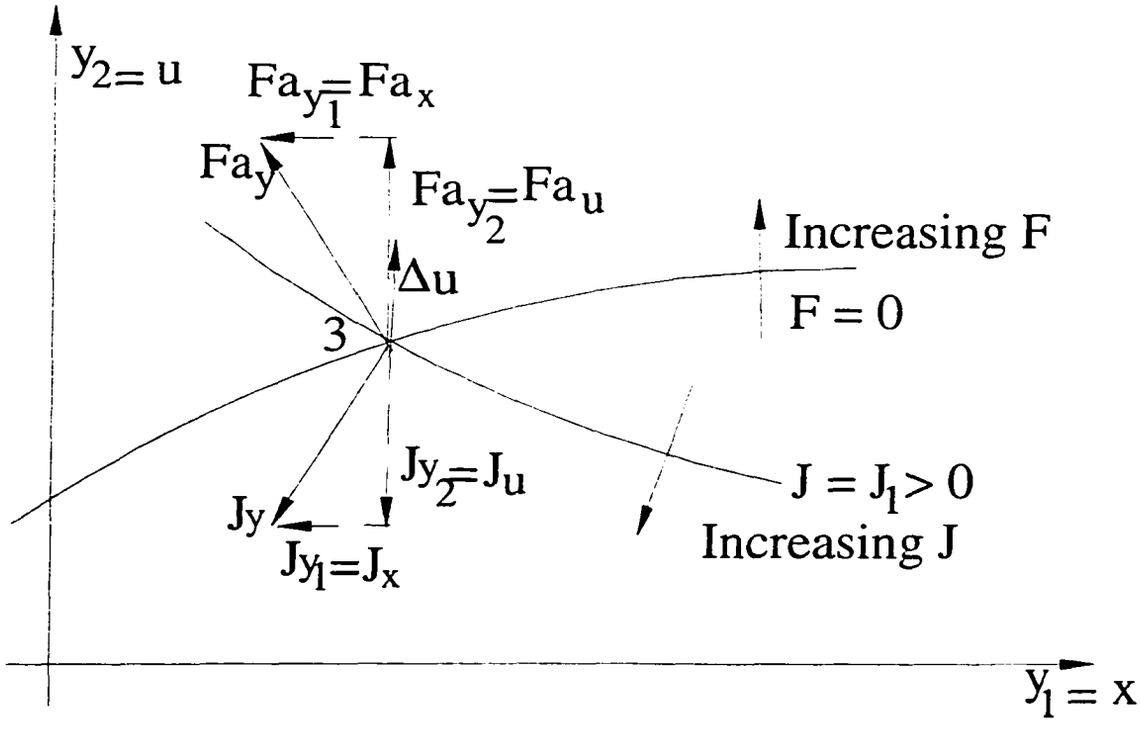

Figure 3.7a Illustration of Sorting Options

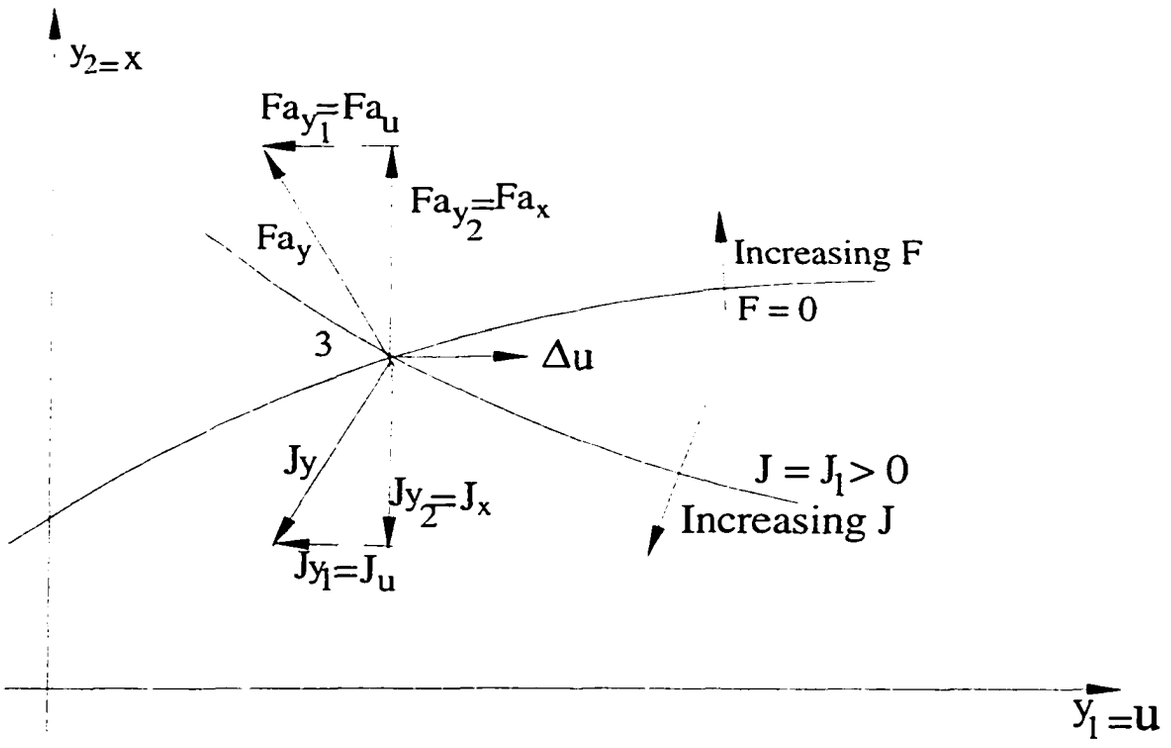

Figure 3.7b Illustration of Sorting Options

The numerical algorithm strategy discussed in Figure 3.3 and 3.6 can be thought of as generic and applicable for general problems. Such algorithms can be specifically tailored for individual problems such as those found in this dissertation. Thus, Figure 3.8 describes the numerical algorithm strategy actually implemented to solve the dissertation research problem. Note the strategy does not consider preliminary constraint satisfaction logic. Sensor placement for highly elastic vehicles with many modes and a requirement for minimum phase behavior can often lead to a highly constrained or over constrained problem statement. There may be only small regions within the parameter space, or none at all, where minimum phase behavior may be rigorously achieved. Rather than relaxing the constraint objectives, the strategy is to simply interpret *H* as the actual cost, and the

search will proceed in a direction that best reduces the value of H. Because the constraints are directly accessible, the algorithm uses a direct Lagrange multiplier strategy, and thus no distinction is made between state parameters and decision parameters. In most cases in this dissertation, the parameter vector y has two elements that correspond to sensor positions x_{s1} and x_{s2} (see Figures 2.1 and 2.2). All derivatives

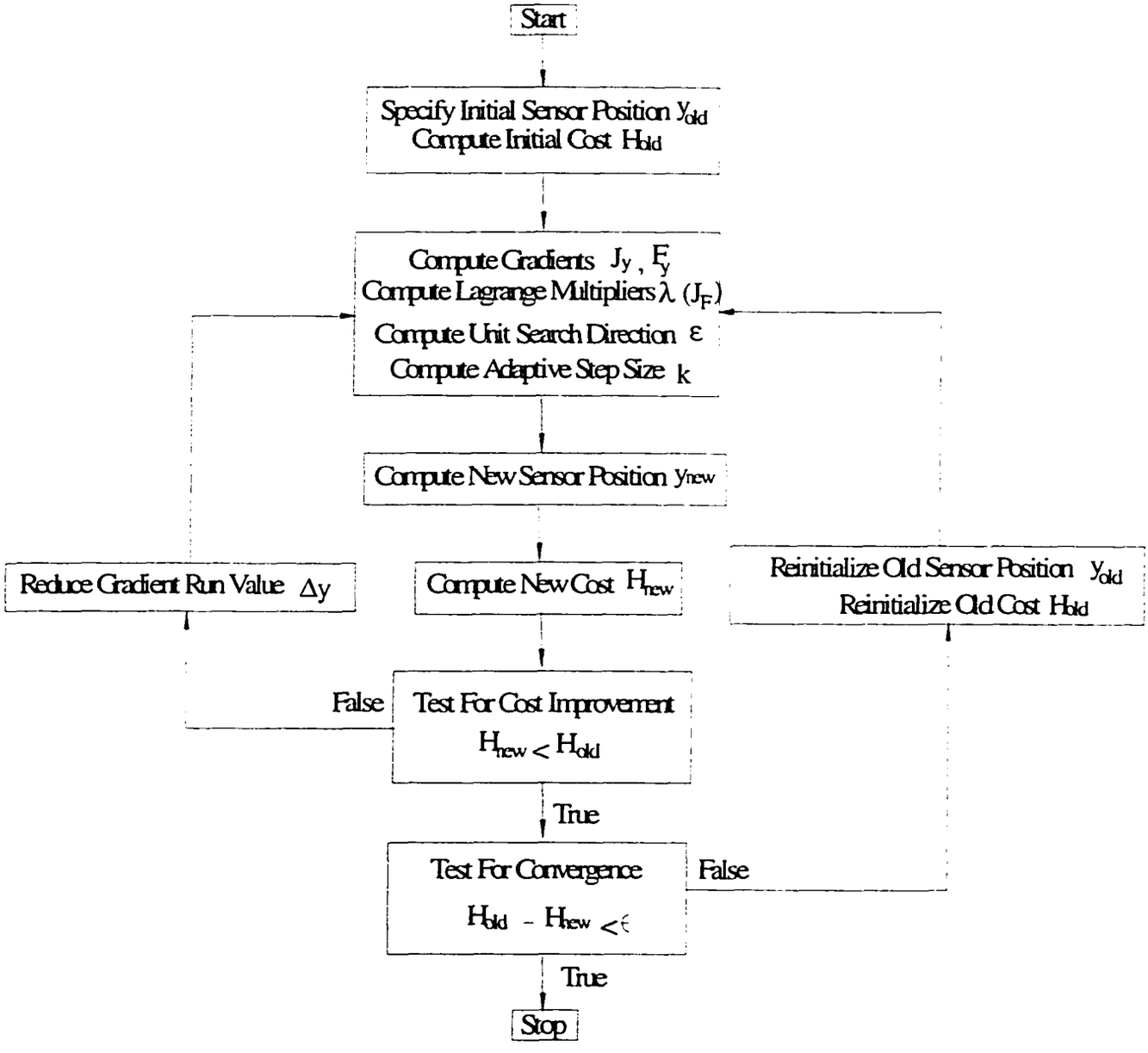

Figure 3.8 Implemented Numerical Algorithm

are computed implicitly with a finite difference scheme, and the increment gain is adaptable providing nonuniform stepping. Finally, stopping criteria is based on actual reduction of the H value, rather than H_y.

In Figure 3.8, the new cost H_{new} is computed as in Equation (3.54) using y_{new}. The new sensor positions are computed according to

$$y_{new} = y_{old} + k\varepsilon \tag{3.73}$$

with

$$y = \begin{bmatrix} x_{s1} & x_{s2} \end{bmatrix}^T$$

$$\varepsilon = \begin{bmatrix} \varepsilon_1 & \varepsilon_2 \end{bmatrix}^T \tag{3.74}$$

$$k = \begin{bmatrix} k_1 & 0 \\ 0 & k_2 \end{bmatrix}$$

The components of the unit search direction vector ε are

$$\varepsilon_i = \frac{H_{x_{si}}}{\sqrt{H_{x_{s1}}^2 + H_{x_{s2}}^2}} \tag{3.75}$$

for $i = 1, 2$

The augmented cost gradients in Equation (3.75) are computed according to

$$H_{x_{si}} = J_{x_{si}} + \lambda^T F_{x_{si}} \tag{3.76}$$

for $i = 1,2$

The cost and constraint gradients appearing above are obtained from

$$
\begin{aligned}
J_{x_{s1}} &= \frac{J(x_{s1}+\Delta x_{s1}, x_{s2}) - J(x_{s1}-\Delta x_{s1}, x_{s2})}{2\Delta x_{s1}} \\
J_{x_{s2}} &= \frac{J(x_{s1}, x_{s2}+\Delta x_{s2}) - J(x_{s1}, x_{s2}-\Delta x_{s2})}{2\Delta x_{s2}} \\
F_{j_{x_{s1}}} &= \frac{F_j(x_{s1}+\Delta x_{s1}, x_{s2}) - F_j(x_{s1}-\Delta x_{s1}, x_{s2})}{2\Delta x_{s1}} \\
F_{j_{x_{s2}}} &= \frac{F_j(x_{s1}, x_{s2}+\Delta x_{s2}) - F_j(x_{s1}, x_{s2}-\Delta x_{s2})}{2\Delta x_{s2}}
\end{aligned}
\qquad (3.77)
$$

$$\text{for } j = 1,2,\ldots\ldots q$$

Finally, the Lagrange multipliers in Equation (3.76) are computed by

$$
\begin{aligned}
\lambda_j &= 0 && \text{if } F_j < 0 \\
\lambda_j &= -\left(\frac{J(F_1,\ldots F_j+\Delta F_j,\ldots F_q) - J(F_1,\ldots F_j-\Delta F_j,\ldots F_q)}{2\Delta F_j}\right) && \text{if } F_j \geq 0
\end{aligned}
\qquad (3.78)
$$

$$\text{for } j = 1,2,\ldots\ldots q$$

The final discussion addressing the numerical algorithm in Figure 3.8 concerns the individual step size parameters k_i appearing in Equation (3.74). If k_i is small, the discrete sensor placement step will closely approximate the gradient path, but convergence will be slow since the gradient must be calculated many times. On the other hand, if k_i is large, convergence will initially be very fast, but the algorithm will eventually oscillate about the optimum. It is clear that some mechanism must be utilized for reducing the step size as the optimum point is approached. In general, large steps are desirable when the current solution is far away from the optimum. Further, a decrease in step size when an oscillation commences is desirable. Many schemes can be employed, such as reducing the step size by a fixed amount after a specified number of steps or when the cost function fails to decrease. In Figure 3.8, the adaptive step size parameter is

formulated as a function of the gradient value and the increment of the independent value used to construct the gradient, or

$$k_i = f(H_{x_u}, \Delta x_{si}) \tag{3.79}$$

Specifically, the parameter k_i is computed by the rule

$$k_i = \frac{\theta_i}{\theta^*} \Delta x_{si} \tag{3.80}$$

where θ^* is a specified constant and θ is calculated below.

$$\theta_i = \tan^{-1} \frac{\partial H}{\partial x_{si}} \tag{3.81}$$

The idea behind this adaptive rule is to increase the step size gain value in high slope regions and to decrease this value in shallow areas. Since the increment parameter Δx_{si} is used to calculate the augmented cost slope, this increment must be small, especially near the stationary point to ensure accurate slope information. Note in Figure 3.8, these increment values, or

$$\Delta y = \begin{bmatrix} \Delta x_{s1} & \Delta x_{s2} \end{bmatrix}^T \tag{3.82}$$

are reduced (halved) when the new cost value is bigger than the old value. For all runs in this dissertation, algorithm parameter values are selected as $\Delta x_{si}=1$ *in* (initial), $\theta^*=10$ *deg*, and $\epsilon = 10^{-4}$.

3.6 Sensor Placement Cost and Constraint Functionals

This section addressess the formulation and identification of sensor placement criteria (i.e., cost and constraint functions) for optimization, which are tightly coupled to

important closed-loop dynamic characteristics, and the selected design technique that effectively leverages these characteristics. As discussed in Section 2.4, the Evans root migration design strategy, and thus geometric pole-zero structure in the complex frequency plane, are of high interest. Closed-loop design objectives break down into rigid-body and aeroelastic objectives. The rigid-body design objectives are largely accounted for by using pitch rate feedback signals and proportional plus integral compensation logic. Thus, rigid-body design objectives are not directly considered in the cost function statement. However, as noted in Figures 2.17 and 2.19, situations arise where the rigid-body behavior couples with the 1^{st} aeroelastic mode characteristics. In these situations, the rigid-body behavior can be adjusted indirectly by changing the mode 1 term appearing in the cost function. Thus, the cost function is based exclusively on aeroelastic design objectives.

Aeroelastic design goals are broken down as either phase stabilization or gain stabilization objectives associated with key aeroelastic dipoles as noted in Figure 2.14. Various geometric pole-zero root structures or root loci structures can be linked to the gain and phase stabilization objectives. For example, with gain stabilization objectives (mode cancellation), an obvious relationship to consider is separation distance between the zero and pole. Define the dipole vector δ_i for mode i as the complex distance from pole to zero, or

$$\delta_i = p_i - z_i \tag{3.83}$$

where $s=-p_i$ and $s=-z_i$ denote the aeroelastic mode i pole and zero values. Thus, the dipole magnitude is simply

$$\mu_i = | \delta_i | \tag{3.84}$$

and small values are desirable for gain stabilization. A general cost function targeting gain stabilization behavior based on dipole magnitude is thus

Gain Stabilization Cost 1:

$$J = \sum_{i=1}^{n} w_i \mu_i \tag{3.85}$$

where w_i are weighting parameters and n represents the number of aeroelastic modes. By minimizing the cost, the dipole magnitudes are minimized, resulting in gain stabilization. Note key dipoles can be highlighted by nonzero w_i's.

If phase stabilization (damping augmentation) is the design objective, a corresponding relationship is the directional orientation between the zero and pole. The dipole angle is denoted by

$$\alpha_i = \angle \delta_i \tag{3.86}$$

Here, desirable values are near $3\pi/2$ *rad* for phase stabilization (see Figure 2.14). Because of this offset from *0 rad*, introduce the complementary dipole angle α_i' and its absolute value α_i'' as

$$\alpha_i' = \angle \delta_i - 3\pi / 2 \tag{3.87}$$

$$\alpha_i'' = | \alpha_i' | \tag{3.88}$$

A general cost function illiciting phase stabilization behavior based on complementary dipole angle is thus

Phase Stabilization Cost 1:

$$J = \sum_{i=1}^{n} w_i \alpha_i'' \tag{3.89}$$

By minimizing the cost, the complementary dipole angles (or their absolute values) are minimized, resulting in phase stabilization.

The cost functions in Equations (3.85) and (3.89) focus on pole-zero centered information. Cost functions can also be based on migration path centered information. Such cost functions may capture features not fully accounted for in dipole-based cost functions and *vice versa*. For example, even for cases where $\mu_i \approx 0$ *rad/s* or $\alpha_i \approx 3\pi/2$ *rad*, the pole migration may follow an unexpected and undesirable path or initial direction, theoretically speaking. Migration path based cost functions may be more appropriate in these situations. For gain stabilization objectives, the length of the migration path is an appropriate criterion. If *ds* denotes the infinitesimal distance traveled along the i^{th} migration path, the total path length is

$$\lambda_i = \int_{\substack{s=-p_i \\ along\ \ loci}}^{s=-z_i} |\, ds \,| = \int_{\substack{k_k=0 \\ along\ \ loci}}^{k_k=\infty} \left| \frac{ds}{dk_k} \right| dk_k \tag{3.90}$$

assuming $k_{g_{11}} > 0$ (recall Equation (2.33)). Desirable λ_i values for gain stabilization objectives are near *0 rad/s*. A general cost function based on path length would thus be

Gain Stabilization Cost 2:

$$J = \sum_{i=1}^{n} w_i \lambda_i \tag{3.91}$$

Gain stabilization behavior would occur when the path length, or the cost, is minimized.

With phase stabilization objectives, the corresponding criterion is the angle along the migration path averaged by the path length itself. Denote the migration path angle θ_i at one point along the loci as the angle between the real axis and the tangent to the migration path at the location *s*, or

$$\theta_i = \angle ds \tag{3.92}$$

For phase stabilization objectives, desirable θ_i values are near $\pi\, rad.$ The complementary migration path angle and its absolute value are thus introduced as

$$\theta_i' = \theta_i - \pi \tag{3.93}$$

$$\theta_i'' = |\theta_i'| \tag{3.94}$$

The averaged complementary migration path angle (absolute value) is computed by

$$\phi_i = \frac{1}{\lambda_i} \int_{\substack{s=-p_i \\ along\ loci}}^{s=-z_i} \theta_i'' |\, ds\, | = \frac{1}{\lambda_i} \int_{\substack{k_k=0 \\ along\ loci}}^{k_k=\infty} \theta_i'' \left| \frac{ds}{dk_k} \right| dk_k \tag{3.95}$$

Note the upper limit of integration can be lowered to emphasize the initial segment of the entire path. A general cost function based on path angle would thus be

Phase Stabilization Cost 2:

$$J = \sum_{i=1}^{n} w_i\, \phi_i \tag{3.96}$$

Phase stabilization behavior would occur when this cost is minimized.

A special case of this last criterion occurs when only the initial path angle is considered. Note the migration path angle θ_i at the initial point along the path is equivalent to the departure angle θ_{di} defined in Equation (2.39), or

$$\theta_i\, |_{s=-p_i} = \theta_{d_i} \tag{3.97}$$

This equality gives rise to a complementary departure angle and its absolute value as

$$\theta_{d_i}' = \theta_{d_i} - \pi \tag{3.98}$$

$$\theta_{d_i}'' = |\theta_{d_i}'| \tag{3.99}$$

Under this special case, note the averaged complementary migration path angle (absolute value) reduces to

$$\phi_i = \theta''_{d_i} \tag{3.100}$$

and the cost function in Equation (3.96) simplifies to

$$J = \sum_{i=1}^{n} w_i \, \theta''_{d_i} \tag{3.101}$$

In this dissertation, optimal sensor placement studies are based exclusively on Equations (3.85) and (3.101), or a combination thereof. The selection of μ_i over λ_i for gain stabilization cost is founded on subjective and objective bases. Historically speaking, manual sensor placement efforts with aeroelastic vehicles most commonly deals with minimization of 1^{st} aeroelastic mode content within the feedback signal. Placement criteria are based on simple inspection of the transfer function aeroelastic zero location relative to the pole. Construction and consideration of the migration path is typically not considered. Additionally, if path length was to be considered, an accurate calculation of path length would require a fine compensator gain grid, and this would lead to high computational burdens with a high dynamic order vehicle within an iterative optimization search algorithm. For these reasons, μ_i based cost is selected over λ_i based cost. Selection of ϕ_i ($\theta_i'' = \theta''_{di}$) over α_i (α_i'') for phase stabilization cost is based simply on the importance of the initial path direction for lightly damped modes such as those associated with aeroelastic vehicles.

To sample the type of cost function surface being addressed in this dissertation for insight and understanding, Figures 3.9 and 3.10 show three dimensional plots of J vs. x_{s1}

and x_{s2} for two simplified gain and phase stabilization cost functions given below for the flexible aircraft model described in Chapter 2.

$$J = w_1 \mu_1 + w_3 \mu_3 \tag{3.102}$$

$$J = w_1 \theta''_{d_1} + w_3 \theta''_{d_3} \tag{3.103}$$

Inclusion of only modes *1* and *3* is due to trade offs noticed in manual sensor placement studies (see Figures 2.18-2.19 and Reference 45). Numerical parameters used in constructing these cost surfaces are $w_1=w_3=1$ *s/rad* or *1/deg*, $h_1=h_2=1$, $z_k=2$ *rad/s* for the phase stabilization case, and $z_k=1$ *rad/s* for the gain stabilization case. First note the cost surface is symmetric about the plane $x_{s1}=x_{s2}$. In Figure 3.9a, note there are two general regions consisting of high and low plateaus. To be on the low plateau, both sensors must lie in the aft regions of the airframe. Thus, careful sensor placement can lead to significant improvements. In the close-up view in Figure 3.9b, note in the low cost regions, the surface is relatively flat, but there exists a long narrow trough with multiple local minimum points. The trough is steep on one side and shallow on the other. Figure 3.10 shows similar traits, but the surface is even flatter. This relatively flat surface may pose a difficult challenge to extract the remaining cost reductions from a gradient based search algorithm. Further, the starting sensor locations may strongly influence which local minimum point is approached. The reader is reminded that modified cost H will be minimized (not J), and the $\lambda^T F$ constraint cost is not included in Figures 3.9-3.10. The reader should also realize that construction of Figures 3.9-3.10 is computationally intensive and is infeasible to construct for every weighting, compensator, and blend selection investigated, and is intractable for more than two sensors. Information in

Figures 3.9 and 3.10 is only for general insight and will not be applicable for specific optimization cases presented in Chapters 4-6.

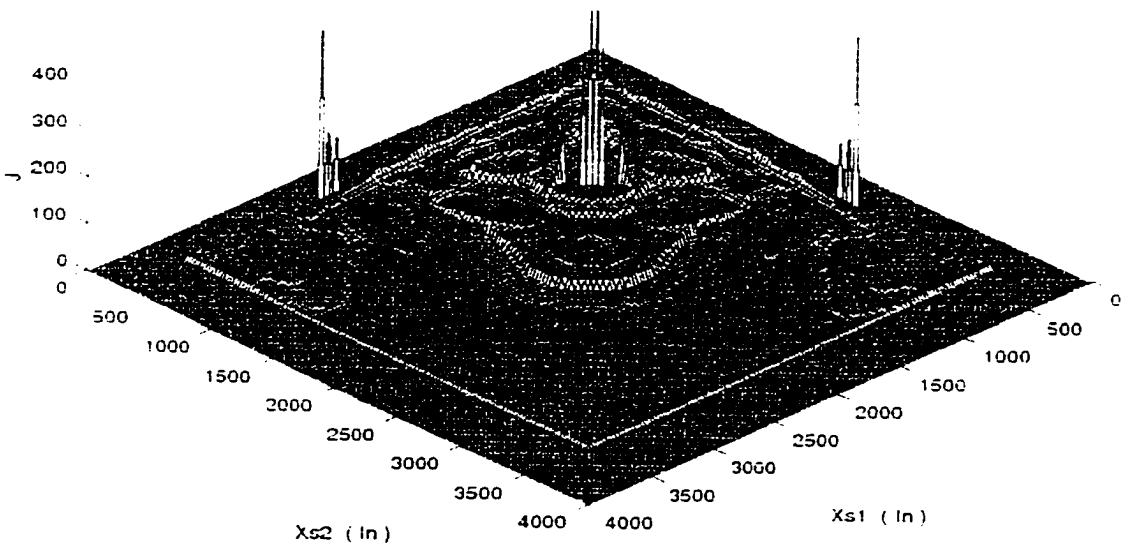

a)

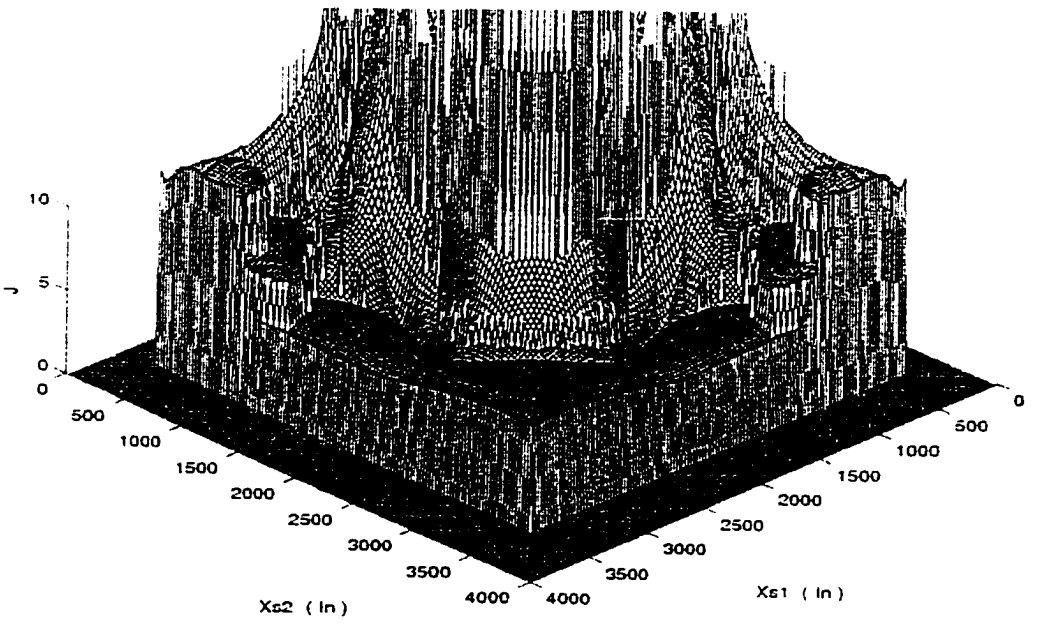

b)

Figure 3.9 Gain Stabilization Surface Cost Plot

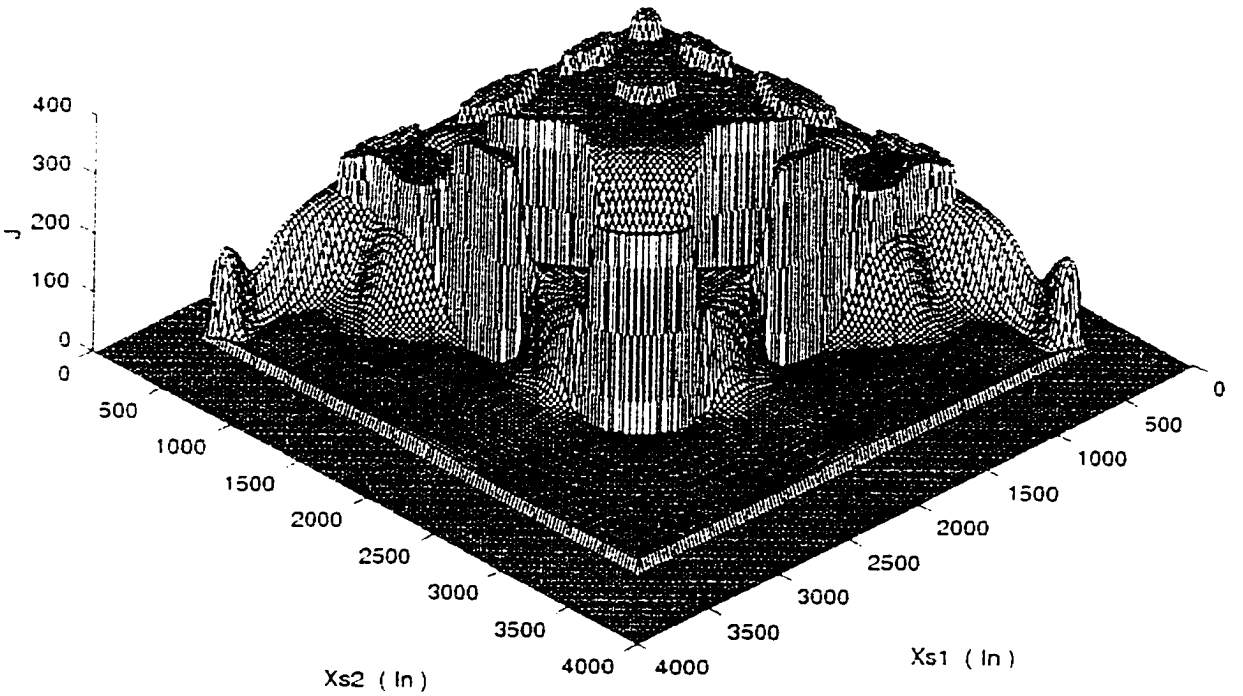

a)

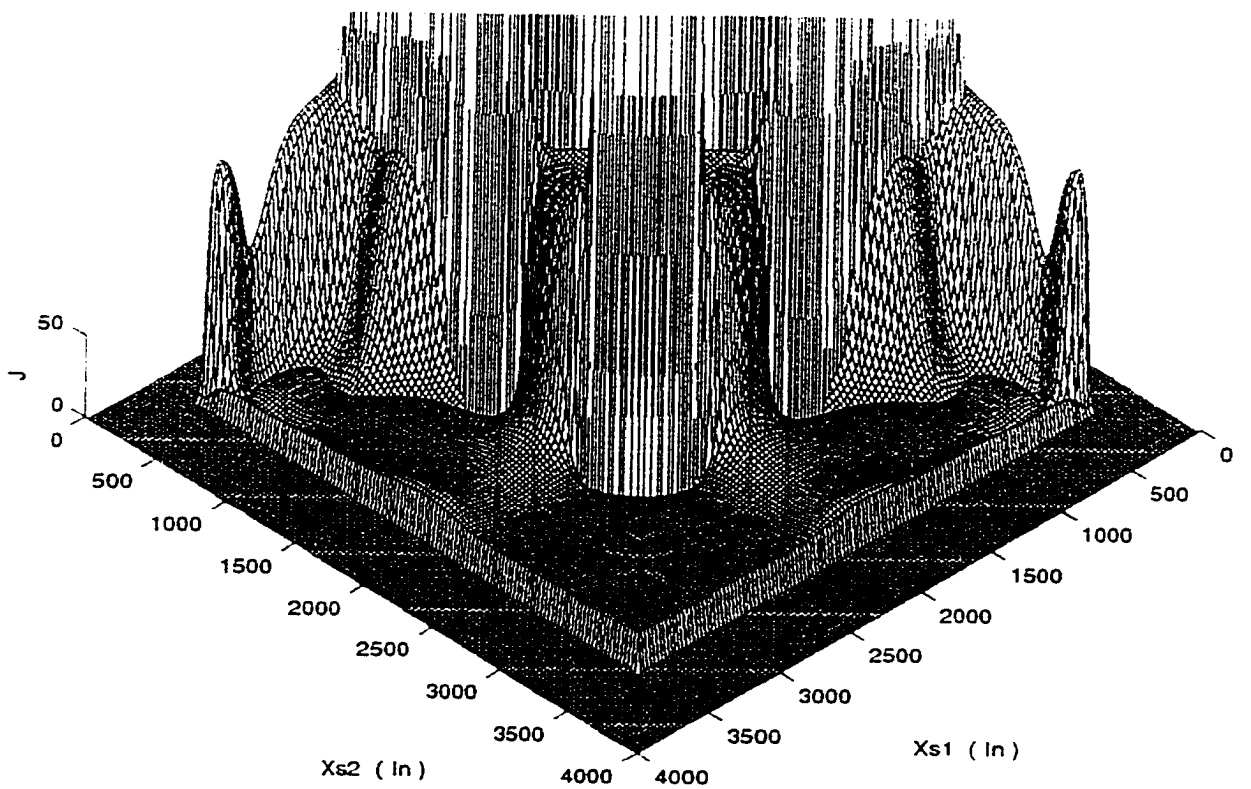

b)

Figure 3.10 Phase Stabilization Surface Cost Plot

Feedback sensors cannot be placed freely but rather must satisfy certain practical design constraints. In many cases, nonminimum phase aeroelastic zeros are present in transfer functions corresponding to arbitrarly placed sensors. Right-half plane zeros are undesirable since they will always attract a closed-loop pole for sufficient loop gain. These zeros are to be avoided in all situations. To force all transfer function zeros into the stable region, constraint equations must account for this behavior. Thus, all cost functions in this dissertation will be subject to

Minimum Phase Constraints:

$$F_i = \mathrm{Re}(-z_i) \leq 0, \quad (i=1,2,.....n) \tag{3.104}$$

where F_i is the inequality constraint function and $s = -z_i$ denotes the aeroelastic mode i zero location. If rigorously enforced, these constraint equations insure that all aeroelastic zeros will lie in the left-half plane. Additional constraints require the sensors to lie on the airframe and within regions where the function fits to the raw mode shape data are accurate (see Section 2.3 and Appendix). Thus, in addition to Equation (3.104), all dissertation cost functions will be subject to

On The Body Constraints:

$$F_i = x_{si} - \overline{x_s} \leq 0 \tag{3.105}$$

$$(i=n+1,\ n+2,.....n+n_\Omega)$$

$$F_i = \underline{x_s} - x_{si} \leq 0 \tag{3.106}$$

$$(i=n+n_\Omega+1,\ n+n_\Omega+2,.....n+2n_\Omega)$$

In Equation (3.105)-(3.106), $\bar{x}_s$ and $\underline{x}_s$ denote upper and lower bounds on acceptable sensor positions. When rigorously applied, these constraints insure the sensors lie on the

airframe. In this dissertation, on the body constraint parameters are fixed as $\underline{x}_s$=*300 in* and $\bar{x}_s$=*3,500 in.*

Figure 3.11 illustrates the feasible and infeasible sensor placement regions rigorously imposed by the minimum phase and on the body constraints in Equations (3.104)-(3.106) for two sensors associated with the flexible aircraft model from Chapter 2. Numerical parameters used in constructing Figure 3.11 include h_1=h_2=*1* and $\underline{x}_s$ =*300 in*, and $\bar{x}_s$ = *3,500 in.* First note the feasible/infeasible regions are symmetric about the line $x_{s1} = x_{s2}$. The on the body constraints carve out a rectangular region of feasibility. The composite minimum phase constraint of all eighteen aeroelastic modes leaves a small oddly shaped area where at least one sensor is generally located in the aft region of the fuselage. This result is consistent with Figure 2.17 and 2.2 where it was noted that a collocated elevator and rate gyro leads to minimum phase behavior. Note the feasible region in Figure 3.11 generally overlaps the low cost region in Figures 3.9-3.10. The relatively small feasible region in Figure 3.11 suggests the aeroelastic sensor placement problem is highly constrained. This observation justifies the algorithm search strategy in Figure 3.8, which does not address the initial constraint satisfaction logic discussed in Figure 3.3 and 3.6. Recall the dissertation strategy is simply to interpret $H=J+\lambda^T F$ as the cost and any reduction in H, either from J or $\lambda^T F$, is desirable.

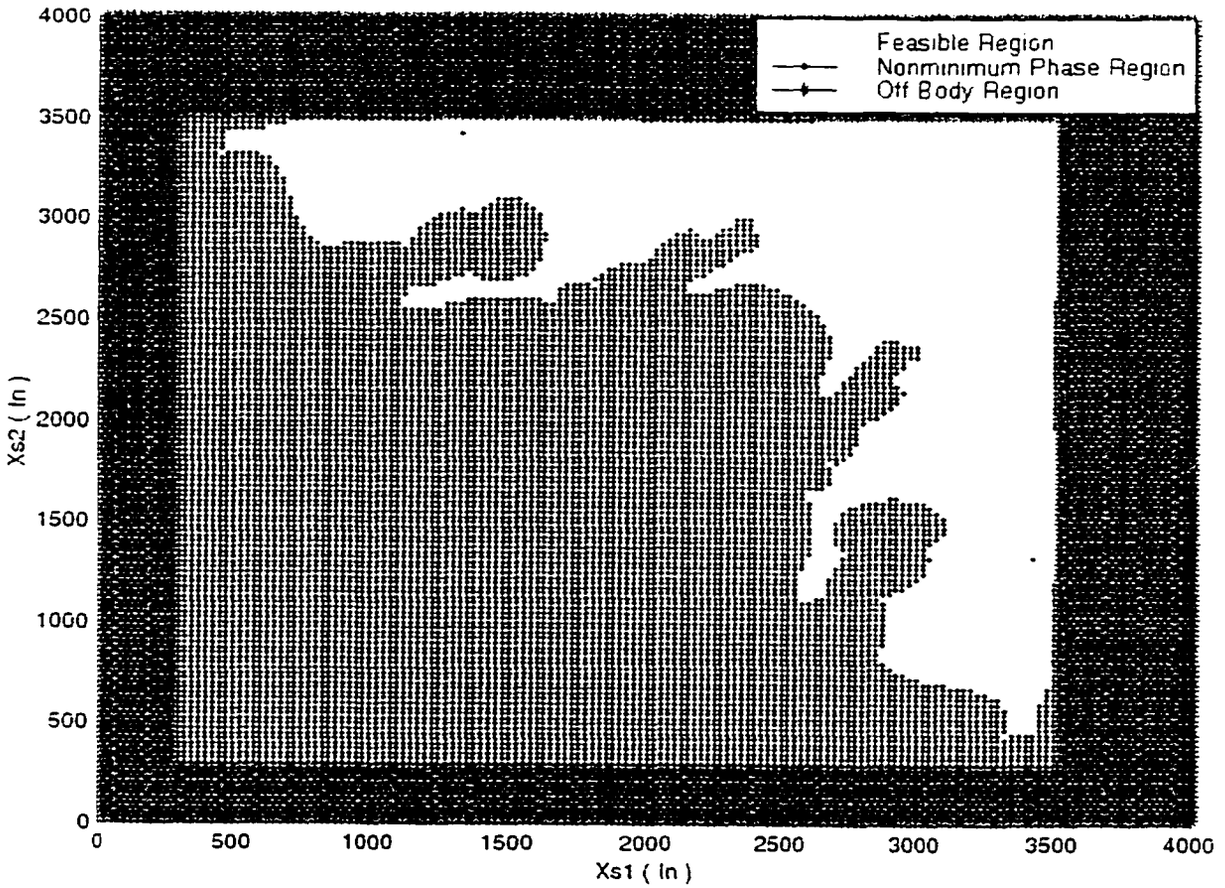

Figure 3.11 Feasible Sensor Placement Regions

Now that specific cost and constraint functions are laid out, a few additional comments on the numerical algorithm (see Figure 3.8) are warranted. The minimum phase and on the body constraints (Equation (3.104)-(3.106)) are of such structure that direct computation of the Lagrange multipliers is feasible (see Equation (3.78)). For the minimum phase constraints, the j^{th} Lagrange multiplier in Equation (3.78) can be calculated by giving small increments to the real part of each aeroelastic zero as follows: For a certain sensor position, the open-loop transfer function can be represented as

$$\hat{y}(s)/u(s) = k(s)(h_1(s)g_{11}(s) + h_2(s)g_{21}(s)) = k\frac{(s+z_1)(s+z_2)\cdots}{(s+p_1)(s+p_2)\cdots} \qquad (3.107)$$

where root sorting has resulted in the aeroelastic zeros $-z_j$ corresponding to $j=1, 2, \ldots..n$. Let $z_j = \sigma_j - i\omega_j$. Note the constraints F_j in Equation (3.104) are equivalent to $-\sigma_j$. Thus, let $\Delta F_j = \Delta\sigma_j$ where $\Delta\sigma_j$ denotes the increment value applied to the zero's real part when computing $\lambda_j=-J_{Fj}$ in Equation (3.78). When the aeroelastic zero is complex and its real part is perturbed by $\Delta\sigma_j$, the corresponding conjugate zero must also be perturbed to preserve symmetry about the real axis. Implementation and utilization of this Lagrange multiplier construction is computationally intensive. Computation of the Lagrange multipliers associated with the on the body constraints is much simpler since the constraints are nothing more than offsets of the sensor positions (see Equations (3.105)-(3.106)). In this dissertation, the constraint increment parameter is fixed at $\Delta\sigma_j=0.1$ *rad/s*.

Since the root migration framework is symmetric about the real axis, only the upper quadrant contributions to the cost in Equations (3.85) and (3.101) are used. The conjugate contribution terms are not included in the numerical algorithm. This stipulation significantly reduces computational burdens. Computation of the departure angle based cost function in Equation (3.101) is straight forward and poses no difficulty. The departure angles are computed according to Equation (2.40), or a modified version, thereof. This computational ease is not the case when considering the dipole magnitude based cost function in Equation (3.85). Here, each aeroelastic dipole must be computationally identified from a list of transfer function roots at each iteration. This process is computationally intensive and is described below.

First, out of all the open-loop transfer function poles, the aeroelastic poles in the upper quadrants of the complex plane are identified and sorted in ascending order according to their natural frequency values. Figure 2.22 clearly shows that the

corresponding closed-loop pole does not always migrate towards the closest zero. This possibility complicates the dipole (i.e., zero) identification process. The zero used in Equation (3.83) to construct the dipole vector is defined to be the zero the open-loop pole migrates towards as $|k_k|$ approaches ∞. The only reliable way to identify this zero is to construct the root locus at each iteration in the numerical search and sort the aeroelastic zeros according to the final location along each aeroelastic pole migration path. The k_k grid used to construct the migration paths must be sufficiently fine to render accurate resolution during the piecewise migration steps. This process is computationally intensive.

Several subtle points in this aeroelastic zero sorting process arise when implementing this strategy in computer software. Sometimes the aeroelastic pole will migrate towards a real axis aeroelastic zero such as the 12^{th} mode in Figure 2.15c migrating towards the zero located at *+25.9 rad/s* in Figure 2.4 and Table 2.1. In this situation, both the lower quadrant and upper quadrant poles form a break-in point on the real axis with one migration path heading towards the real axis zero and the other heading toward $+\infty$ *rad/s*. If the upper quadrant pole path is identified as heading towards $+\infty$ *rad/s*, the migration path must be switched to the lower quadrant pole path after reaching the real axis.

Sometimes the 1^{st} aeroelastic mode and rigid pitch mode will couple in the sense that the aeroelastic pole migration path ends at the compensator zero, which physically is not an aeroelastic zero. Likewise, the rigid pitch pole migration ends at a pair of complex roots physically associated with the 1^{st} aeroelastic mode. Figure 2.17 and 2.19 are examples of this behavior. These situations raise the question of whether the zeros should

be swapped before dipole vector construction. In this dissertation, when this situation is identified, the zeros are swapped before dipole vector construction. Implementation of sorting logic for this situation is non-trivial. In fact, when dynamic blending filters or variable static blending filters are considered, the appearance of multiple low frequency complex zeros made this sorting logic intractable, and the dipole is reverted to the original definition.

CHAPTER 4

OPTIMAL SENSOR PLACEMENT: GAIN STABILIZATION

4.1 Introduction

This chapter deals with computing optimal sensor locations using gain stabilization objectives. This procedure is based on minimizing aeroelastic dipole magnitudes as described in Equation (3.85). Dipole magnitude values for selected aeroelastic modes will be minimized using the optimization method presented in Figure 3.8. During optimization, inequality constraints addressing minimum phase zero and on the body sensor behavior, as presented in Equations (3.104)-(3.106), are enforced. The general form of the cost function utilized in this chapter, based on dipole magnitude with inequality constraints, can be written as

$$H = \sum_{i=1}^{18} w_i \mu_i + \sum_{i=1}^{22} \lambda_i F_i \tag{4.1}$$

In this study, only the key dipole magnitude values of the low frequency modes *1* and *3* and an additional high frequency mode (*10*) that affects control system stability are considered. Thus, the only nonzero weights in Equation (4.1) will be w_1, w_3, and w_{10}. This selection is based on knowledge obtained during manual sensor placement efforts. The solution strategy is to start with simple blend filters and progress to more advanced blending logic (and hence more design freedom) when necessary. Static and dynamic filters with fixed parameters, as well as variable parameters, will be considered.

Weighting factors are selected based on relative dipole magnitude values and are refined to tailor the solution results. Different initial positions for sensor locations will also be tested and used for solution refinement. The compensator zero parameter is specified and fixed (z_k=*1 rad/s*) to allow an acceptable trade off between the mode *1* dipole magnitude tightness and the rigid pitch damping. For the most desirable sensor placement solutions, the time responses and general behavior of the closed-loop system will be tested and evaluated.

4.2 Sensor Placement with Fixed Static Blending

In this section, optimal gyro placement corresponding to the flight control system architecture shown in Figure 2.20 will be investigated. Optimization parameters are the two gyro locations x_{s1} and x_{s2}. The blending filters in the feedback signals will be considered constant, static values equal to one for each filter. The static filters can be represented by the following expressions.

$$h_1(s) = 1 \tag{4.2}$$

$$h_2(s) = 1 \tag{4.3}$$

The fixed static filters in both Equations (4.2) and (4.3) express the simplest blending logic. These filters represent spectrally uniform and equally balanced blending. The procedure for finding the optimal sensor locations depends on the initial sensor positions used in the optimal search strategy. From Figure 3.9, as well as from manual placement experience, candidate initial sensor locations can be determined. The weighting factors of the cost function terms are initially assigned equal to one. Based on the optimization results, these values will be adjusted in order to find desirable solutions satisfying the

system requirements. If the solution characteristics are unsatisfactory, other dipole terms will be added to the cost function with appropriate weighting factors, or other initial sensor locations will be sought, dependent on the evaluation of the optimization results.

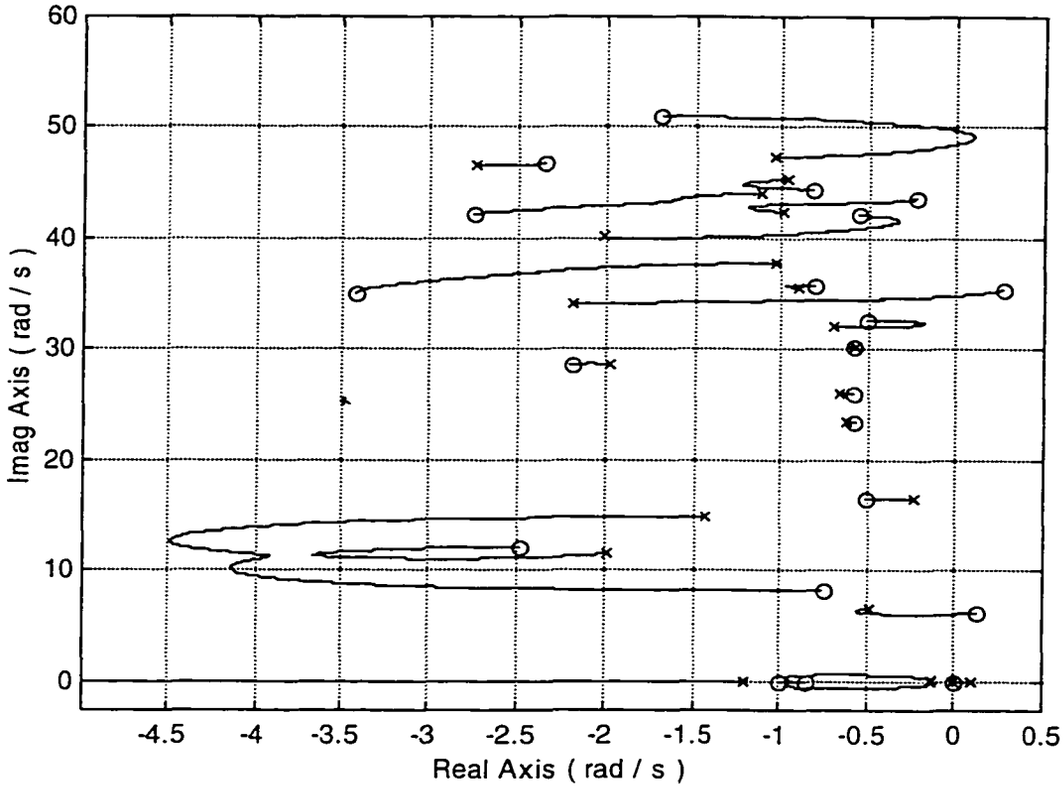

Figure 4.1 Root Locus Plot for x_{s1}=*850 in* and x_{s2}=*2,750 in* (z_k=*1 rad/s*)

As a baseline, consider the augmentation characteristics associated with a manual sensor placement solution. For the initial sensor positions of x_{s1}=*850 in* and x_{s2}=*2,750 in*, the resulting root locus diagram is illustrated in Figure 4.1. Observe in Figure 4.1 the relaxed stability pole near the origin is stabilized and good levels of damping in the rigid pitch mode are achieved (see migration path initiating from near the origin and wrapping

around towards the real axis compensator zero). These trends indicate desirable rigid-body augmentation. Aeroelastic augmentation is not so favorable. Note the 3^{rd} aeroelastic dipole has a considerable magnitude value (μ_3=*6.6176 rad/s*). This large value allows the 3^{rd} aeroelastic mode to have a big influence on the overall time response. The mode 1 dipole magnitude value is not as large as for mode *3*, but is still excessively large (μ_1=*0.7487 rad/s*). Also observe from Figure 4.1, as loop gain is increased both mode *1* and mode *10* are destabilized due to nonminimum phase zeros. These right-half plane zeros can lead to reduced structural mode damping, phase loss in the control loop, and possibly response reversal. These unacceptable characteristics must be corrected with improved sensor locations.

For the initial sensor positions of x_{s1}=*850 in* and x_{s2}=*2,750 in*, the optimization algorithm is applied to the augmented cost function

$$H = w_1\mu_1 + w_3\mu_3 + \sum_{i=1}^{22} \lambda_i F_i \tag{4.4}$$

with weights w_1=w_3=*1 s/rad*. The resulting optimal sensor positions are x_{s1}=*861.5 in* and x_{s2}=*2,744 in*. With sensors placed at these optimal values, the resulting root locus diagram is illustrated in Figure 4.2. Comparing Figure 4.2 with 4.1, note the dipole magnitude values for both aeroelastic mode *1* and *3* have decreased from *0.7487* to *0.7372 rad/s*, and from *6.6176* to *2.8603 rad/s*, receptively. However, the mode 1 dipole magnitude reduction is modest and the reduction of mode *3's* dipole magnitude primarily arises due to a switch in the associated dipole zero, and not in significant zero movement. These reductions are consistent with the objectives of Equation (4.4) where the initial and final *H* values are *7.4616* and *7.4167*, respectively. In Figure 4.2, the zeros of the 1^{st} and 10^{th} aeroelastic modes still lie in the right-half plane. Recall the numerical algorithm does

not rigorously address constraint satisfaction and this is why nonminimum phaseness still remains. This strategy was by choice due to the very limited feasible sensor region (see Figure 3.11). However, the strategy does treat $\lambda_i F_i$ as an additional cost and as noted above, the overall cost is reduced to a local minimum.

Technically speaking, Figure 4.2 shows improved results compared to Figure 4.1 (i.e., smaller μ_1 and μ_3). Practically speaking, however, the two results are not significantly different (sensors only moved *10 in* or less). In simpler terms, mode *1* and *3* are not sufficiently gain stabilized, and mode *1* and mode *10* destabilization (i.e., less stable as loop gain increases) is unacceptable. The cost function in Equation (4.4) was tested with many different weight factors but failed to result in improved conditions. The results in Figure 4.2 can be considered as the best for the cost function structure in Equation (4.4) and the given starting positions. In other words, for the given cost function and initial sensor positions, very little optimization or design freedom is available and additional changes must be considered for any further improvement.

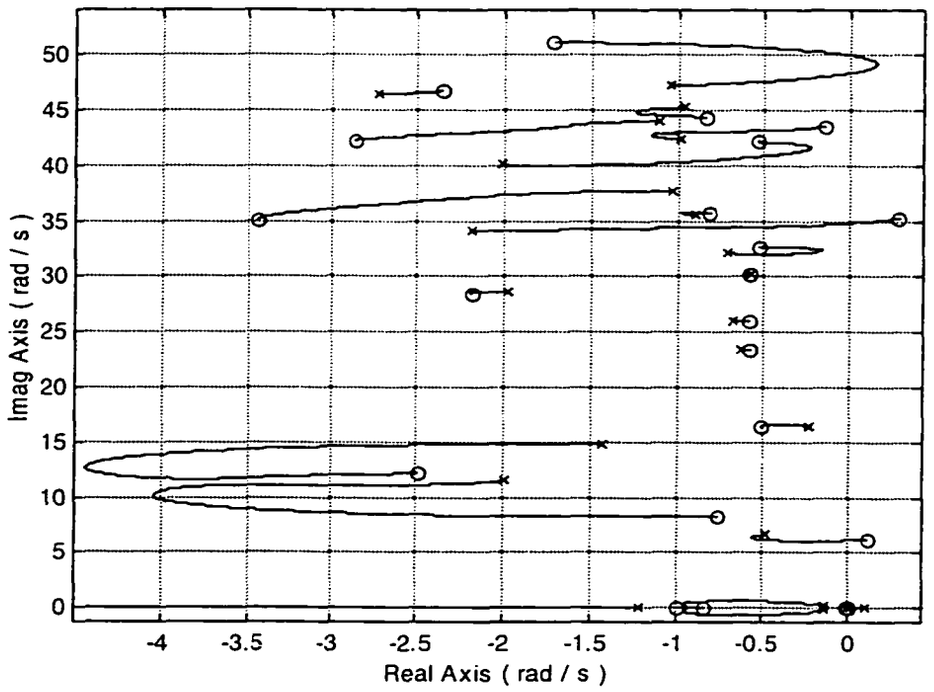

Figure 4.2 Root Locus Plot for x_{s1}=*861.5 in* and x_{s2}=*2,744 in*

To overcome this situation, an additional term representing the dipole magnitude value of the 10^{th} aeroelastic mode is included in the objective function. The updated cost function can be written in the following form.

$$H = w_1\mu_1 + w_3\mu_3 + w_{10}\mu_{10} + \sum_{i=1}^{22} \lambda_i F_i \tag{4.5}$$

The cost function of Equation (4.5) is used to obtain optimal sensor locations by starting the sensors in the same previous initial positions, but using different values of the weighting factors. For weight factors of w_1=*2 s/rad*, w_3=*3 s/rad*, and w_{10}=*5 s/rad*, it is found that the optimal positions of the sensors are x_{s1}=*880.6 in* and x_{s2}=*2,999.6 in*. Note one of the sensors moved approximately *20 ft*. The root locus plot of the control system when the sensors are placed in these optimal positions is illustrated in Figure 4.3. In addition, Figure 4.4 shows the augmented cost function value at each optimization

iteration, while Figure 4.5 shows the track of sensor positions during the search. It is noticed by comparing Figure 4.3 with Figure 4.1 that the dipole magnitude values for both modes *3* and *10* decreased from *6.6176* to *6.3274 rad/s* and from *2.7580* to *1.8877 rad/s*, respectively, while the dipole magnitude value for the 1^{st} mode increased from *0.7487* to *1.5909 rad/s*. Observe from Figures 4.2 and 4.3 that by giving a bigger weight value for mode *3*, and by including a mode *10* cost with a large weight value, the magnitude dipole values for these modes are decreased and the nonminimum phase zero behavior has been eliminated (although this is not guaranteed by the numerical algorithm). A clear trade between mode *1* and mode *3* exists: when the magnitude dipole value for one of them decreases, the magnitude dipole value for the other increases. In general, the magnitude dipole values for both mode *1* and *3* indicate that both modes are still not sufficiently gain stabilized.

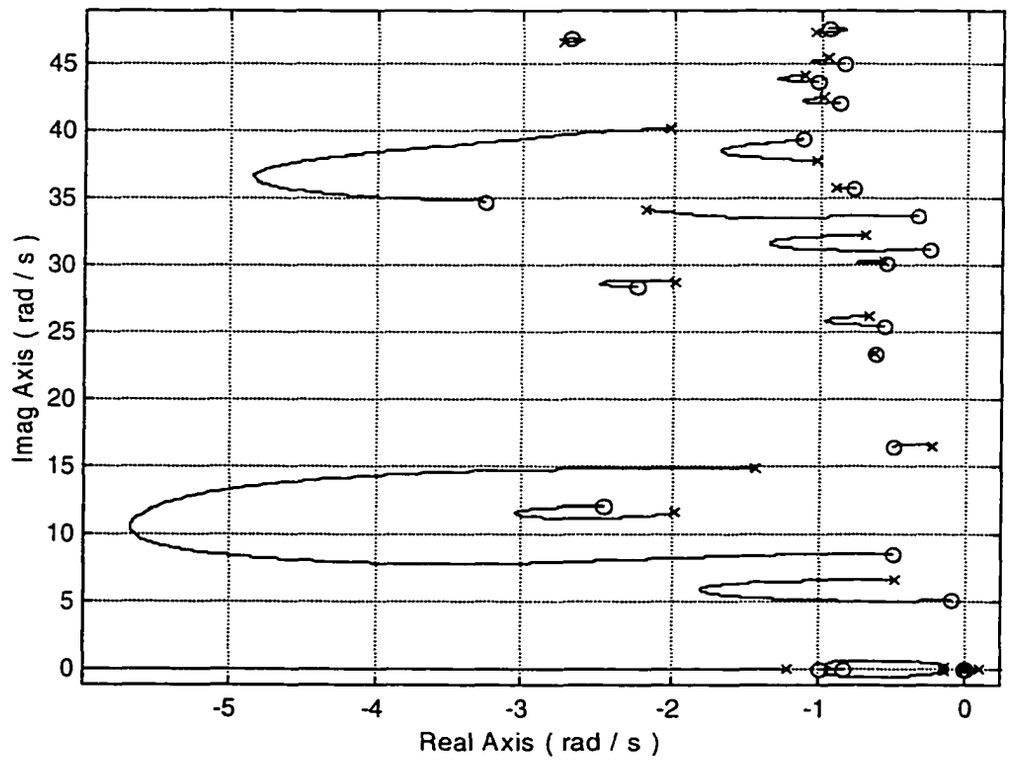

Figure 4.3 Root Locus Plot for x_{s1}=*880.6 in* and x_{s2}=*2,999.6 in*

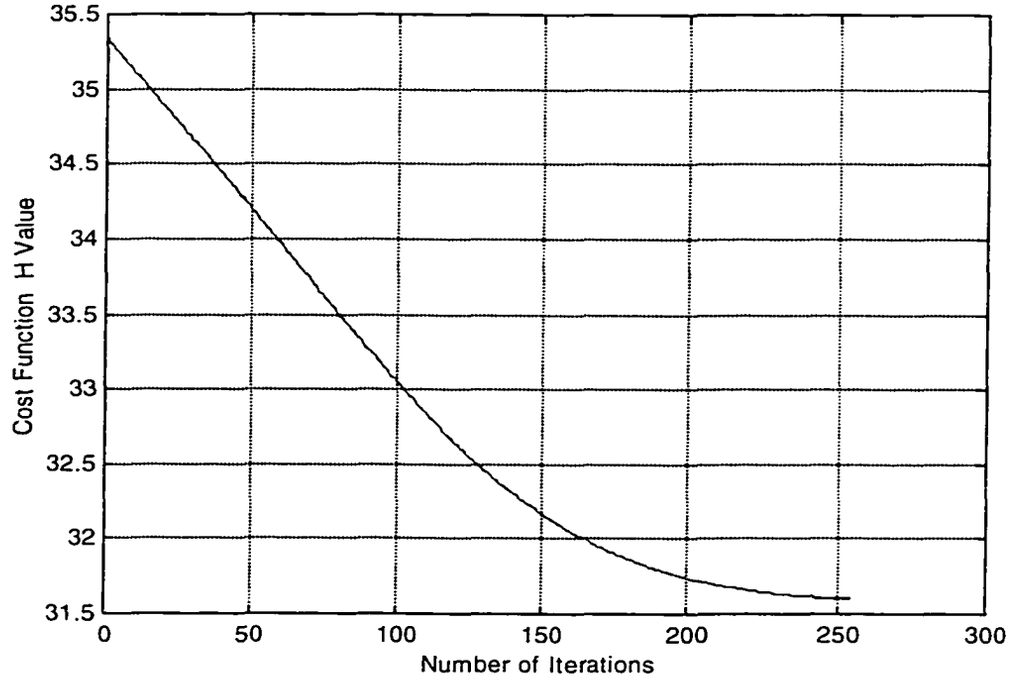

Figure 4.4 Cost Function History for x_{s1}=*880.6 in* and x_{s2}=*2,999.6 in*

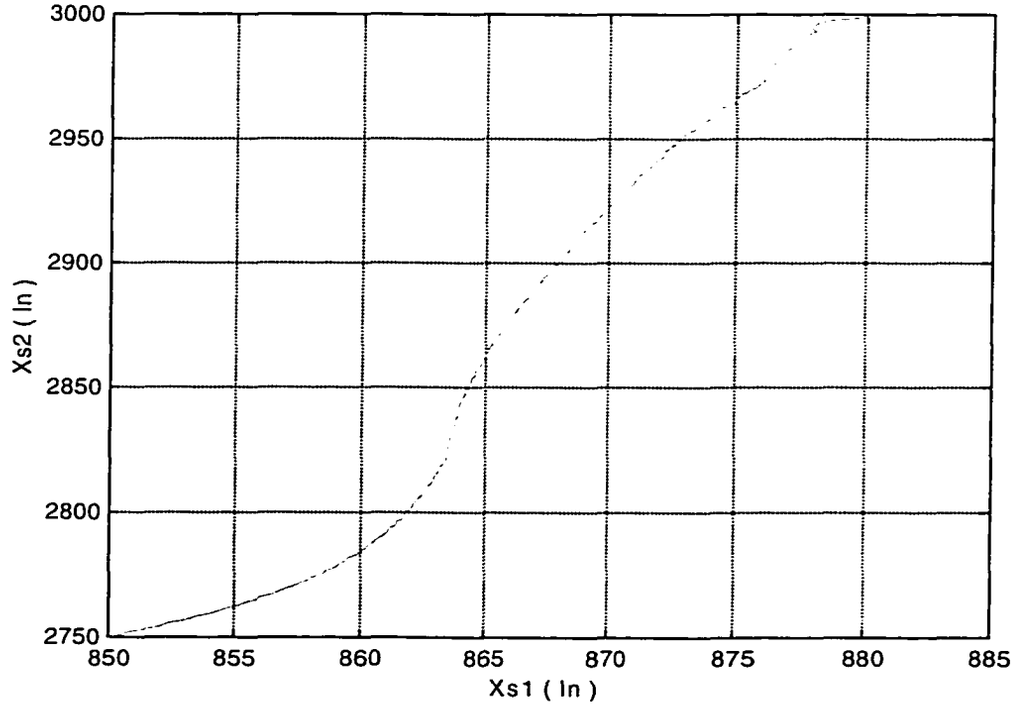

Figure 4.5 Sensor Position History for x_{s1}=*880.6 in* and x_{s2}=*2,999.6 in*

Recall that many local minimums exist (see Figure 3.9) and that these solutions depend on the initial sensor positions. In an attempt to improve upon the solution results presented thus far, another set of initial sensor positions will be used. The flight control system root locus plot for manually placed sensors at $x_{s1}=2.100$ *in* and $x_{s2}=2.900$ *in* is shown in Figure 4.6. Although aeroelastic mode *10* is still nonminimum phase, this figure reveals that the magnitude dipole values for most aeroelastic modes are better than ones in Figure 4.1. The magnitude dipole values for both modes *1* and *3* are $\mu_1= 2.6940$ *rad/s* and $\mu_3=1.7258$ *rad/s*, respectively.

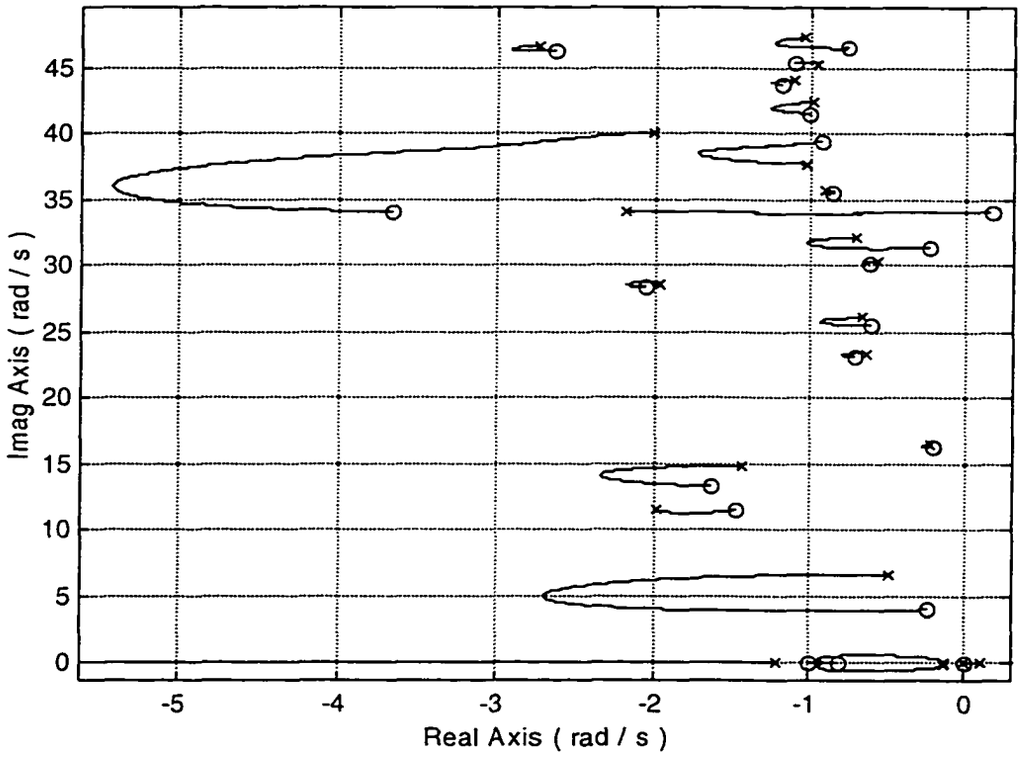

Figure 4.6 Root Locus Plot for $x_{s1}=2.100$ *in* and $x_{s2}=2.900$ *in*

The noted manual placement values will be used as new initial positions in the optimization algorithm in order to attempt an improvement to the gain stabilization objectives. Reconsider the augmented cost function in Equation (4.4). Figure 4.7 outlines the root locus plot for the flight control system when $w_1=1$ *s/rad* and $w_3=1$ *s/rad* are used as weighting factors in the augmented cost function. It is noticed from this figure that the magnitude dipole value for the 1^{st} aeroelastic mode has been slightly decreased from *2.6940* to *2.3032 rad/s* while the magnitude dipole value for the 3rd aeroelastic mode has been significantly decreased from *1.7258* to 0.1593 *rad/s*. An acceptable rigid body mode is also achieved. A majority of aeroelastic modes are stable except the 10^{th} aeroelastic mode as well as the 13^{th} aeroelastic mode. For these modes, the constraint terms F_{10} as well as F_{13} are violated and the corresponding modes go to instability for high gain values. Note in this case the search algorithm allowed F_{13} to become violated after initially starting in compliance, but the overall H cost value decreased. The optimal sensor locations are found at $x_{s1}=2,099.1$ *in* and $x_{s2}=2,684.4$ *in*. It is found that the optimization algorithm using the objective function in Equation (4.4), for different values of weighting factors, is unable to find any optimal sensor positions, where all high frequency modes remain stable for high gain values. In other words, there were no feasible solutions present which satisfy the constraint equations (zeros in left-half plane).

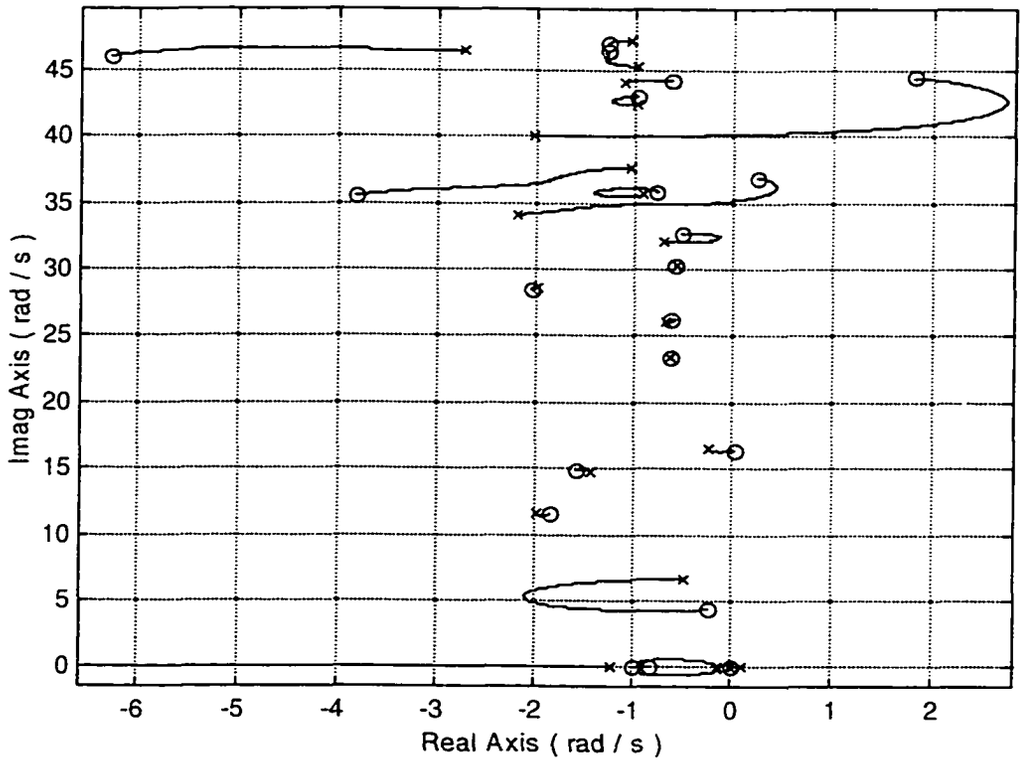

Figure 4.7 Root Locus Plot for $x_{s1}=2,099.1$ *in* and $x_{s2}=2,684.4$ *in*

To overcome this situation, an additional term representing the magnitude dipole value of the 10^{th} aeroelastic mode multiplied by an appropriate weighting factor is added to the cost function (see Equation (4.5)). The magnitude term μ_{13} could have also been selected in the cost function but was not because in Figure 4.6, F_{13} is satisfied and μ_{10} is highly affective in keeping all higher frequency aeroelastic zeros in the left-half plane (see Figure 4.3). Thus, the same augmented cost function as in Equation (4.5) will be minimized using the optimization algorithm. It is found that the appropriate objective function for static filters in the feedback path requires $w_1=2$ *s/rad*, $w_3=1$ *s/rad*, and $w_{10}=1$ *s/rad* as weighting factors when the sensors are initially placed at $x_{s1}=2,100$ *in* and $x_{s2}=2,900$ *in*. The optimization solution indicates that the optimal location of sensors are

x_{s1}=*1,925.3 in* and x_{s2}=*2,823.1 in*. The root locus plot corresponding to these values is illustrated in Figure 4.8. It is noticed from this figure that the flight control system is stable for different gain values. Also it is noted that all constraint equations are satisfied where all zeros belonging to the aeroelastsic modes lie in the stable region. In addition, the desirable augmentation of the rigid-body mode is preserved. Comparing this figure with Figure 4.6, it is clear that the dipole magnitude of the *10th* mode is decreased from *2.3413* to *0.0445 rad/s*, and from *2.6347* to *2.3314 rad/s* for the *1st* mode, while it lightly increased for the *3rd* mode from *1.4891* to *1.5810 rad/s*. Figure 4.9 shows the objective function value versus the number of iterations while Figure 4.10 shows the sensor position trace.

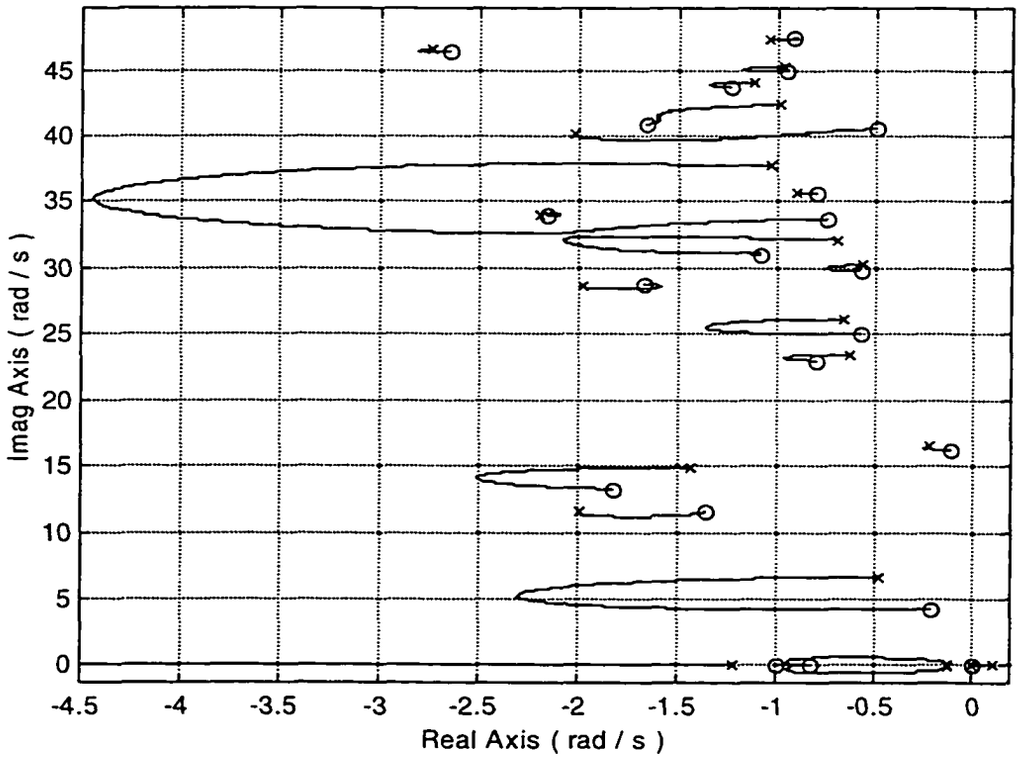

Figure 4.8 Root Locus Plot for x_{s1}=*1,925.3 in* and x_{s2}=*2,823.1 in*

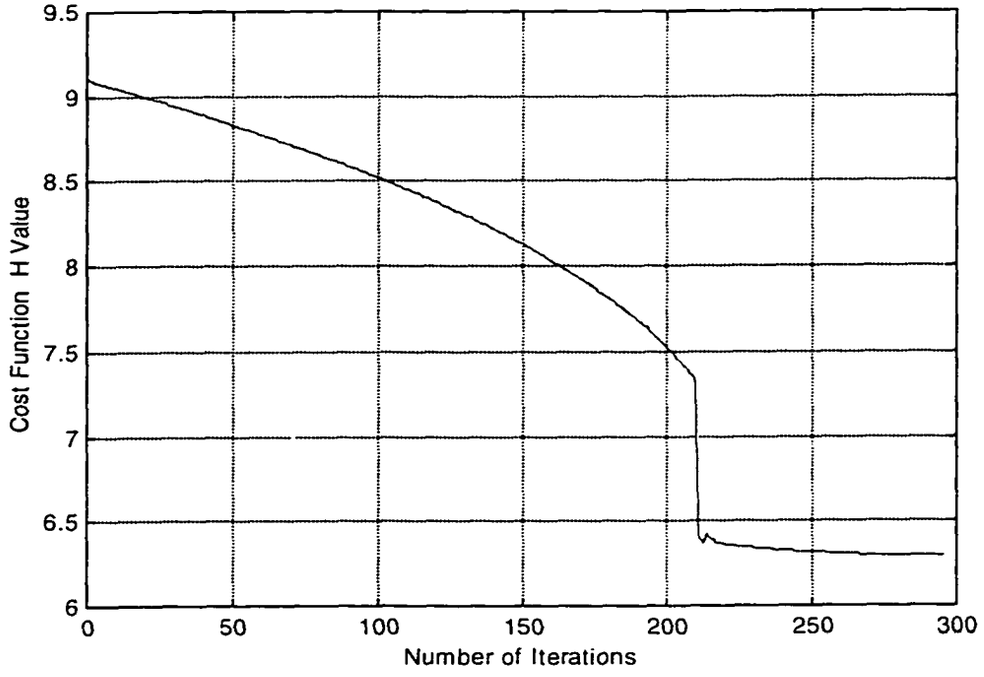

Figure 4.9 Cost Function History for x_{s1}=*1,925.3 in* and x_{s2}=*2,823.1 in*

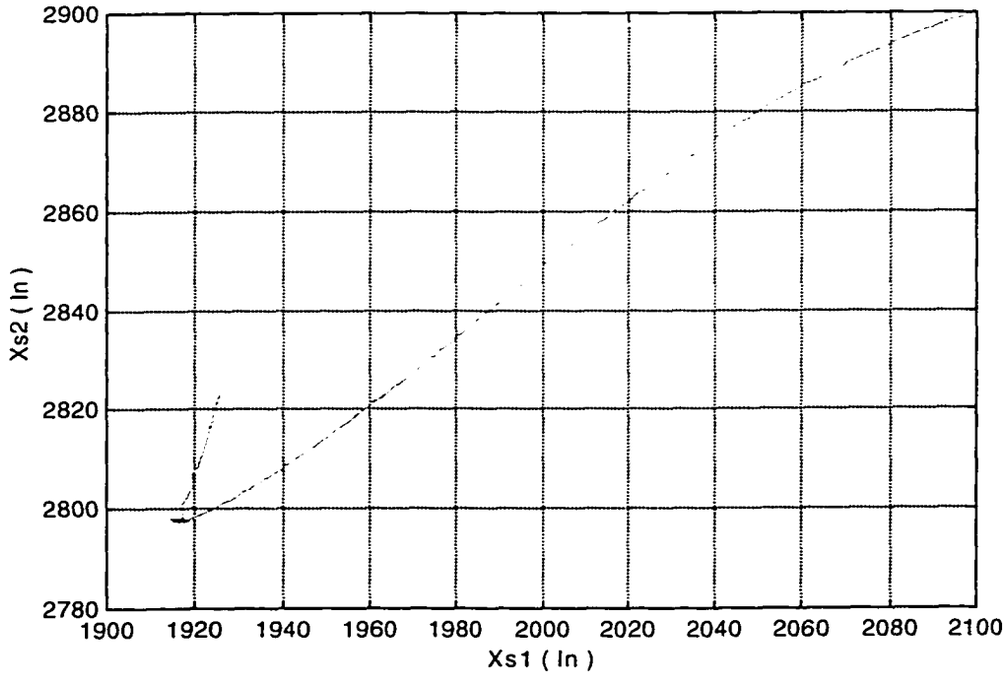

Figure 4.10 Sensor Position History for x_{s1}=*1,925.3 in* and x_{s2}=*2,823.1 in*

The final case will be tested using two unity static blending filters with different signs such as $h_1(s)=-1$ and $h_2(s)=1$. The optimization software is applied to an augmented cost function represented in Equation (4.4) using $w_1=1$ *s/rad* and $w_3=1$ *s/rad* as weighting factors for modes *1* and *3* respectively. Placing the sensors at initial positions $x_{s1}=750$ *in* and $x_{s2}=2{,}850$ *in*, the optimal locations are found to be at $x_{s1}=892.7$ *in* and $x_{s2}=2{,}701.4$ *in*. Figure 4.11 shows the root locus plot for the flight control system when the sensors are placed in the resulting optimal positions. This figure reveals that using two opposite sign blended feedback signals result in undesirable rigid-body control. This effect is not unexpected since the feedback signal $\hat{q}$ ($\hat{y}$) in Figure 2.20 is devoid of any rigid pitch rate contribution, or

$$\hat{q} = h_1(s)q_1 + h_2(s)q_2$$

$$= (-1)\{q - \sum_{j=1}^{18} \phi_j'(x_{s1})\dot{\xi}_j\} + (+1)\{q - \sum_{j=1}^{18} \phi_j'(x_{s2})\dot{\xi}_j\} \tag{4.6}$$

$$= \sum_{j=1}^{18} \{\phi_j'(x_{s1}) - \phi_j'(x_{s2})\}\dot{\xi}_j$$

Also note from this figure that the magnitude dipole value for mode *1* is very big ($\mu_1=5.2488$ *rad/s*), while mode *3* is well gain stabilized ($\mu_3=0.0195$ *rad/s*). Constraint equations F_4 and F_{16} are violated, thus the corresponding aeroelastic modes have nonminimum phase zeros. Due to the break down of rigid-body control, this filtering strategy is not pursued any further in this dissertation.

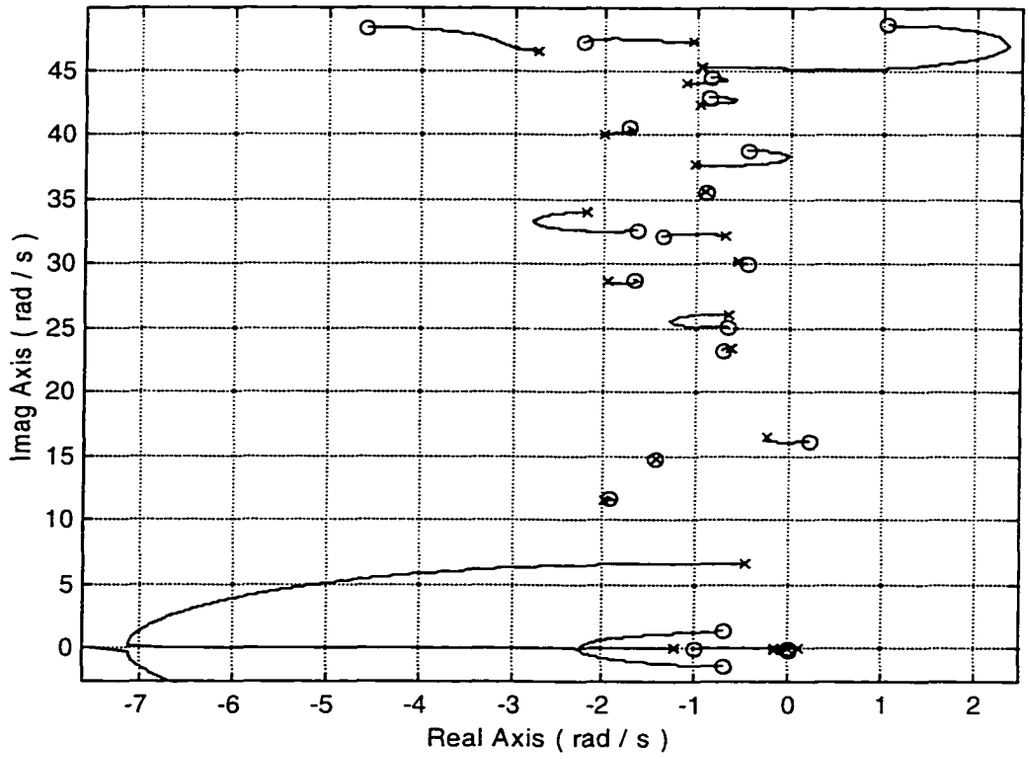

Figure 4.11 Root Locus Plot for x_{s1} =892.7 *in* and x_{s2} = 2,701.4 *in*

The main conclusion from the results presented in this section is that fixed static blending (see Equations (4.2)-(4.3)) is highly restrictive and does not allow sufficient design freedom to fully achieve the desired gain stabilization objectives. The numerical optimization search algorithm appears to be working well and does what is asked of it. The computed sensor locations tend to reduce selected dipole magnitudes with high weightings, but due to significant trades between the modes and insufficient design freedom, the dipole magnitudes are never significantly reduced. To alleviate the problem, the next section allows more freedom in the blending filter structure.

4.3 Sensor Placement with Variable Static Blending

In this section, optimal gyro placement corresponding to the system in Figure 2.20 is again considered. The feedback blending filters will be considered as variable, static values. Based on the ability to shift loop gain between k_k and h_1-h_2 in Equation (2.43) and Figure 2.20, there is no loss of generality if one filter is held fixed and the other allowed to vary. Here, the static gain parameter of the first filter will be considered variable, while the parameter value of the second filter will be considered constant (unity). The static filters can be expressed as

$$h_1(s) = c_1 \tag{4.7}$$

$$h_2(s) = 1 \tag{4.8}$$

The variable static filter structure in Equations (4.7)-(4.8) introduces the next level of design freedom beyond that considered in Section 4.2. The filters here represent spectrally uniform but unbalanced blending. Optimization parameters here include the two gyro locations x_{s1} and x_{s2} and the filter parameter c_1. To avoid unexpected exploitation by the optimizer, the variable filter parameter will be constrained to lie within certain bounds. Thus, introduce two additional constraints

$$F_{23} = c_1 - \overline{c_1} \le 0 \tag{4.9}$$

$$F_{24} = \underline{c_1} - c_1 \le 0 \tag{4.10}$$

where $\overline{c_1}$ and $\underline{c_1}$ denote upper and lower bounds on c_1. The numerical algorithm is run with $\underline{c_1} = 0.1$ and $\overline{c_1} = 10$.

The first case will be tested by selecting the variable blending filter parameter with an initial value of c_1=5. The starting sensor locations are chosen to be at x_{s1}=2,100

in and x_{s2}=*2,950 in*. The corresponding root locus plot for this manual selection is illustrated in Figure 4.12. Comparing this figure to Figure 4.6, where the (approximately) same initial sensor locations are applied but a different blending parameter value ($h_1(s)=1$) is used, it is noted that increasing the parameter value of the static filter number *1* increases the magnitude dipole value of the effective mode *10* relative to that in Figure 4.6. Note that mode *9* is technically the nonminimum phase mode ($F_9>0$), but because of the near by zero, this feature is essentially tied to mode 10. Additionally the F_3 constraint is violated and mode *3* becomes unstable and has a nonminimum phase zero, while mode 6 becomes unstable for a certain range of gain values.

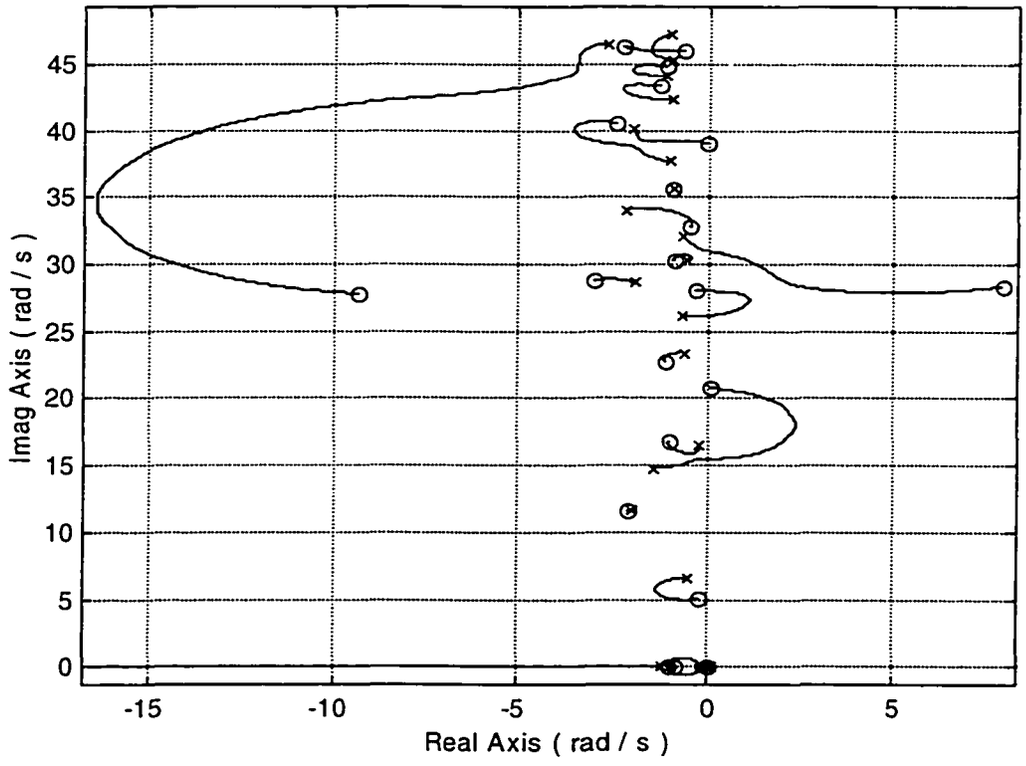

Figure 4.12 Root Locus Plot for x_{s1}=*2,100 in*, x_{s2}=*2,950 in* and c_1=*5*

When minimizing the augmented cost function (see Equation (4.4) with F_{23}, F_{24} included) using $w_1=w_3=1$ *s/rad* as weighting factors, the optimization tool failed to find suitable positions for the sensors, for which all aeroelastic zeros lie in left-hand plane. The final results indicate that the sensors are located at $x_{s1}=2,265.5$ *in* and $x_{s2}=2,982.4$ *in* while the final value of the filter parameter is $c_1=2.5$. The root locus plot of flight control system for these results is shown in Figure 4.13. Comparing Figure 4.13 with Figure 4.12, it is noticed that the aeroelastic mode *3* becomes highly gain stabilized and its dipole value drops from *6.1960* to *0.0341 rad/s*, while the dipole value of the first mode increased from *1.6076* to *2.4656 rad/s*. Also the dipole magnitude value of aeroelastic

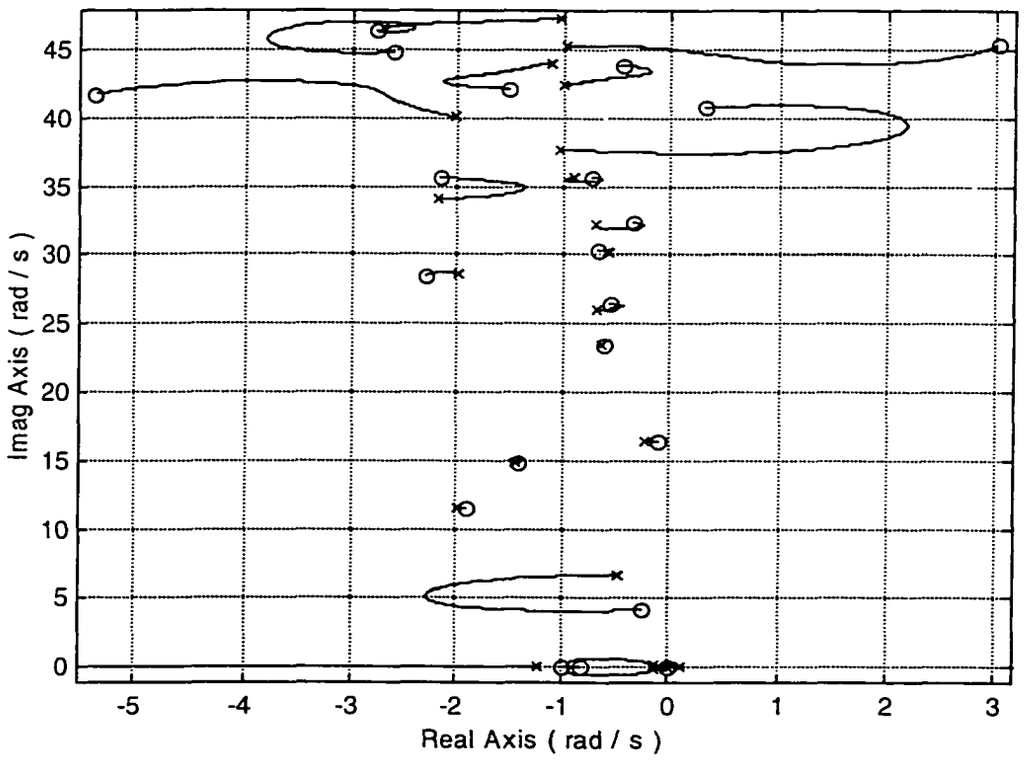

Figure 4.13 Root Locus Plot for $x_{s1}= 2,265.5$ *in*, $x_{s2}=2,982.4$ *in* and $c_1=2.5$

mode *10* is decreased and this mode becomes stable for different gain values, while the constraints F_{12} and F_{16} become violated leading to nonminimum phase zeros. Note that even though F_{12} and F_{16} become violated during the optimization process, F_3 and F_{10} become satisfied and the H value is reduced. The results in Figure 4.13 are also comparable to Figure 4.7, when assertaining the benefit of the variable filter. For this case, no significant benefit is attained.

In an attempt to correct the high frequency problems in Figure 4.13, reconsider the augmented cost function represented in Equation (4.5) with F_{23} and F_{24} included and with the same previous initial values. Also select the weighting factors as $w_1=1$ *s/rad*, $w_3=1$ *s/rad* and $w_{10}=5$ *s/rad*. The optimization process again failed to find appropriate positions of sensors at which the selected dipole values are minimized and all aeroelastic modes are stable for different gain values. Figures 4.14a and 4.14b show the root locus plot when the sensors are placed at the final optimal results $x_{s1}=2,429.7$ *in* and $x_{s2}=2,923.2$ *in* and while the blending parameter is $c_1=4.6$. Comparing both Figures 4.14a and 4.14b with Figure 4.12, it is noticed that the dipole value of the first mode is increased from *1.6076 rad/s* to *2.6100 rad/s* while the dipole value of the third mode is decreased from *6.1960 rad/s* to *0.4438 rad/s* which becomes stable for different gain values. Also, the constraint F_{14} is violated and aeroelastic mode *14* becomes unstable for high gain value. This high frequency stability problem is again objectionable.

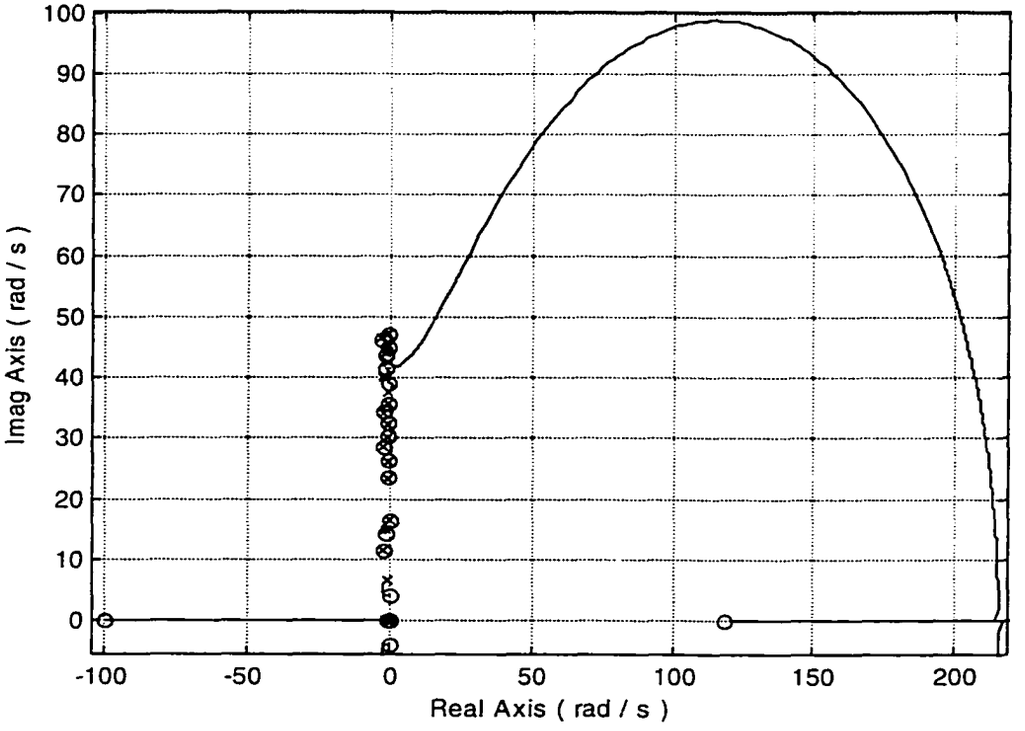

Figure 4.14a Root Locus Plot for x_{s1}= *2,429.7 in*, x_{s2}=*2,923.2 in* and c_1=*4.6*

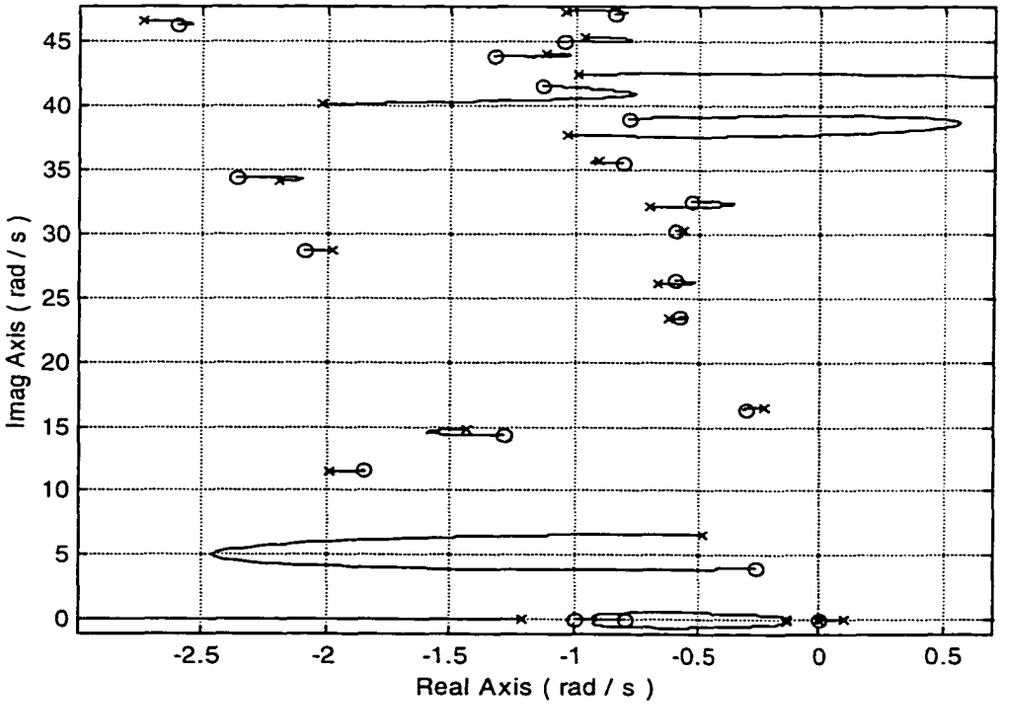

Figure 4.14b Root Locus Plot for x_{s1}= *2,429.7 in*, x_{s2}=*2,923.2 in* and c_1=*4.6*

It is obvious from the previous results that using $x_{s1}=2,100\ in$ and $x_{s2}=2,950\ in$ as initial sensor positions is not an appropriate choice for finding desirable solutions. To improve upon the previous results, different initial positions such as $x_{s1}=850\ in$ and $x_{s2}=2,750\ in$ will be considered. The root locus plot for these manually selected positions with the initial blending parameter of $c_1=5$ is illustrated in Figure 4.15. This figure reveals that many aeroelastic modes are unstable for high gain values. Comparing this figure with Figure 4.12, it is clear that the 3^{rd} mode becomes stable but the 1^{st} mode goes unstable, and both modes have larger dipole magnitude values.

Applying an optimization algorithm using the objective function in Equation (4.5) with the weighting factors $w_1=5\ s/rad$, $w_3=3\ s/rad$, and $w_{10}=2\ s/rad$, the optimization algorithm is able to find suitable sensor positions at which the critical dipole magnitude values are decreased, but still is unable to force all areoelastic modes to have minimum phase zeros. Both Figures 4.16a and 4.16b show the root locus plot when the sensors are placed at the calculated positions $x_{s1}=1,324.1\ in$ and $x_{s2}=2,371.9\ in$ with the calculated value of the filter parameter $c_1=0.9$. Comparing these figures with Figure 4.15, it is noticed that the dipole value decreased from *6.6061* to *0.4249 rad/s* for the first mode and decreased from *10.0313* to *0.1540 rad/s* for the third mode. Also, all constraint equations are satisfied except F_{12}. The aeroelastic mode *12* becomes unstable for high gain values and has a nonminimum phase zero.

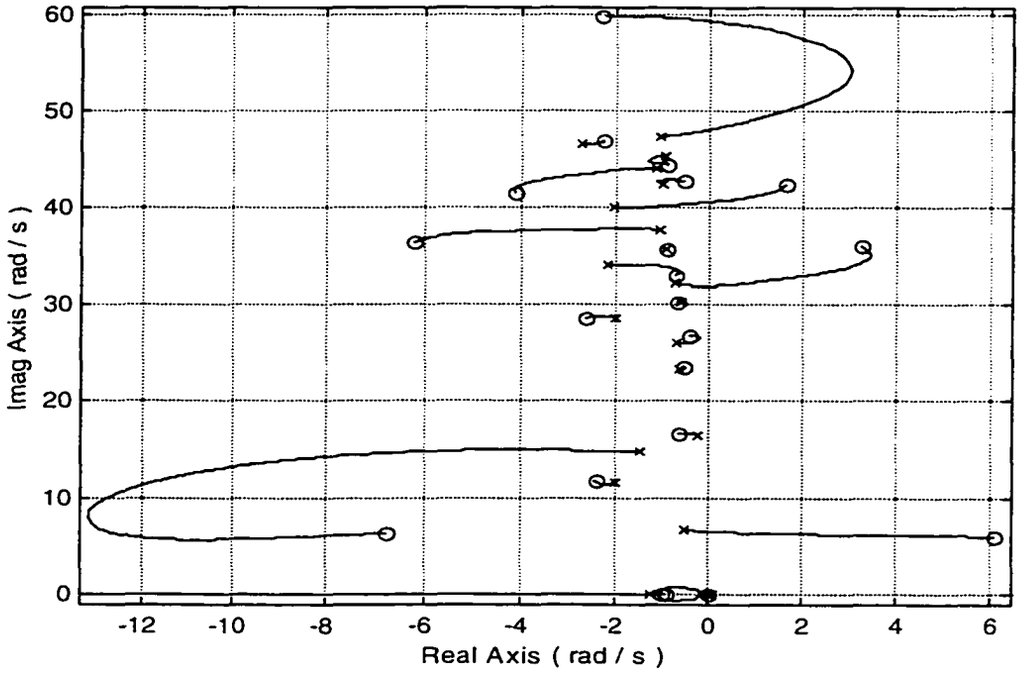

Figure 4.15 Root Locus Plot for x_{s1}=*850 in*, x_{s2}=*2,750 in* and c_1=*5* (z_k=*1 rad/s*)

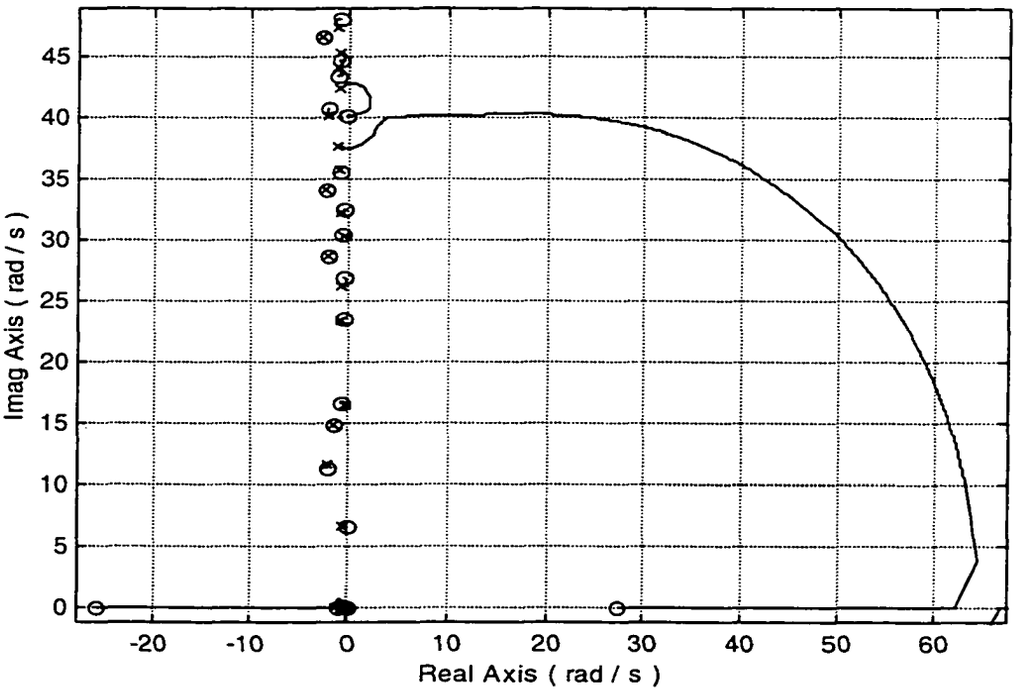

Figure 4.16a Root Locus Plot for x_{s1}= *1,324.1 in*, x_{s2}=*2,371.9 in* and c_1=*0.9*

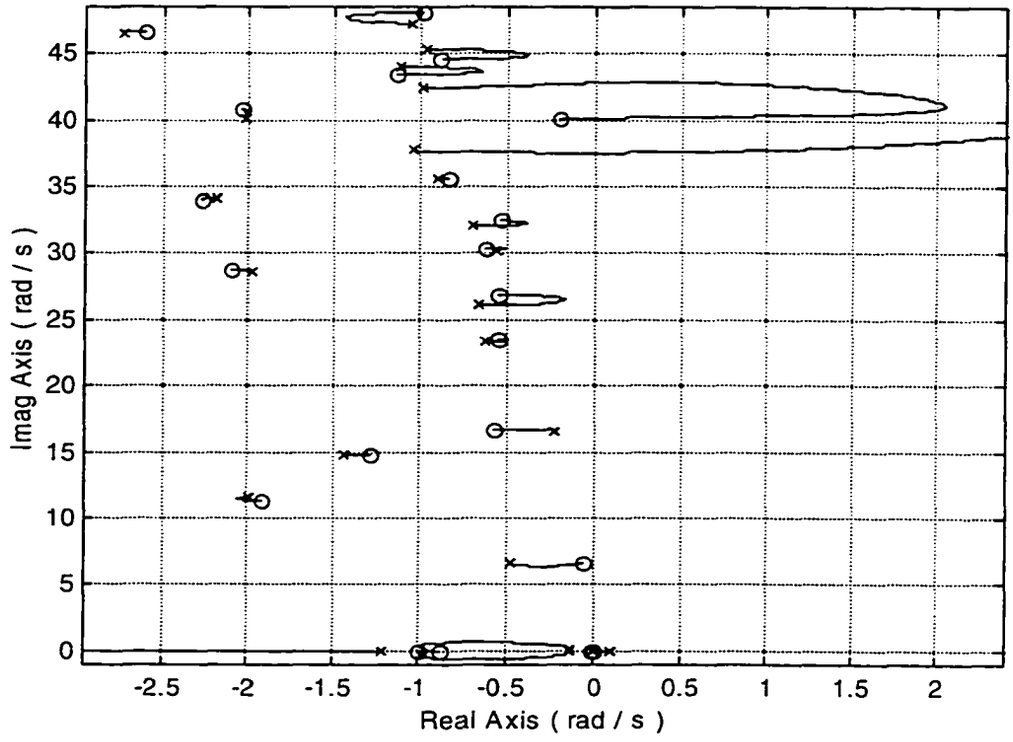

Figure 4.16b Root Locus Plot for x_{s1}= *1,324.1 in*, x_{s2}=*2,371.9 in* and c_1=*0.9*

A final case will be tested using the previous initial sensor locations as well as the same augmented cost function but with a different filter parameter value. The new value will be considered as c_1=*0.5*. Optimization results indicate that the optimal sensor locations are x_{s1}= 1,325.7 *in* and x_{s2}=2,369.8 *in* while the optimal parameter value is again c_1=*0.9*. Figures 4.17a and 4.17b show the flight control system root locus for the optimal calculated values. It is noticed from results, as well as the figures, that choosing any value for the static blending filter parameter c_1 (or the same initial sensor locations and cost function structure) does not affect the final results. The optimal solution is relatively insensitive to the starting value for c_1.

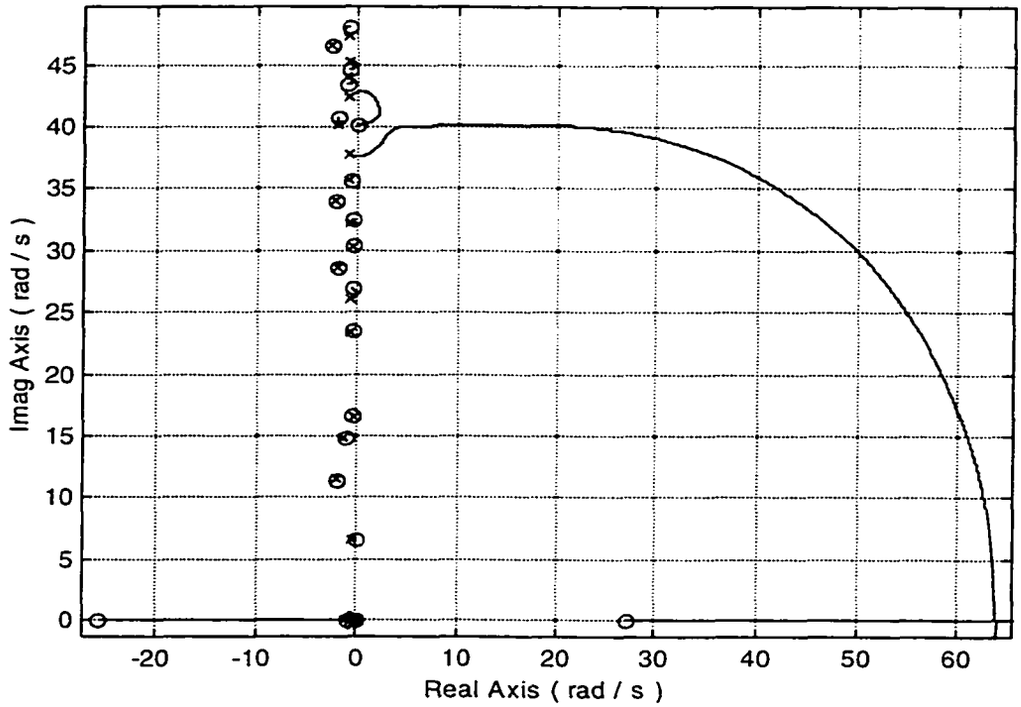

Figure 4.17a Root Locus Plot for x_{s1}=*1,325.7 in*, x_{s2}=2,369.8 *in* and c_1=*0.9*

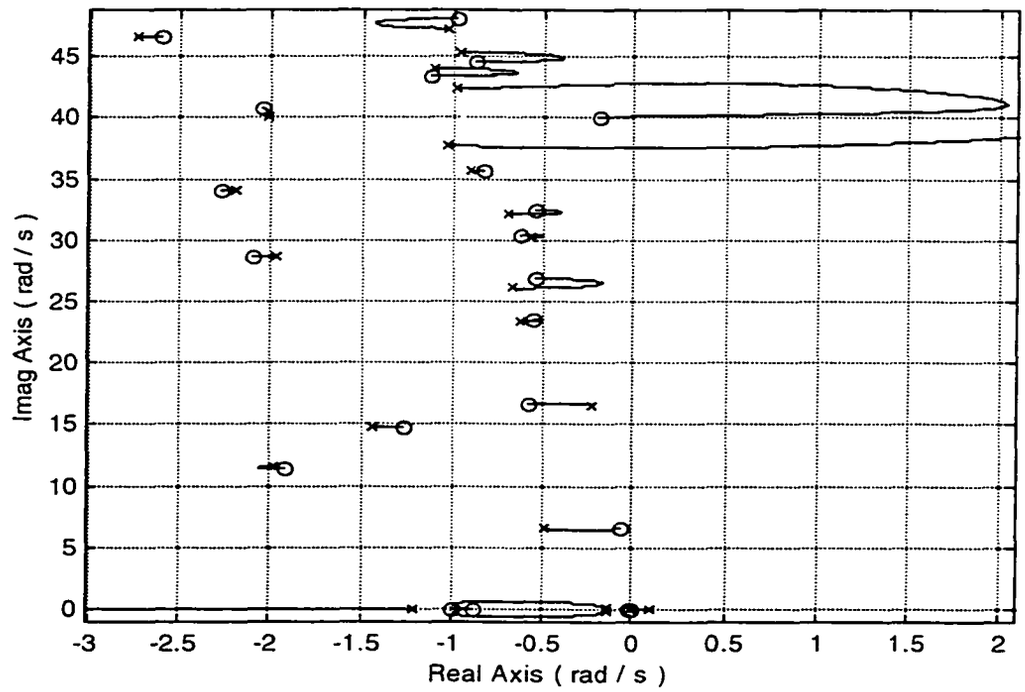

Figure 4.17b Root Locus Plot for x_{s1}=*1,325.7 in*, x_{s2}=2,369.8 *in* and c_1=*0.9*

The main conclusion from the results presented in this section is that variable static blending does not offer much design freedom beyond that of the fixed static blending cases. Some measurable improvements are seen in the ability to gain stabilize the critical modes (*1* and *3*), but there is always a lingering right-half plane zero associated with a higher frequency mode. More design freedom is needed in the optimization process.

4.4 Sensor Placement with Fixed Dynamic Blending

In the previous Sections 4.2 and 4.3, the flight control system blend filter structure is considered to have a static form. In this section, another prospect will be considered to significantly enhance design freedom beyond that considered in previous sections. This prospect deals with a fixed but dynamic filter structure. Two simple blending filter types will be considered and are based on problem experience from manual sensor placement efforts. Figure 4.18 shows the two types of blending strategies and the corresponding filter equations are indicated below.

Low and Band Pass:

$$h_1(s) = c_1 \frac{a}{s+a} \tag{4.11}$$

$$h_2(s) = c_2 \frac{s}{s+a} \frac{b}{s+b} \tag{4.12}$$

Low and High Pass:

$$h_1(s) = c_1 \frac{a}{s+a} \tag{4.13}$$

$$h_2(s) = c_2 \frac{s}{s+a} \tag{4.14}$$

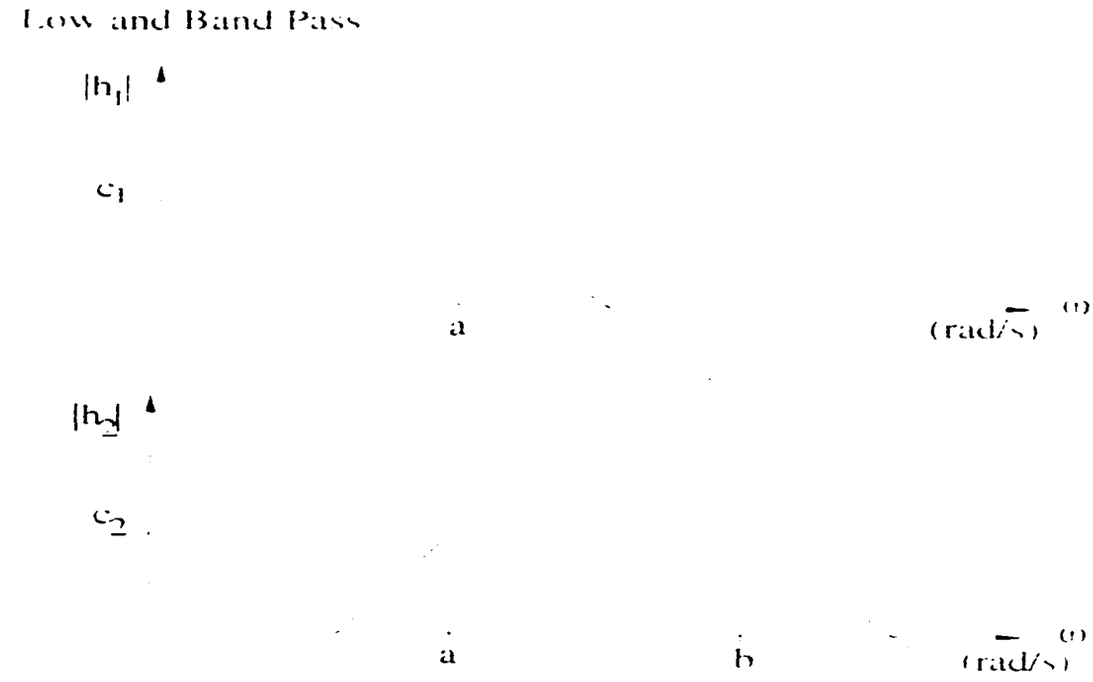

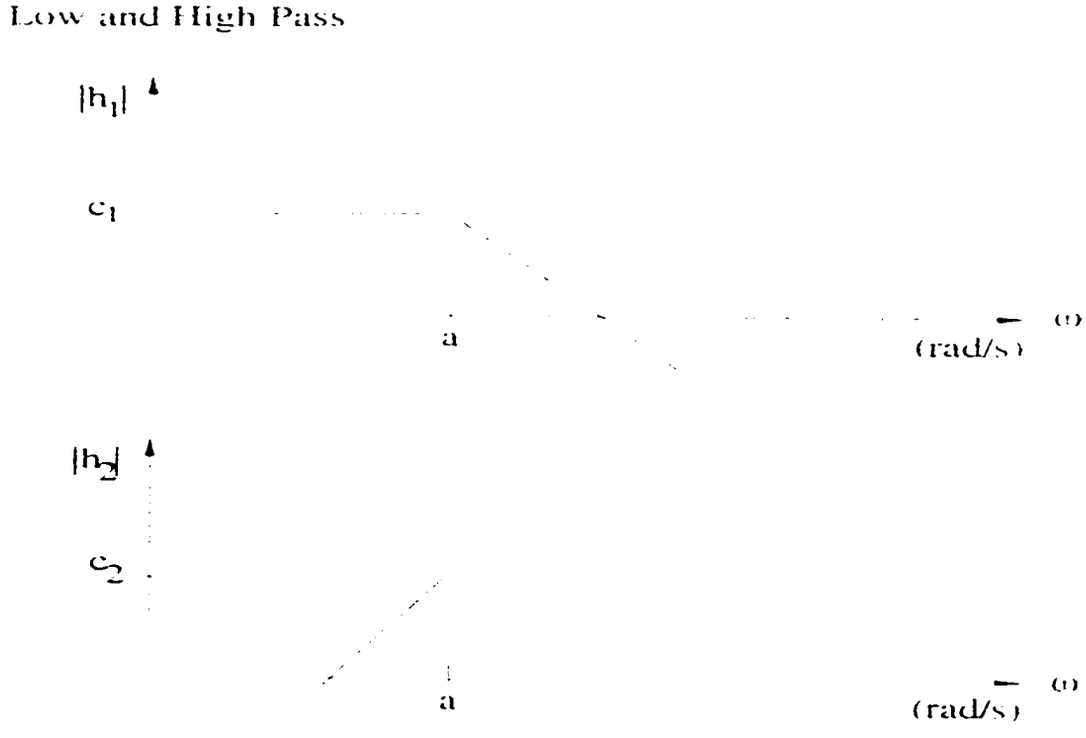

Figure 4.18 Dynamic Blend Filters

The basic strategy here is to blend desirable low frequency features in the gyro number *1* feedback signal with desirable high frequency traits in the gyro number *2* feedback signal. This strategy assumes that gyro *1* is located some where near the mid fuselage region while gyro *2* is located in an aft region of the fuselage. These locations tend to yield desirable gain stabilization characteristics in bounded frequency windows (see Section 2.5). The two strategies differ only in how attenuation at high frequency is treated, with the low-high pass strategy introducing lesser phase loss in the control loop. The fixed dynamic filter structures in Equations (4.11)-(4.14) represent spectrally nonuniform and possibly unbalanced blending. These filters introduce the next level of complexity in the design process. Because of the fixed nature of the filters, optimization parameters in this section only include the two gyro locations x_{s1} and x_{s2}.

The low pass and band pass filter structure indicated in Figure 4.18 will be considered first. Based on knowledge obtained from Chapter 2, the low and band pass filter parameters are selected as $a=7$ *rad/s*, $b=31$ *rad/s*, and $c_1=c_2=1$. This selection provides a transition between the two feedback signal at a frequency between the critical 1^{st} and 3^{rd} aeroelastic modes, as well as equally balanced strength between the two signals. The optimization algorithm is applied to the augmented cost function in Equation (4.4) for initial sensor locations $x_{s1}=850$ *in* and $x_{s2}=2,750$ *in*, for weighting factors $w_1=w_3=1$ *s/rad*, and for the filter parameters indicated previously. Figure 4.19 illustrates the root locus plot when the sensors are located on the final solution.

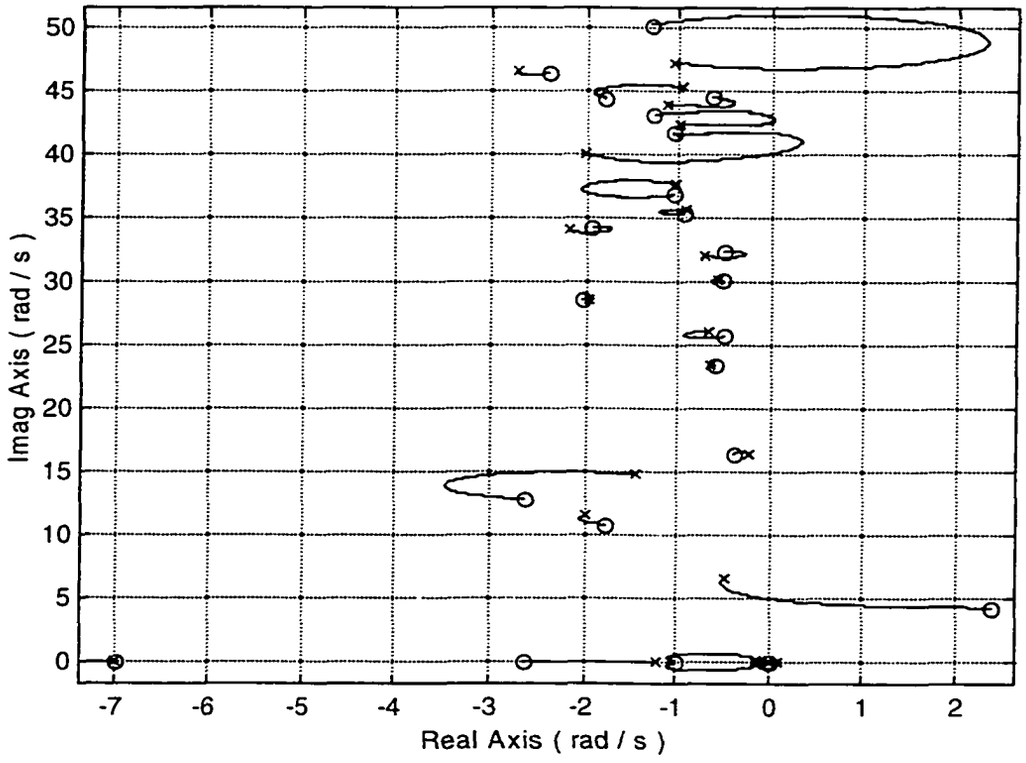

Figure 4.19 Root Locus Plot for x_{s1}=*867.4 in* and x_{s2}=*2,726.3 in*

It is noticed that when the sensors are located at x_{s1}=*867.4 in* and x_{s2}=*2,726.3 in*, constraint F_1 is violated and the corresponding mode *1* has a nonminimum phase zero. Note the sensors moved very little from the starting locations. Thus, a local minimum exists near the starting condition, and this local minimum is highly undesirable. In general, the optimization results using the low-band pass blending logic are not very successful in satisfying control design requirements. It is concluded after using many different forms of the augmented cost function, as well as different weighting factor values and initial sensor positions, the constraint F_1 remains violated.

As fully discussed in the References 42 and 44, a root locus analysis on the $\hat{y}$ numerator in Equation (2.43) leads to the conclusion that phase loss in the low-band pass filter approach tends to push the 1^{st} aeroelastic zero into the right-half plane. In other words, the transition provided by the low-band pass blend logic is to harsh and disrupts the near by dipole structures. The low-band pass filter is not considered any further in this chapter. Thus, consider the low-high pass blending logic proposed in Figure 4.18. The filter parameters are selected as $a=3$ *rad/s*, $c_1=1$, and $c_2=7$. The signal $\hat{y}$ in Figure 2.20 sees no phase loss from this logic.

Applying the optimization algorithm using the augmented cost function shown in Equation (4.4) with weighting factors $w_1=w_3=1$ *s/rad* for initial sensor locations $x_{s1}=2,100$ *in* and $x_{s2}=2,950$ *in*, the optimal sensor locations are found to be $x_{s1}=2,101.1$ *in* and $x_{s2}=2,477.5$ *in*. Figure 4.20 shows the root locus plot when the sensors are manually placed while Figure 4.21 shows the root locus plot when the sensors are optimally placed.

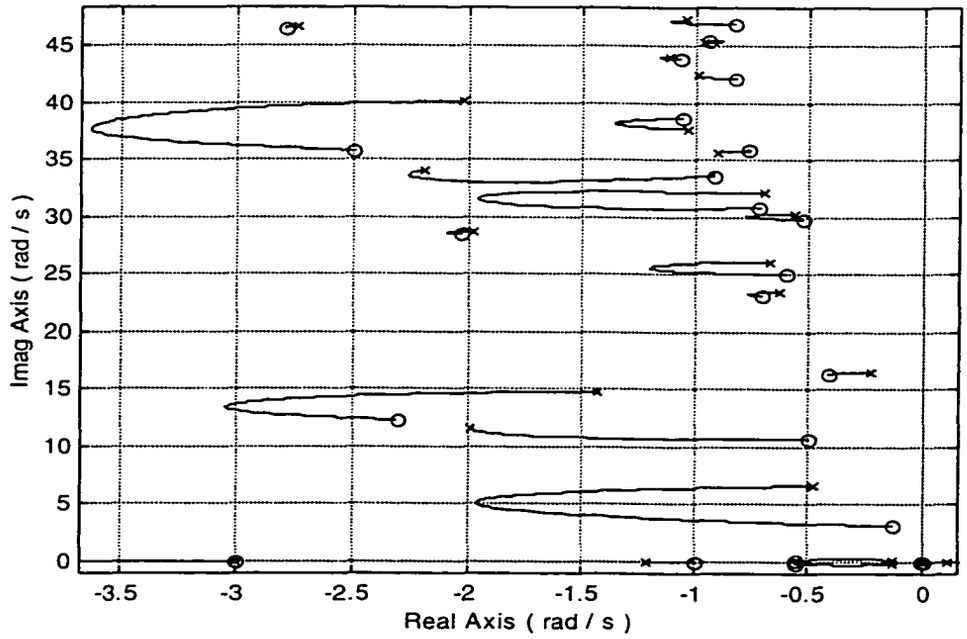

Figure 4.20 Root Locus Plot for $x_{s1}=2,100$ *in* and $x_{s2}=2,950$ *in* ($z_k=1$ *rad/s*)

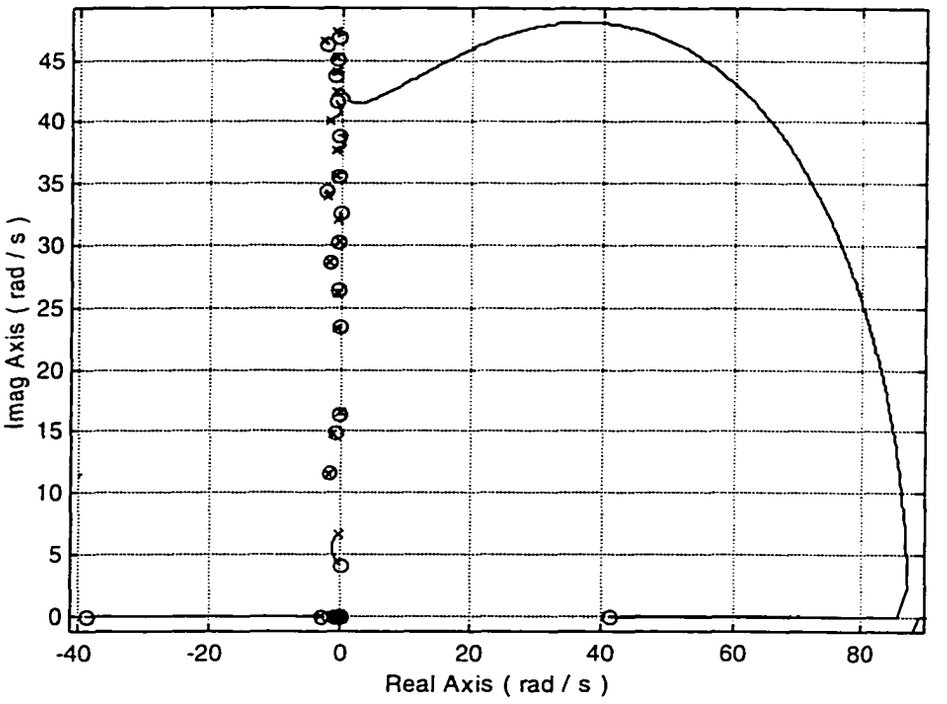

Figure 4.21a Root Locus Plot for x_{s1}=2,101.1 *in* and x_{s2}=2,477.5 *in*

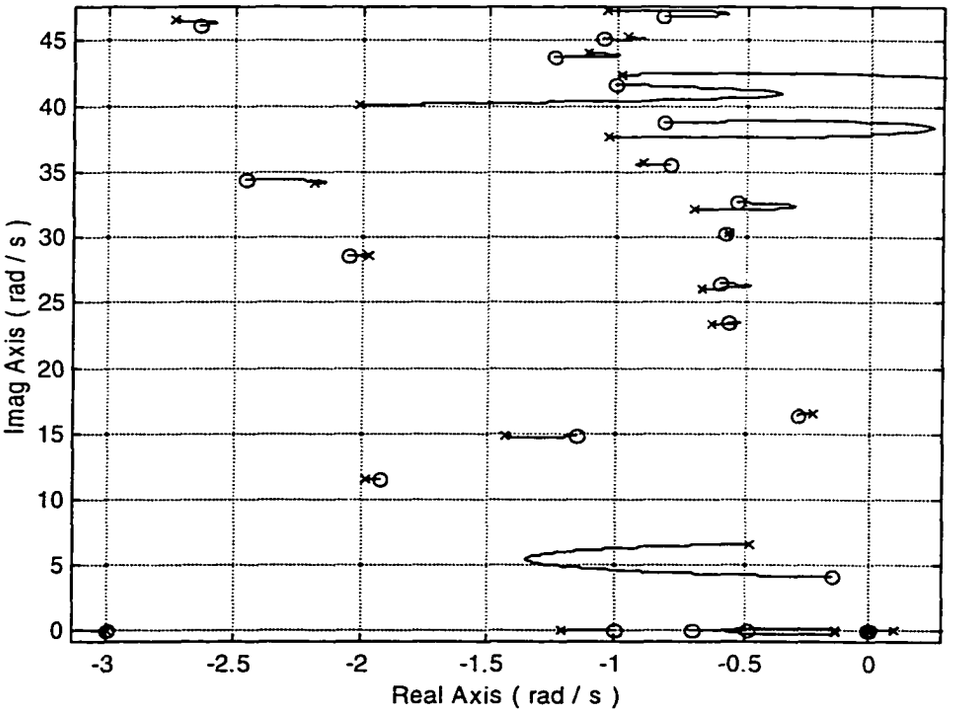

Figure 4.21b Root Locus Plot for x_{s1}=2,101.1 *in* and x_{s2}=2,477.5 *in*

By comparing these last two figures, it is noted that mode *3* becomes fairly well gained stabilized, the magnitude dipole value of the 3^{rd} mode is decreased from *2.6642* to *0.2832 rad/s*. Mode *1* could be more gain stabilized (a change in μ_1 from *3.5055* to *2.5156 rad/s*), but at least constraint F_1 is satisfied. In fact, all constraints are satisfied except F_{14} where its corresponding mode is unstable for high gain values. Figure 4.22 shows the augmented cost function value at each optimization iteration while Figure 4.23 shows the sensor position track during the search. Note the first sensor remains essentially fixed at its initial value (x_{s1}=*2,100 in*). This is consistent with Figure 2.2 where mode slope *1* is approximately zero ($\phi_1'(2,100) \approx 0$) and leads to modest mode *1* gain stabilization. On the other hand, the second sensor moves approximately *475 in* (x_{s2}=*2,477.5 in*) to a location where $\phi_3'(2,477.5) \approx 0$ yielding high gain stabilization.

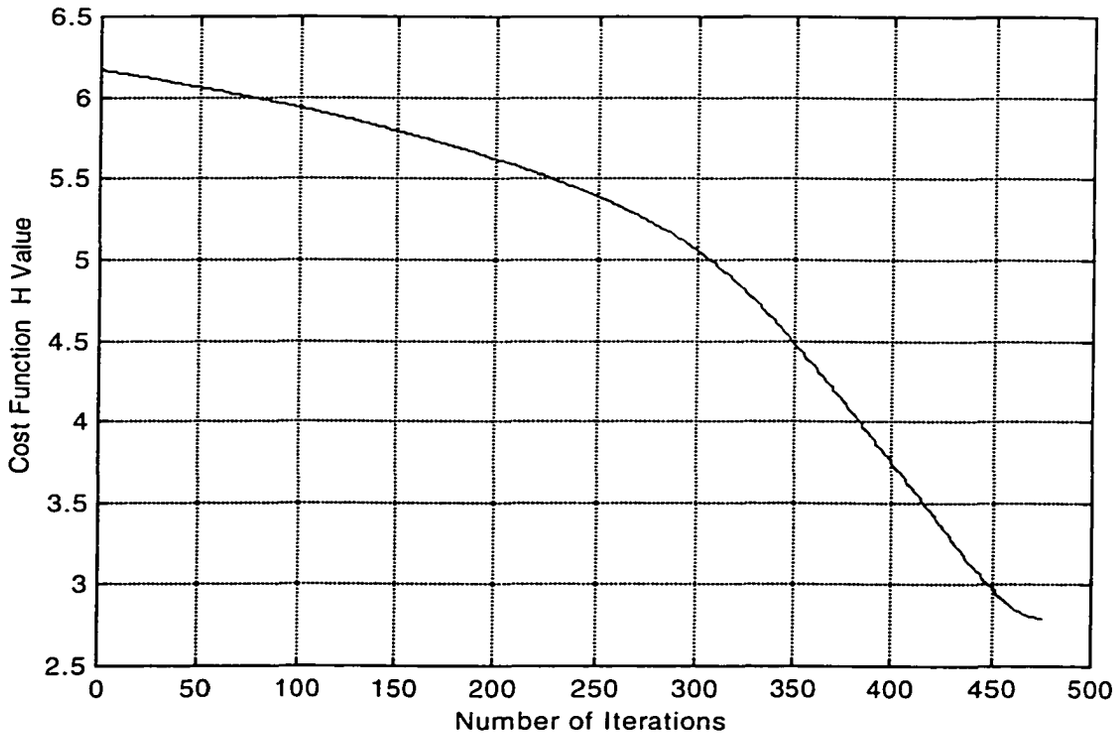

Figure 4.22 Cost Function History for x_{s1}=*2,101.1 in* and x_{s2}=*2,477.5 in*

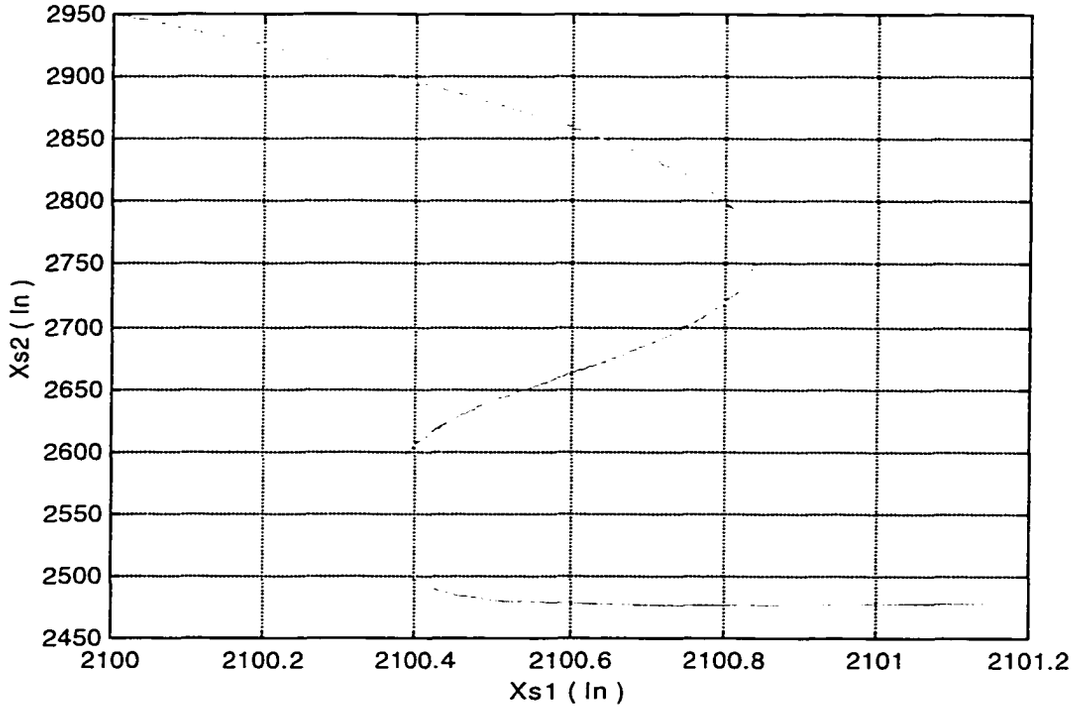

Figure 4.23 Sensor Position History for x_{s1}=*2,101.1 in* and x_{s2}=*2,477.5 in*

To enhance gain stabilization for mode *1*, another highly similar case is run, except the cost function weights are selected as w_1=*3 s/rad* and w_3=*1 s/rad*. Increased w_1 should mandate an improved μ_1 value. Figure 4.24 shows the resulting root migration plot for the optimal solution x_{s1}=*2,716.5 in* and x_{s2}=*2,475.7 in*. When comparing Figure 4.24 with 4.20, the mode 1 and 3 dipole magnitude values decreased from *3.5055* to *2.4889 rad/s* and from 2.6642 to *0.1241 rad/s*, respectively. These results are unexpected and show the highly nonlinear behavior of this optimization problem. Instead of finding a new x_{s1} value that significantly reduces μ_1, the optimizer found an x_{s1} value that reduces μ_3 more. Nevertheless, solutions portrayed in Figures 4.21 and 4.24 are judged to be two of the better solutions in this chapter. Figures 4.25-4.26 show the corresponding search history results.

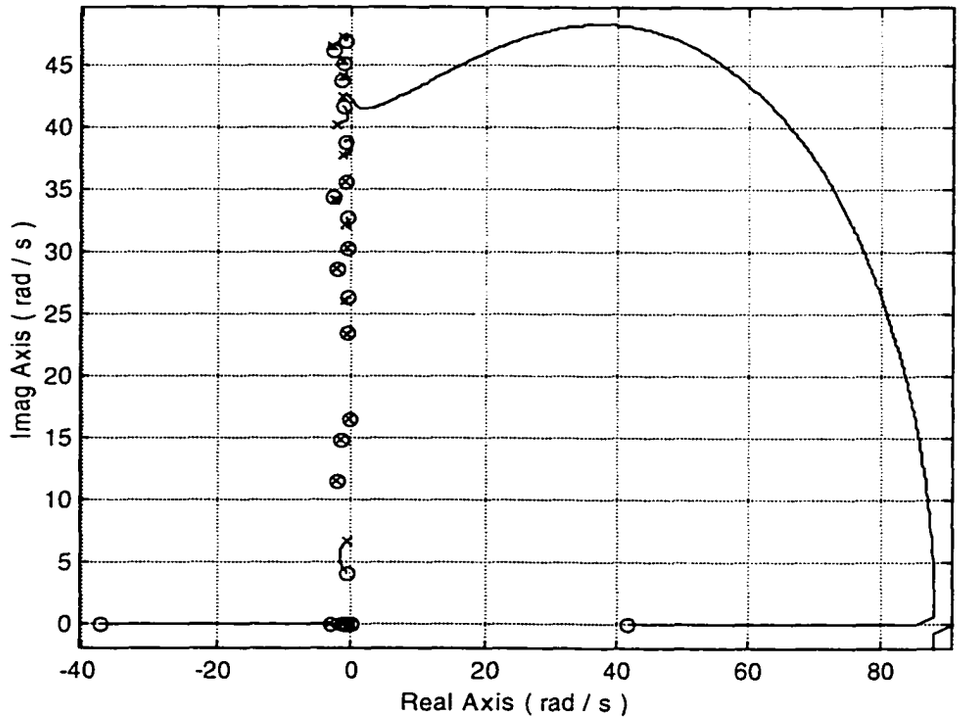

Figure 4.24a Root Locus Plot for x_{s1}=*2,716.5 in* and x_{s2}=*2,475.7 in*

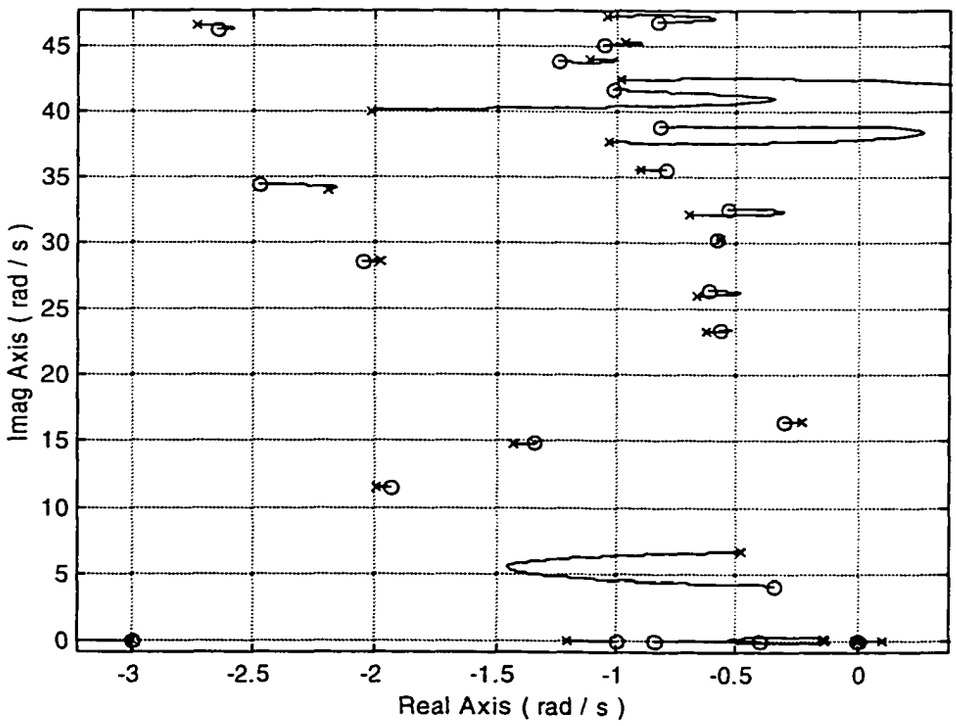

Figure 4.24b Root Locus Plot for x_{s1}=*2,716.5 in* and x_{s2}=*2,475.7 in*

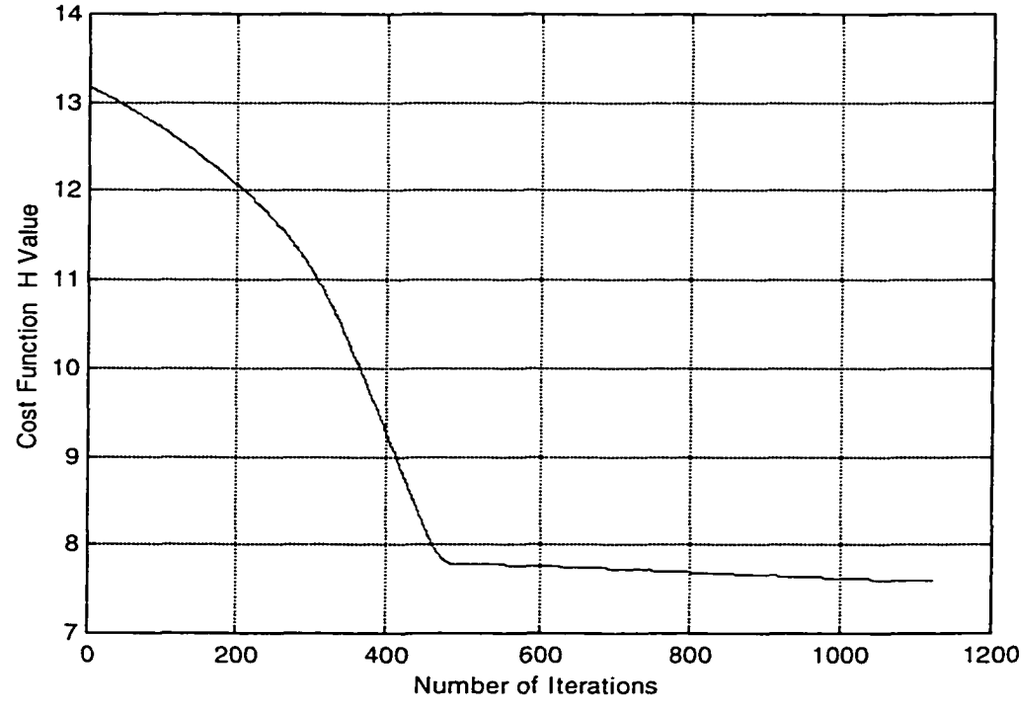

Figure 4.25 Cost Function History for x_{s1}=2,716.5 *in* and x_{s2}=2,475.7 *in*

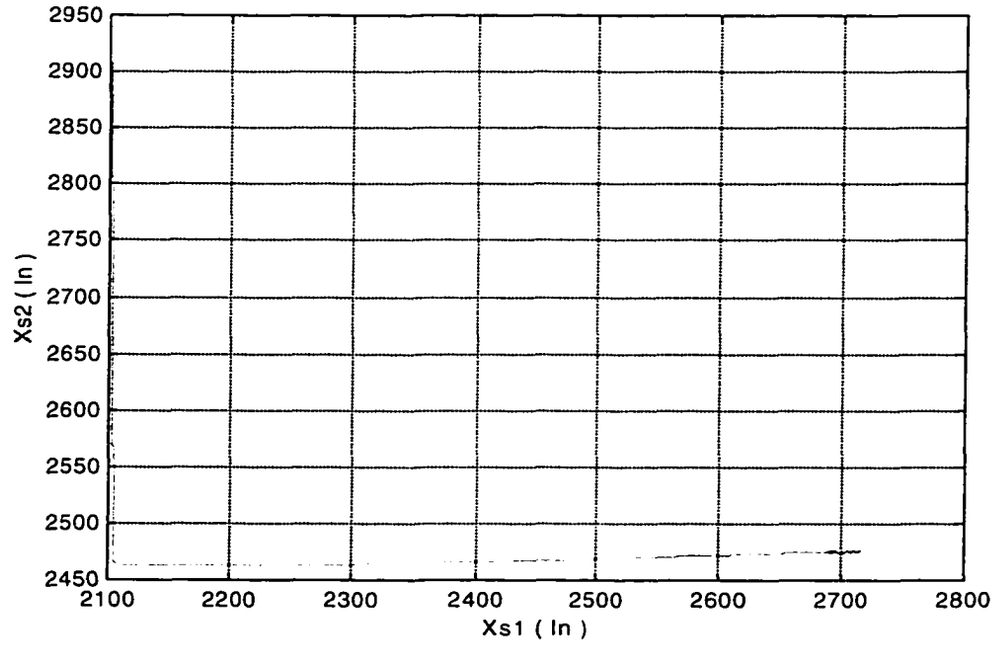

Figure 4.26 Sensor Position History for x_{s1}=2,716.5 *in* and x_{s2}=2,475.7 *in*

4.5 Sensor Placement with Variable Dynamic Blending

In Section 4.4, cases were run with a fixed blending structure; thus, the full potential of the dynamic filters was not exploited. For example, it is observed that when the low-high pass filter parameter a is decreased and c_2 is increased manually using the Figure 4.21 solution, the mode *1* dipole becomes much tighter. In other words, there may be additional solution enhancements that can be extracted from this filter structure. In this section, the low-high pass dynamic blending strategy will be exploited further by allowing one independent parameter and one dependent parameter of the dynamic filters to be optimized simultaneously during sensor placement. The parameter a in Equations (4.13)-(4.14) will be considered variable inside the optimization algorithm. Further the parameter c_2 will be allowed to vary according to the schedule $c_2=2a$. Constraints similar to these in Equations (4.9)-(4.10) for a are enforced where $\underline{a} = 0.1$ *rad/s* and $\overline{a} = 10$ *rad/s*.

Consider a case starting with optimization variables $x_{s1}=2,100$ *in*, $x_{s2}=2,950$ *in*, and $a=5$ *rad/s*. Other parameter values that are fixed include $c_1=1$. Cost function (Equation (4.4)) weights are $w_1=w_3=1$ *s/rad*. The optimal solution yields $x_{s1}=2,101.8$ *in* and $x_{s2}=2,477.2$ *in* and $a=5$ *rad/s*. The corresponding root locus plot is given in Figure 4.27. These results are quite unexpected. Note the filter parameter a did not change during the optimization. Further analysis revealed components of the gradient vector associated with x_{s1} and x_{s2} dominated the corresponding component for a by several orders of magnitude. Thus, the optimizer essentially ignored the directional information corresponding to a during iterative stepping. Even though manual changes in the parameter a lead to significant root locus changes, additional changes due to x_{s1} and x_{s2} wash out these effects. Also note x_{s1} changed very little while x_{s2} moved approximately

475 in. In fact, these sensor locations are virtually identical to those found in the solution for Figure 4.21. Thus, the root locus features in Figures 4.27 and 4.21 look highly similar (even though c_1 and c_2 are somewhat different). Little additional benefit was extracted from considering a variable dynamic filter for this single test case.

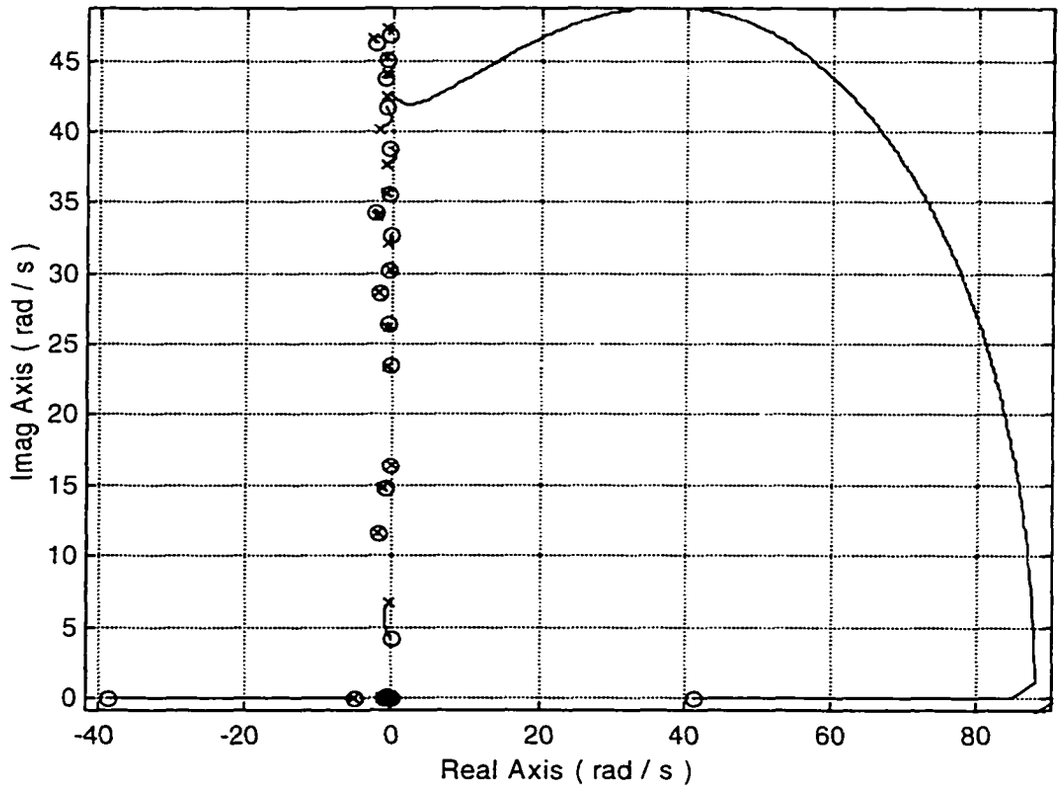

Figure 4.27a Root Locus Plot for x_{s1}=*2,101.8 in*, x_{s2}=*2,477.2 in* and a=*5 rad/s*

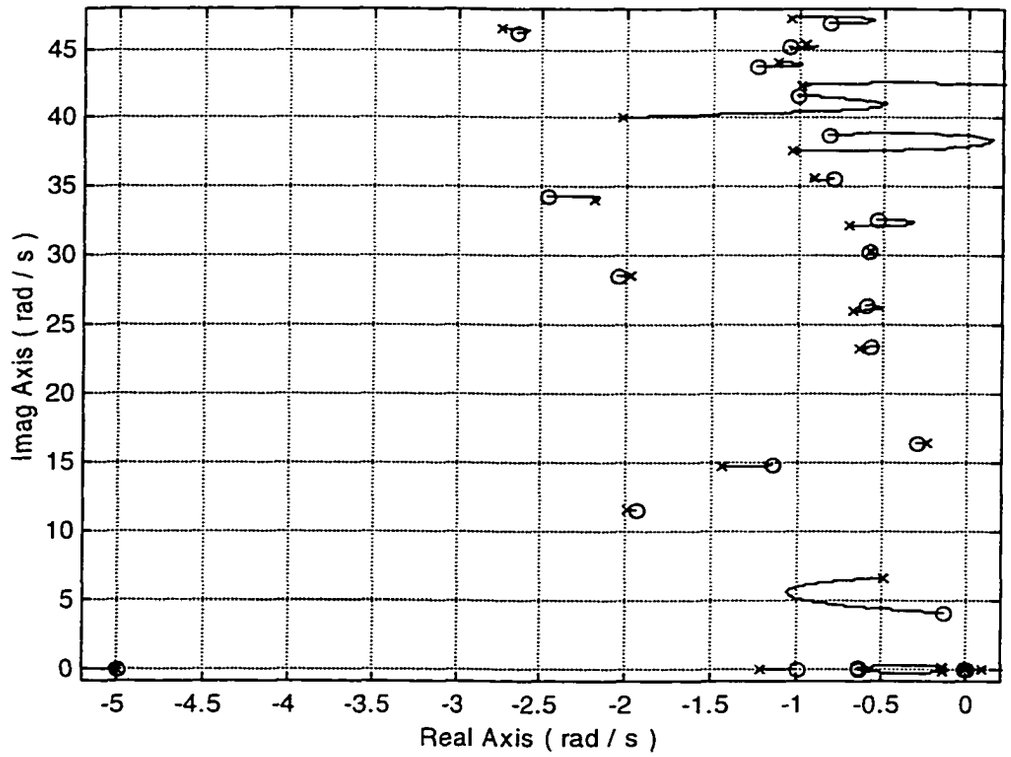

Figure 4.27b Root Locus Plot for x_{s1}=*2,101.8 in*, x_{s2}=*2,477.2 in* and *a=5 rad/s*

4.6 Closed-Loop Vehicle Evaluation

In this section, one of the more promising sensor placement solutions will be carried through to the final step of flight control design and evaluation. Two candidate sensor placement solutions based on gain stabilization are potential cases. These solutions correspond to the variable static blending case given in Figure 4.14 and the fixed dynamic blending (low-high pass) case given in Figure 4.24. The Figure 4.14 case is highlighted here based on its simpler blending logic.

Figure 4.28 shows the Figure 4.14 root locus plot with closed-loop pole locations explicitly indicated for a compensator gain value of k_k=*0.066 rad/rad/s*. For this gain value, the rigid pitch mode (mid period mode) damping and natural frequency are ζ_{mp}

$=0.7043$ and $\omega_{mp}=0.8349$ *rad/s*. These values are considerably improved relative to the open-loop values obtainable from Table 2.1. These values should provide acceptable flying qualities for a large transport. After augmentation, the unstable slow mode in Table 2.1 is relocated to $s=-0.0040$ *rad/s* providing a stable closed-loop airframe. Even though the desire here was to gain stabilize the aeroelastic modes, Figure 4.28 indicates a mode *1* damping ratio of $\zeta_{f_1}=0.2277$, which is also much improved relative to Table 2.1. Finally, note that even though two higher frequency aeroelastic modes have a potential instability, for the selected gain value they are stable.

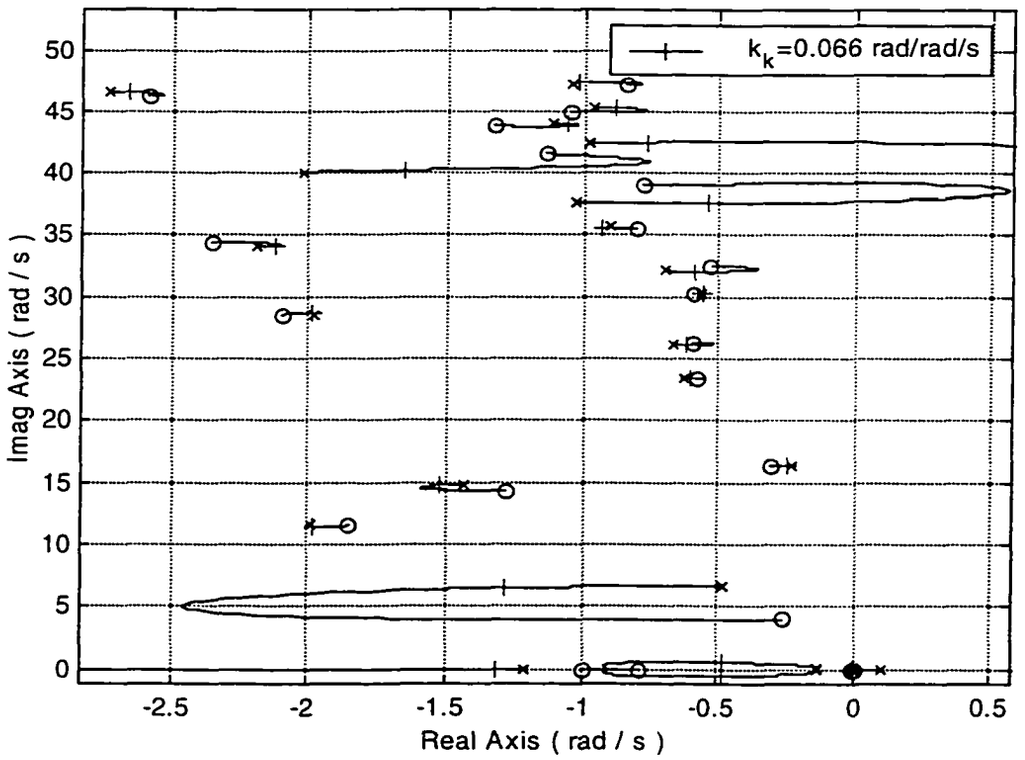

Figure 4.28 Closed-Loop Poles for $x_{s1}=2,429.7$ *in*, $x_{s2}=2,923.2$ *in* and $c_1=4.6$

Figure 4.29 shows the corresponding time response for $\hat{q}$ due to a *0.01 rad/s* pitch rate command $\hat{q}_c$ (see Figure 2.20 and Equation (2.43)). First note that $\hat{q}$ does not correspond to any pitch rate signal along the fuselage, but rather is a linear combination of two physical pitch rate signals. Further note that individual pitch rate responses may vary from that shown in Figure 4.29 due to different output characteristics. These other responses are not considered here. In general, the closed-loop response in Figure 4.29 is significantly improved when compared to the open-loop responses given in Figure 2.7-2.8. First and foremost, the closed-loop response is stable. The gross response consists of a single overshoot occurring around *3 s* with a decay to steady state after *6 s*. Note the system behaves as a rate command Type *1* system in the short term. This behavior is the mid-period modal contribution to the overall response. Also note in the response two distinct high frequency ripples with frequency content of approximately *6 rad/s* and *40 rad/s*. These vibrations are originating from the 1^{st} and 12^{th} aeroelastic modes (see Figure 4.28). By careful placement of the feedback sensors, these vibrations have been minimized by gain stabilization strategies, but residual oscillations still remain. The impact of these residual vibrations on piloted flying qualities is an open issue. These residual vibrations can be reduced by leveraging the loop gain (k_k), but the rigid pitch response quickness and damping is degraded. Given the extreme nature of the vehicle airframe and the associated flight control challenge, the final results appear to be reasonably successful.

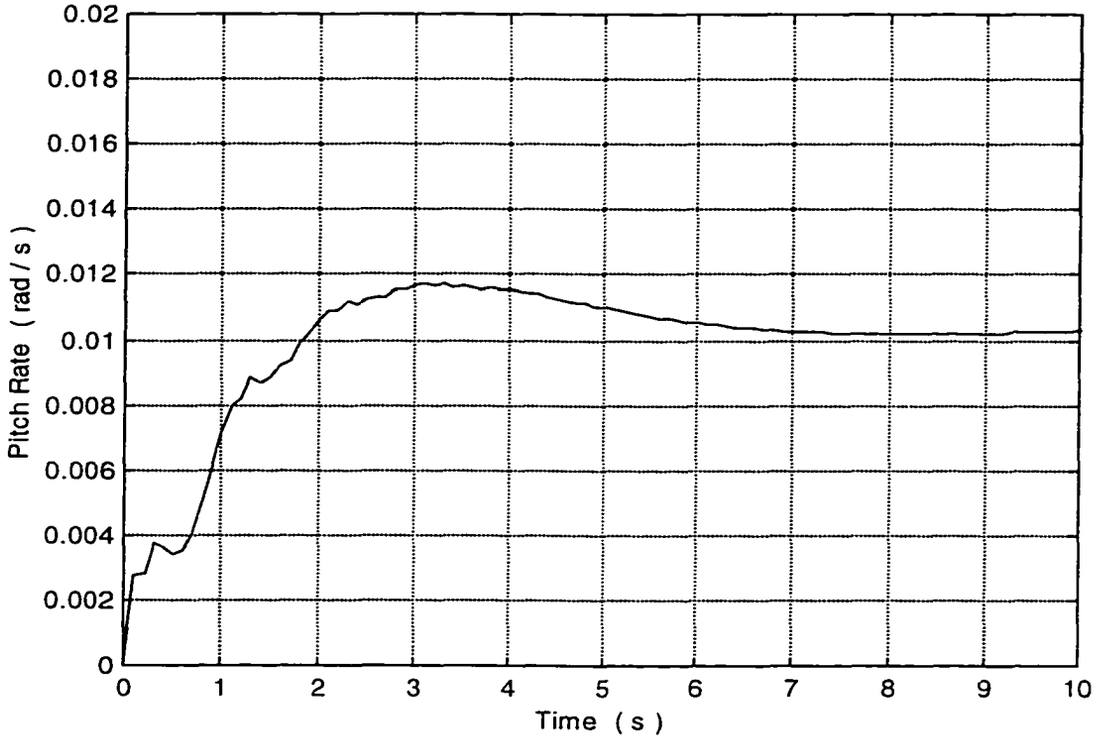

Figure 4.29 Step Response for x_{s1}=2,429.7 *in*, x_{s2}=2,923.2 *in* and c_1=4.6

CHAPTER 5

OPTIMAL SENSOR PLACEMENT: PHASE STABILIZATION

5.1 Introduction

This chapter deals with computing optimal sensor locations using phase stabilization objectives. This procedure is based on minimizing aeroelastic complementary departure angles as described in Equation (3.100)-(3.101). Complementary departure angle values for selected aeroelastic modes will be minimized using the optimization method presented in Figure 3.8. During optimization, inequality constraints addressing minimum phase zero and on the body sensor behavior as presented in Equations (3.104)-(3.106) are enforced. The general form of the cost function utilized in this chapter, based on complementary departure angle with inequality constraints, can be written as

$$H = \sum_{i=1}^{18} w_i \phi_i + \sum_{i=1}^{22} \lambda_i F_i \tag{5.1}$$

Previous studies revealed a direct trade exists between mode *1* and *3*. These two modes are critical to the stability of the system. Therefore, only the key complementary departure angle values of the low frequency modes *1* and *3* that affect control system stability are considered. Thus, the only nonzero weights in Equation (5.1) will be w_1 and w_3. This selection is based on knowledge obtained during manual sensor placement efforts. The solution strategy is to start with simple blend filters and progress to more

advanced blending logic (and hence more design freedom) when necessary. Static and dynamic filters with fixed parameters, as well as variable parameters, will be considered. Weighting factors are selected based on relative complementary departure angle values and are refined to tailor the solution results. Different initial positions for sensor locations will also be tested and used for solution refinement. The compensator zero parameter is specified and fixed (z_k=2 *rad/s*) to facilitate augmenting rigid pitch damping and natural frequency. For the most desirable sensor placement solutions, the time responses and general behavior of the closed-loop system will be tested and evaluated.

5.2 Sensor Placement with Fixed Static Blending

In this section, optimal gyro placement corresponding to the flight control system architecture shown in Figure 2.20 will be investigated. Optimization parameters are the two gyro locations x_{s1} and x_{s2}. The blending filters in the feedback signals will be considered as constant, static values equal to one for each filter. The static filters can be represented by the following expressions.

$$h_1(s) = 1 \tag{5.2}$$

$$h_2(s) = 1 \tag{5.3}$$

The fixed static filters in both Equations (5.2) and (5.3) express the simplest blending logic. These filters represent spectrally uniform and equally balanced blending. The procedure for finding the optimal sensor locations depends on the initial sensor positions used in the optimal search strategy. From Figure 3.10, as well as from manual placement experience, candidate initial sensor locations can be determined. The weighting factors of the cost function terms are initially assigned equal to one. Based on the optimization

results, these values will be adjusted in order to find desirable solutions satisfying the system requirements. If the solution characteristics are unsatisfactory, other departure angle terms will be added to the cost function with appropriate weighting factors, or other initial sensor locations will be sought, dependent on the evaluation of the optimization results.

As a benchmark, consider the root migration characteristics associated with Figure 5.1 for sensor positions $x_{s1}=850\ in$ and $x_{s2}=2,750\ in$. These positions could have originated from an inconclusive manual placement study, for example. Observe in Figure 5.1 the relaxed stability pole near the origin. The control system architecture (see Figure 2.20) is effective in stabilizing this mode and providing high levels of damping and quickness in the rigid pitch mode (see migration path initiating from near the origin and wrapping around the real axis compensator zero). These trends imply desirable rigid-body augmentation. The aeroelastic augmentation characteristics are much less desirable. Observe from Figure 5.1, as loop gain is increased both mode *1* and mode *10* are destabilized due to undesirable complementary departure angles ($\phi_1 = 46.11\ deg$, $\phi_{10} = 171.7497\ deg$). On the other hand, the mode *3* complementary departure angle is nearly optimum ($\phi_3 = 5.714\ deg$). Also note the zeros associated with mode *1* as well as mode *10* are nonminimum phase. Reduced structural mode damping, phase loss in the control loop, and possibly response reversal may result from this control and are unacceptable characteristics which must be corrected with improved sensor locations.

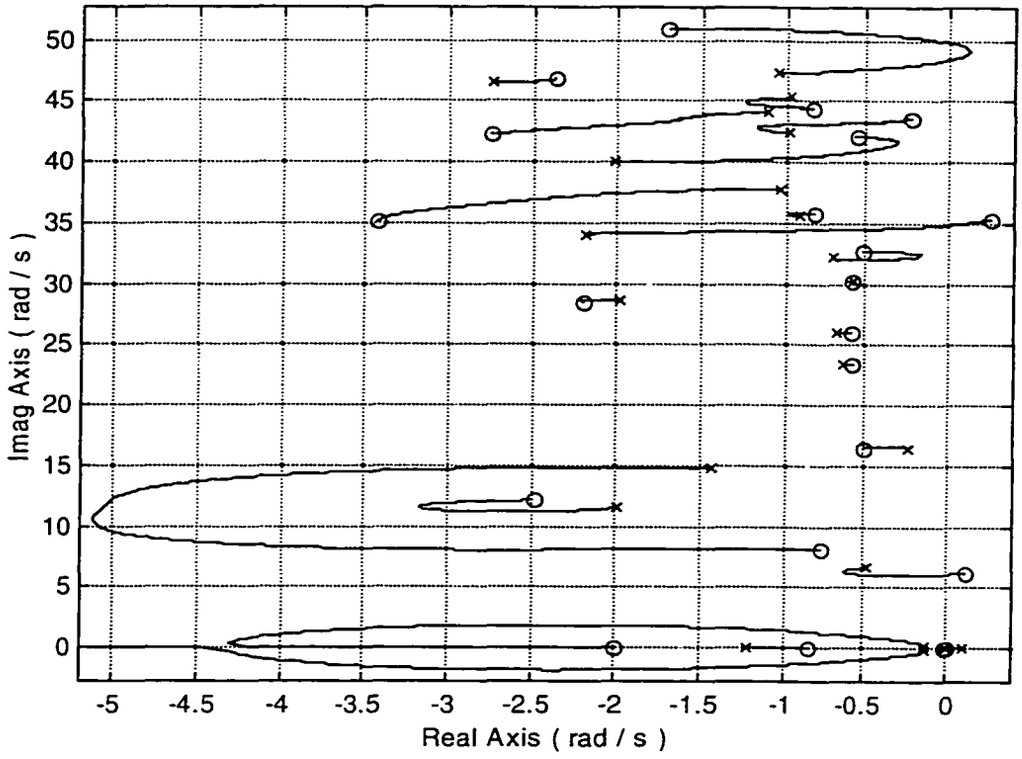

Figure 5.1 Root Locus Plot for x_{s1}=*850 in* and x_{s2}=*2,750 in* (z_k=*2 rad/s*)

For the initial sensor positions of x_{s1}=*850 in* and x_{s2}=*2,750 in*, and for the weights of w_1= *1 1/deg* and w_3=*1 1/deg*, the optimization algorithm is applied to Equation (5.4), or

$$H = w_1\phi_1 + w_3\phi_3 + \sum_{i=1}^{22} \lambda_i F_i \tag{5.4}$$

The resulting optimal sensor positions are x_{s1}=*926.6 in* and x_{s2}=*2,734.6 in*. The resulting root locus plot when the sensors are placed at these optimal locations is illustrated in Figure 5.2. Note the complementary departure angle for mode *1* in Figure 5.2 has not changed much from that shown in Figure 5.1. From Figure 5.2, it is also noticed that the constraints F_1 and F_{10} are still violated. Note both aeroelastic modes *1* and *10* have

nonminimum phase zeros. This result is again an artifact of the implemented search algorithm in Figure 3.8. Because of the limited region of feasibility, dedicated constraint satisfaction is not considered. However, the overall cost is reduced and this reduction can originate with improved constraint satisfaction (note the mode *1* zero is closer to the imaginary axis in Figure 5.2 than in 5.1). The optimization algorithm with selected values of weighting factors and starting positions is unable to satisfy all constraint equations indicating a design change is needed.

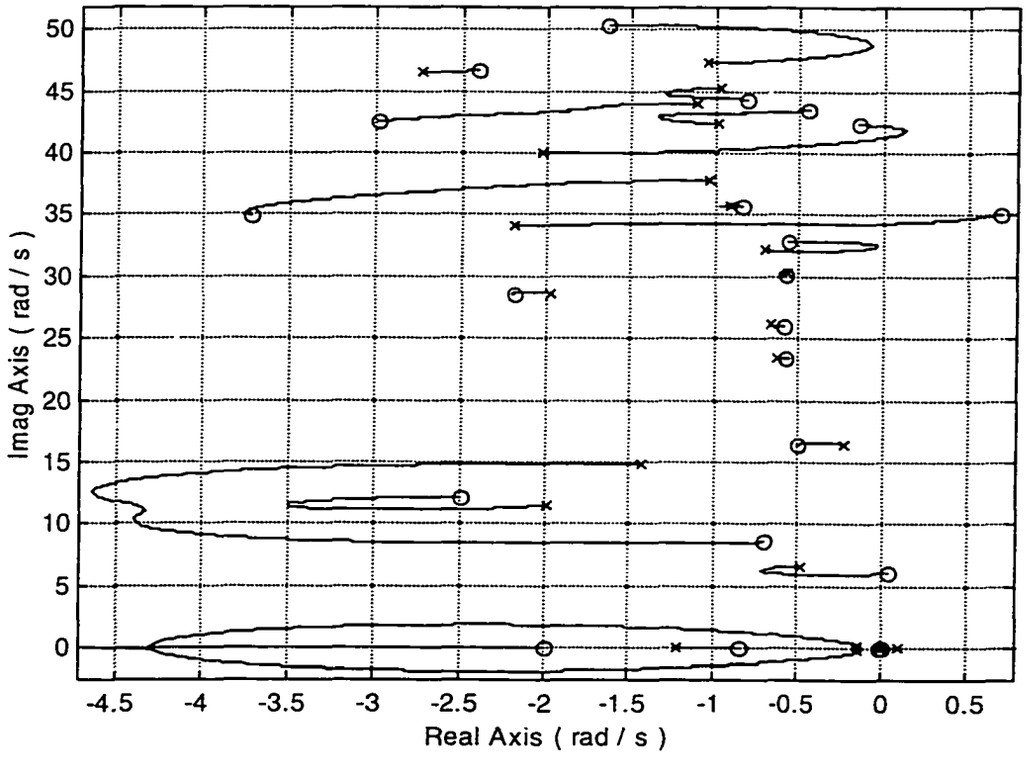

Figure 5.2 Root Locus Plot for x_{s1}=926.6 *in* and x_{s2}=2,734.6 *in*

Consider increasing the weighting factor for aeroelastic mode *1* from *1 1/deg* to *3 1/deg* and keeping the weight factor for mode *3* as *1 1/deg*. The optimization tool is applied to Equation (5.4) with the same previous initial placement of sensors. The optimization results indicate that the best sensor locations are $x_{s1}=903.4$ *in* and $x_{s2}=2,937.2$ *in*. The flight control system root locus when the sensors are placed at these optimal values is illustrated in Figure 5.3. Comparing the root locus features in Figure 5.3 with Figure 5.1, the optimal solution shows that both the 1^{st} and the 3^{rd} aeroelastic modes have desirable complementary departure angles. Numerically, the complementary departure angle for mode *1* is significantly decreased from *46.11 deg* to *0.003 deg*, but the complementary departure angle for mode *3* is slightly increased from *5.71 deg* to *6.16 deg*. Examining the locations of aeroelastic mode zeros, the original zeros previously laying in the unstable region have been forced to move into the stable region. These two results are consistent with the proposed cost function and constraints in Equation (5.4). Additionally, preservation of rigid-body stability augmentation characteristics is achieved. An implication from these observations and sensor placement strategy is the flight control system is stable with improved damping for a wide range of gain values. Also, the minimization history in terms of the objective function vs. number of iterations and the sensor location search path are shown in Figures 5.4-5.5. Note a change in sensor location of approximately *200 in* or less results in a large reduction of H. Also, it is noted from this plot that the complementary departure angle of the 10^{th} aeroelastic mode is undesirable. This behavior is somewhat accepted, however, since the constraint F_{10} is satisfied.

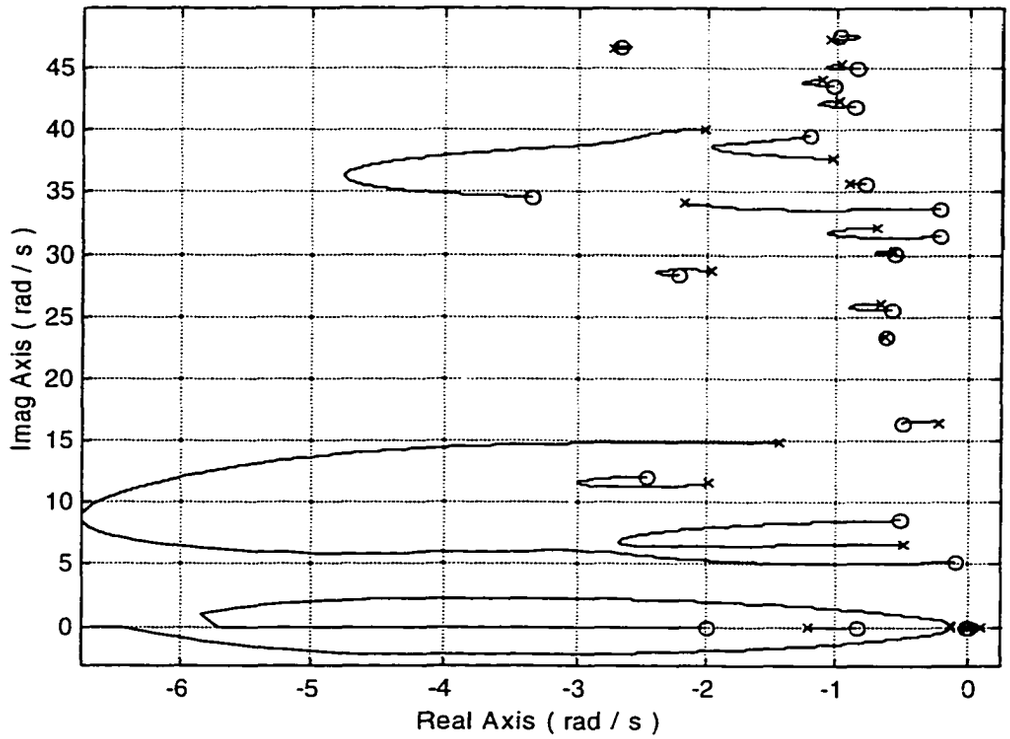

Figure 5.3 Root Locus Plot for x_{s1}=*903.4 in* and x_{s2}=*2,937.2 in*

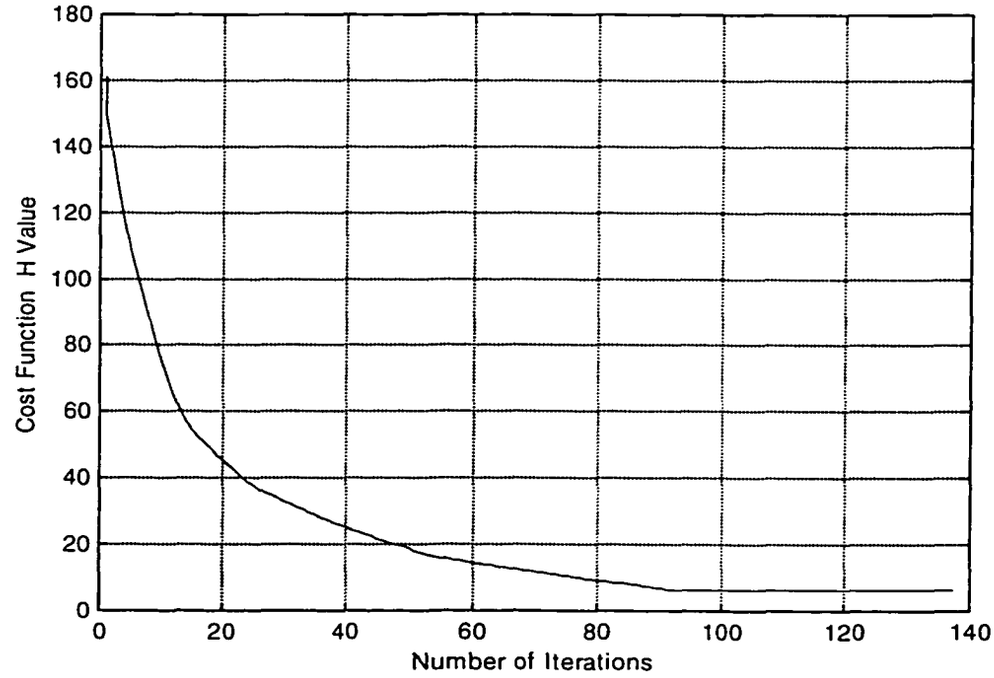

Figure 5.4 Cost Function History for x_{s1}=*903.4 in* and x_{s2}=*2,937.2 in*

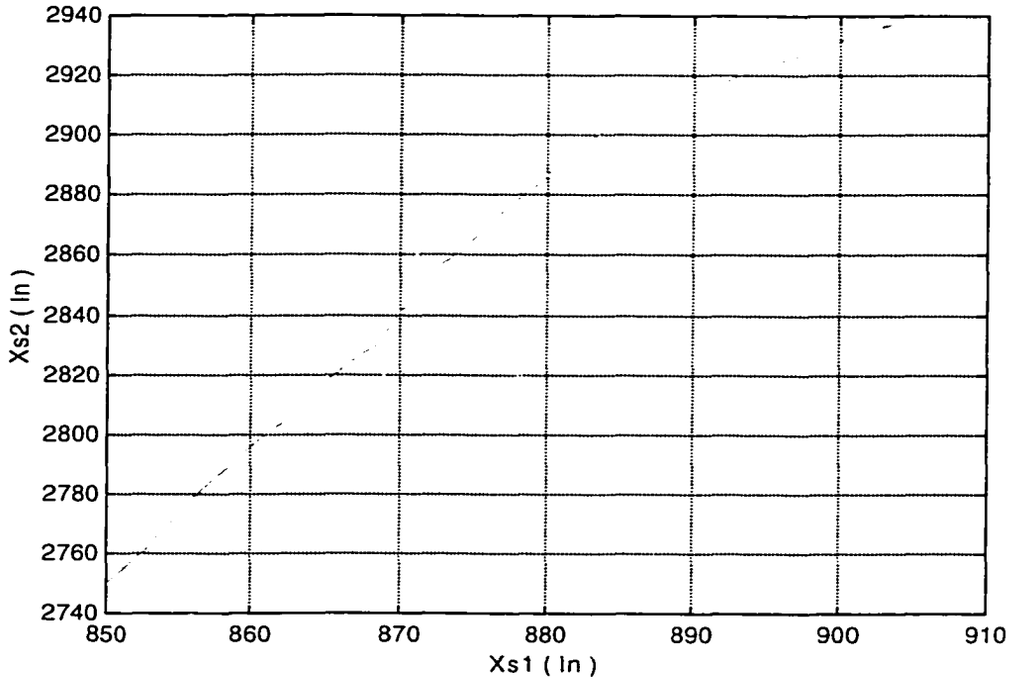

Figure 5.5 Sensor Position History for x_{s1}=*903.4 in* and x_{s2}=*2,937.2 in*

The main conclusion from the results presented in this section is that fixed static blending (see Equations (5.2)-(5.3)) is very effective and allows sufficient design freedom to achieve the desired phase stabilization objectives in nearly all aspects. Selected modes become or remain well phase stabilized and the corresponding complementary departure angle values are near zero. The computed sensor locations tend to reduce the complementary departure angle with high weightings with an observable design trade. The only remaining quasi-significant deficiency is the departure angle for mode *10*. One approach to address this small deficiency would be inclusion of ϕ_{10} in the cost function. This solution approach was not explored. To possibly alleviate this problem, the next section explores more sophisticated blending structures.

5.3 Sensor Placement with Variable Static Blending

In this section, optimal gyro placement corresponding to the system in Figure 2.20 is again considered. The feedback blending filters will be considered as variable, static values. Based on the ability to shift loop gain between k_k and h_1-h_2 in Equation (2.43) and Figure 2.20, there is no loss of generality if one filter is held fixed and the other allowed to vary. Here, the static gain parameter of the first filter will be considered variable, while the parameter value of the second filter will be considered constant (unity). The static filters can be expressed as

$$h_1(s) = c_1 \tag{5.5}$$

$$h_2(s) = 1 \tag{5.6}$$

The variable static filter structure in Equations (5.5)-(5.6) introduces the next level of design freedom beyond that considered in Section 5.2. The filters here represent spectrally uniform but unbalanced blending. Optimization parameters here include the two gyro locations x_{s1} and x_{s2} and the filter parameter c_1. To avoid unexpected exploitation by the optimizer, the variable filter parameter will be constrained to lie within certain bounds. Thus, introduce two additional constraints

$$F_{23} = c_1 - \overline{c_1} \le 0 \tag{5.7}$$

$$F_{24} = \underline{c_1} - c_1 \le 0 \tag{5.8}$$

where $\overline{c_1}$ and $\underline{c_1}$ denote upper and lower bounds on c_1. The numerical algorithm is run with $\underline{c_1} = 0.1$ and $\overline{c_1} = 10$.

The first case will be tested by giving the variable blending filter parameter an initial value of c_1=5. Figure 5.6 shows the root locus plot of the flight control system

with the specified blend filter parameter and with sensors placed initially at x_{s1}=*850 in* and x_{s2} =*2,750 in.* It is noted from this figure that constraints F_1, F_9 and F_{13} are violated. Aeroelastic mode *18* is also unstable for an intermediate range of gain values. The 1^{st} aeroelastic mode has a highly undesirable complementary departure angle. An optimization algorithm will be applied to Equation (5.4) with constraints F_{23}, F_{24} included to minimize the complementary departure angle for both modes *1* and *3*, and to force the nonminimum phase zeros to move to the stable region. Since the 1^{st} aeroelastic mode has an extremely undesirable complementary departure angle (ϕ_1 =*160.5048 deg*), a larger weight factor will be assigned to this mode compared to the one assigned to mode *3*. The weighting factors are w_1=*1 1/deg* and w_3=*0.5 1/deg*. The optimal solution indicates the best sensor positions are at x_{s1} =*823.7 in* and x_{s2}=*2,759.5 in* while the optimal blend filter parameter is c_1=*0.8*. Figure 5.7 illustrates the root locus plot when the optimal values are considered. It is noted from this plot that both the 1^{st} mode and the 3^{rd} mode have desirable complementary departure angles. Numerically, the complementary departure angle for the 1^{st} mode is greatly decreased from *160.5048 deg* to *0.5664 deg* while the complementary departure angle for the 3^{rd} mode is slightly increased from *5.1238 deg* to *5.7133 deg*. Also, it is noted that aeroelastic mode *10* has an undesirable complementary departure angle, but all constraint equations are satisfied (although this result is not always guaranteed) and an acceptable rigid-body pitch mode is achieved. The cost function value for each iteration is illustrated in Figure 5.8. Note Figure 5.8 shows a temporary increase in the *H* value. The cost function history plots show all trial iterations, even iterations that failed to decrease the *H* value. Observe how the algorithm changes

the adaptive step size or the gradient construction increment, and the H value continues its decreasing history.

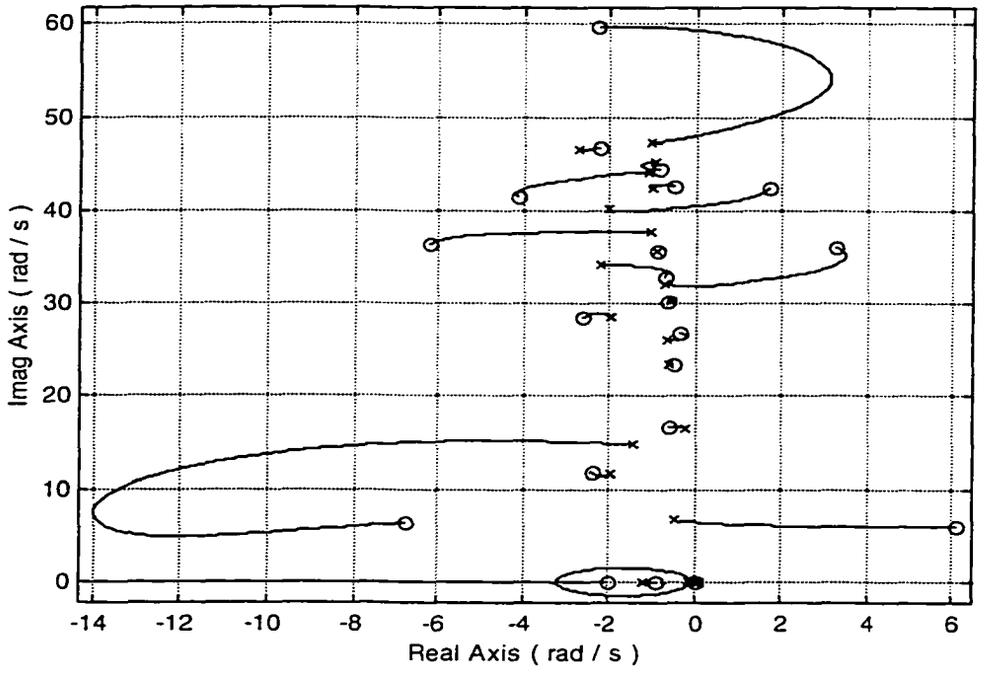

Figure 5.6 Root Locus Plot for x_{s1}=*850 in*, x_{s2}=*2,750 in* and c_1=*5* (z_k=*2 rad/s*)

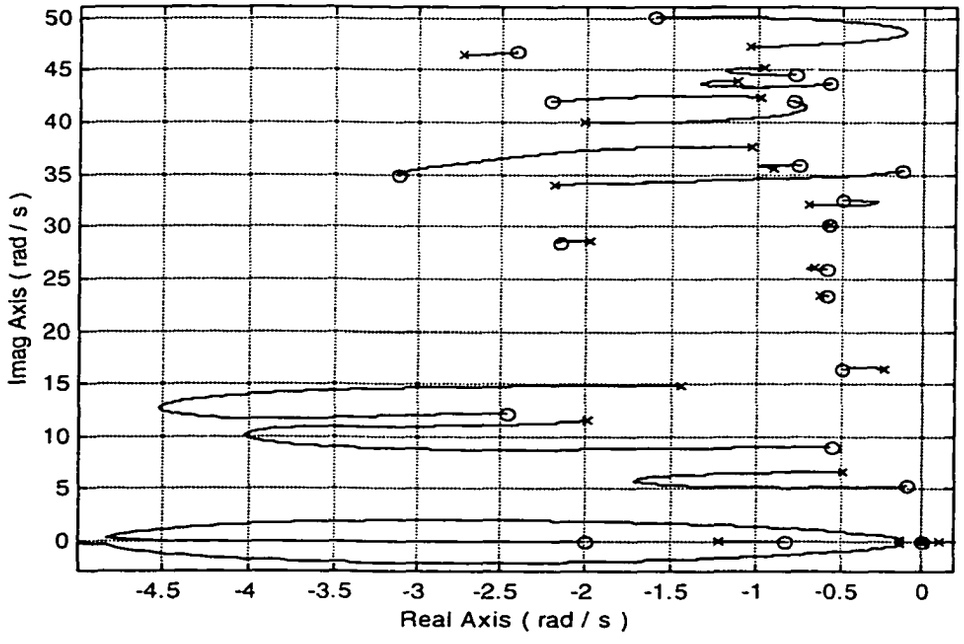

Figure 5.7 Root Locus Plot for x_{s1}=*823.7 in*, x_{s2}=*2,759.5 in* and c_1=*0.8*

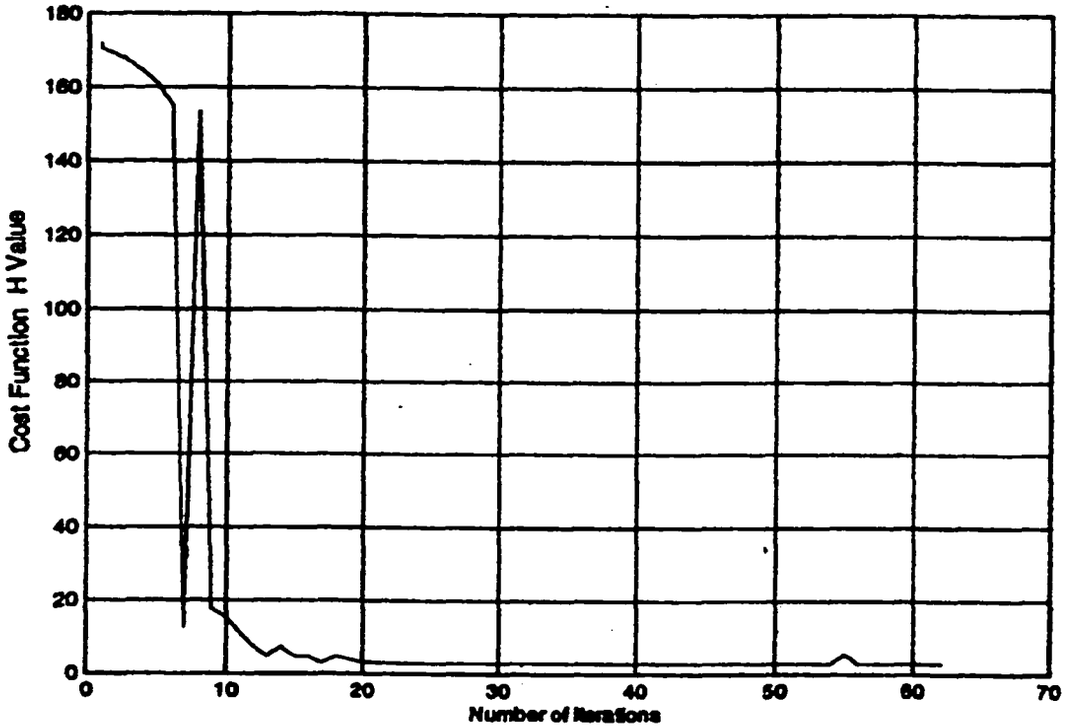

Figure 5.8 Cost Function History for x_{s1}=*823.7 in*, x_{s2}=*2,759.5 in* and c_1=*0.8*

Another case will be tested using the same initial values used in the previous case but with different weighting factor values. The values w_1=*3 1/deg* and w_3=*1 1/deg* will be considered here. The results indicate optimal sensor positions will be x_{s1}= *845.7 in* and x_{s2}=*2,789.1 in*, and c_1=*0.8*. The root locus plot when the sensor are located in these positions is shown in Figure 5.9. Comparing this figure with Figure 5.6, it is noticed the complementary departure angle for mode *1* has dropped from *160.5048 deg* in the initial case to *1.7720 deg* in the optimal case, while the complementary departure angle for mode *3* has slightly increased from *5.1238 deg* to *5.98 deg*. These results indicate the complementary departure angle for both critical modes (*1* and *3*) are not decreasing

simultaneously. When the complementary departure angle of the 1^{st} mode is decreasing, the complementary departure angle of the 3^{rd} mode is increasing or *vice versa*.

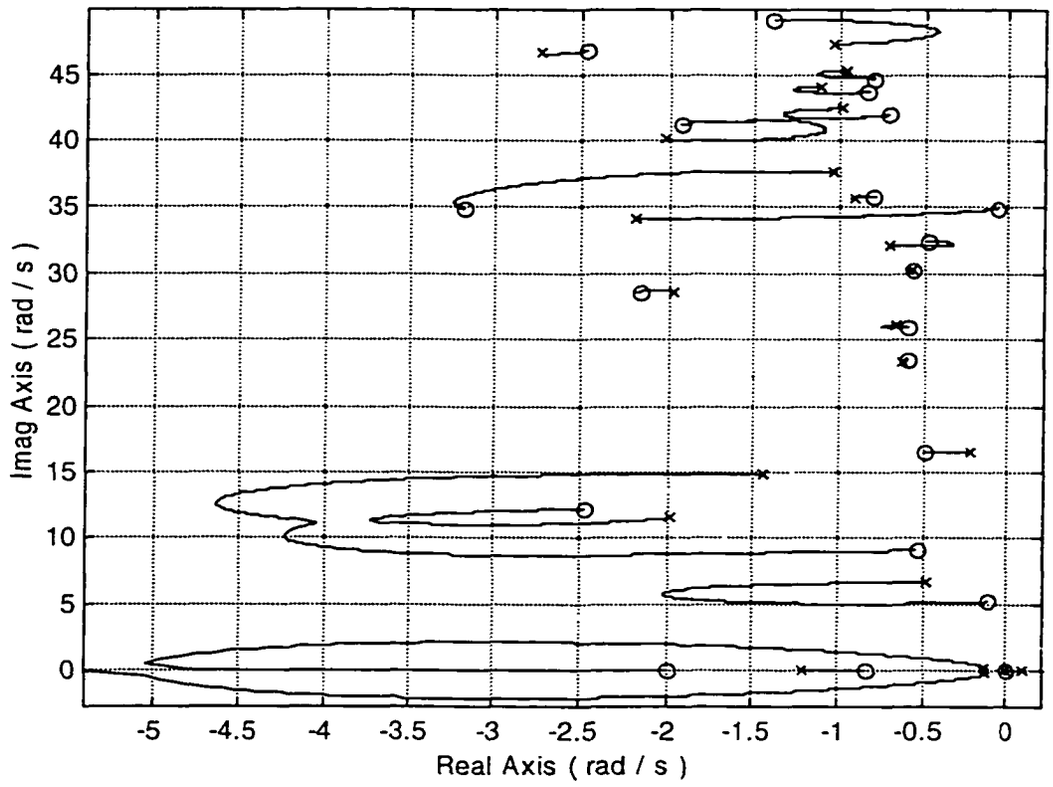

Figure 5.9 Root Locus Plot for x_{s1}= *845.7 in*, x_{s2}=*2,789.1 in* and c_1=*0.8*

A major conclusion from the investigations presented in this section is that, although the variable static blending filters transform a very poor manual solution with three nonminimum phase zeros into a minimum phase system with a greatly improved ϕ_1 value without disrupting the ϕ_3 value, these more sophisticated blend filters do not offer much leverage for improving the ϕ_{10} value beyond the fixed static cases. Therefore, more design freedom is explored in the next section.

5.4 Sensor Placement with Fixed Dynamic Blending

In the previous Sections 5.2 and 5.3, the flight control system blending filter is considered to have static form. In this section, another prospect beyond the previous forms will be considered to find the optimal location of sensors. This prospect deals with a fixed dynamic filter architecture. The main objective of using such a filter is to provide more freedom in designing and tailoring optimal sensor solutions. Several forms of dynamic filters will be considered and tested to satisfy design requirements. Two simple blending filter strategies are considered and coincide with the filters presented in Figure 4.18 and Equations (4.11)-(4.14). These filters again represent spectrally nonuniform and unbalanced blending. Because of the fixed nature of the filters, optimization parameters in this section only include the two gyro positions x_{s1} and x_{s2}.

When using the low-band pass filters, the optimizer is unable to satisfy design requirements. An optimization algorithm applied to the augmented cost function represented in Equation (5.4) for different initial sensor locations as well as different weighting factors failed to find suitable solutions for the sensor locations in which all constraint equations are satisfied. In general, the 1^{st} aeroelastic mode tends to have a nonminimum phase zero and an undesirable complementary departure angle. Thus, the low-high pass filters will be tested. It is found that this kind of filter tends to facilitate constraint F_1 satisfaction. Figure 5.10 shows the root locus plot of the flight control system when the sensors are initially placed at $x_{s1}=850\ in$ and $x_{s2}=2,750\ in$ and when the dynamic filters are selected with $a=3\ rad/s$, $c_1=1$, and $c_2=7$. Comparing this figure with Figure 5.1, it is noted that nonminmium phase zeros are moved to the stable region. Also,

the complemenatry departure angle of the first mode is improved (ϕ_1 =*46.11* to *14.7506 deg*).

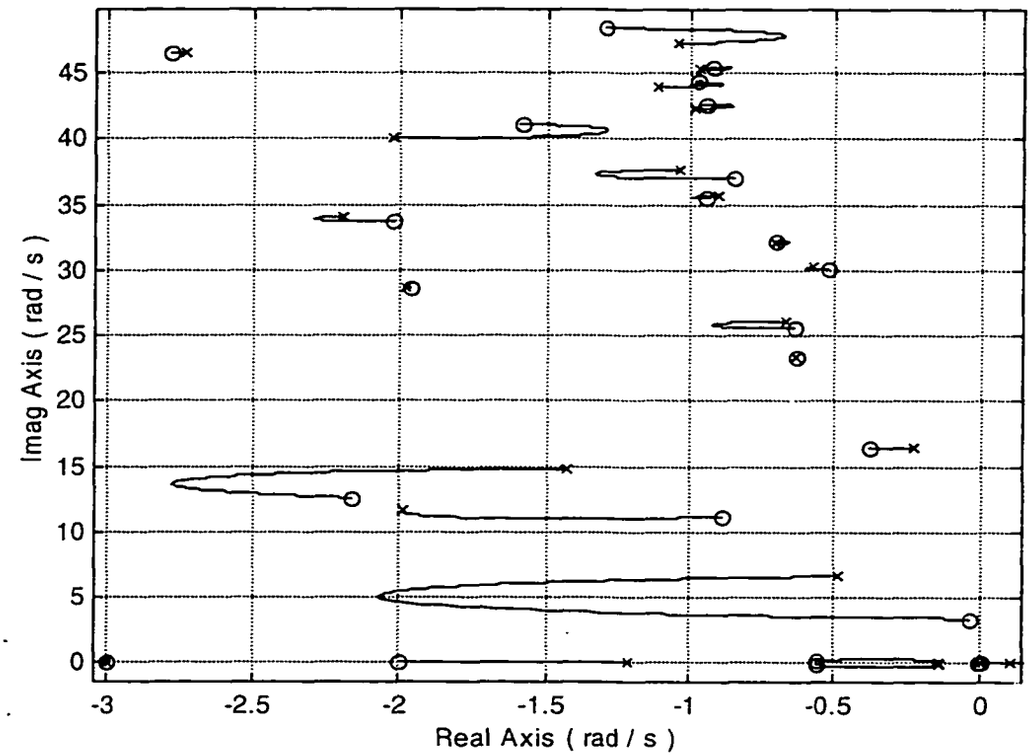

Figure 5.10 Root Locus Plot for x_{s1}=*850 in* and x_{s2}=*2,750 in*, z_k=*2 rad/s*, (Dynamic Blend)

To minimize the complementary departure angles for both modes *1* and *3*, an optimization procedure will be applied on the augmented cost function shown in Equation (5.4) with weighting factors w_1=w_3=*1 1/deg*. An optimization solution indicates the most desirable locations for the sensors are found to be at x_{s1}=*622.6 in* and x_{s2}=*2,877.8 in*. Figure 5.11 shows the root locus plot when the sensors are located at the optimized solution. Comparing Figure 5.11 with Figure 5.10, it is noted that both mode *1* and *3* are well phase stabilized, the complementary departure angle of the 1^{st} mode is decreased from *14.7506* to *1.7252 deg* while the complementary departure angle of the

3^{rd} mode is slightly decreased from *3.5290* to *3.2068 deg*. All constraint equations remained satisfied. Most importantly to note is the undesirable mode *10* departure angle has been eliminated with utilization of dynamic blending filters, although it may require improvement with further tailoring. Figure 5.12 shows the augmented cost function value at each optimization iteration while Figure 5.13 shows the track of the sensor positions during the search.

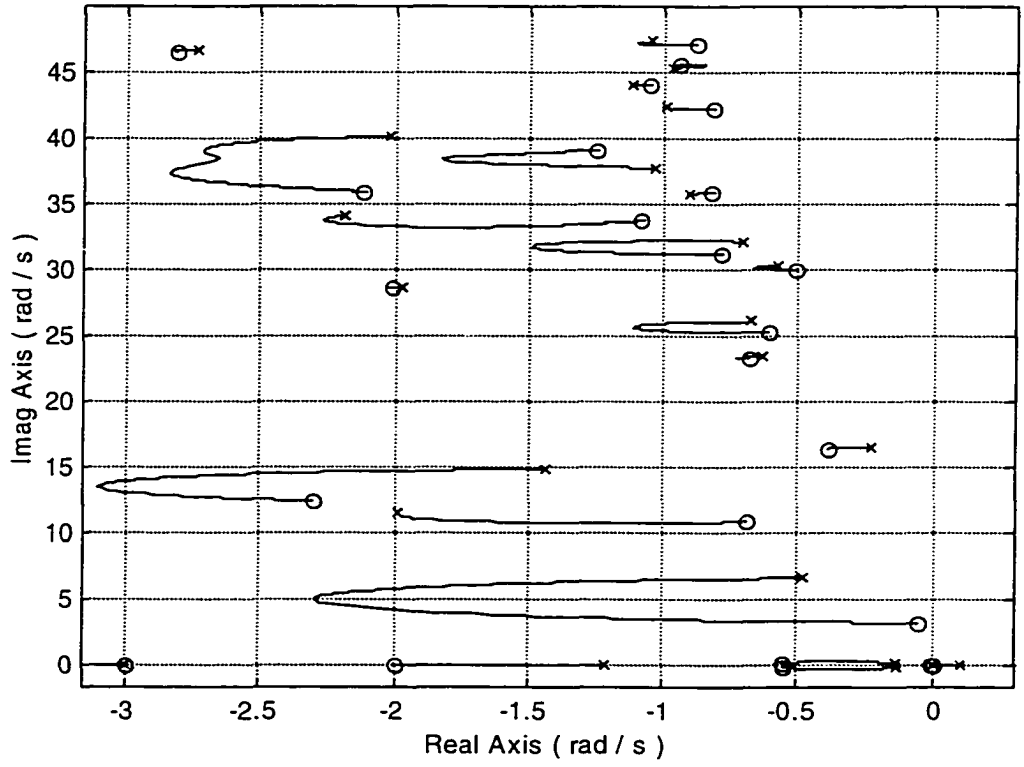

Figure 5.11 Root Locus Plot for x_{s1}=*622.6 in* and x_{s2}=*2,877.8 in*

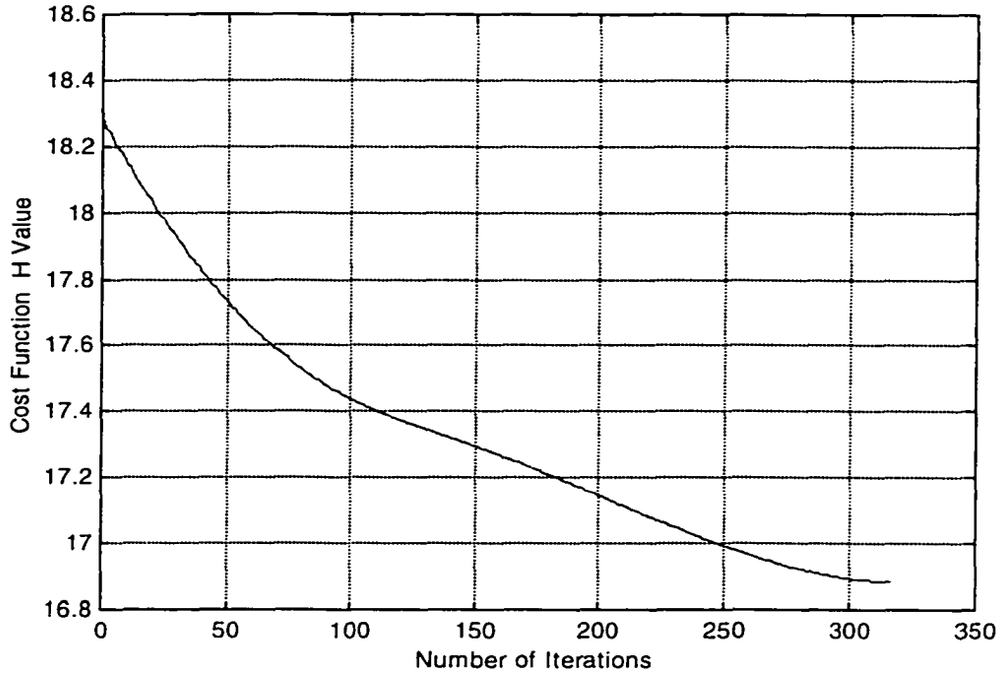

Figure 5.12 Cost Function History for x_{s1}=622.6 *in* and x_{s2}=2,877.8 *in*

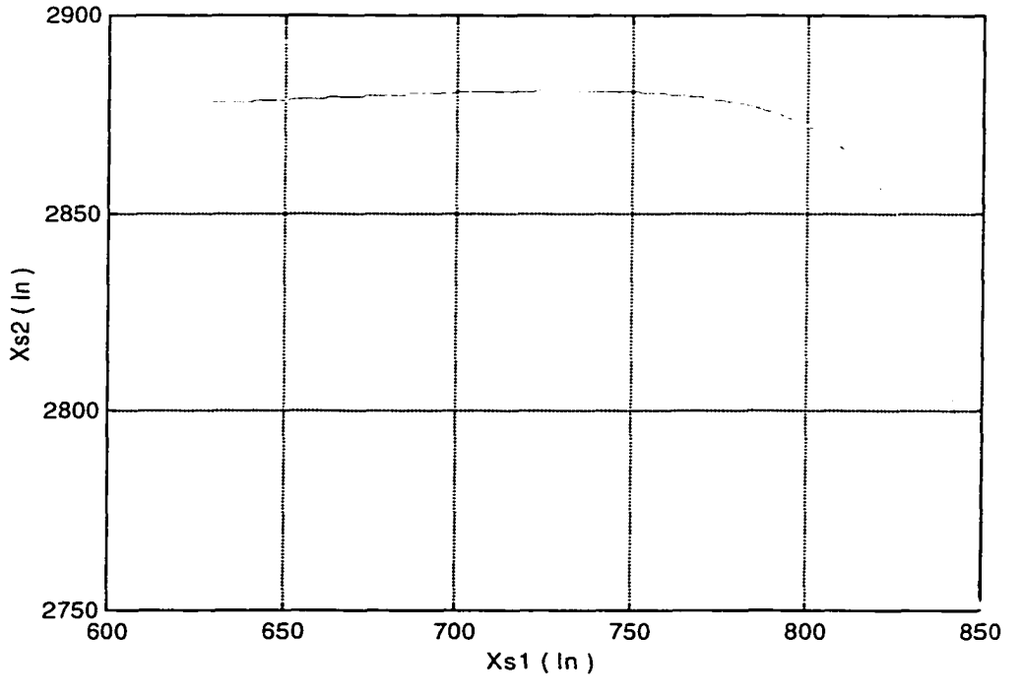

Figure 5.13 Sensor Position History for x_{s1}=622.6 *in* and x_{s2}=2,877.8 *in*

In an attempt to improve upon the previous results, another case will be tested. The same dynamic filters $a=3$ *rad/s*, $c_1=1$, and $c_2=7$ as well as the same weigthing factors $w_1=w_3=1$ *1/deg* will be used, but different initial locations for the sensors will be considered. Figure 5.14 illustrates the root locus plot when the sensors are located in the initial placement such as $x_{s1}=2,100$ *in* and $x_{s2}=2,950$ *in*.

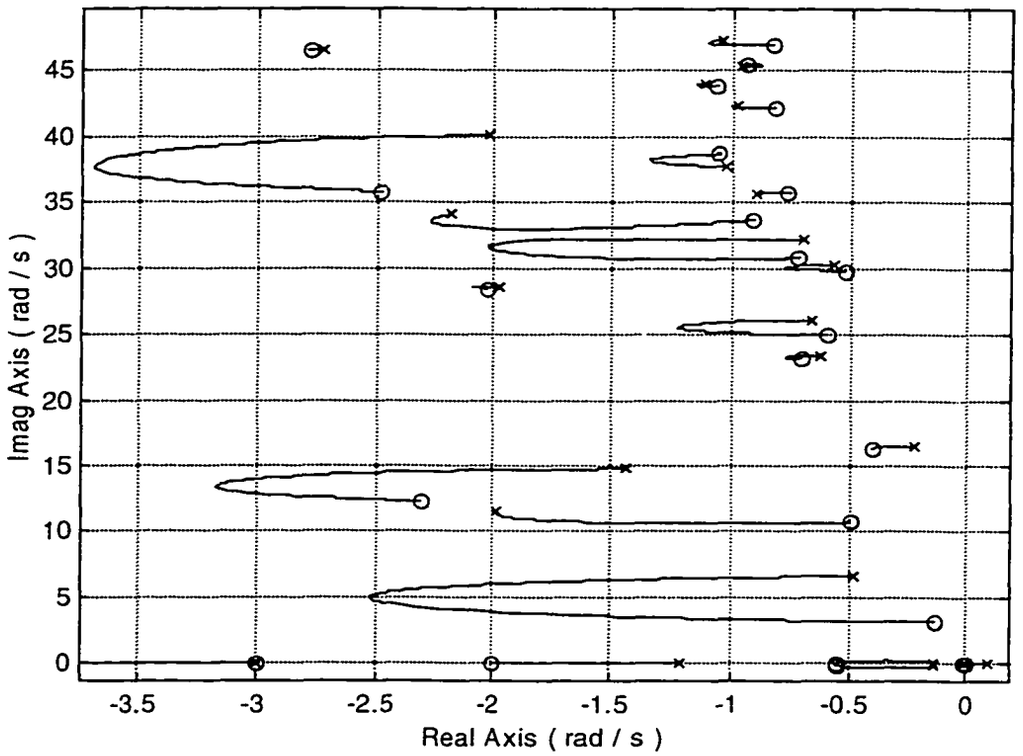

Figure 5.14 Root Locus Plot for $x_{s1}=2,100$ *in* and $x_{s2}=2,950$ *in* ($z_k=2$ *rad/s*)

Applying the search algorithm on Equation (5.4), the computational results indicate the optimal locations are found to be $x_{s1}=3,195.3$ *in* and $x_{s2}=2,755.9$ *in*. Figure 5.15 shows the root locus plot of the flight control system for the optimized solution. Comparing Figure 5.15 with Figure 5.14 reveals the complementary departure angle for

the 1^{st} mode is decreased from *9.9666* to *6.4469 deg.* while the complementary departure angle for the 3^{rd} mode is decreased from *6.0560* to *1.8702 deg.* Figures 5.16 and 5.17 illustrate the cost minimization history and the sensor location path, respectively. Note the altered starting values have resulted in a drastically different solution for x_{s1} when compared with Figure 5.11 (*3,195.3 in* vs. *622.6 in*). Here the first gyro is to be mounted near the vehicle tail while in Figure 5.11, the gyro should be mounted near the vehicle nose. Although drastically different mounting locations exist, the local minimum solutions (i.e., root migration characteristics) appear highly similar.

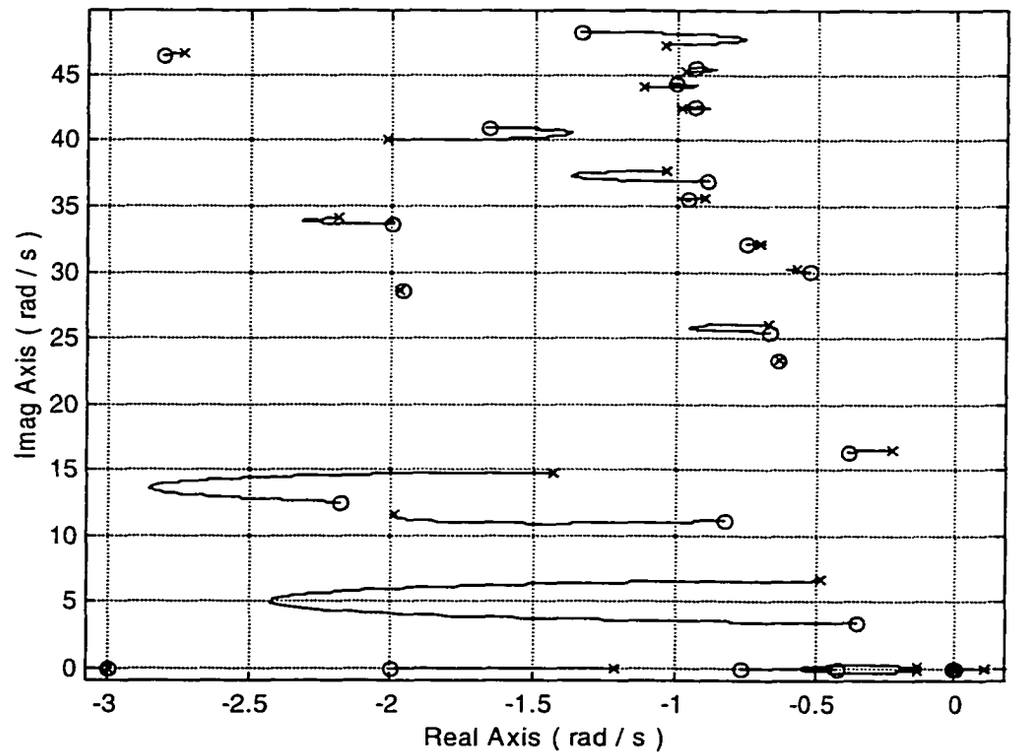

Figure 5.15 Root Locus Plot for x_{s1}=*3,195.3 in* and x_{s2}=*2,755.9 in*

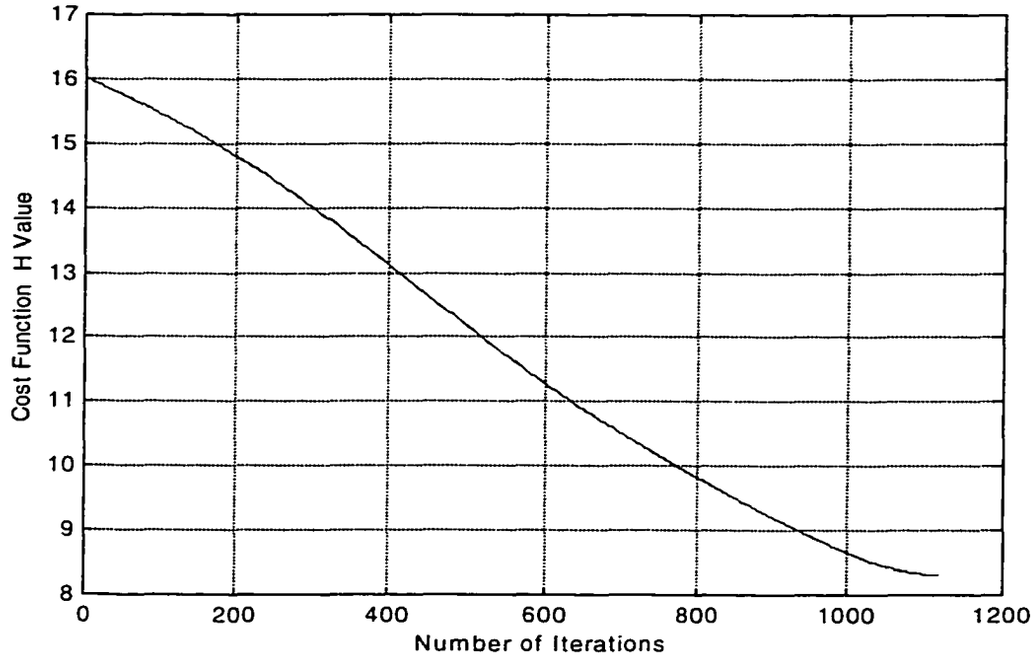

Figure 5.16 Cost Function History for x_{s1}=3,195.3 *in* and x_{s2}=2,755.9 *in*

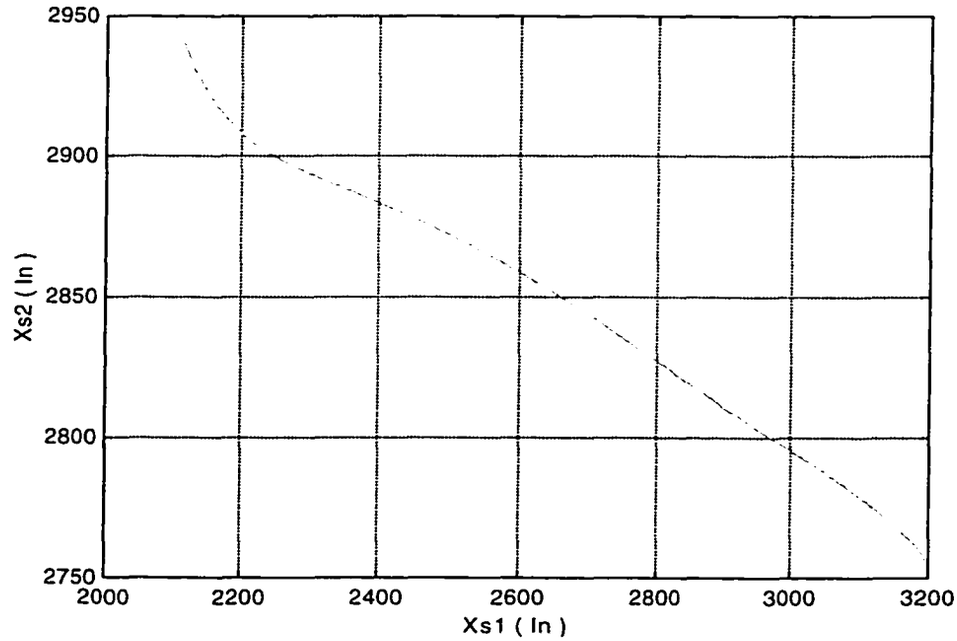

Figure 5.17 Sensor Position History for x_{s1}=3,195.3 *in* and x_{s2}=2,755.9 *in*

5.5 Sensor Placement with Variable Dynamic Blending

In Section 5.4, cases were run with a fixed blending structure. Thus, the full potential of the dynamic filters was not exploited. It is noted from application that multiplying the second feedback signal by a higher gain while minimizing the sensor cut off parameter value helps to reduce nonminimum phaseness of the 1^{st} aeroelastic mode. For example, it is observed that when the low-high pass filter parameter a is decreased and c_2 is increased manually using the Figure 5.11 solution, the mode *1* zero translates deeper into the left-half plane. In other words, there may be additional solution enhancements that can be extracted from this filter structure. In this section, the low-high pass dynamic blending strategy will be exploited further by allowing one independent parameter and one dependent parameter of the dynamic filters to be optimized. The parameter a in Equations (4.13)-(4.14) will be considered variable inside the optimization algorithm. Further the parameter c_2 will be allowed to vary according to the schedule $c_2=2a$. Constraints for the parameter a ($0.1<a<10$ *rad/s*) are again enforced during the optimization.

Consider a case starting with optimization variables $x_{s1}=2.100$ *in* and $x_{s2}=2.950$ *in*, and $a=3$ *rad/s*. Other parameter values that are fixed include $c_1=1$. Cost function (Equation (5.4)) weights are $w_1=w_3=1$ *1/deg*. The optimal solution yields $a=1.8$ *rad/s* and no change for x_{s1} and x_{s2} ($x_{s1}=2.100$ *in* and $x_{s2}=2.950$ *in*). The corresponding root locus plot is given in Figure 5.18. These results are quite unexpected. Note the sensor positions x_{s1} and x_{s2} did not change during the optimization. Further analysis revealed the components of the gradient vector associated with x_{s1} and x_{s2} are dominated by the corresponding component for a by several orders of magnitude. Thus, the optimizer

essentially ignored the directional information corresponding to x_{s1} and x_{s2} during iterative stepping. Even though manual changes in x_{s1} and x_{s2} lead to significant root locus changes, additional changes due to a wash out these effects. This result is in direct contrast to that found in Section 4.5. It is noted from Figure 5.18 that the complementary departure angles for both aeroelastic modes *1* and *3* are well phase stabilized ($\phi_1 = 0.0001$ *deg*, $\phi_3 = 1.4185$ *deg*), all constraint equations are satisfied, and the rigid-body mode is successfully augmented. Little additional benefit was extracted from considering a variable dynamic filter for this single test case. Two small benefits may be improved ϕ_{13} and ϕ_{18} values compared with those in Figure 5.15.

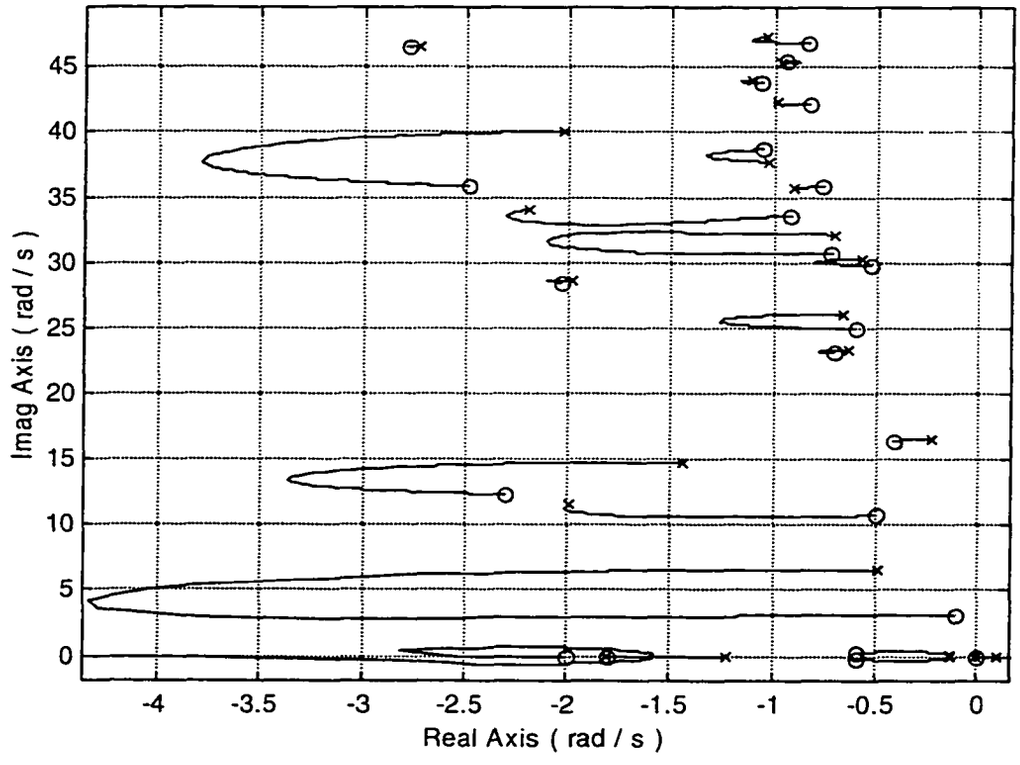

Figure 5.18 Root Locus Plot for x_{s1}=*2,100 in*, x_{s2}=*2,950 in* and a=*1.8 rad/s*

5.6 Closed-Loop Vehicle Evaluation

In this section, one of the more promising sensor placement solutions will be carried through to the final step of flight control design and evaluation. Three candidate sensor placement solutions based on phase stabilization are potential cases. These solutions correspond to the variable static blending case given in Figure 5.7 and the fixed dynamic blending (low-high pass) cases given in Figure 5.11 and 5.15. The Figure 5.7 case is highlighted here based on the simpler blending logic.

Figure 5.19 shows the Figure 5.7 root locus plot with closed-loop pole locations explicitly indicated for a compensator gain value of k_k=*0.58 rad/rad/s*. For this gain value, the rigid pitch mode (mid period mode) damping and natural frequency are ζ_{mp} =*0.6169* and ω_{mp} =*2.2063 rad/s*. These values are considerably improved relative to the open-loop values obtainable from Table 2.1. These values should provide acceptable flying qualities for a large transport. After augmentation, the unstable slow mode in Table 2.1 is relocated to *s=-0.0070 rad/s* providing a stable closed-loop airframe. The desire here was to phase stabilize the aeroelastic modes, and Figure 5.19 indicates a mode *1* damping ratio of ζ_{f_1} =*0.1994*, which is also much improved relative to Table 2.1. Finally, note that there are no predicted instabilities for any gain value.

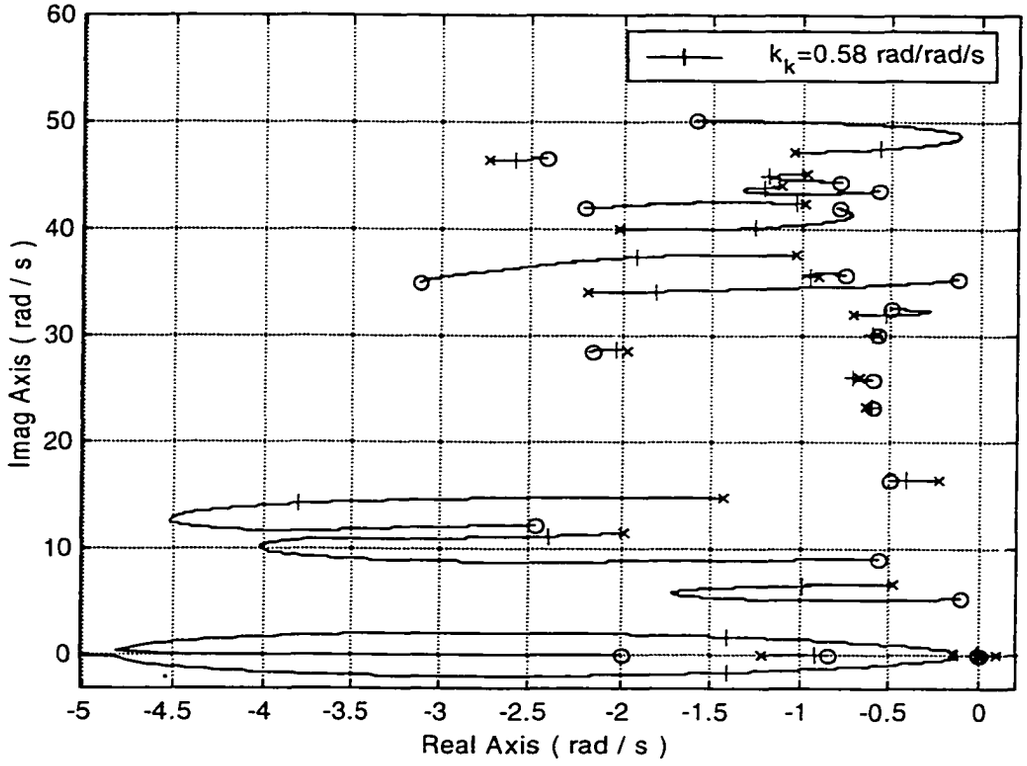

Figure 5.19 Closed-Loop Poles for x_{s1}=*823.7 in*, x_{s2}=*2,759.5 in* and c_1=*0.8*

Figure 5.20 shows the corresponding time response for $\hat{q}$ due to a *0.01 rad/s* pitch rate command $\hat{q}_c$ (see Figure 2.20 and Equation (2.43)). First note that $\hat{q}$ does not correspond to any pitch rate signal along the fuselage but rather is a linear combination of two physical pitch rate signal. Further note that individual pitch rate responses may vary from that shown in Figure 5.20 due to different output characteristics. These other responses are not considered here. In general, the closed-loop response in Figure 5.20 is significantly improved when compared to the open-loop responses given in Figure 2.7-2.8. First and foremost, the closed-loop response is stable. The gross response consists of

a single overshoot occurring around *1.2 s* with a decay to steady state after *3 s*. Note the system behaves as a rate command Type *1* system in the short term. This behavior is the mid-period modal contribution to the overall response. Also note in the response one distinct high frequency ripple with frequency content of approximately *10 rad/s*. This vibration is originating from the 3^{rd} aeroelastic mode (see Figure 5.19). Even though the 3^{rd} mode is damped considerably relative to the open-loop value, the closed-loop pole is distanced from the corresponding zero (i.e., a loose dipole) and the time response suffers. This phenomenon is often overlooked in elastic control design. The impact of this residual vibration on piloted flying qualities is an open issue. This residual vibration could be reduced by lowering the loop gain (k_k), but the rigid pitch response quickness and damping is degraded. Given the extreme nature of the vehicle airframe and the associated flight control challenge, the final results appear to be reasonably successful.

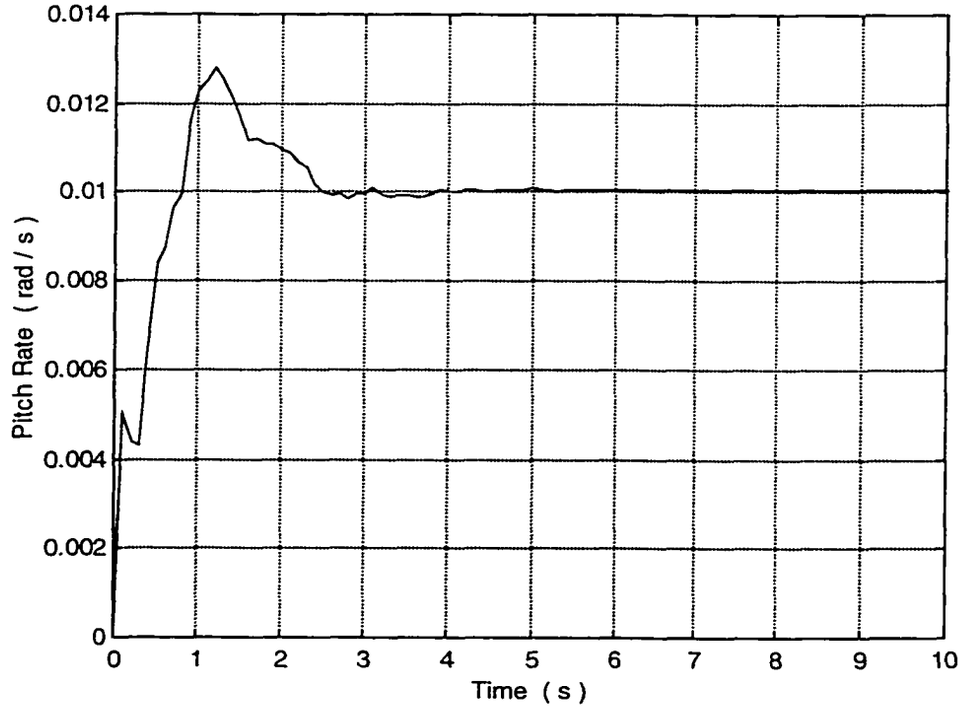

Figure 5.20 Step Response for x_{s1}=*823.7 in*, x_{s2}=*2,759.5 in* and c_1=*0.8*

CHAPTER 6

OPTIMAL SENSOR PLACEMENT: GAIN-PHASE STABILIZATION

6.1 Introduction

In Chapter 4, objective functions based on dipole magnitude are minimized to obtain optimal sensor positions, while in Chapter 5 other objective functions based on complementary departure angle are minimized to find optimal positions of the sensors. This chapter deals with computing optimal sensor locations using mixed gain and phase stabilization objectives. The cost function will be based on the complementary departure angle, as well as the dipole magnitude. The goal of utilizing this cost function is to improve the stability and performance of the control system by minimizing the complementary departure angles for critical aeroelastic modes, as well as degrading the influences of key aeroelastic modes by minimizing the dipole magnitude values. The general form of the cost function utilized in this chapter, based on dipole magnitude and complementary departure angle with inequality constraints, can be written as

$$H = \sum_{i=1}^{18} w_{\mu_i} \mu_i + \sum_{i=1}^{18} w_{\phi_i} \phi_i + \sum_{i=1}^{22} \lambda_i F_i \tag{6.1}$$

where w_{μ_i} and w_{ϕ_i} refer to weighting factors for the dipole magnitude and complementary departure angle costs, respectively, for the i^{th} mode.

Considering the first and third aeroelastic modes are the critical modes in the control system design, the only nonzero weights in Equation (6.1) will be

w_{μ_1}, w_{μ_2}, w_{ϕ_1} and w_{ϕ_2}. This selection is based on knowledge obtained during manual sensor placement efforts. The solution strategy is to start with simple blend filters and progress to more advanced blending logic (and hence more design freedom) when necessary. Static and dynamic filters with fixed parameters, as well as variable parameters, will be considered. Weighting factors are selected based on relative dipole magnitude values, as well as complementary departure angle values, and are refined to tailor the solution results. Different initial positions for sensor locations will also be tested and used for solution refinement. Primarily for rigid-body pitch tailoring, it has been found in Chapter 4-5 that the compensator parameter is best chosen as z_k=2 *rad/s* when the cost function based on complementary departure angle is used, while a selection of z_k=1 *rad/s* is most appropriate when the cost function based on dipole magnitude is used. Therefore, different compensation parameter values are also used for solution refinement. Also, additional optimization cases with a variable compensator parameter, in addition to variable sensor locations, will be considered. In these cases, several types of blending strategies are considered. For the most desirable sensor placement solutions, the time responses and general behavior of the closed-loop system will be tested and evaluated.

6.2 Sensor Placement with Fixed Static Blending

In this section, optimal gyro placement corresponding to the flight control system architecture shown in Figure 2.20 is investigated. Optimization parameters are the two gyro locations x_{s1} and x_{s2}. The blending filters in the feedback signals will be considered

constant, static values equal to one for each filter. The static filters can be represented by the following expressions.

$$h_1(s) = 1 \tag{6.2}$$

$$h_2(s) = 1 \tag{6.3}$$

The fixed static filters in both Equations (6.2) and (6.3) express the simplest blending logic. These filters represent spectrally uniform and equally balanced blending. The procedure for finding the optimal sensor locations depends on the initial sensor positions used in the optimal search strategy. From Figure 3.9 and Figure 3.10, as well as from manual placement experience, candidate initial sensor locations can be determined. The weighting factors of the cost function terms are initially assigned equal to one. Based on the optimization results, these values will be adjusted in order to find desirable solutions satisfying the system requirements. If the solution characteristics are unsatisfactory, other dipole magnitude or departure angle terms will be added to the cost function with appropriate weighting factors, or other initial sensor locations will be sought dependent on the evaluation of the optimization results.

Two different compensator parameter values are investigated using the mixed cost function optimization strategy. The first case considers the Equation (2.41) compensator with z_k=*2 rad/s*. For this case, the sensors initially will be placed at x_{s1}=*850 in* and x_{s2}=*2,750 in* and Figure 5.1 shows the corresponding baseline root locus plot. The optimization algorithm is applied to the augmented cost function represented in Equation (6.4) using w_{μ_1}=*1 s/rad*, w_{μ_3}=*1 s/rad*, w_{ϕ_1}=*1 1/deg* and w_{ϕ_3}=*1 1/deg*.

$$H = w_{\mu_1}\mu_1 + w_{\mu_3}\mu_3 + w_{\phi_1}\phi_1 + w_{\phi_3}\phi_3 + \sum_{i=1}^{22} \lambda_i F_i \tag{6.4}$$

Results indicate the optimal sensor positions are found at x_{s1}=*907.4 in* and x_{s2}=*2,934.6 in*.

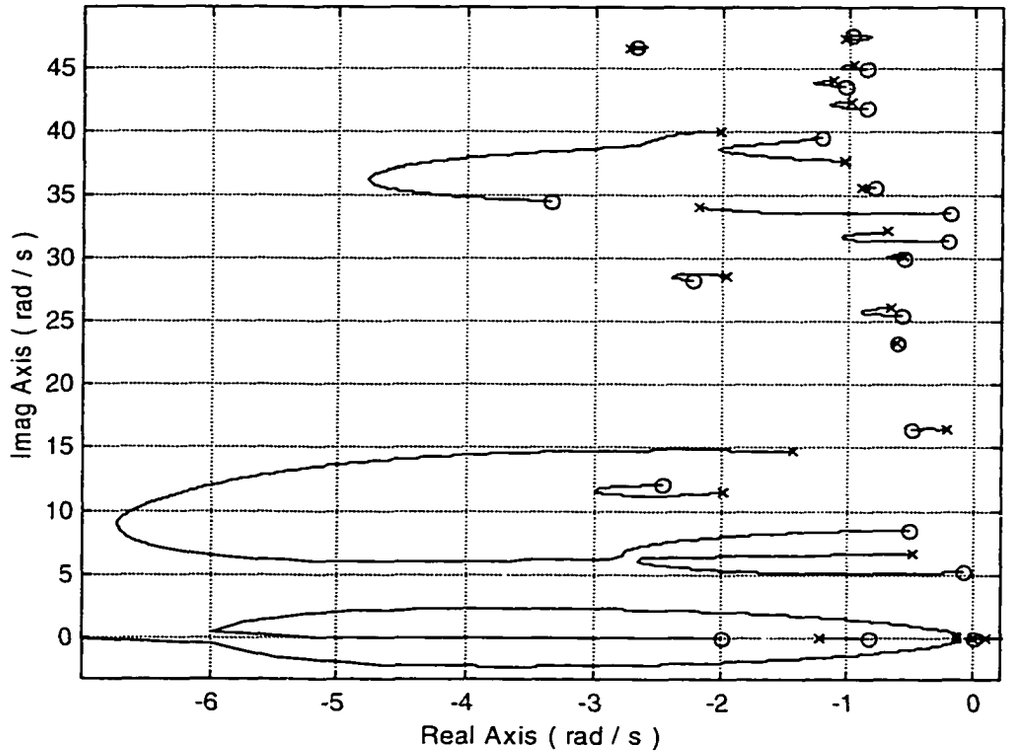

Figure 6.1 Root Locus Plot for x_{s1}=*907.4 in* and x_{s2} =*2,934.6 in*

Figure 6.1 shows the root locus plot when the sensors are placed at the optimal locations. It is noticed from this plot that acceptable rigid body augmentation, as well as stable aeroelastic modes, are achieved. Comparing this plot with the plot in Figure 5.1, stability of the 10^{th} aeroelastic mode is achieved without updating the weighting factor values (as required in Chapter 5, Figure 5.3). It is noticed from the root locus plot in Figure 6.1 that the complementary departure angle of the first mode is decreased from *46.116 deg* to *0.0004 deg* but the complementary departure angle of the third mode is increased from *5.714 deg* to *6.3282 deg*. Also it is noticed that the dipole magnitude

value of the third mode is decreased from *6.6176 rad/s* to *6.2487 rad/s* but the dipole magnitude value of the first mode is increased from *0.7487 rad/s* to *1.4344 rad/s*. Comparing Figure 6.1 with Figure 5.3, it is obvious that both optimal sensor location results are close (x_{s1}=*907.4-903.4 in* and x_{s2} =*2,934.6-2,937.2 in*). Figure 6.2 shows the total cost function value versus the number of iterations, while Figure 6.3 shows the positions of both sensors during iteration.

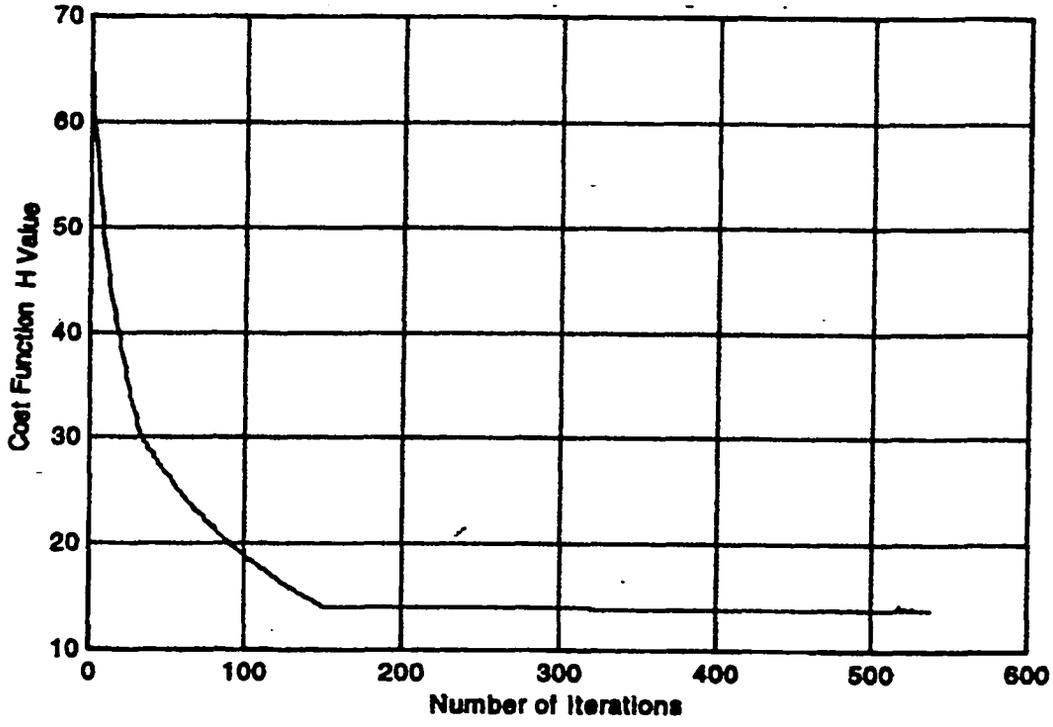

Figure 6.2 Cost Function History for x_{s1}=*907.4 in* and x_{s2} =*2,934.6 in*

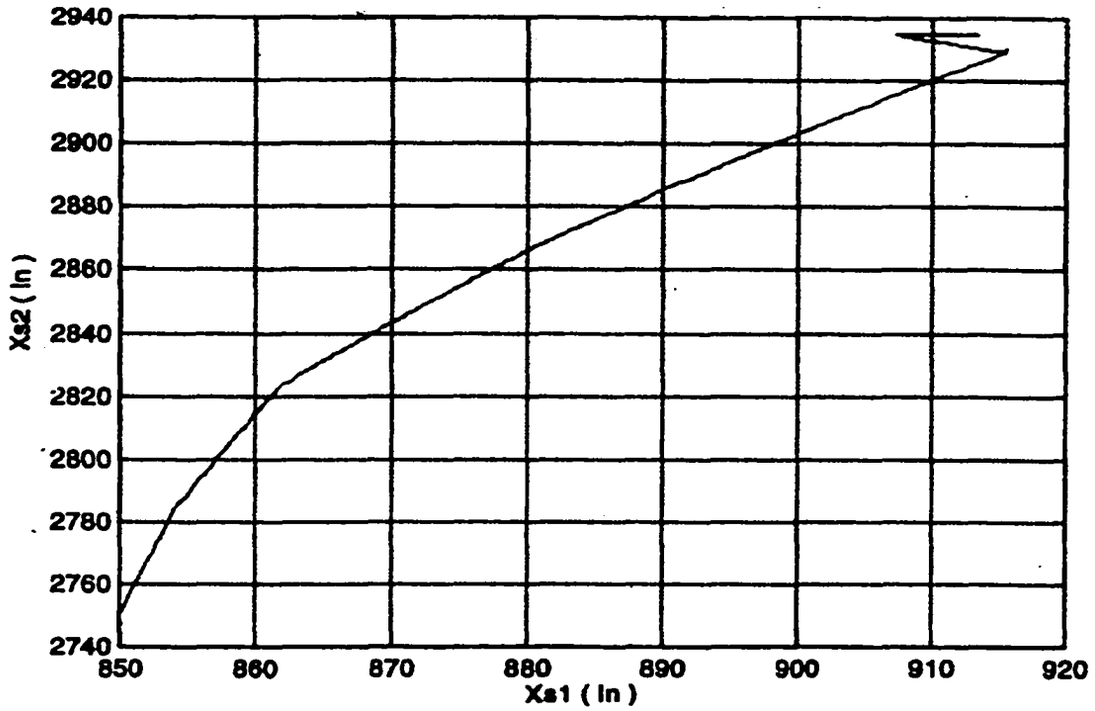

Figure 6.3 Sensor Position History for x_{s1}=*907.4 in* and x_{s2} =*2,934.6 in*

Another case is investigated with compensator parameter specified as z_k=*1 rad/s*. Also, different initial sensor positions are nearly considered. The new sensor locations are x_{s1}=*2,100 in* and x_{s2}=*2,950 in*. These values are nearly consistent with Figure 4.6 in Chapter 4. Applying the optimization algorithm on Equation (6.4) using w_{μ_1}=*5 s/rad*, w_{μ_3} =*1 s/rad*, w_{ϕ_1} =*0.1 1/deg* and w_{ϕ_3} =*0.1 1/deg* as weighting factors results in the solution x_{s1}=*2,222.1 in* and x_{s2}=*2,671.1 in*. The root locus plot for the flight control system when the sensors are placed in the optimal positions is shown in Figure 6.4. It is noticed from this plot that all aeroelastic modes have minimum phase zeros. Nevertheless, aeroelastic mode *13* is unstable for an intermediate range of gain values. Comparing with all previous results in Chapters 4, 5, and 6, this is the first case where the

dipole magnitude values as well as departure angles of the most critical aeroelastic modes are reduced simultaneously. Both the dipole magnitude values as well as the complementary departure angle values of both modes *1* and *3* are decreased relative to their initial values. The complementary departure angle of the first mode is decreased from *3.8119 deg* to *2.6283 deg* while the complementary departure angle of the third mode is decreased from *8.1095 deg* to *0.0050 deg*. Also, the dipole magnitude value decreased from *2.6940 rad/s* to *2.4434 rad/s* for the first mode and from *1.7258 rad/s* to *0.0457 rad/s* for the third mode. Note that applying the optimization tool to Equation (6.4) does not require implementing an additional cost term for the 10^{th} aeroelastic mode (see Figures 4.6, 4.7 and 4.8, and note x_{s1}=*2,900 in* rather than *2,950 in*). Figures 6.5 and 6.6 show the cost function values as a function of the iteration number and sensor position tracks, respectively.

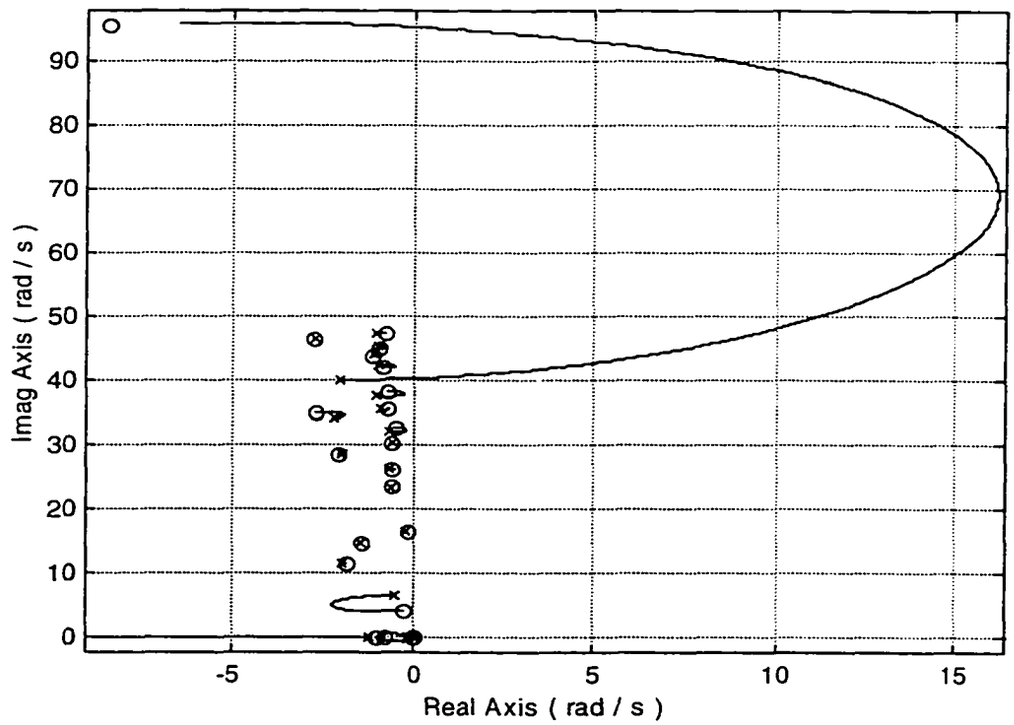

Figure 6.4 Root Locus Plot for x_{s1}=*2,222.1 in* and x_{s2}=*2,671.1 in*

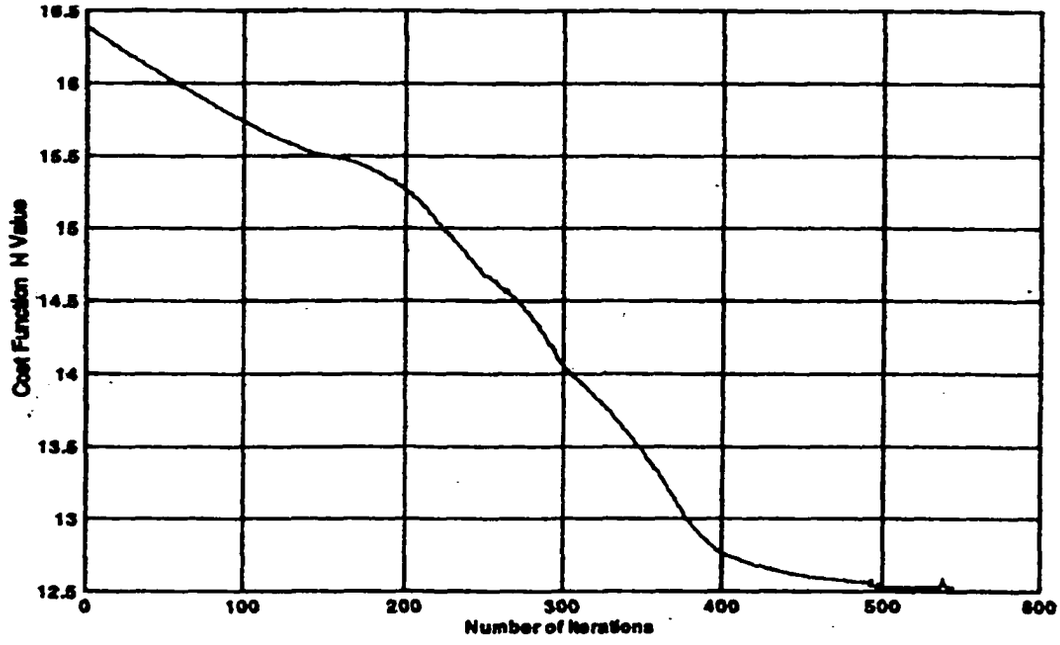

Figure 6.5 Cost Function History for x_{s1}=2,222.1 *in* and x_{s2}=2,671.1 *in*

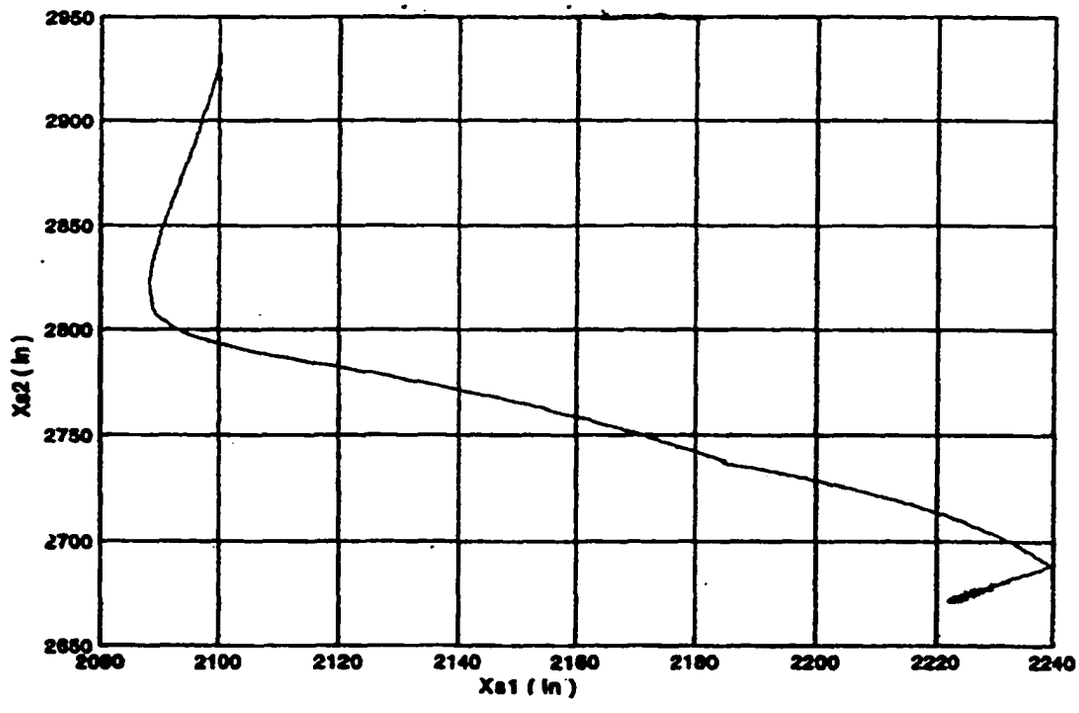

Figure 6.6 Sensor Position History for x_{s1}=2,222.1 *in* and x_{s2}=2,671.1 *in*

6.3 Sensor Placement with Variable Static Blending

In this section, optimal gyro placement corresponding to the system in Figure 2.20 is again considered. The feedback blending filters will be considered as variable, static values. Based on the ability to shift loop gain between k_k and h_1-h_2 in Equation (2.43) and Figure 2.20, there is no loss of generality if one filter is held fixed and the other allowed to vary. Here, the static gain parameter of the first filter will be considered variable, while the parameter value of the second filter will be considered constant (unity). The static filters can be expressed as

$$h_1(s) = c_1 \tag{6.5}$$

$$h_2(s) = 1 \tag{6.6}$$

The variable static filter structure in Equations (6.5)-(6.6) introduces the next level of design freedom beyond that considered in Section 6.2. The filters here represent spectrally uniform but unbalanced blending. Optimization parameters here include the two gyro locations x_{s1} and x_{s2} and the filter parameter c_1. To avoid unexpected exploitation by the optimizer, the variable filter parameter will be constrained to lie within certain bounds. Thus, introduce two additional constraints

$$F_{23} = c_1 - \overline{c_1} \le 0 \tag{6.7}$$

$$F_{24} = \underline{c_1} - c_1 \le 0 \tag{6.8}$$

where $\overline{c_1}$ and $\underline{c_1}$ denote upper and lower bounds on c_1. The numerical algorithm is run with $\underline{c_1} = 0.1$ and $\overline{c_1} = 10$.

As in Section 6.2, two different fixed dynamic compensaters are considered and include z_k=*1 rad/s* or z_k=*2 rad/s*. In the first case, the sensors are initially placed at

x_{s1}=*850 in* and x_{s2}=*2,750 in*, while the variable static blend filter is given an initial value c_1=*5*. The compensator lead parameter is considered to have constant value z_k=*2 rad/s*. These values are consistent with Section 5.3. The corresponding root locus plot was previously shown in Figure 5.6. The optimization algorithm is applied on Equation (6.4) with weighting factors w_{μ_1}=*5 s/rad*, w_{μ_1}=*5 s/rad*, w_{ϕ_1}=*1 1/deg* and w_{ϕ_1}=*1 1/deg*. The optimization solution is x_{s1}=*821.6 in* and x_{s2}=*2,757.9 in*, while the optimal value of the variable blend filter is c_1=*0.8*. Figure 6.7 shows the root locus plot when the optimal results are implemented in the flight control system.

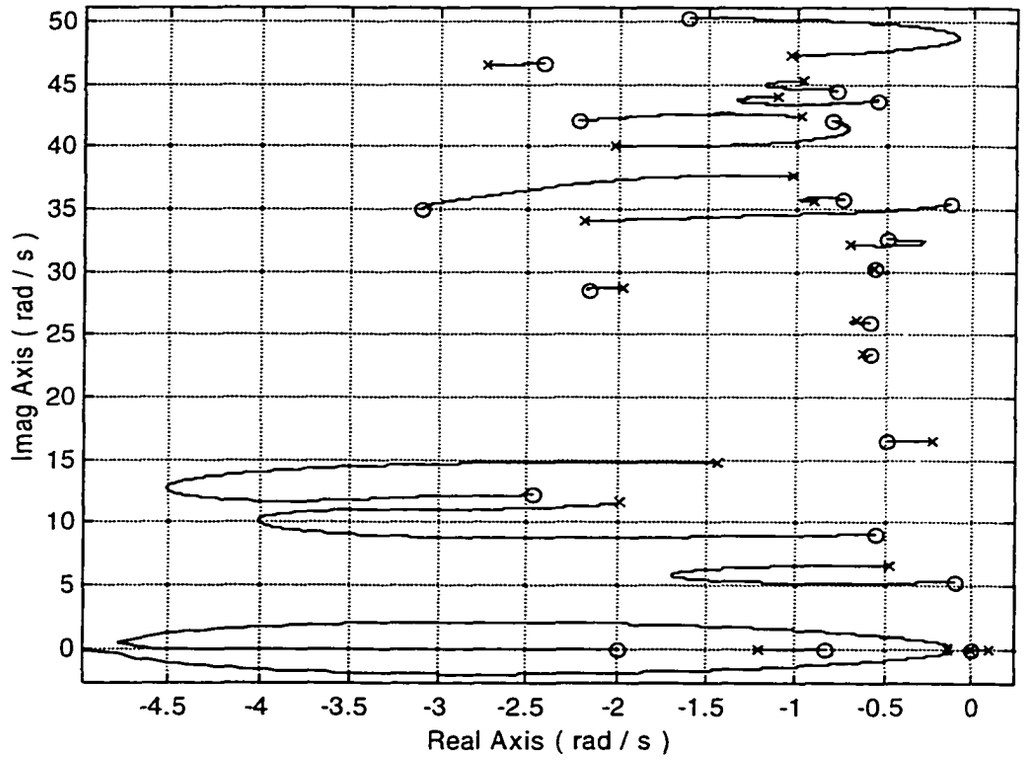

Figure 6.7 Root Locus Plot for x_{s1}=*821.6 in*, x_{s2}=*2,757.9 in* and c_1=*0.8*

It is clear by comparing this figure with Figure 5.7 that the two optimal results are highly similar with approximately the same sensor placements and blend filter parameters. The complementary departure angle for the 1^{st} aeroelastic mode decreased to *0.0083 deg* compared with *0.5664 deg* in Figure 5.7, while the complementary departure angle for the 3^{rd} aeroelastic mode decreased to *5.6986 deg* compared with *5.7133 deg*, but it is increased relative to the initial value (*5.1238 deg*). In an absolute sense, the complementary departure angle for mode *1* is significantly decreased from *160.5048 deg* (see Figure 5.6) to *0.0083 deg*. Comparing with the initial values, the dipole magnitude value for the 1^{st} aeroelastic mode is decreased from *6.6061 rad/s* to *1.3947 rad/s*, while the dipole magnitude value for the 3^{rd} aeroelastic mode is decreased from *10.0313 rad/s* to *2.8162 rad/s*.

In the second case, the parameter of the forward path dynamic compensator is considered to have constant value of z_k=*1 rad/s*. The sensors are initially placed at x_{s1}=*2,100 in* and x_{s2}=*2,950 in*, while the variable static blend filter is considered to have an initial value of c_1=*5*. This condition is consistent with Section 4.3 and Figure 4.12. Optimization is applied to Equation (6.4). Solution results indicate that optimization failed to find optimal sensor locations at which either all aeroelastic modes are stable for all gain values or the rigid-body mode is augmented appropriately. Changing the weighting factor values does not lead to a desirable solution. For example, the optimization procedure is applied to the augmented cost function using w_{μ_1}=*5 s/rad*, w_{μ_1}=*5 s/rad*, w_{ϕ_1}=*1 1/deg* and w_{ϕ_1}=*1 1/deg* as weighting factors. Figure 6.8 illustrates the root locus plot when the sensors are placed at the solution result x_{s1}=*2,472.4 in* and x_{s2}=*2,966.1 in* and with c_1=*3.3*. Note the troublesome mode *14*.

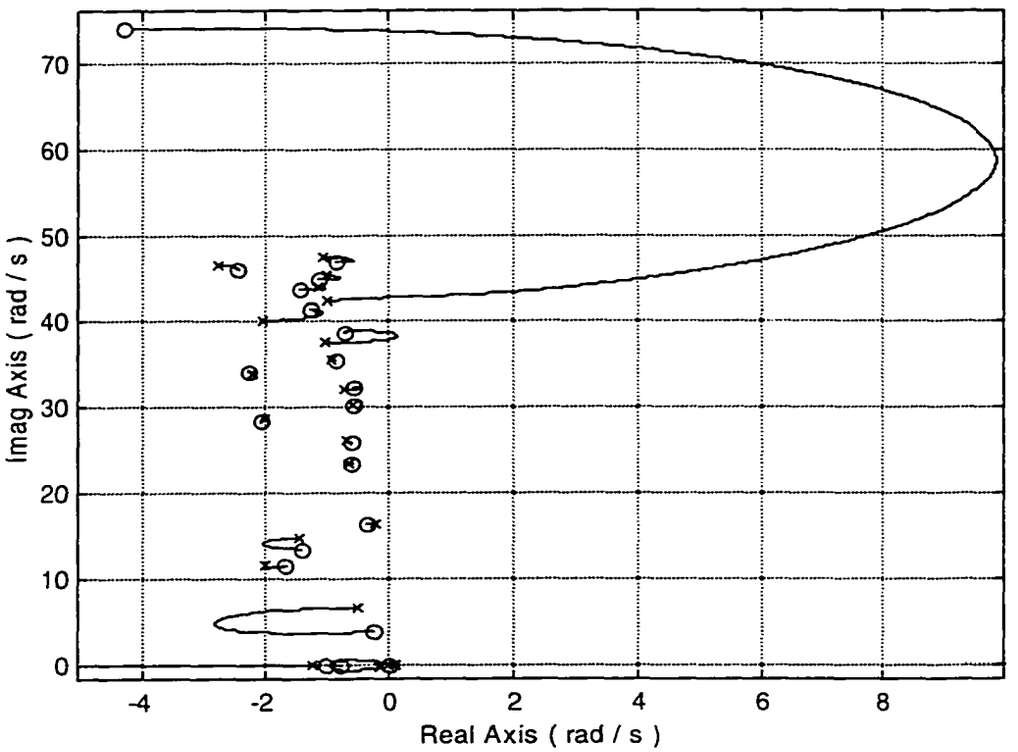

Figure 6.8 Root Locus Plot for x_{s1}=2,472.4 *in*, x_{s2}=2,966.1 *in* and c_1=3.3

6.4 Sensor Placement with Fixed Dynamic Blending

The static filters from Section 6.3 in the feedback paths of the flight control system shown in Figure 2.20 are replaced by low and high pass dynamic filters. The structure of these filters are shown in Figure 4.18 and Equations (4.13)-(4.14), where the filter parameters are a=3 *rad/s*, c_1=1 and c_2=7. Two different initial placements of the sensors along with two different compensator parameter values are investigated. First, consider the sensors initially located at x_{s1}=850 *in* and x_{s2}=2,750 *in*, while the compensator parameter is z_k=2 *rad/s*. The root locus for this flight control system is illustrated in Figure 5.10. The optimization results due to applying the search tool on

Equation (6.4) with weighting factors $w_{\mu_1} = w_{\mu_2} = 1$ *s/rad*, and $w_{\phi_1} = w_{\phi_2} = 1$ *1/deg* reveals the optimal sensor placements are x_{s1}=*623.2 in* and x_{s2}=*2,843.3 in*. Note using the augmented mixed cost function based on both complementary departure angle and dipole magnitude leads to similar results as in the purely phase stabilization cost function for the same conditions (see Figure 5.11). Figure 6.9 shows the root locus plot for the mixed optimal solution found here.

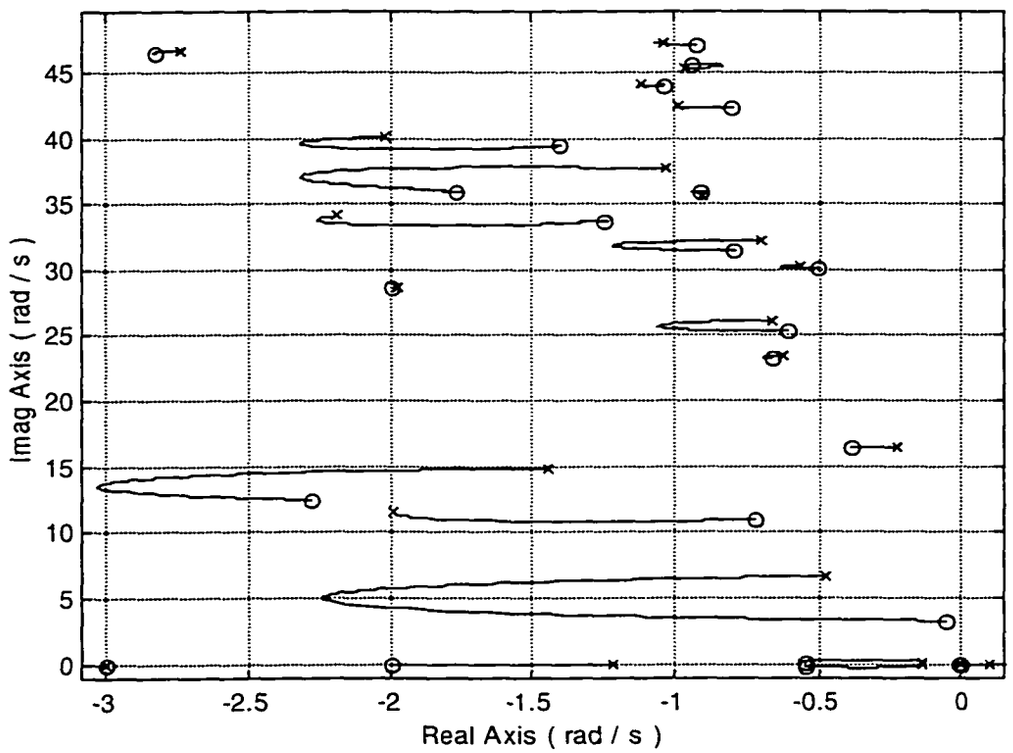

Figure 6.9 Root Locus Plot for x_{s1}=*623.2 in* and x_{s2}=*2,843.3 in*

Comparing this figure with Figure 5.10, observe the complementary departure angle for the 1^{st} mode is slightly decreased from *14.7506 deg* to *13.7839 deg* while the complementary departure angle for the 3^{rd} mode is slightly decreased from *3.5290 deg* to *3.1491 deg*. Also, the dipole magnitude value for the 1^{st} mode is slightly decreased from

3.3947 to *3.2523 rad/s*, while the dipole magnitude value for the 3^{rd} aeroelastic mode is increased from *2.3472* to *2.5206 rad/s*. Figure 6.10 and 6.11 show the augmented cost function value at each optimization iteration and the track of sensor positions during the search, respectively. Note the similarity to Figures 5.12-5.13.

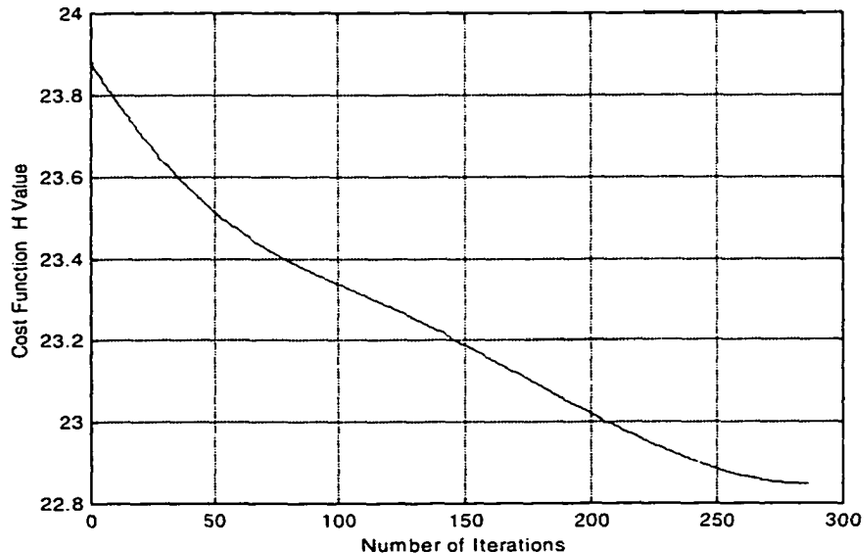

Figure 6.10 Cost Function History for x_{s1}=*623.2 in* and x_{s2}=*2,843.3 in*

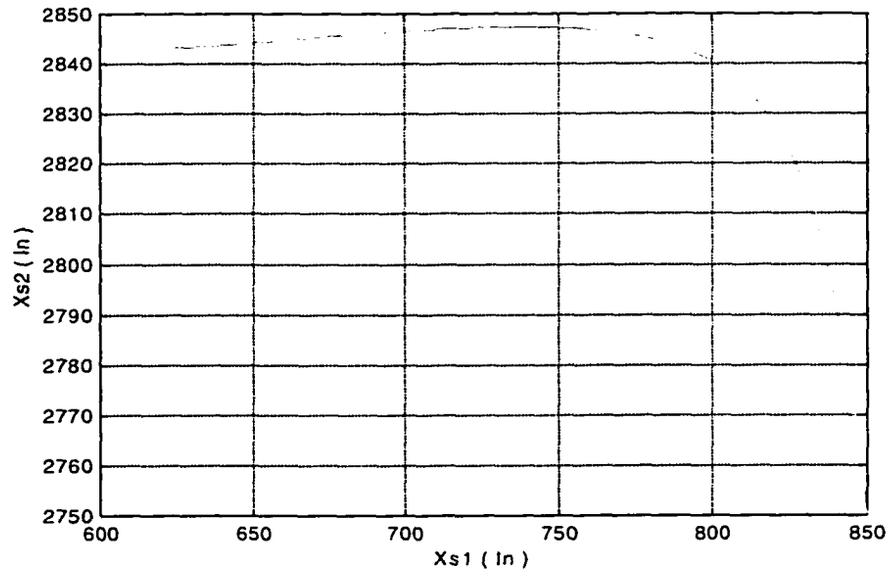

Figure 6.11 Sensor Position History for x_{s1}=*623.2 in* and x_{s2}=*2,843.3 in*

Consider now the sensors initially placed in different locations. The new locations are x_{s1}=*2,100 in* and x_{s2}=*2,950 in*, while the new value for the compensator parameter is z_k=*1 rad/s*. The flight control system root locus with these new values is outlined in Figure 4.20. By applying optimization to the augmented cost function in Equation (6.4) while considering $w_{\mu_1} = w_{\mu_4} = 1$ *s/rad*, and $w_{\phi_1} = w_{\phi_4} = 1$ *1/deg* as weighting factors, solution results x_{s1}=*3,186 in* and x_{s2}=*2,583.6 in* are generated. Figures 6.12a and 6.12b show the optimal root locus plot. Comparing this figure with Figure 4.20, it is clear the complementary departure angle values and dipole magnitude values for both modes *1* and *3* decreased simultaneously relative to the initial values. The complementary departure angle for the 1^{st} mode is decreased from *18.3969 deg* to *15.0552 deg*. For the 3^{rd} mode, it decreased from *9.9272 deg* to *5.9625 deg*. Also, the dipole magnitude value for the 1^{st} mode is slightly decreased from *3.5055* to *2.8291 rad/s*, while for the 3^{rd} mode it decreased from *2.6642* to *1.3322 rad/s*. Note using the mixed augmented cost function based on both complementary departure angle and dipole magnitude leads to a uniquely different result than with the purely gain stabilization augmented cost function (see Figure 4.21). Examination of the root locus plot in Figure 6.12 shows the aeroelastic mode *14* is unstable for a medium range of gain values. Both aeroelastic mode *1* and *3* are well gain stabilized, and have acceptable complementary departure angles. Figure 6.13 illustrates the augmented cost function values for each iteration, while Figure 6.14 shows the track of sensor locations during the search.

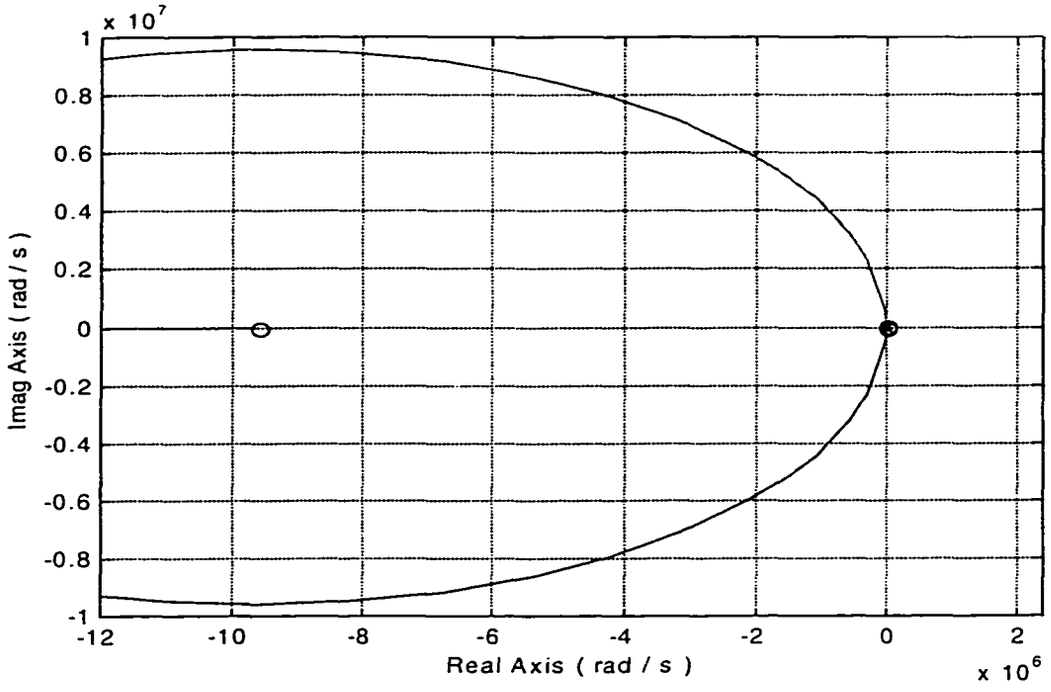

Figure 6.12a Root Locus Plot for x_{s1}=*3,186 in* and x_{s2}=*2,583.6 in*

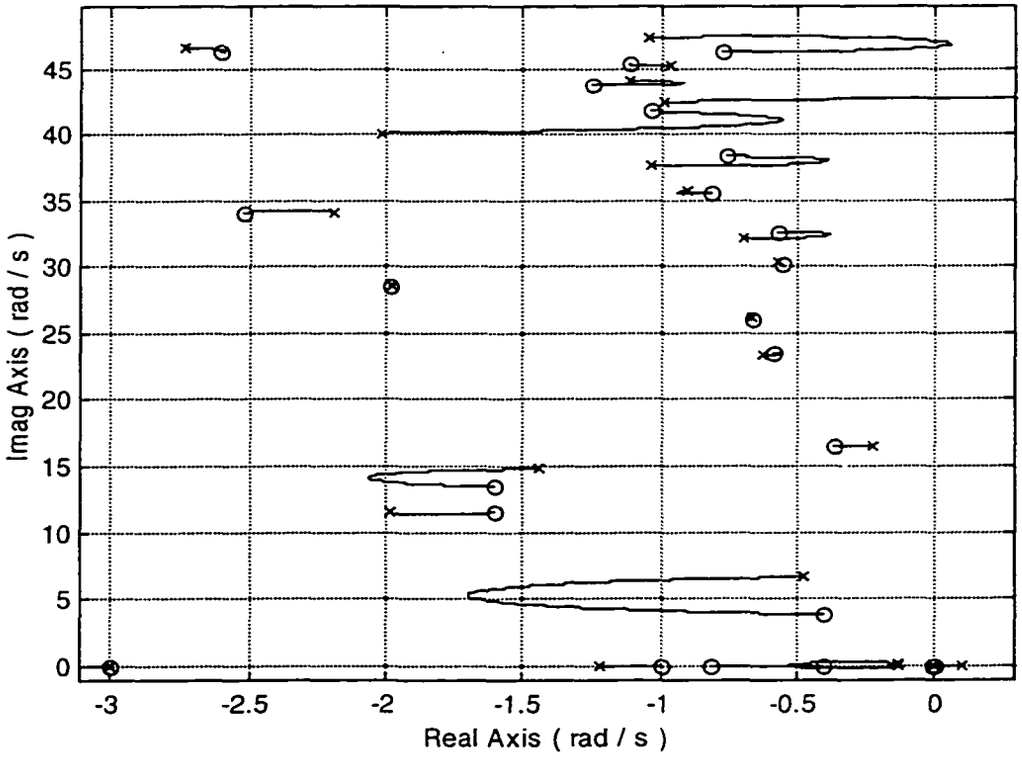

Figure 6.12b Root Locus Plot for x_{s1}=*3,186 in* and x_{s2}=*2,583.6 in*

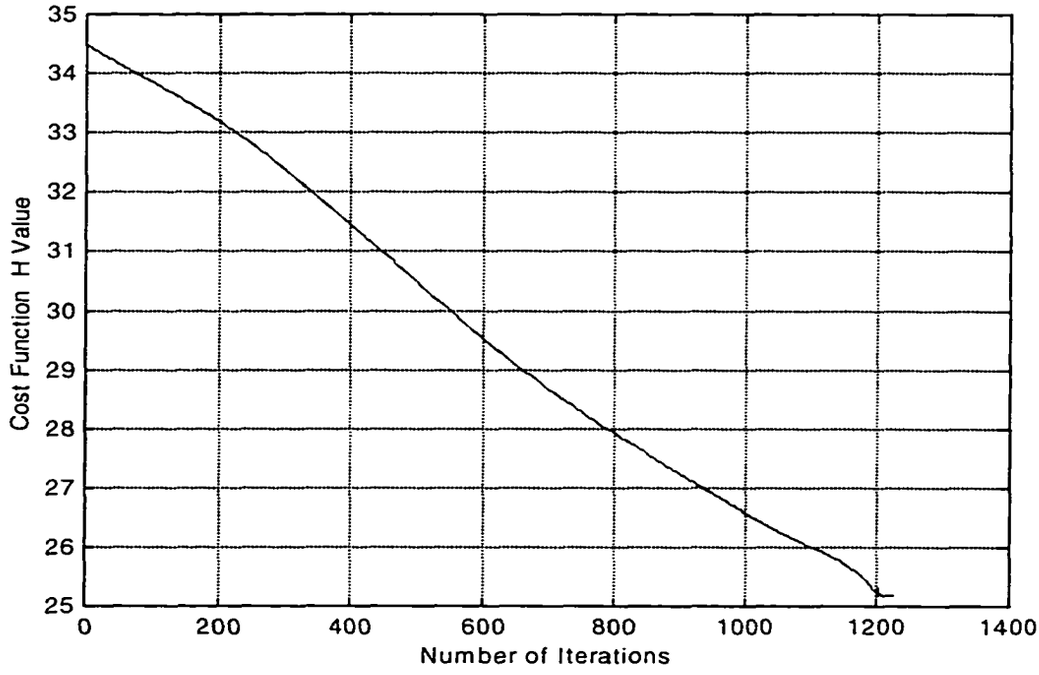

Figure 6.13 Cost Function History for x_{s1}=3,186 *in* and x_{s2}=2,583.6 *in*

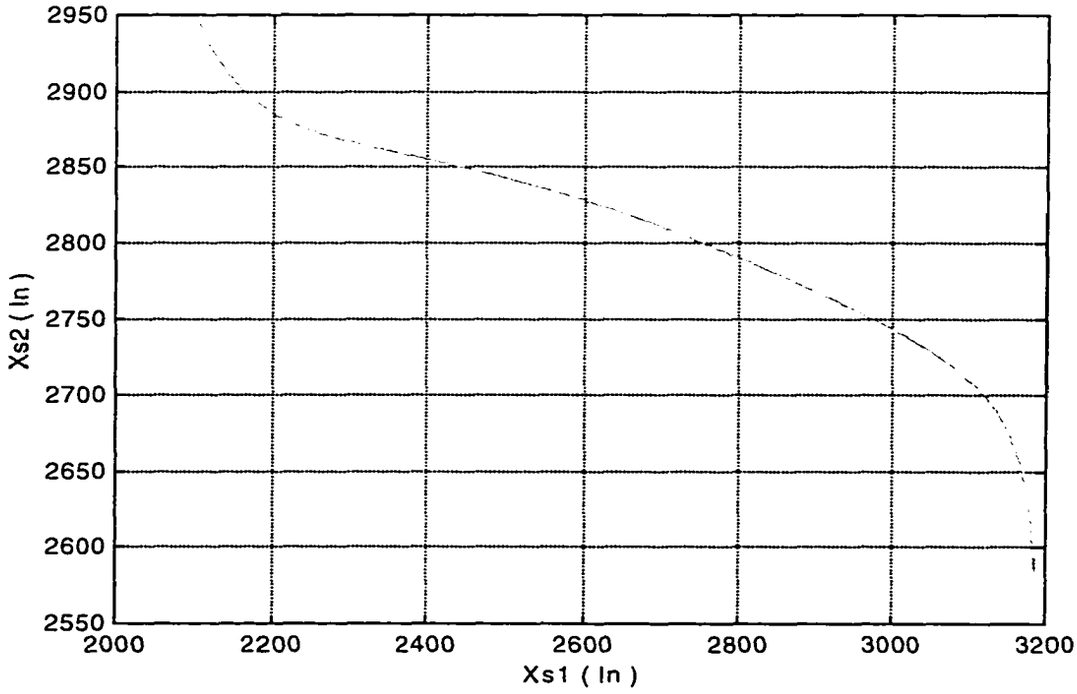

Figure 6.14 Sensor Position History for x_{s1}=3,186 *in* and x_{s2}=2,583.6 *in*

6.5 Sensor Placement with Variable Dynamic Blending

In this section, the low-high pass dynamic blend filters shown in Figure 4.18 and Equations (4.13)-(4.14) are considered with a variable parameter. This parameter is optimized in order to improve upon previous results in determining desirable sensor locations. The parameter a is considered variable during the optimization procedure, but it is bounded in the range between *0.1* and *10 rad/s*. The first filer gain is constant at $c_1=1$, while the second filter is variable with dependency on a according to $c_2=2a$. Two different initial placements of the sensors along with two different compensator parameter values are investigated. First, consider the sensors as initially located at $x_{s1}=850$ *in* and $x_{s2}=2,750$ *in*, while the blend filter parameter is $a=5$ *rad/s*. The compensator is characterized by $z_k=2$ *rad/s*. Figure 6.15 illustrates the root locus plot when these values are considered.

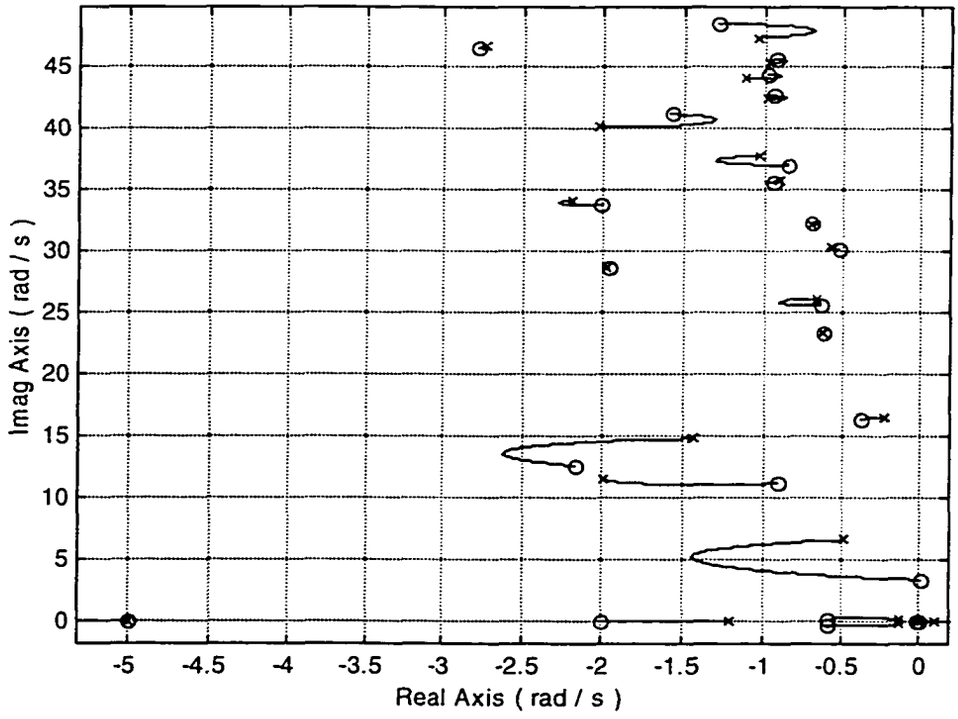

Figure 6.15 Root Locus Plot for $x_{s1}=850$ *in*, $x_{s2}=2,750$ *in* and $a=5$ *rad/s*

An optimization tool is applied on Equation (6.4) with appropriate weighting factors w_{μ_1} =3 *s/rad*, w_{μ_2} =1 *s/rad*, and w_{ϕ_1} = w_{ϕ_2} =1 *1/deg*. Optimization results indicate the optimal sensor locations are x_{s1}=850.1 *in* and x_{s2}=2,750.6 *in* and the optimal sensor parameter is *a=1.4 rad/s*. The flight control root locus plot when the optimal values are considered is shown in Figure 6.16. Comparing Figure 6.16 with Figure 6.15 reveals the complementary departure angle values for both modes *1* and *3* are decreased relative to the initial values, while the dipole magnitude value are slightly increased relatively to the initial values. Numerically, the complementary departure angle for the 1^{st} mode is decreased from *28.7960 deg* to *2.7255 deg* while the complementary departure angle for the 3^{rd} mode is decreased from *10.7864 deg* to *2.7493 deg*. Also, the dipole magnitude

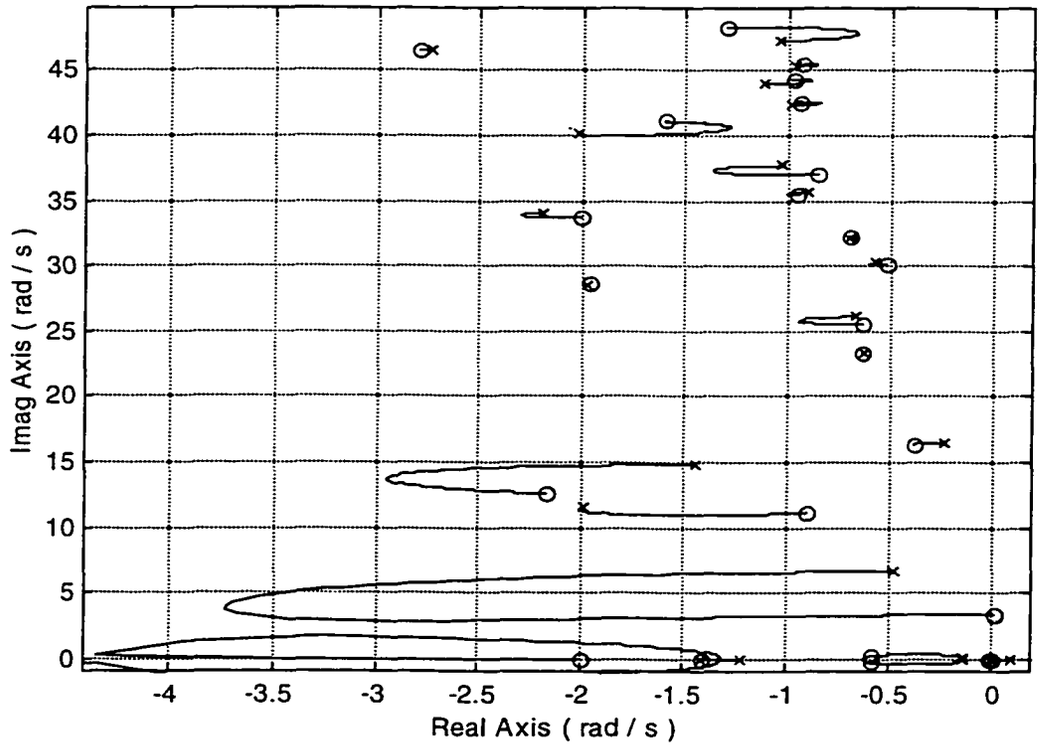

Figure 6.16 Root Locus Plot for x_{s1}=850.1 *in*, x_{s2}=2,750.6 *in* and *a=1.4 rad/s*

value for the 1^{st} mode is increased from *3.2592* to *3.2601 rad/s*, and from *2.3430* to *2.3444 rad/s* for the 3^{rd} mode. Note, the sensor locations do not move because the cost function slope corresponding to the filter parameter dominates over the other slopes. Figure 6.17 shows the augmented cost function at each iteration number.

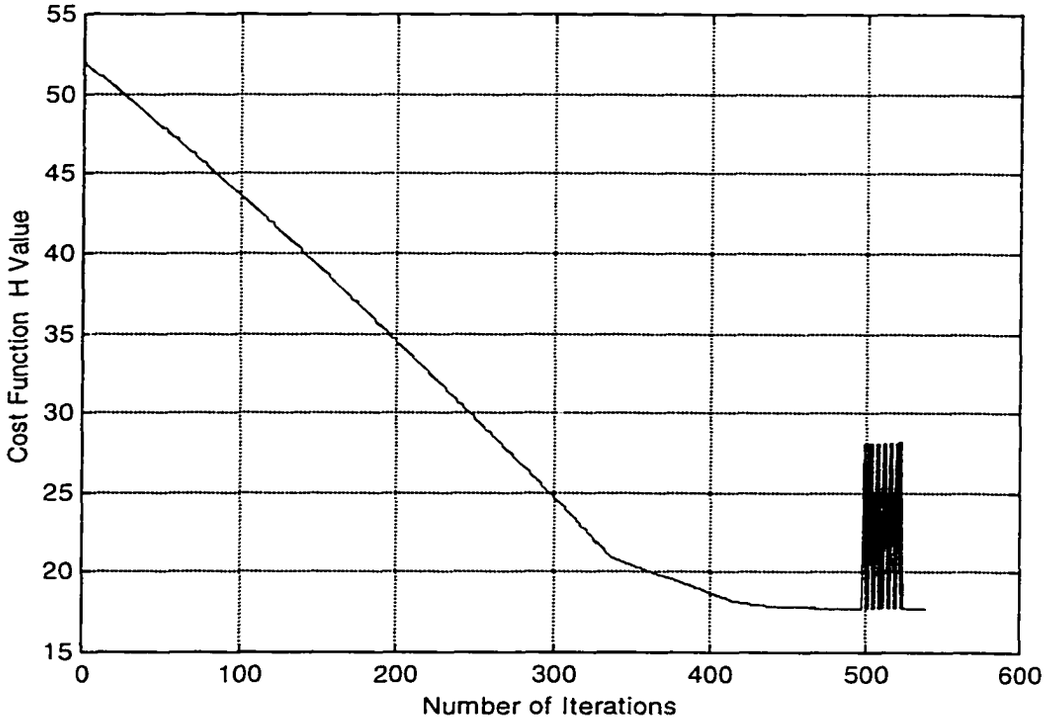

Figure 6.17 Cost Function History for x_{s1}=*850.1 in*, x_{s2}=*2,750.6 in* and a=*1.4 rad/s*

Different initial sensor locations are considered next, while the same initial filter parameter as in the previous case is assigned. The new locations are x_{s1}=*2,100 in* and x_{s2}=*2,950 in*. Considering the compensator parameter to have a value z_k=*1 rad/s*, the root locus of the flight control system using these values is illustrated in Figure 6.18. Applying an optimization tool on the augmented cost function with $w_{\mu_1} = w_{\mu_2}$ =*1 s/rad*,

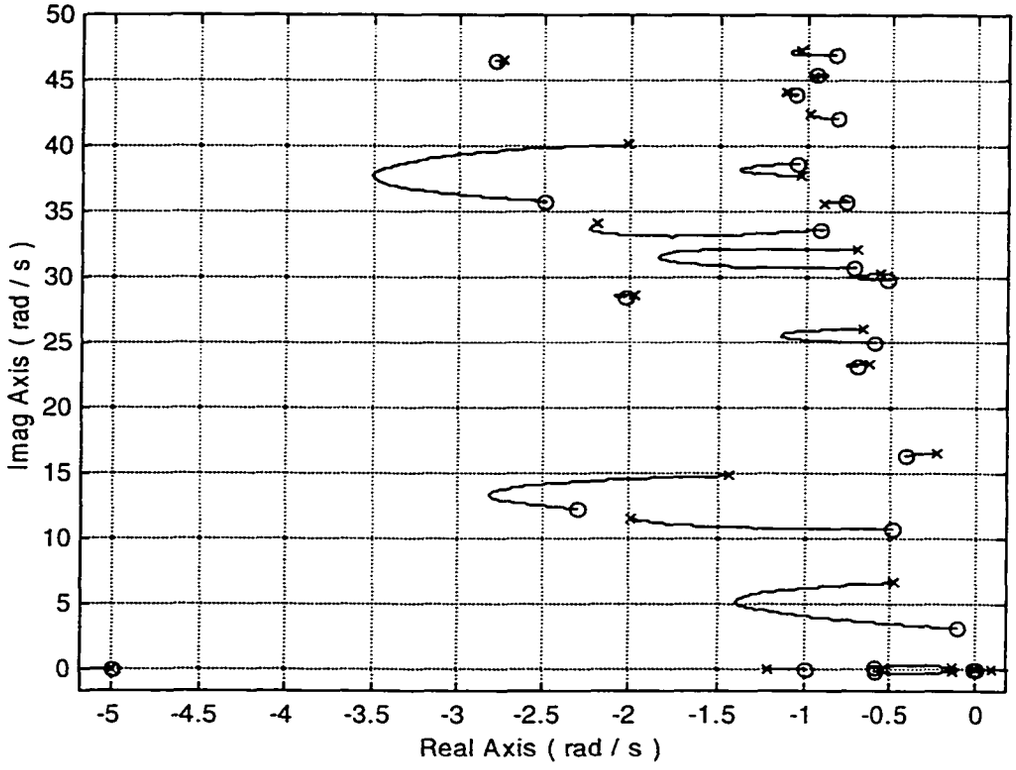

Figure 6.18 Root Locus Plot for x_{s1}=*2,100 in*, x_{s2}=*2,950 in* and *a=5 rad/s*

and $w_{\phi_1} = w_{\phi_2}$ =*1 1/deg* as weighting factors, the optimization results refer the optimal sensor locations are x_{s1}=*2,100.2 in* and x_{s2}=*2,949.8 in* while the optimal filter parameter is *a=1 rad/s*. Figure 6.19 outlines the root locus plot for these values. As in the previous case, the sensor locations do not move appreciably due to the higher cost surface slope for the filter parameter relative to the slopes corresponding to the sensor locations. Comparing Figure 6.19 with Figure 6.18 reveals that the complementary departure angle for the 1^{st} mode is decreased from *31.8005 deg* to *2.0523 deg* while the complementary departure angle for the 3^{rd} mode is decreased from *17.5824 deg* to *2.3762 deg*. Also, the dipole magnitude value for the 1^{st} mode is slightly decreased from *3.5066* to *3.5063*

rad/s, while the dipole magnitude for the 3^{rd} mode is also slightly decreased from *2.6654* to *2.6652 rad/s*. Figure 6.20 shows the cost function history.

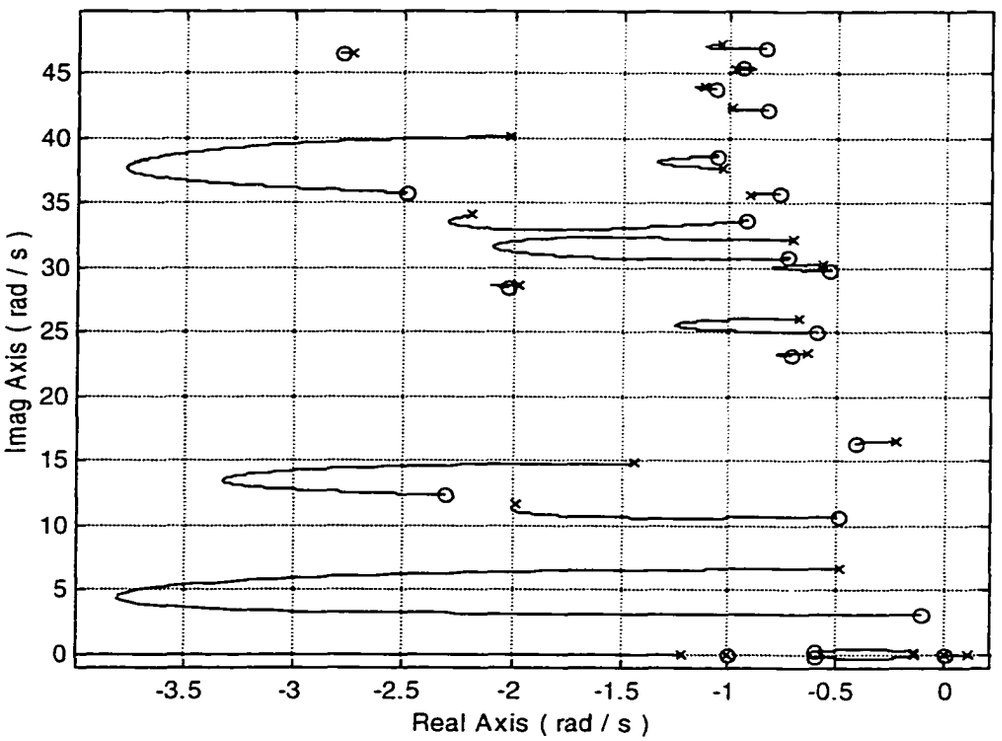

Figure 6.19 Root Locus Plot for x_{s1}=*2,100.2 in*, x_{s2}=*2,949.8 in* and *a=1 rad/s*

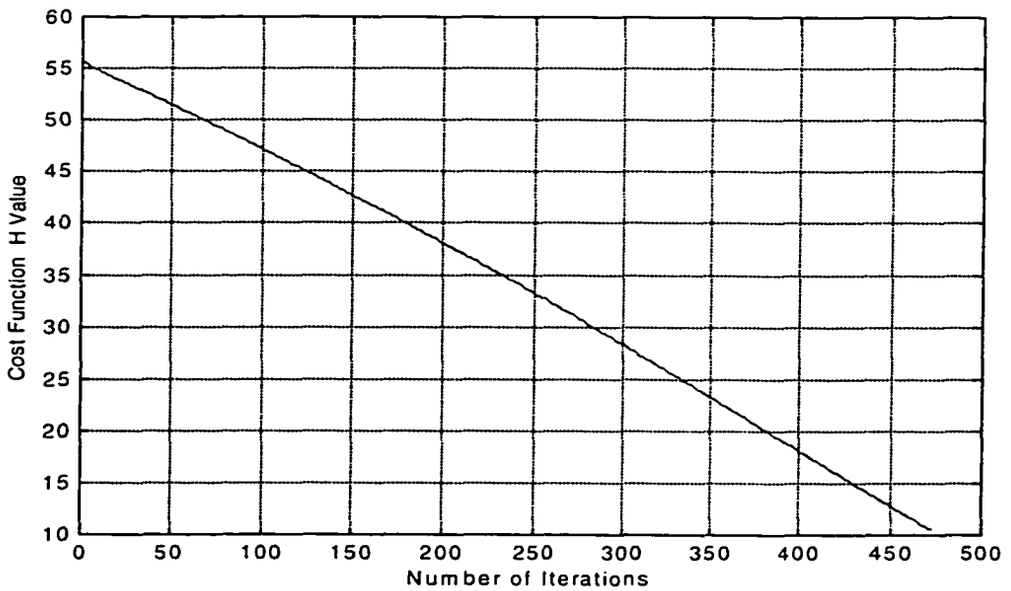

Figure 6.20 Cost Function History for x_{s1}=*2,100.2 in*, x_{s2}=*2,949.8 in* and *a=1 rad/s*

In general, using the augmented cost function based on both complementary departure angle and dipole magnitude to optimize the sensor locations, as well as the filter parameter, does not affect the dipole magnitude values of the critical aeroelastic modes. These modes are not being gain stabilized. However, the departure angle is influenced strongly in a beneficial manner.

6.6 Sensor Placement with Variable Dynamic Compensating

In this section, a new problem class not previously considered in this dissertation is addressed. Here, the forward path compensator parameter z_k used in the flight control system is optimized simultaneously with the sensor locations x_{s1} and x_{s2}. This problem class is considered because experience has shown that z_k can have a large influence on the characteristics of the rigid pitch mode and first aeroelastic mode, and their interaction. The compensator variable z_k is constrained in the range between *0.5* and *2.5 rad/s* with appropriate constraints appended to the cost function. Two types of fixed blending filters (static and low-high pass dynamic) are investigated, and different initial sensor placements are considered. An optimization algorithm is applied on the augmented cost function represented in Equation (6.4) using appropriate values for the weighting factors.

First of all, the fixed static blend filters represented in Equations (6.2)–(6.3) with unit parameter values will be considered. The investigation case is optimized by placing the sensors at initial locations such as at x_{s1}=*850 in* and x_{s2}=*2,750 in*. The initial value of the compensator variable is chosen equal to z_k=*1.5 rad/s*. Figure 6.21 illustrates the root locus plot when the initial values are considered. Note that both aeroelastic modes *1* and

10 have nonminimum phase zeros. This plot has similar characteristics as in Figures 4.1 and 5.1.

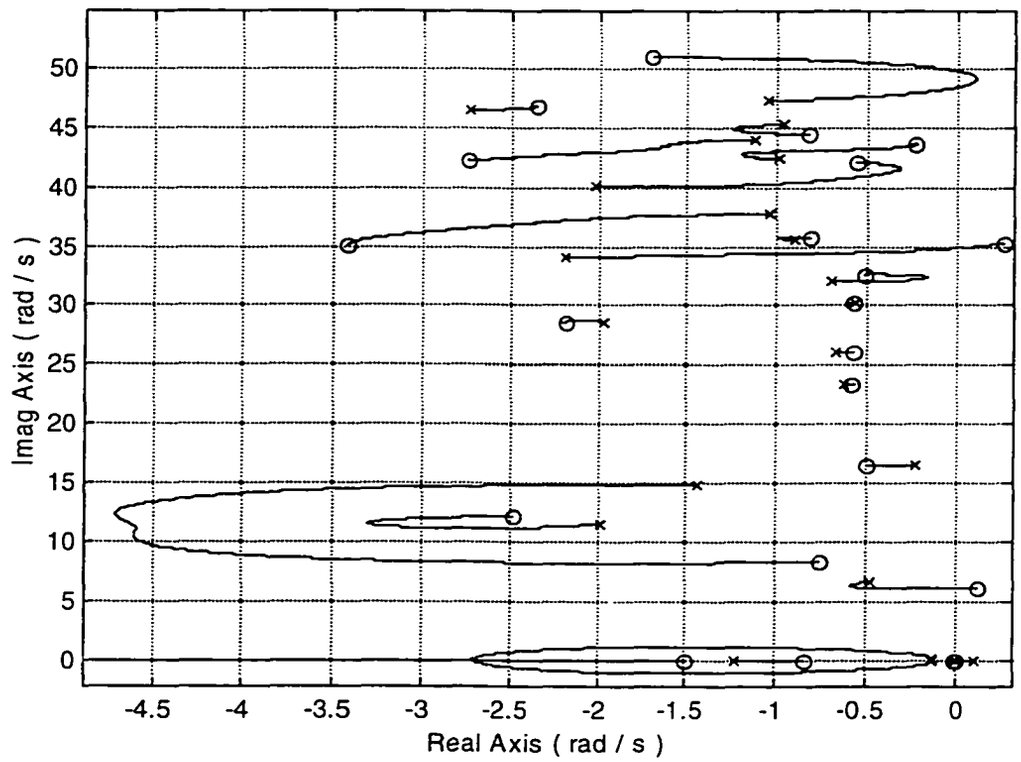

Figure 6.21 Root Locus Plot for x_{s1}=*850 in*, x_{s2}=*2,750 in* and z_k=*1.5 rad/s* (Static Blend)

The optimization algorithm is applied to the augmented cost function represented in Equation (6.4) with additional constraints for z_k. Appropriate values for the weighting factors are found to be w_{μ_1}=*5 s/rad*, w_{μ_3}=*10 s/rad*, w_{ϕ_1}=*1 1/deg*, and w_{ϕ_3}=*3 1/deg*. The optimization results are x_{s1}=*1,209.1 in*, x_{s2}=*3,003.8 in*, and z_k=*0.5 rad/s*. The root locus plot corresponding to these optimal results is shown in Figure 6.22. Comparing Figure 6.22 with 6.21 reveals that all constraint equations are satisfied. Both aeroelastic modes *1* and *3* are well phase stabilized. Also it is noticed that the complementay departure angles

of both modes *1* and *3* decreased from *50.2792 deg* to *3.4820 deg* and from *3.77795 deg* to *0.8198 deg*, respectively. The dipole magnitude of the third mode is decreased from *6.6176 rad/s* to *2.8464 rad/s*, but the dipole magnitude for the first mode is increased from *0.7487 rad/s* to *2.0865 rad/s*. Note with z_k=*0.5 rad/s*, the quickness of the rigid pitch motion is limited.

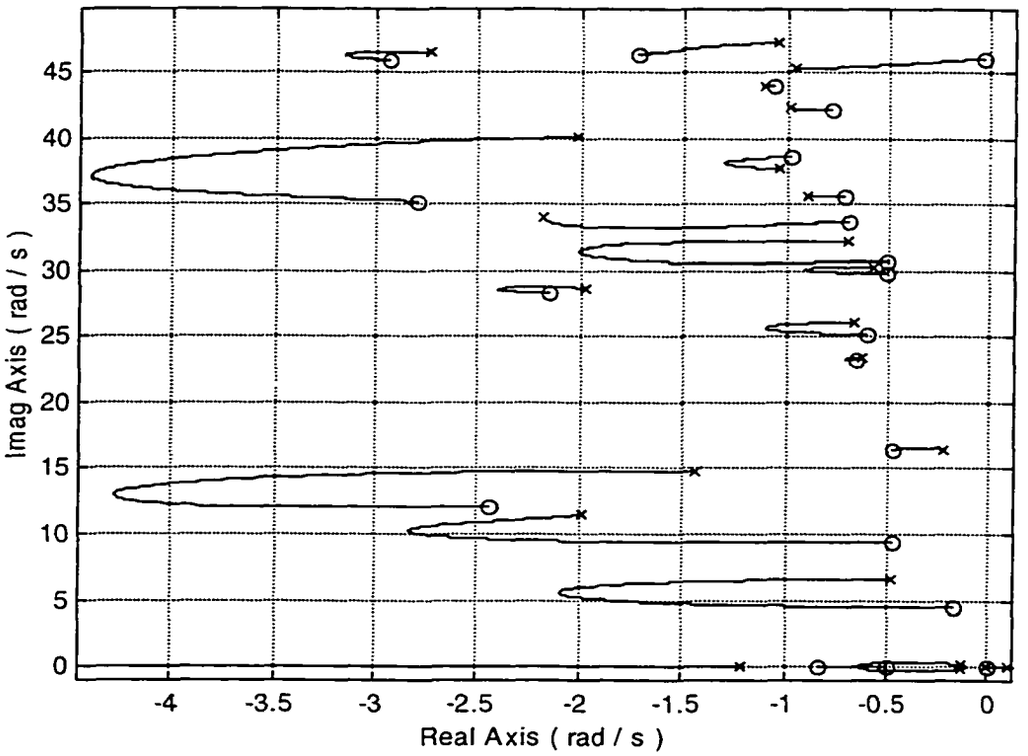

Figure 6.22 Root Locus Plot for x_{s1}=*1,209.1 in*, x_{s2}=*3,003.8 in* and z_k=*0.5 rad/s*

Another case is considered using different values for the sensor locations. The new initial sensor locations are x_{s1}=*2,100 in* and x_{s2}=*2,950 in*. The compensator parameter is again specified initially as z_k=*1.5 rad/s*. Figure 6.23 illustrates the root locus plot for the initial values. The optimization algorithm is again applied on Equation (6.4)

with z_k constraints added. Weight factors used in the solution are w_{μ_1}=5 *s/rad*, w_{μ_2} =1 *s/rad*, w_{ϕ_1} =0.1 *1/deg*, and w_{ϕ_2} =1 *1/deg*. Optimal sensor position solutions are x_{s1}=2,222.5 *in* and x_{s2}=2,673.2 *in*, while the optimal compensator solution is z_k=0.7 *rad/s*. The root locus plot with the sensors placed at the optimal locations and with the compensator at its optimal value is shown in Figure 6.24.

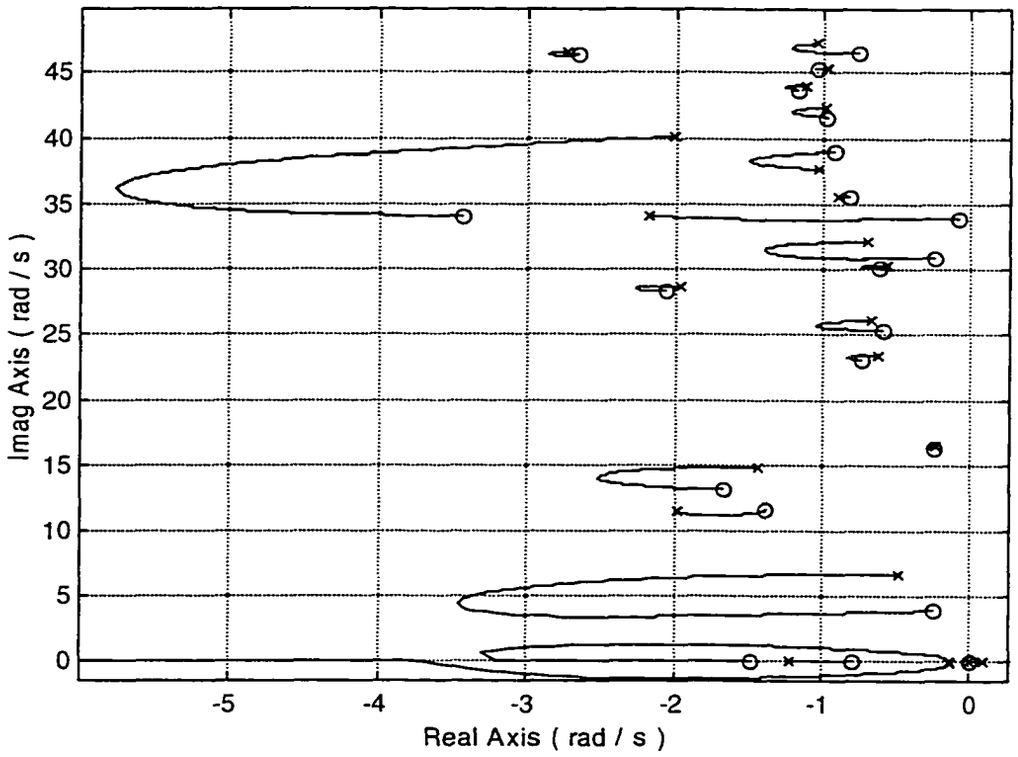

Figure 6.23 Root Locus Plot for x_{s1}=2,100 *in*, x_{s2}=2,950 *in* and z_k=1.5 *rad/s* (Static Blending)

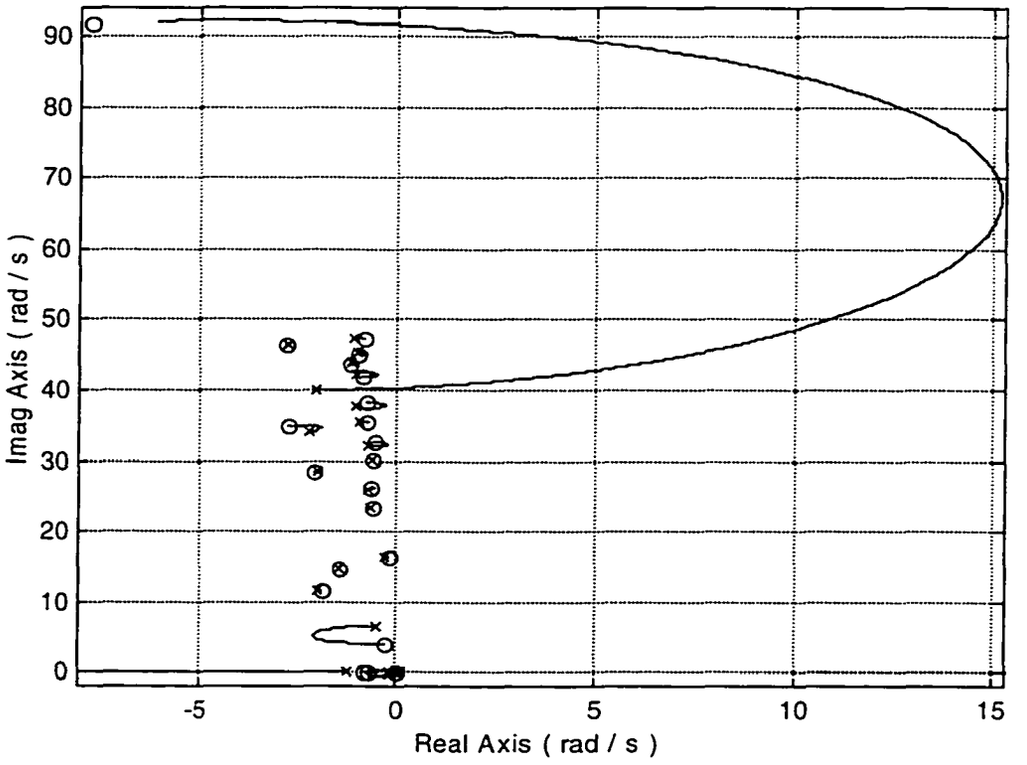

Figure 6.24 Root Locus Plot for x_{s1}=*2,222.5 in*, x_{s2}=*2,673.2 in* and z_k=*0.7 rad/s*

Comparing Figure 6.24 with the Figure 6.23 reveals that both complementary departure angle and dipole magnitude for the first mode, as well as for the third mode, are decreased. It is noticed that the complementary departure angle value decreased from *8.0746 deg* to *0.3047 deg* for the first mode and from *10.0453 deg* to *0.0051deg* for the third mode. Also it is noticed that the dipole magnitude value for both modes *1* and *3* are decreased from *2.6940 rad/s* to *2.4478 rad/s* and from *1.7258 rad/s* to *0.0646 rad/s*, respectively. Note the third aeroelastic mode is well gain stabilized, although aeroelastic mode *13* becomes unstable for a certain range of gain values. All constraint equations are satisfied.

To explore a new design space, a different fixed blending strategy is considered. These fixed filters are considered to have dynamic structure (low-high pass). They are shown in Figure 4.18 and Equations (4.13)-(4.14). With these kinds of dynamic filters implemented in the feedback signals of flight control system, the optimization code is applied to Equation (6.4) in order to find the optimal locations for the sensors, as well as for the compensator parameter. In the first case, the sensors are initially placed at x_{s1}=*850 in* and x_{s2}=*2,750 in*, while z_k=*1.5 rad/s* is also considered initially. Figure 6.25 shows the root locus plot of flight control system when the previous data are considered.

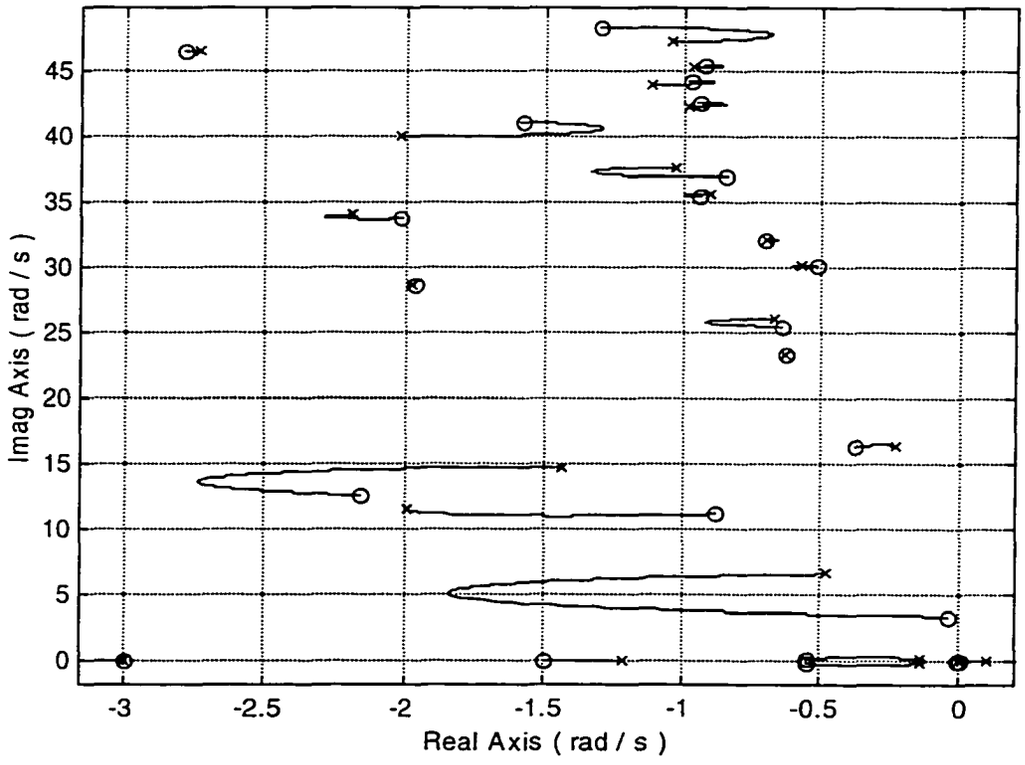

Figure 6.25 Root Locus Plot for x_{s1}=*850 in*, x_{s2}=*2,750 in* and z_k=*1.5 rad/s* (Dynamic Blend)

Applying the optimization algorithm on Equations (6.4) with z_k constraints and with appropriate weighting factors such as w_{μ_1}=*5 s/rad*, w_{μ_2}=*1 s/rad*, w_{ϕ_1}=*1 1/deg*, and w_{ϕ_2}=*1*

1/deg, the procedure results in x_{s1}=*641.5 in*, x_{s2}=*2,843.8 in*, and z_k=*2.5 rad/s*. The root locus plot corresponding to these results is shown in Figure 6.26. Comparing Figure 6.26 with Figure 6.25, the complementary departure angle values are decreased form *18.9181 deg* to *9.8505 deg* for the first mode and from *5.4643 deg* to *1.2453 deg* for the third mode. Also it is noticed that the dipole magnitude value for both modes *1* and *3* are slightly increased from *3.2523 rad/s* to *3.3957 rad/s* and from *2.3472 rad/s* to *2.5213 rad/s* respectively. Although the complementary departure angles of both modes *1* and *3* are not extremely small, these modes are well phase stabilized. Mode *13* augmentation has also improved considerably. Figure 6.27 shows the augmented cost function value at each iteration, while Figure 6.28 illustrates the track of the sensor positions during the search.

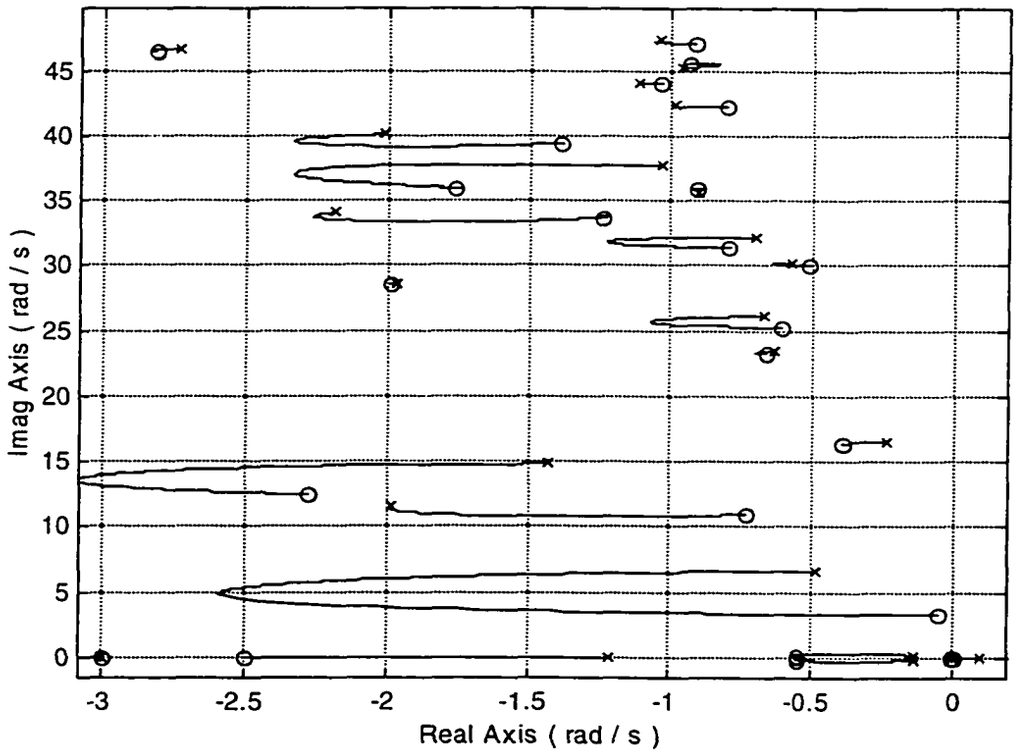

Figure 6.26 Root Locus Plot for x_{s1}=*641.5 in*, x_{s2}=*2,843.8 in* and z_k=*2.5 rad/s*

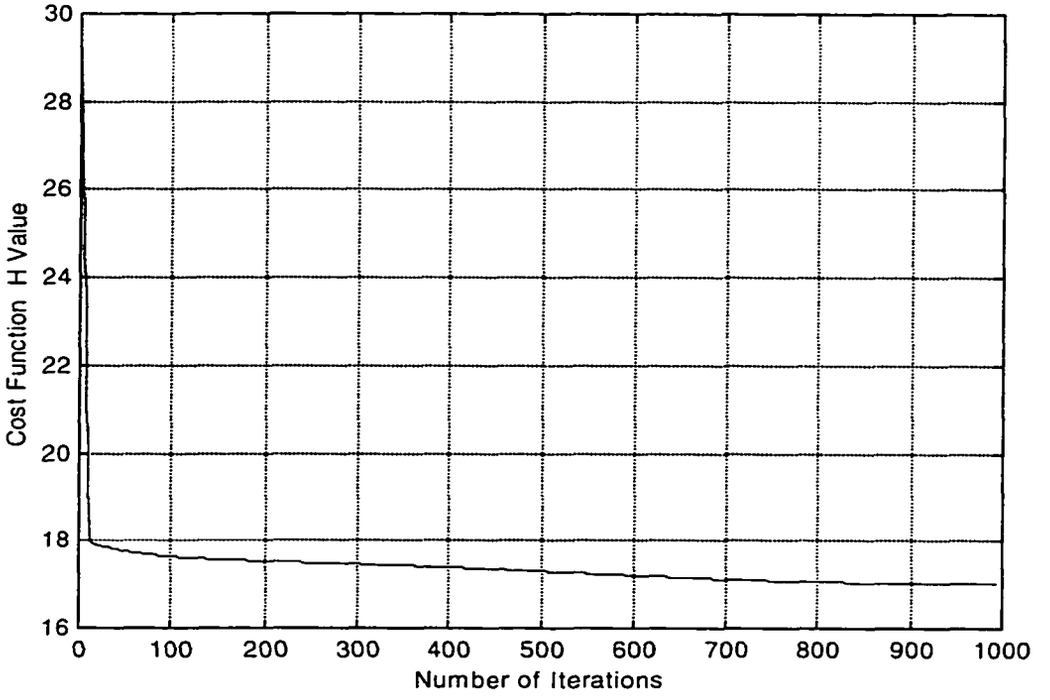

Figure 6.27 Cost Function History for x_{s1}=*641.5 in*, x_{s2}=*2,843.8 in* and z_k=*2.5 rad/s*

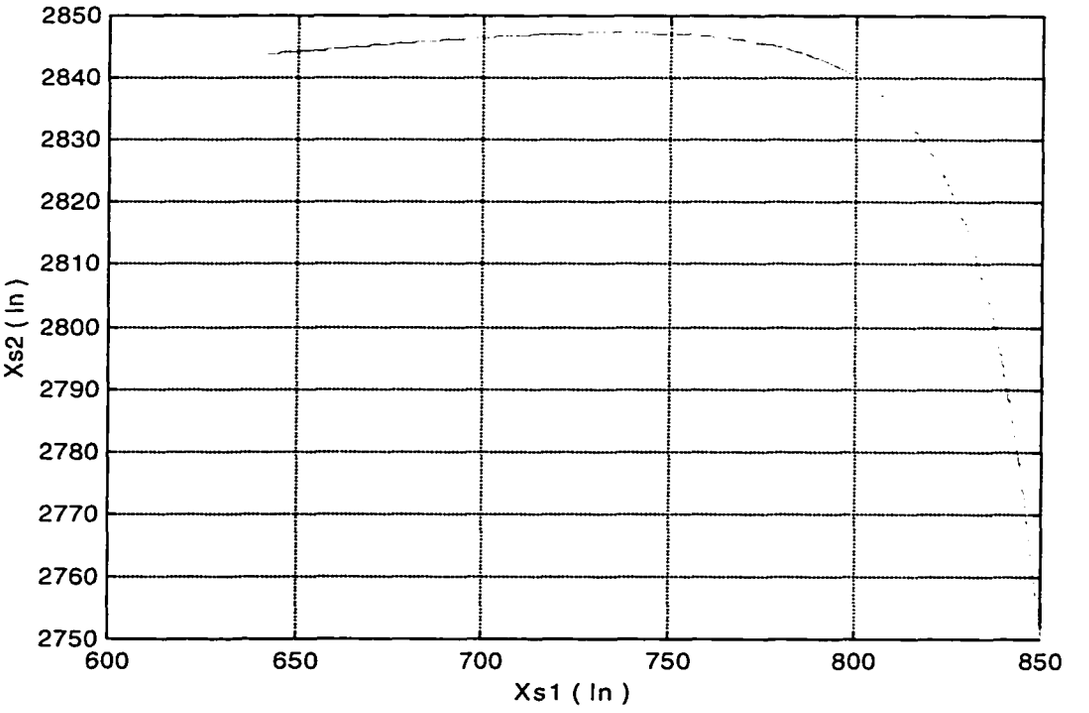

Figure 6.28 Sensor Position History for x_{s1}=*641.5 in*, x_{s2}=*2,843.8 in* and z_k=*2.5 rad/s*

To improve the previous results, the second case is tested under different initial sensor locations. The new locations are $x_{s1}=2,100\ in$ and $x_{s2}=2,950\ in$, while the compensator parameter will have the same previous initial value of $z_k=1.5\ rad/s$. The root locus plot of the flight control system when the initial values are considered is shown in Figure 6.29. Applying the optimization algorithm on the augmented cost function with

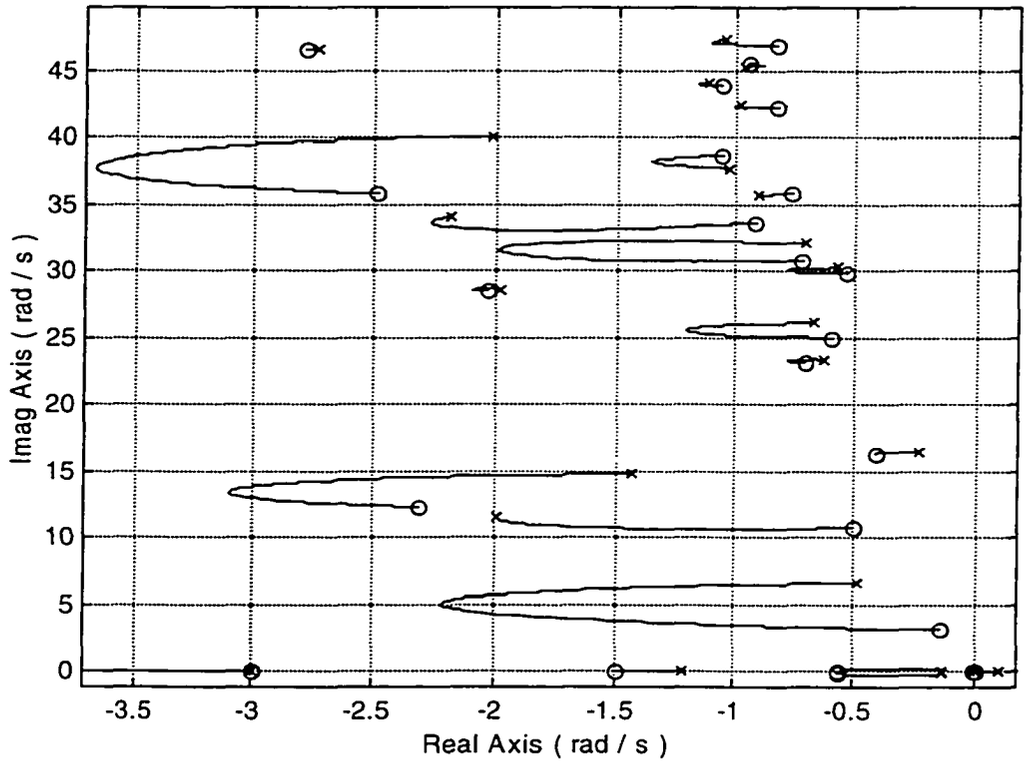

Figure 6.29 Root Locus Plot for $x_{s1}=2,100\ in$, $x_{s2}=2,950\ in$ and $z_k=1.5\ rad/s$ (Dynamic Blending)

the previous weighting factors, the optimization results indicate that the optimal locations of sensors are $x_{s1}=3,185\ in$ and $x_{s2}=2,583.7\ in$, while the optimal value of compensator parameter is $z_k=2.5\ rad/s$. Figure 6.30 outlines the root locus plot of flight control system when the optimal values are considered. Comparing Figure 6.30 with Figure 6.29, the

complementary departure angle value for the *1st* aeroelastic mode is decreased form *14.1342 deg* to *2.6232 deg* while the complementary departure angle value for the *3rd* aeroelastic mode is decreased from *7.9913 deg* to *0.1790 deg*. Also it is noticed that the dipole value for both modes *1* and *3* are decreased from *3.5055 rad/s* to *2.8 rad/s* and from *2.6642 rad/s* to *1.3 rad/s* respectively. Note, both complementary departure angles and dipole magnitudes are decreased simultaneously. Figure 6.31 shows the cost function value at each iteration while Figure 6.32 illustrates the sensor position track during the search.

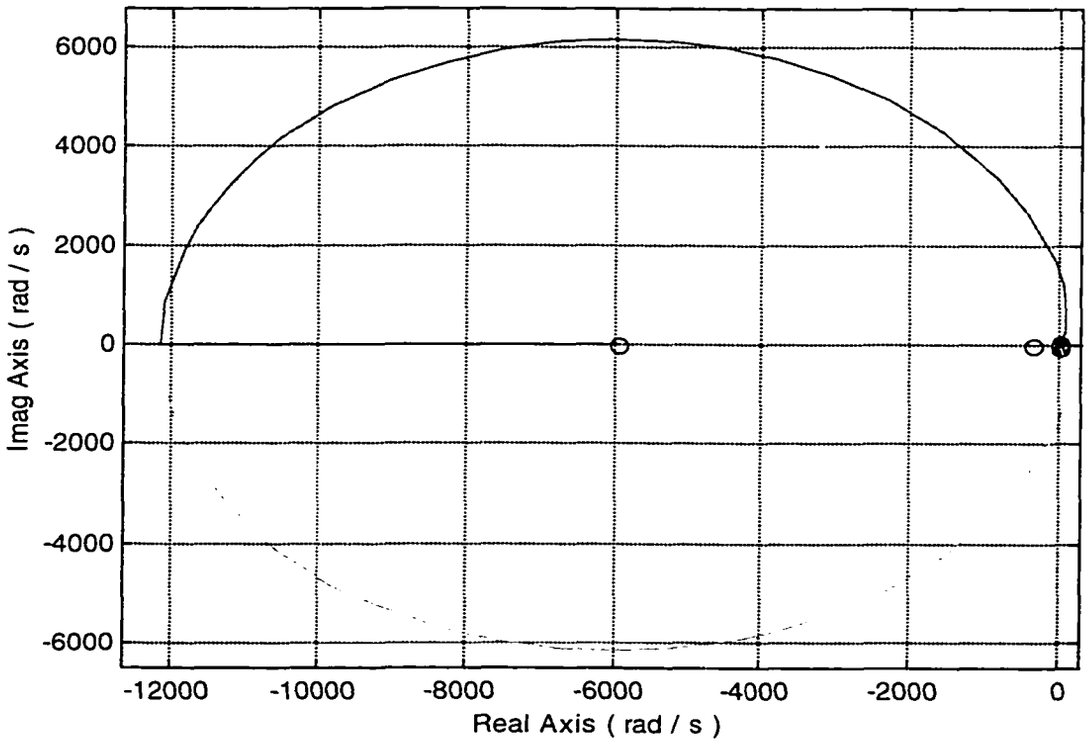

Figure 6.30a Root Locus Plot for x_{s1}=*3,185 in*, x_{s2}=*2,583.7 in* and z_k=*2.5 rad/s*

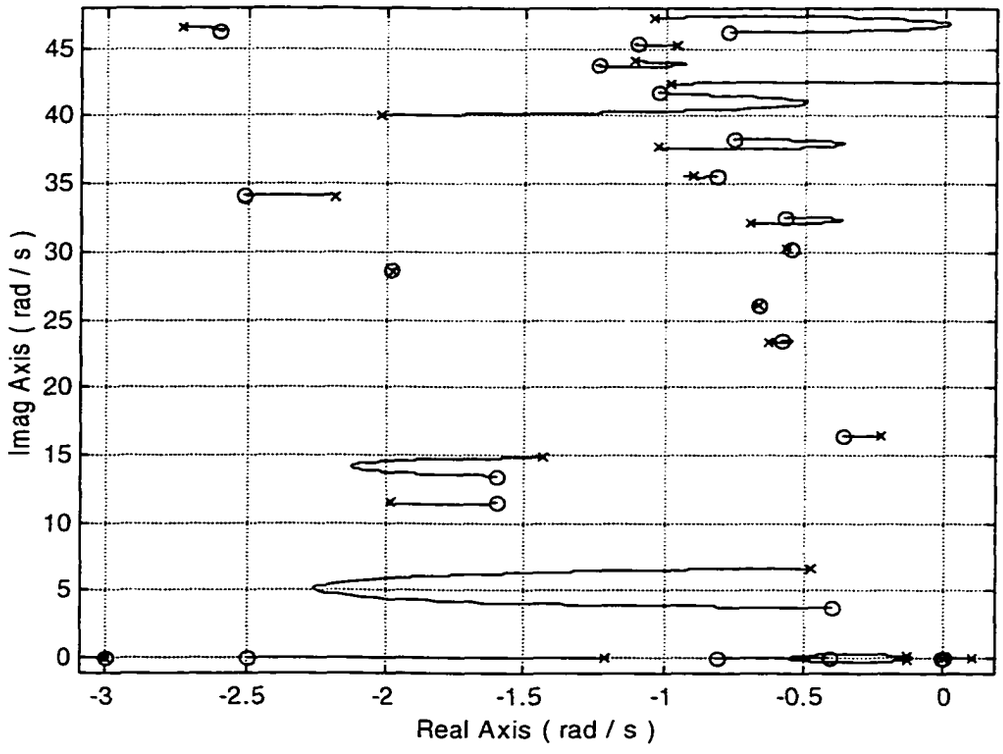

Figure 6.30b Root Locus Plot for x_{s1}=3,185 *in*, x_{s2}=2,583.7 *in* and z_k=2.5 *rad/s*

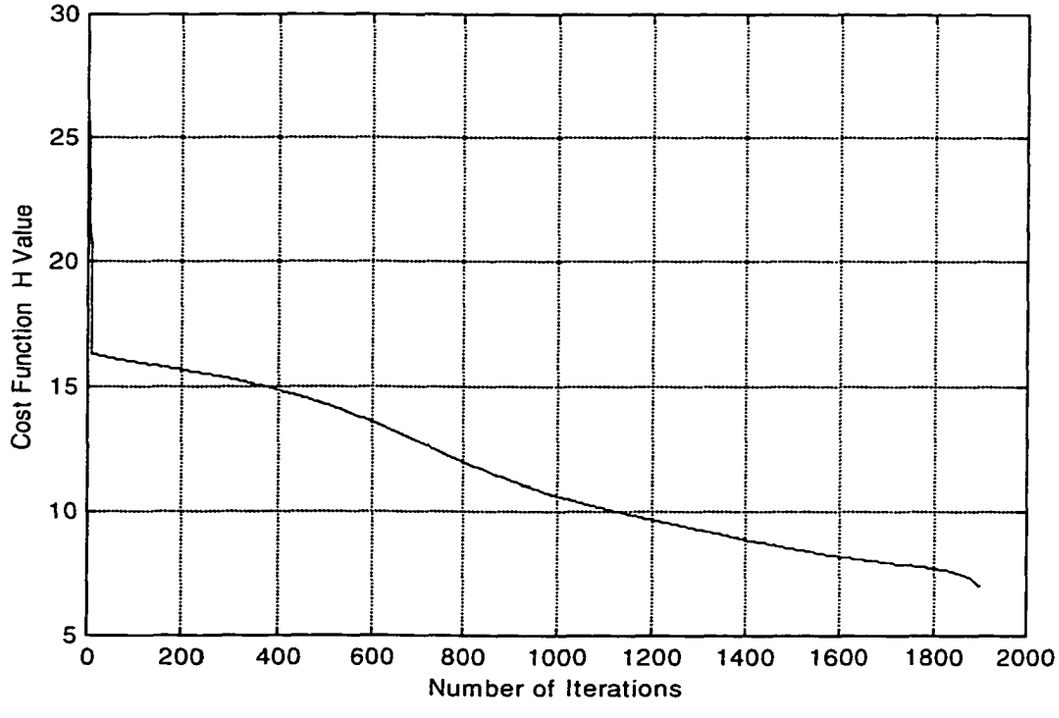

Figure 6.31 Cost Function History for x_{s1}=3,185 *in*, x_{s2}=2,583.7 *in* and z_k=2.5 *rad/s*

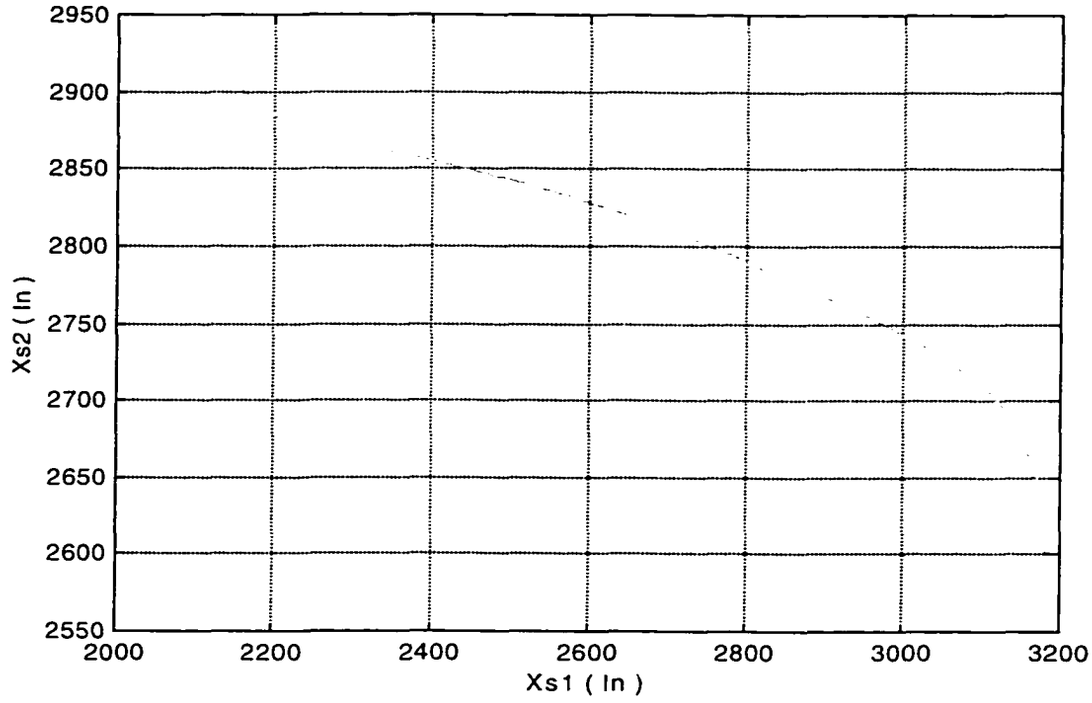

Figure 6.32 Sensor Position History for x_{s1}=*3,185 in*, x_{s2}=*2,583.7 in* and z_k=*2.5 rad/s*

6.7 Closed-Loop Vehicle Evaluation

In this section, the more promising sensor placement solutions will be carried through to the final step of flight control design and evaluation. Two candidate sensor placement solutions based on mixed gain-phase stabilization are considered here. These solutions correspond to the fixed static blending with variable compensator case given in Figure 6.24 and the fixed dynamic blending (low-high pass) with variable compensator case given in Figure 6.26. The Figure 6.26 case is highlighted to consider a dynamic blending solution.

Figure 6.33 shows the Figure 6.26 root locus plot with closed-loop pole locations explicitly indicated for a compensator gain value of k_k=*0.13 rad/rad/s*. For this gain

value, the rigid pitch mode (mid period mode) damping and natural frequency are ζ_{mp} $=0.8235$ and $\omega_{mp}=0.5613$ *rad/s*. These values are considerably improved relative to the open-loop values obtainable from Table 2.1. Note these modes are driven very close to a pair of complex zeros eliminating their contribution to the closed-loop dynamics. The fast mode from Table 2.1 moves out along the real axis and becomes the primary rigid pitch mode. After augmentation, the unstable slow mode in Table 2.1 is relocated to *s=-0.0017 rad/s* providing a stable closed-loop airframe. Figure 6.33 indicates a mode *1* damping ratio of $\zeta_{f_1}=0.4776$, which is also much improved relative to Table 2.1. Finally, note that at high gain values, all modes are projected to remain stable.

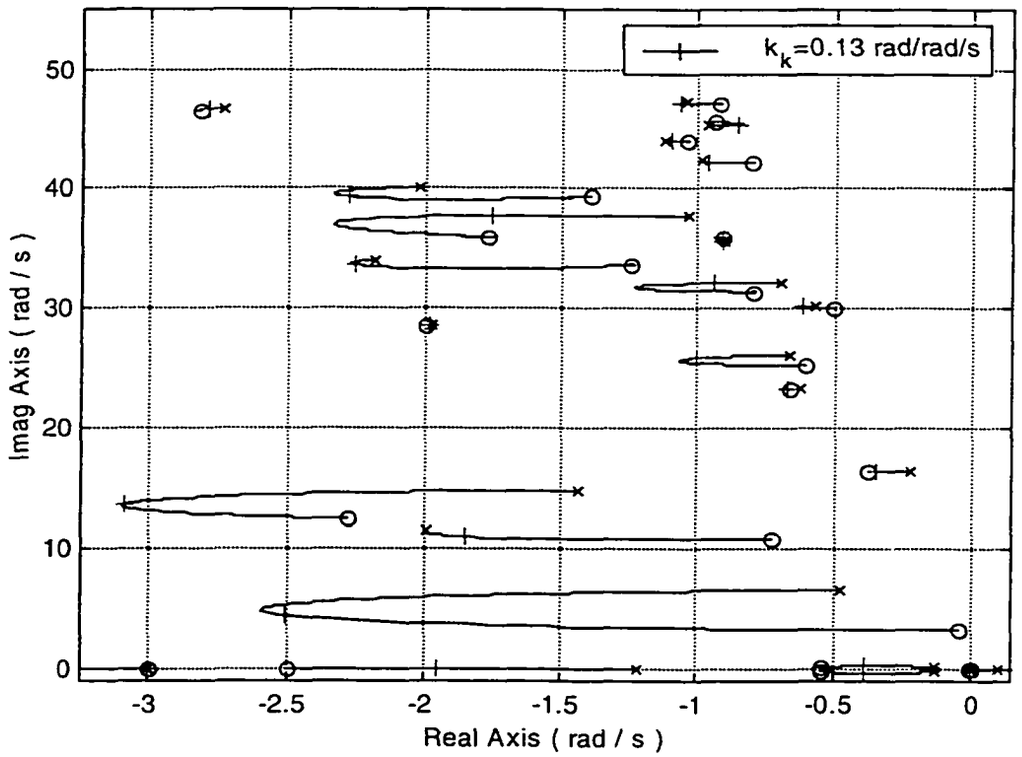

Figure 6.33 Closed-Loop Poles for $x_{s1}=641.5$ *in*, $x_{s2}=2,843.8$ *in* and $z_k=2.5$ *rad/s*

Figure 6.34 shows the corresponding time response for $\hat{q}$ due to a *0.01 rad/s* pitch rate command $\hat{q}_c$ (see Figure 2.20 and Equation (2.43)). In general, the closed-loop response in Figure 6.34 is significantly improved when compared to the open-loop responses given in Figure 2.7-2.8. First and foremost, the closed-loop response is stable. The gross response consists of very rapid first order type response. Note the system behaves as a rate command Type *1* system in the short term. This behavior is the augmented fast mode contribution to the overall response. Also note in the response one distinct high frequency ripple with frequency content of approximately *6 rad/s*. This vibration is originating from the 1^{st} aeroelastic mode (see Figure 6.33). This behavior is a prime example of how higher damping from phase stabilization can actually degrade the system response. Nevertheless, the final results appear to be reasonably successful.

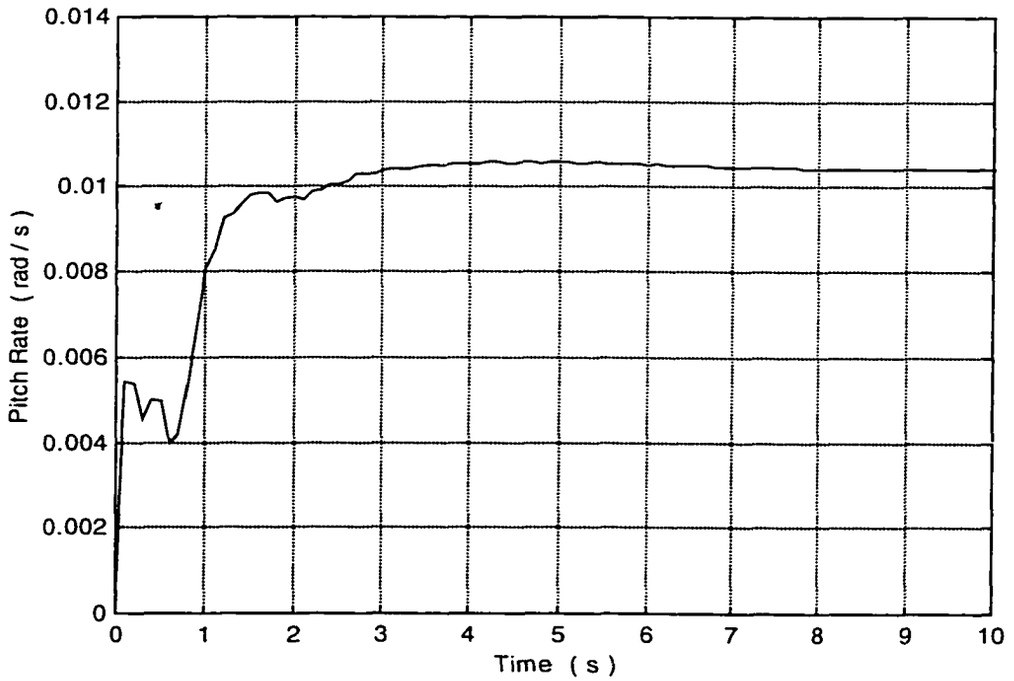

Figure 6.34 Step Response for x_{s1}=*641.5 in*, x_{s2}=*2,843.8 in* and z_k=*2.5 rad/s*

CHAPTER 7

CONCLUSIONS AND RECOMMENDATIONS

7.1 Conclusions

In this dissertation, a new systematic methodology and strategy to find the optimal position of sensors used in feedback flight control systems for a highly flexible vehicle is developed. This method is based on conventional Evans root migration flight control design techniques. Formulation of sensor placement criteria and cost functions for optimization are developed which link key closed-loop dynamic characteristics to the control design technique. With the Evans design technique, these criteria are based on open-loop transfer function pole-zero geometric features. Cost functions based on complementary departure angle are considered to influence the root locus paths of critical aeroelastic modes to initially move away from the imaginary axis (phase stabilization), while cost functions based on dipole magnitude are utilized to decrease and even cancel the influence of critical aeroelastic modes on the system dynamics as seen by the sensors at their specific locations (gain stabilization). Mixed cost functions based on complementary departure angle, as well as dipole magnitude, are considered also. Constraint equations are considered to ensure that all aeroelastic zeros lie in the stable region. Specialized optimization software based on the gradient or steepest descent method is generated to minimize these different types of cost and constraint equations. In the objective function, individual cost terms are multiplied by suitable weighting factors.

To improve the flight control system characteristics, other variables such as blending filter parameters and compensator parameters are optimized along with sensor positions.

For the augmented cost function investigations in Chapter 4 based on dipole magnitude (gain stabilization), implementing only two cost terms associated with critical modes *1* and *3* is not sufficient for yielding desirable solutions. In this strategy, one or more high frequency aeroelastic modes always penetrated the instability region. The presence of an additional term representing one of these high frequency dipole magnitude values must be implemented in the cost function to achieve desirable solutions. In many cases during the optimization process, the dipole magnitude value of either mode 1 or mode 3 would decrease relative to its initial value while the other value would increase. Seldom did both dipole magnitude values decrease simultaneously, thus illustrating a gain stabilization trade exists between these critical modes. Adjustment of the relative cost weight between these modes can be used to tune the solution characteristics, but this process is highly nonlinear, sometimes leading to unexpected results. Fixed static blending filters appear to be fairly restrictive towards meeting gain stabilization objectives. Additional design freedom offered by variable static, fixed dynamic, and variable dynamic blend filters allowed solution results to closer approach the desired gain stabilization objectives. However, these additional freedoms tended to generate high frequency loci that penetrate the right-half plane for sufficiently high gain. Consequently, these extra design freedoms must be exploited carefully and cautiously. Results indicated that the initial sensor locations used in the optimization process can have a significant influence on the solution characteristics.

For the augmented cost function investigations in Chapter 5 based on complementary departure angle (phase stabilization), utilization of only two cost terms associated with critical modes *1* and *3* is sufficient for generating desirable solutions. In this strategy, the higher frequency aeroelastic modes tend to remain stable. In most cases during the minimization process, the complementary departure angles for modes *1* and *3* did not decrease simultaneously, relative to their initial values. A phase stabilization trade between these critical modes was observed in the results. This trade can be tailored by adjusting the cost function weights in a relative fashion; however, this process can be highly nonlinear. Fixed and variable static blend filters are very effective and allow sufficient design freedom to achieve the desired phase stabilization objective. Dynamic blending filters helped to simultaneously decrease the complementary departure angles for both modes *1* and *3*, and can be used to tailor other root locus features. Results also indicated that initial sensor positions can have a profound effect on the optimal sensor solution characteristics.

The high-speed, highly flexible transport poses a difficult and challenging sensor placement problem. For example, in both the gain stabilization and phase stabilization investigations, a clear trade-off is noted between modes *1* and *3*. This behavior is traceable to the inherent conflicts between the mode shapes noted in Chapter 2. With all 18 modes present, placement of sensors which yields minimal cost while simultaneously satisfying imposed constraints is extremely challenging. Optimal sensor placement based on phase stabilization appears to be an easier problem (for this particular vehicle) when compared to the gain stabilization based placement problem. In the former, several solutions exist where the complementary departure angles are very near optimum for

critical modes ($\phi_{1,3} \approx 0$ *deg*). In the latter, simultaneous achievement of tight dipole structures for the critical modes ($\mu_{1,3} < 1$ *rad/s*) was difficult to achieve.

For the mixed augmented cost function investigations in Chapter 6 based on both dipole magnitude and complementary departure angle (gain-phase stabilization), some of the previously noted problems are overcome. Optimal sensor solutions that simultaneously have reduced dipole magnitude and complementary departure angle values for critical modes *1* and *3* relative to their initial values are reliably generated from this strategy. This trend held regardless of the type of blending filter strategy that was utilized (i.e., static or dynamic, fixed or variable). The compensator lead parameter plays an important role in influencing the low frequency rigid and first aeroelastic mode behavior. In Chapter 6, cases are considered where the optimization is allowed to find the best compensator lead parameter value while simultaneously placing the sensors. The variable compensator parameter allowed further progress to be made towards the mixed gain-phase stabilization objectives.

7.2 Recommendations

Several logical extensions to this dissertation and its contents are recommended as future work. The initial recommendation is to increase understanding of the current results to better plan other follow on investigations to improve the methodology and process for optimal sensor placement. One obvious area to explore is further testing of various dynamic filters and different kinds of compenators with fixed or variable parameters to improve flight control characteristics. The work in this dissertation by no means exhausted the space of suitable design filters. This dissertation also only

considered two feedback signals of the rate gyro type. Another recommendation is to consider more than two feedback signals, possibly using a combination of rate gyros and accelerometers. The control architecture could also be upgraded with more than one input. Updating the optimization software to minimize multiple parameters is advisable in these cases. Modification of the software to rigorously address inequality constraints is also highly recommended. Different sensor placement criteria such as frequency response or time response based objective functions should also be developed and tested using the optimization tool. Closed-loop sensor placement criteria are also recommended for future work. For a problem containing many local minima, a gradient search procedure may not be the most appropriate optimization technique. Consideration of other optimization techniques is also recommended.

REFERENCES

1. Boeing Commercial Airplane Group, "High-Speed Civil Transport Study," NASA-CR-4233, Langley Research Center, Hampton, Virginia, September, 1989.

2. Douglas Aircraft Company, "Study of High-Speed Civil Transports," NASA-CR-4235, Langley Research Center, Hampton, Virginia, September, 1989.

3. Ray, J. K., Carlin, C. M., and Lambregts, A. A., "High-Speed Civil Transport Flight – and Propulsion – Control Technological Issues," NASA-CR-186015, Dryden Flight Research Facility, Edwards, California, March, 1992.

4. McCarty, C. A., Feather, J. B., Dykman, J. R., Page, M. A., and Hodgkinson, J., "Design and Analysis Issues of Integrated Control Systems for High-Speed Civil Transports," NASA-CR-186022, Dryden Flight Research Facility, Edwards, California, May, 1992.

5. McRuer, D., Ashkenas, I., and Graham, D., Aircraft Dynamics and Automatic Control, Princeton University Press, Princeton, New Jersey, 1973.

6. Ashkenas, I. L., and McRuer, D. T., "Approximate Airframe Transfer Functions and Application to Single Sensor Control Systems," WADC-TR-58-82, Wright Air Development Center, Wright-Patterson AFB, Ohio, June, 1958.

7. Stevens, B. L., and Lewis, F. L., Aircraft Control and Simulation, John Wiley & Sons, New York, New York, 1992.

8. McLean, D., Automatic Flight Control Systems, Prentice Hall, New York, New York, 1990.

9. Proceedings of the Aeroservoelastic Specialists Meeting, Volume I and II, AFWAL-TR-84-3105, Flight Dynamics Laboratory, Wright-Patterson AFB, Ohio, October, 1984.

10. Pearce, B. F., Johnson, W. A., and Siskind, R. K., "Analytical Study of Approximate Longitudinal Transfer Functions for a Flexible Airframe," ASD-TDR-62-279, Aeronautical Systems Division, Air Force System Command, Wright-Patterson AFB, Ohio, June, 1962.

11. Pearce, B. F., and Siskind, R. K., "The Application of Flexible Airframe Transfer Function Approximations and the Sensitivity of Airframe Transfer Functions to Elastic Mode Shapes," ASD-TDR-63-334, Part II, Flight Control Laboratory, Aeronautical Systems Division, Air Force System Command, Wright-Patterson AFB, Ohio, July, 1963.

12. Pearce, B. F., "Coupling of the Rigid and Elastic Degrees of Freedom of an Airframe," ASD-TDR-63-334, Part III, Flight Control Laboratory, Aeronautical Systems Division, Air Force System Command, Wright-Patterson AFB, Ohio, July, 1963.

13. Pass, H. R., and Pearce, B. F., "Coupling of the Rigid and Elastic Degrees of Freedom of an Airframe - Autopilot System," ASD-TDR-63-334, Part IV, Flight Control Laboratory, Aeronautical Systems Division, Air Force System Command, Wright-Patterson AFB, Ohio, July, 1963.

14. Johnston, D. E., and Johnson, W. A., "Feasibility of Conventional Control Techniques for Large Highly Coupled Elastic Boost Vehicles," STI-TR-146-2, System Technology Inc., Hawthorne, California, March, 1967.

15. Wykes, J. H., and Mori, A. S., "An Analysis of Flexible Aircraft Structural Mode Control," AFFDL-TR-65-190, Flight Dynamics Laboratory, Wright-Patterson AFB, Ohio, June, 1966.

16. Wykes, J. H., "Structural Dynamic Stability Augmentation and Gust Alleviation of Flexible Aircraft," Proceedings of the AIAA 5th Annual Meeting and Technical Display, AIAA Paper No. AIAA-68-1067, Philadelphia, Pennsylvania, October, 1968.

17. Ashkenas, I. L., Magdaleno, R. E., and McRuer, D. T., "Flight Control and Analysis Methods for Studying Flying and Ride Qualities of Flexible Transport Aircraft," NASA-CR-172201, Langley Research Center, Hampton, Virginia, August, 1983.

18. Chan, S. Y., Cheng, P. Y., Myers, T. T., Klyde, D. H., Magdaleno, R. E., and McRuer, D. T., "Advanced Aeroservoelastic Stabilization Techniques for Hypersonic Flight Vehicles," NASA-CR-189702, Langley Research Center, Hampton, Virginia, November, 1992.

19. U.S. Department of Defense, "Military Standard: Flying Qualities of Piloted Aircraft," MIL-STD-1797A, Aeronautical Systems Division, Wright-Patterson AFB, Ohio, January, 1990.

20. Newman, B., "Proposed Flying Quality Metrics and Simulation Studies for Elastic Vehicles," Proceedings of the AIAA Atmospheric Flight Mechanics Conference, San Diego, California, July, 1996, pp. 500-509.

21. Raney, D. L., "The Impact of Structural Vibration on Flying Qualities of a Supersonic Transport," Proceedings of the AIAA Atmospheric Flight Mechanics Conference, Montreal, Quebec, Canada, August, 2001.

22. Raney, D. L., Jackson, E. B., and Buttrill, C. S., "Simulation Study of the Impact of Aeroelastic Characteristics on Flying Qualities of a High Speed Civil Transport," Pending NASA-TR, Langley Research Center, Hampton, Virginia, 2002.

23. Gevarter, W. B., "Basic Relations for Control of Flexible Vehicles," AIAA Journal, Vol. 8, No. 4, April, 1970, pp. 666-672.

24. Martin, G. D., "On the Control of Flexible Mechanical Systems," Ph.D. Dissertation, Department of Aeronautics and Astronautics, Stanford University, Stanford, California, May, 1978.

25. Balas, M. J., "Direct Velocity Feedback Control of Large Space Structures," Journal of Guidance and Control, Vol. 2, No. 3, May-June, 1979, pp. 252-253.

26. Arbel, A., and Gupta, N., "Robust Co-Located Control for Large Flexible Space Structures," Proceeding of the AACC Joint Automatic Control Conference, San Francisco, California, August, 1980, p. FP1-E.

27. Larson, V., and Likins, P. W., "Optimal Estimation and Control of Elastic Spacecraft," Advances in Control and Dynamic Systems, Vol. XIII, Academic Press, New York, New York, 1977.

28. Wie, B., "On the Modeling and Control of Flexible Structures," Ph.D. Dissertation, Department of Aeronautics and Astronautics, Stanford University, Stanford, California, June, 1981.

29. Schmidt, D. K., and Newman, B. A., "Modeling, Model Simplification and Stability Robustness with Aeroelastic Vehicles," Proceedings of the AIAA Guidance, Navigation, and Control Conference, Minneapolis, Minnesota, August, 1988, pp. 210-221.

30. Newman, B. A., and Schmidt, D. K., "Numerical and Literal Aeroelastic-Vehicle-Model Reduction for Feedback Control Synthesis," Journal of Guidance, Control, and Dynamics, Vol. 14, No. 5, September-October, 1991, pp. 943-953.

31. Newman, B. A., "Aerospace Vehicle Model Simplification for Feedback Control," Ph.D. Dissertation, School of Aeronautics and Astronautics, Purdue University, West Lafayette, Indiana, August, 1992.

32. Livneh, R., and Schmidt, D. K., "New Literal Approximations for the Longitudinal Dynamic Characteristics of Flexible Flight Vehicles," Proceedings of the AIAA Guidance, Navigation, and Control Conference, Hilton Head, South Carolina, August, 1992, pp. 536-545.

33. Livneh, R., "Improved Literal Approximations for the Lateral-Directional Dynamics of Rigid Aircraft," Proceedings of the AIAA Guidance, Navigation, and Control Conference, Baltimore, Maryland, August, 1995, pp. 1197-1207.

34. Newman, B. A., and Kassem, A. H., "Analytical Relationships for Linear Quadratic Aeroelastic Flight Control Eigenvalues," Journal of Guidance, Control, and Dynamics, Vol. 20, No. 6, November-December, 1997, pp. 1149-1156.

35. Kassem, A. H., and Newman, B. A., "Symbolic Analysis of Linear Quadratic Control Numerator and Denominator Factors," Proceedings of the AIAA Guidance, Navigation, and Control Conference, Boston, Massachusetts, August, 1998, pp. 1434-1444.

36. Kassem, A. H., and Newman, B. A., "Optimal Closed-Loop Analytic Relationships via Cost Function Imbedding," Proceedings of the AIAA Guidance, Navigation, and Control Conference, Portland, Oregon, August, 1999, pp.1180-1189.

37. Kassem, A. H., "Approximate Analytical Relationships for Linear Optimal Aeroelastic Flight Control Laws," Ph.D. Dissertation, Department of Aerospace Engineering, Old Dominion University, Norfolk, Virginia, August, 1998.

38. McRuer, D. T., Myers, T. T., and Thompson, P. M., "Literal Singular-Value-Based Flight Control System Design Techniques," Journal of Guidance, Control, and Dynamics, Vol. 12, No. 6, November-December, 1989, pp. 913-919.

39. Newman, B. A., and Schmidt, D. K., "Aeroelastic Vehicle Multivariable Control Synthesis with Analytical Robustness Evaluation," Journal of Guidance, Control, and Dynamics, Vol. 17, No. 6, November-December, 1994, pp. 1145-1153.

40. Wilhite, A. W., and Shaw, R. J., "HSCT Research Picks Up Speed," Aerospace America, Vol. 35, No. 8, August, 1997, pp. 24-29, 41.

41. Newman, B., and Kassem, A., "Investigation of Inner Loop Flight Control Strategies for High-Speed Research," NASA-CDCR-10008, Langley Research Center, Hampton, Virginia, August, 1996.

42. Newman, B., "Multivariable Techniques for High-Speed Research Flight Control Systems," NASA-CDCR-10019, Langley Research Center, Hampton, Virginia, March, 1998.

43. Newman, B., and Kassem, A., "Investigation of Inner Loop Flight Control Strategies for High-Speed Research," NASA-CR-1999-209522, Langley Research Center, Hampton, Virginia, December, 1999.

44. Newman, B., "Multivariable Techniques for High-Speed Research Flight Control Systems," NASA-CR-1999-209528, Langley Research Center, Hampton, Virginia, December, 1999.

45. Newman, B., and Buttrill, C., "Conventional Flight Control for an Aeroelastic Relaxed Static Stability High-Speed Transport," Proceedings of the AIAA Guidance, Navigation, and Control Conference, Baltimore, Maryland, August, 1995, pp. 717-726.

46. Myers, T. T., McRuer, D. T., and Johnston, D. E., "Flying Qualities and Control System Characteristics for Superaugmented Aircraft," NASA-CR-170419, Dryden Flight Research Facility, Edwards, California, June, 1984.

47. McRuer, D. T., Johnston, D. E., and Myers, T. T., "A Perspective on Superaugmented Flight Control Advantages and Problems," Active Control Systems-Review, Evaluation and Projections, AGARD Conference Proceedings No. 384, Toronto, Canada, October, 1984, pp. 3.1-3.16.

48. Al-Shehabi, A. G., and Newman, B. A., "Aeroelastic Vehicle Sensor Placement for Feedback Control Applications Using Phase Stability," Proceedings of the AIAA Guidance, Navigation, and Control Conference, Denver, Colorado, August, 2000, pp. 627-635.

49. Al-Shehabi, A. G., and Newman, B. A., "Aeroelastic Vehicle Sensor Placement for Feedback Control Applications Using Gain Stability," DSC Vol.69-1, Proceedings of the ASME International Mechanical Engineering Congress and Exposition, Orlando, Florida, November, 2000, pp. 221-228.

50. Al-Shehabi, A. G., and Newman, B. A., "Aeroelastic Vehicle Optimal Sensor Placement for Feedback Control Applications Using Mixed Gain-Phase Stability," Proceedings of the AACC American Control Confrence, Arlington, Virginia, June, 2001, pp. 1848-1852.

51. Al-Shehabi, A. G., and Newman, B. A., "Optimal Sensor Placement and Compensation Selection for Aeroelastic Control," Proceedings of the AIAA Guidance, Navigation, and Control Conference, Montreal, Quebec, Canada, August, 2001.

52. Padula, S. L., and Kincaid, R. K., "Optimization Strategies for Sensor and Actuator Placement," NASA-TM-1999-209126, Langley Research Center, Hampton, Virginia, April, 1999.

53. Lim, K. B., "Method for Optimal Actuator and Sensor Placement for Large Flexible Structures," Journal of Guidance, Control, and Dynamics, Vol. 15, No. 1, January-February, 1992, pp. 49-57.

54. Maghami, P. G., and Joshi, S. M., "Sensor/Actuator Placement for Flexible Space Structures," IEEE Transactions on Aerospace and Electronic Systems, Vol. 29, No. 2, April, 1993, pp. 345-351.

55. Linberg, R. E., and Longman, R. W., "On the Number and Placement of Actuators for Independent Modal Space Control," Journal of Guidance, Control, and Dynamics, Vol. 7, No. 2, March-April, 1984, pp. 215-221.

56. DeLorenzo, M. L., "Sensor and Actuator Selection for Large Space Structure Control," Journal of Guidance, Control, and Dynamics, Vol. 13, No. 2, March-April, 1990, pp. 249-257.

57. Furuya, H., and Haftka, R. T., "Combining Genetic and Deterministic Algorithms for Locating Actuators on Space Structures," Journal of Spacecraft and Rockets, Vol. 33, No. 3, May-June, 1999, pp. 422-427.

58. Furuya, H., and Haftka, R. T., "Static Shape Control of Space Trusses with Partial Measurements," Journal of Spacecraft and Rockets, Vol. 32, No. 5, September-October, 1995, pp. 856-865.

59. Chiu, D., and Skelton, R. E., "Selecting Measurments and Controls in LQG Problems," Proceedings of the 20th IEEE Conference on Decision and Control, San Diego, California, December, 1981, pp. 491-494.

60. Haftka, R. T., "Optimal Placement of Controls for Static Deformations of Space Structures," AIAA Journal, Vol. 22, No. 9, 1984, pp. 1293-1298.

61. Burdisso, R., and Haftka, R., "Optimal Placement of Actuators for Correcting Distortions in Large Truss Structures," AIAA Journal, Vol. 27, No. 10, 1989, pp. 1406-1411.

62. Juang, J. N., and Rodriguez, G., "Formulation and Application of Large Structure Sensor and Actuator Placement," Proceedings of the 2nd VPI&SU/AIAA Symposium on Dynamics and Control of Large Flexible Spacecraft, Blacksburg, Virginia, June, 1979, pp. 249-262.

63. Hakim, S., and Fuchs, M. B., "Quasistatic Optimal Actuator Placement with Minimum Worst Case Distortion Criterion," AIAA Journal, Vol. 34, No. 7, July, 1996, pp. 1505-1511.

64. Lim, K. B., Lake, R. C., and Heeg, J., "Effective Selection of Piezoceramic Actuators for an Experimental Flexible Wing," Journal of Guidance, Control, and Dynamics, Vol. 21, No. 5, September-October, 1998, pp. 704-709.

65. Adams Jr., W. M., and Christilf, D. M., "Design and Multifunction Tests of a Frequency Domain-Based Active Flutter Suppression System," Journal of Aircraft, Vol. 32, No. 1, January-February, 1995, pp. 52-60.

66. Nam, C., Kim, Y., and Weisshaar, T. A., "Optimal Sizing and Placement of Piezo-Actuators for Active Flutter Suppression," Smart Materials and Structures, Vol. 5, No. 2. April, 1996, pp. 216-224.

67. Zhou, R. C., Lai, Z., Xue, D. Y., Huang, J. K., and Mei, C., "Suppression of Nonlinear Panel Flutter with Piezoelectric Actuators Using Finite Element Method," AIAA Journal, Vol. 33, No. 6, June, 1995, pp. 1098-1105.

68. Zhou, R. C., Mei, C., and Huang, J. K., "Suppression of Nonlinear Panel Flutter at Supersonic Speeds and Elevated Temperatures," AIAA Journal, Vol. 34, No. 2, February, 1996, pp. 347-354.

69. Meyn, L. A., and Lanser, W. R., "Forebody Flow Control on a Full-Scale F/A-18 Aircraft," Journal of Aircraft, Vol. 31, No. 6, November-December, 1994, pp. 1365-1371.

70. Lucius, G. A., and Kenneth, C. C., "Side Force Augmentation at High Angle of Attack from Pneumatic Vortex Control," Journal of Aircraft, Vol. 31, No. 4, July-August, 1994, pp. 818-825.

71. Agosta-Greenman, R. M., Gee, K., Cummings, R. M., and Schiff, L. B., "Computational Investigation of Tangential Slot Blowing on a Generic Chined Forebody," Journal of Aircraft, Vol. 32, No. 4, July-August, 1995, pp. 811-817.

72. Nelson, P. A., Wright, M. C. M., and Rioual, J. K., "Automatic Control of Laminar Boundary-Layer Transition," AIAA Journal, Vol. 35, No. 1, January, 1997, pp. 85-90.

73. Lin, J. C., Robinson, S. K., McGhee, C. C., and Valarezo, W. O., "Separation Control on High-Lift Airfoils via Micro-Vortex Generator," Journal of Aircraft, Vol. 31, No. 6, November-December, 1994, pp. 818-825.

74. Kandil, O. A., and Yang, Z., "Adaptive Suction and Blowing Flow Control Effectiveness for Twin-Tail Buffet Response," Proceedings of the AIAA Applied Aerodynamics Conference, Norfolk, Virginia, June, 1999, pp. 204-214.

75. Holnicki, S. J., Lopez, A. F., and Rodellar, J., "Optimal Location of Actuators for Active Damping of Vibration," AIAA Journal, Vol. 31, No. 7, July 1993, pp. 1274-1279.

76. Choe, K., and Baruh, H., "Actuator Placement in Structural Control," Journal of Guidance, Control, and Dynamics, Vol. 15, No. 1, January-February, 1992, pp. 40-48.

77. Baruh, H., and Choe, K., "Sensor Placement in Structural Control," Journal of Guidance, Control, and Dynamics, Vol. 13, No. 3, May-June, 1990, pp. 524-533.

78. Roh, H. S., and Park, Y., "Actuator and Exciter Placement for Flexible Structures," Journal of Guidance, Control, and Dynamics, Vol. 20, No. 5, September-October, 1997, pp. 850-856.

79. Xu, K., Warnitchai, P., and Igusa, T., "Optimal Placement and Gains of Sensors and Actuators for Feedback Control," Journal of Guidance, Control, and Dynamics, Vol. 17, No. 5, September-October, 1994, pp. 929-934.

80. Kim, Y., and Junkins, J. L., "Measure of Controllability for Actuator Placement," Journal of Guidance, Control, and Dynamics, Vol. 14, No. 5, September-October, 1991, pp. 895-902.

81. Aldraihem, O. J., Singh, T., and Wetherhold, R. C., "Optimal Size and Location of Piezoelectric Actuator/Sensors: Practical Considerations," Journal of Guidance, Control, and Dynamics, Vol. 23, No. 3, May-June, 2000, pp. 509-515.

82. Venkatesan, C., and Udayasankar, A., "Selection of Sensor Locations for Active Vibration Control of Helicopter Fuselages," Journal of Aircraft, Vol. 36, No. 2, March-April, 1999, pp. 434-442.

83. D'Cruz, J., "Active Suppression of Aircraft Panel Vibration with Piezoceramic Strain Actuators," Journal of Aircraft, Vol. 35, No. 1, January-February, 1998, pp. 139-144.

84. Hamernik, T. A., Garica, E., and Stech, D., "Optimal Placement of Damped Struts Using Simulated Annealing," Journal of Spacecraft and Rockets, Vol. 32, No. 4, July-August, 1995, pp. 653-661.

85. Kang, K. Y., Park, H. C., and Agrawal, B., "Optimization of Piezoceramic Sensor/Actuator Placement for Vibration Control of Laminated Plates," AIAA Journal, Vol. 36, No. 9, September, 1998, pp. 1763-1765.

86. Sepulveda, A. E., Jin, I. M., and Schmit, L. A., "Optimal Placement of Active Elements in Control Augmented Structural Synthesis," AIAA Journal, Vol. 31, No. 10, October, 1993, pp. 1906-1913.

87. Kang, Y. K., Park, H. C., Hwang, W., and Han, K. S., "Optimal Placement of Piezoelectric Sensor/Actuator for Vibration Control of Laminated Beams," AIAA Journal, Vol. 34, No. 9, September, 1993, pp. 1906-1913.

88. Salama, M., Bruno, R., Chen, G. S., and Garba, J., "Optimal Placement of Excitations and Sensors by Simulated Annealing," Proceedings of the Second NASA/Air Force Symposium on Recent Advances in Multidisciplinary Analysis and Optimization, Hampton, Virginia, September, 1988, pp. 1441-1457.

89. Chang, I. J., and Soong, T. T., "Optimal Controller Placement in Modal Control of Complex Systems," Journal of Mathematical Analysis and Applications, Vol. 75, No. 2, 1980, pp. 340-358.

90. Sepulveda, A. E., and Schmit, L. A., "Optimal Placement of Actuators and Sensors in Control Augmented Structural Optimization," International Journal for Numerical Methods in Engineering, Vol. 32, No. 6, 1991, pp. 1165-1187.

91. Hu, A., and Liu, L., "Sensor and Actuator Location in Motion Control of Flexible Structures," Journal of Sound and Vibration, Vol. 176, No. 2, October, 1993, pp. 239-261.

92. Liu, C., and Tasker, F. A., "Sensor Placement for Time-Domain Modal Parameter Estimation," Journal of Guidance, Control, and Dynamics, Vol. 19, No. 6, November-December, 1996, pp. 1349-1356.

93. Cobb, R., and Liebst, B. S., "Sensor Placement and Structural Damage Identification from Minimal Sensor Information," AIAA Journal, Vol. 35, No. 2, February, 1997.

94. Kammer, D. C., "Optimal Sensor Placement for Modal Identification Using System-Realization Methods," Journal of Guidance, Control, and Dynamics, Vol. 19, No. 3, 1996, pp. 729-731.

95. Matunaga, S., and Onoda, J., "Actuator Placement with Failure Consideration for Static Shape Control of Truss Structures," AIAA Journal, Vol. 33, No. 6, June, 1995, pp. 1161-1163.

96. Papadopoulos, M., and Garcia, E., "Sensor Placement Methodologies for Dynamic Testing," AIAA Journal, Vol. 36, No. 2, February, 1998, pp. 256-263.

97. Yao, L., Sethares, W. A., and Kammer, D. C., "Sensor Placement for On-Orbit Modal Identification via a Genetic Algorithm," AIAA Journal, Vol. 31, No. 10, October, 1993, pp. 1922-1928.

98. Gupta, N. K., and Hall, W. E., "Design and Evaluation of Sensor System for State and Parameter Estimation," Journal of Guidance, Control, and Dynamics, Vol. 1, No. 6, 1978, pp. 397-403.

99. Le Sourhiet, A., and Le Letty, L., "Optimization of Sensor Location in Distributed Parameter System Identification," Proceedings of the 4th IFAC Symposium on Identification and System Parameter Estimation, Edited by Rajbmon, N. S., North Holland, Amsterdam, The Netherlands, 1978, pp. 1581-1592.

100. Shah, P. C., and Udwadia, F. E., "A Methodology for Optimal Sensor Locations for Identification of Dynamic System," Journal of Applied Mechanics, Vol. 45, No. 1, 1978, pp. 188-196.

101. Salama, M., Rose, T., and Garba, J., "Optimal Placement of Excitations and Sensors for Verification of Large Dynamical Systems," Proceedings of the 28th AIAA Structures, Structural Dynamics, and Materials Conference, Monterey, California, April, 1987, pp. 1024-1031.

102. Kammer, D. C., "Sensor Placement for On-Orbit Modal Identification and Correlation of Large Space Structures," Journal of Guidance, Control, and Dynamics, Vol. 14, No. 2, 1991, pp. 251-259.

103. Simpson, M. T., and Hansen, C. H., "Use of Genetic Algorithms for Optimizing Vibration Actuator Placement for Minimizing Sound Transmission into Enclosed Spaces," Proceedings of the SPIE, Vol. 2717, 1996, pp. 409-421.

104. Wang, B. T., Fuller, C. R., and Dimitriadis, E. K., "Active Control of Noise Transmission Through Rectangular Plate Using Piezoelectric or Point Force Actuator," Journal of Acoustic Society of America, Vol. 90, No. 5, 1991, pp. 2820-2830.

105. Wang, B. T., Fuller, C. R., and Dimitriadis, E. K., "Active Control of Structurally Radiated Noise Using Multiple Piezoelectric Actuators," AIAA Journal, Vol. 29, No. 11, 1991, pp. 1802-1809.

106. Wang, B. T., Burdisso, R. A., and Fuller, C. R., "Optimal Placement of Piezoelectric Actuators for Active Structural Acoustic Control," Journal of Intelligent Material Systems and Strucures, Vol. 5, No. 1, 1994, pp. 67-77.

107. Palumbo, D. L., Padula, S. L., Lyle, K. H., Cline, J. H, and Cabell, R. H., "Performance of Optimized Actuator and Sensor Arrays in an Active Noise Control System," NASA-TM-110281, Langley Research Center, Hampton, Virginia, September, 1996.

108. Lee, A. C., and Chen, S. T., "Collocated Sensor/Actuator Position and Feedback Design in the Control of Flexible Structure System," Journal of Vibration and Acoustics, Vol. 116, No. 148, April, 1994, pp. 146-154.

109. Varadan, V. V., Kim, J., and Varadan, V. K., "Optimal Placement of Piezoelectric Actuators for Active Noise Control," AIAA Journal, Vol. 35, No. 3, March, 1997, pp. 526-533.

110. Bisplinghoff, R. L., and Ashley, H., Principles of Aeroelasticity, Dover, New York, New York, 1962.

111. Boeing Commercial Airplane Division, "An Analysis of Methods for Predicting the Stability Characteristics of an Elastic Airplane," NASA-TR-73277, Ames Research Center, Moffett Field, California, November, 1968.

112. Noll, T., and Blair, M., "A Procedure for Aeroelastic Analyses Involving Aircraft with Analog or Digital Control Systems," AFWAL-TR-86-3040, Vol. I, Flight Dynamics Laboratory, Wright-Patterson AFB, Ohio, January, 1987.

113. Waszak, M. R., and Schmidt, D. K., "Flight Dynamics of Aeroelastic Vehicles," Journal of Aircraft, Vol. 25, No. 6, June, 1988, pp. 563-571.

114. Arbuckle, P. D., and Buttrill, C. S., "Simulation Model-Building Procedure for Dynamic Systems Integration," Journal of Guidance, Control, and Dynamics, Vol. 12, No. 6, November-December, 1989, pp. 894-900.

115. Adams, W. M., and Hoadley, S. T., "ISAC: A Tool for Aeroservoelastic Modeling and Analysis," NASA-TM-109031, Langley Research Center, Hampton, Virginia, December, 1993.

116. Waszak, M. R., Buttrill, C. S., and Schmidt, D. K., "Modeling and Model Simplification of Aeroelastic Vehicles: An Overview," NASA-TM-107691, Langley Research Center, Hampton, Virginia, September, 1992.

117. Ogata, K., Modern Control Engineering, Prentice-Hall, Englewood Cliffs, New Jersey, 1970.

118. D'Azzo, J. J., and Houpis, C. H., Linear Control System Analysis and Design: Conventional and Modern, McGraw-Hill, New York, New York, 1975.

119. Bryson, A. E., and Ho, Y. C., Applied Optimal Control: Optimization, Estimation and Control, Hemisphere Publishing, Washington, District of Columbia, 1975.

120. Merriam, C. W., Optimization Theory and Design of Feedback Control Systems, McGraw-Hill, New York, New York, 1964.

121. Pierre, D. A., Optimization Theory with Application, John Wiley & Sons, New York, New York, 1969.

122. Wismer, D. A., and Chattergy, R., Introduction to Nonlinear Optimization, North Holland, Amsterdam, The Netherlands, 1978.

123. Little, J., Moler, C., and *et al*, "MATLAB Optimization Toolbox User's Guide," The Mathworks, Natick, Massachusetts, December, 1996.

APPENDIX

Figure A.1 shows the large high-speed, highly flexible transport configuration studied throughout this dissertation.

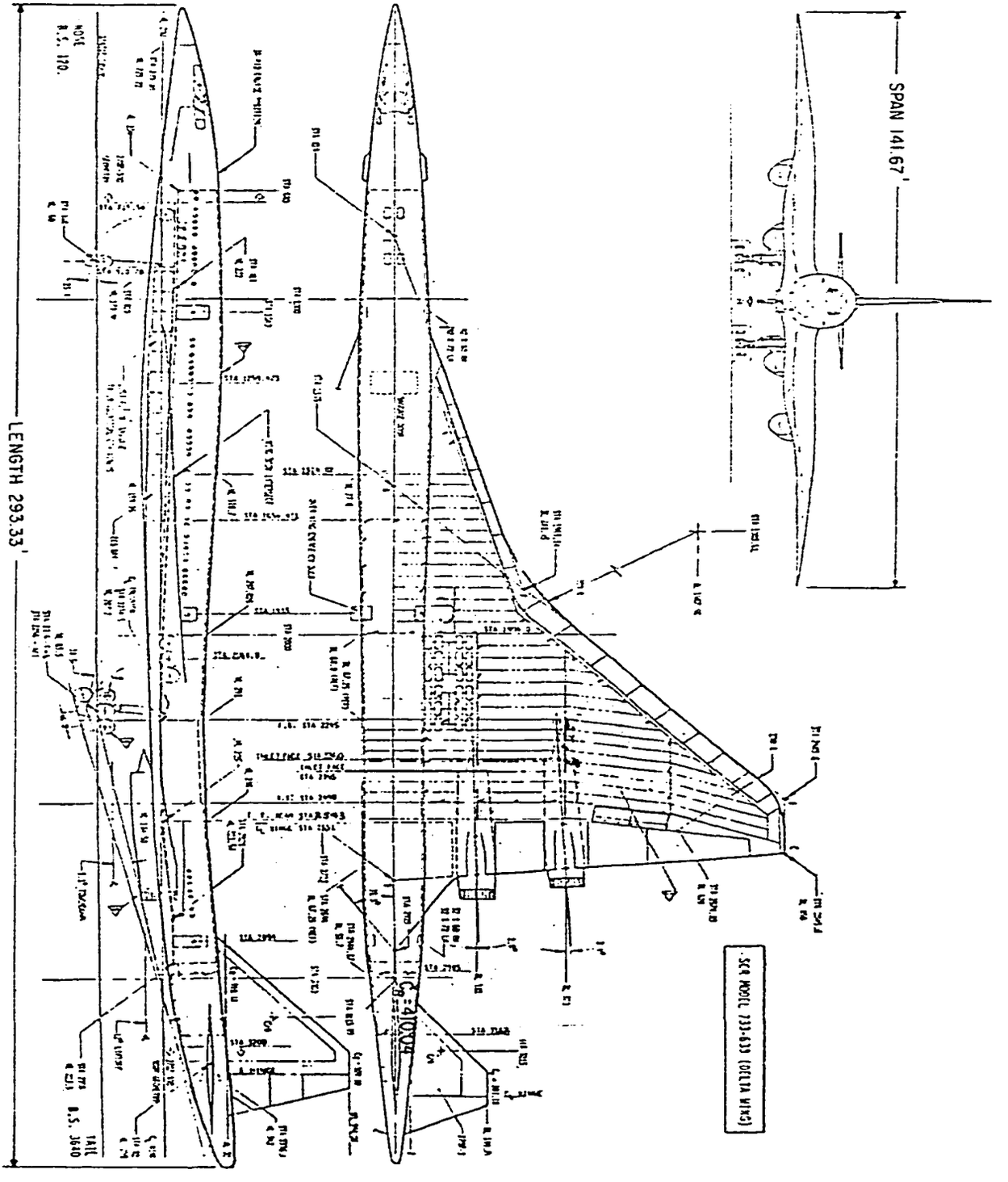

Figure A.1 Aircraft Configuration Geometry

The aircraft model is

$$\dot{x} = Ax + Bu$$
$$y = Cx$$

where

$$x = \begin{bmatrix} u\ (in/s) \\ w\ (in/s) \\ q\ (rad/s) \\ \theta\ (rad) \\ \dot{\xi}_i\ i=1,2,..18\ (1/s) \\ \xi_i\ i=1,2,..18\ (-) \end{bmatrix}, \quad y = \left[q_j'(rad/s) \right], \quad j = 1, 2, \ldots n_\Omega, \quad u = \delta_E$$

$$q_j' = q - \sum_{i=1}^{18} \phi_i'(x_{sj})\dot{\xi}_i ,$$

$$\phi_{z_i}(x_j) = -\phi_{z_u}(x_{sj}), \qquad \phi_{z_u}(x_{sj}) = C_{\phi_{z_u}} \bar{x}_{sj}\ (in), \qquad \phi_i'(x_{sj}) = \frac{d\phi_{z_i}(x_j)}{dx_j} = \frac{d\phi_{z_u}(x_{sj})}{dx_{sj}}$$

$$C_{\phi_{z_u}} = i^{th}\ row\ of\ C_{\phi_{z_i}}, \qquad \bar{x}_{sj} = \left[x_{sj}^{13} \quad x_{sj}^{12} \quad \cdots \quad x_{sj} \quad 1 \right]^T (in),$$

$$x_j = 2{,}364 - x_{sj}$$

(x_j denotes x at the j^{th} sensor location and x_{sj} denotes x_s at the j^{th} sensor location).

A(1:40,1:6)=

-5.8400e-003	1.9800e-002	0	-3.2167e+001	0	0
-8.1771e-002	-6.8135e-001	6.1616e+002	0	-1.0832e-003	1.3990e-002
-8.8947e-005	2.7480e-003	-4.4500e-001	0	3.5669e-004	2.2698e-004
0	0	1.0000e+000	0	0	0
-6.8332e-002	-1.7924e+001	-2.0312e+002	0	-1.1024e+000	8.3863e-001
1.7800e-002	3.5428e+001	6.4376e+002	0	4.3228e-001	-2.4159e+000
1.9193e-002	3.6067e+001	1.4011e+003	0	2.6521e-001	-8.7449e-001
3.2897e-002	3.9370e+001	3.2174e+002	0	3.1875e-001	-5.5220e-001
5.5717e-002	3.0210e+001	2.4162e+002	0	5.2845e-001	-5.9928e-001
6.7948e-003	1.5338e+001	-1.4497e+002	0	2.9993e-002	2.1167e-001
-1.2050e-001	-3.7369e+001	-1.2868e+002	0	-1.0615e+000	-1.4344e+000
-2.6523e-003	-6.5549e+000	-4.8722e+001	0	-1.0621e-002	1.0473e-001
-4.4070e-002	-1.7305e+001	-5.3286e+000	0	-4.7732e-001	1.4192e-001
7.2648e-002	1.4156e+001	6.1114e+002	0	9.8750e-001	-9.0609e-002
-1.9390e-003	-1.5781e+001	-9.5124e+002	0	-2.2698e-001	6.1941e-001
-9.0264e-002	-3.8539e+001	1.0300e+003	0	-5.1322e-001	5.0808e-001
-2.3371e-001	-3.3079e+001	1.1765e+003	0	-1.7226e+000	-8.6371e-002
3.5301e-002	2.8609e+001	-1.3336e+002	0	4.4493e-001	-4.0626e-001
-4.4290e-002	-2.3221e+001	-8.9490e+001	0	-3.1231e-001	3.5362e-001
-1.0144e-001	-4.9829e+001	-1.7174e+003	0	-5.2783e-001	1.3923e+000
-2.4350e-002	-1.8296e+001	7.1774e+001	0	-7.0747e-001	2.2230e-001
-8.5422e-003	1.8333e+001	2.0243e+002	0	1.8416e-001	-1.3611e-001
0	0	0	0	1.0000e+000	0
0	0	0	0	0	1.0000e+000
0	0	0	0	0	0
0	0	0	0	0	0
0	0	0	0	0	0
0	0	0	0	0	0
0	0	0	0	0	0
0	0	0	0	0	0
0	0	0	0	0	0
0	0	0	0	0	0
0	0	0	0	0	0

```
                0           0           0           0           0           0
                0           0           0           0           0           0
                0           0           0           0           0           0
                0           0           0           0           0           0
                0           0           0           0           0           0
                0           0           0           0           0           0]

A(1:40,7:12)=
[               0           0           0           0           0           0
 -1.1417e-004 -1.8165e-002 -8.9377e-004 -5.0994e-003  2.5959e-003 -3.8221e-004
  8.6524e-005 -4.9420e-004 -4.2399e-005  2.7677e-004  1.0011e-004 -1.0061e-004
                0           0           0           0           0           0
 -6.2507e-001 -1.9641e-001 -1.7701e-001 -1.1650e+000  2.5655e-001  1.7959e-001
 -1.0735e+000  4.0244e+000  7.8395e-001  7.1319e-001 -1.5945e+000  6.0659e-001
 -1.8927e+000  1.1276e-001  3.1528e-001  3.6705e-002 -9.5782e-001  5.9841e-001
 -2.7111e-001 -2.0242e+000 -3.6692e-001  1.3450e+000  3.9162e-001 -2.4959e-001
 -6.0047e-001 -6.1448e-001 -1.3631e+000  8.9844e-001 -1.9355e-001 -8.6498e-003
  1.1209e-001 -1.0806e+000  2.0470e-002 -1.2168e+000  3.7496e-001 -7.4291e-002
 -5.9967e-001  4.8374e+000  6.9182e-001 -6.9416e-001 -5.2393e+000  2.0945e+000
  1.8703e-001  2.6607e-002 -5.9437e-002  1.1825e-001  1.9672e-001 -1.1001e+000
  1.3527e-001  4.6699e-001  2.4743e-001 -4.1715e-001 -4.4137e-002  7.1429e-002
 -4.8128e-001  7.0283e-001 -1.5188e-001  7.5892e-001 -1.1997e+000  5.7445e-001
  3.7585e-001  5.2305e-001  3.5249e-001 -1.3170e+000 -9.4712e-002  5.7330e-002
  4.0818e-001  1.5168e+000  6.0246e-001 -8.7368e-001 -2.0437e-001  1.6379e-001
  3.8740e-001  3.3354e+000  1.0422e+000 -2.3084e-001 -8.0768e-001  6.3762e-001
 -3.0004e-002 -7.6375e-001 -1.4618e-001  6.2923e-001  2.2233e-001 -2.6248e-001
  4.4549e-001  8.3423e-001  3.6409e-001 -2.5657e-001 -6.8026e-002 -6.9021e-002
  1.0981e+000  9.8461e-001  6.0602e-001 -1.0093e+000 -4.9711e-001  1.8830e-001
  1.2140e+000  2.7031e+000  1.1083e+000  9.1629e-001 -7.7041e-001  2.9555e-001
 -3.1190e-001 -2.1173e-001 -5.3102e-002 -1.3304e-001  1.3267e-002  9.0184e-002
                0           0           0           0           0           0
                0           0           0           0           0           0
  1.0000e+000   0           0           0           0           0
                0  1.0000e+000           0           0           0           0
                0           0  1.0000e+000           0           0           0
                0           0           0  1.0000e+000           0           0
                0           0           0           0  1.0000e+000           0
                0           0           0           0           0  1.0000e+000
                0           0           0           0           0           0
                0           0           0           0           0           0
                0           0           0           0           0           0
                0           0           0           0           0           0
                0           0           0           0           0           0
                0           0           0           0           0           0
                0           0           0           0           0           0
                0           0           0           0           0           0
                0           0           0           0           0           0]

A(1:40,13:18)=
[               0           0           0           0           0           0
  1.7987e-003 -5.0532e-004  5.1239e-003  8.7093e-003  3.5723e-003 -8.2360e-003
  8.6353e-005  6.2786e-006  1.3187e-004  3.4985e-004  1.8697e-004 -2.8901e-004
                0           0           0           0           0           0
 -3.1741e-001  2.3436e-001  6.8340e-001 -4.3857e-001 -3.1363e-001  7.4990e-001
  3.8139e-001 -1.3560e+000 -3.0100e+000 -2.4315e+000 -1.0897e+000  5.0712e-001
 -6.3529e-001 -5.9861e-001 -1.0929e+000 -2.1977e+000 -1.3226e+000  1.5156e+000
 -5.1230e-001  4.9342e-001  9.1156e-001  4.6368e-001  3.0445e-001  1.7523e-001
 -1.9820e-001 -3.5831e-002 -1.9056e-001 -1.0102e-001 -1.4725e-002  1.4775e-001
 -6.8759e-002  2.8189e-001  1.2191e+000  2.3889e-001 -3.5296e-002 -1.1518e-001
  2.3686e+000 -5.3287e+000 -7.2588e+000 -7.2961e+000 -5.2862e+000  5.1334e-001
 -2.8540e-002  2.2206e-001  1.7079e-002  4.6743e-001  3.9316e-001 -2.7517e-001
 -1.1860e+000  2.6799e-002 -4.3791e-001 -3.5687e-001 -8.0919e-002  3.7721e-001
  1.5173e+000 -3.1141e+000 -1.3187e+000 -1.9522e+000 -2.0593e+000 -1.3289e+000
  4.0535e-001 -3.5601e-001 -2.0659e+000 -4.9329e-001 -2.5463e-001 -1.0578e+000
 -1.9265e-002 -4.3047e-001 -8.2667e-001 -2.7854e+000 -8.7360e-001  3.2320e-001
 -1.0368e+000 -6.3446e-001 -1.7474e+000 -3.4480e+000 -3.9441e+000  2.4962e+000
```

```
 7.8309e-003  3.1775e-001  7.2387e-001  8.9291e-001  4.3684e-001 -2.2209e+000
 4.8712e-002 -1.7884e-001 -9.2175e-001 -4.7585e-001 -1.5666e-001 -3.2185e-001
 7.3909e-001 -1.0830e+000 -1.9374e+000 -1.2085e+000 -1.2397e+000 -1.6774e+000
-2.5871e-001 -1.1775e+000 -2.9359e+000 -4.0693e+000 -2.3091e+000  1.6489e+000
-2.7604e-001  1.7982e-001  3.1797e-001 -1.0726e-001 -1.8491e-001  5.5674e-001
           0            0            0            0            0            0
           0            0            0            0            0            0
           0            0            0            0            0            0
           0            0            0            0            0            0
           0            0            0            0            0            0
           0            0            0            0            0            0
           0            0            0            0            0            0
           0            0            0            0            0            0
 1.0000e+000            0            0            0            0            0
           0 1.0000e+000            0            0            0            0
           0            0 1.0000e+000            0            0            0
           0            0            0 1.0000e+000            0            0
           0            0            0            0 1.0000e+000            0
           0            0            0            0            0 1.0000e+000
           0            0            0            0            0            0
           0            0            0            0            0            0
           0            0            0            0            0            0
           0            0            0            0            0            0]

A(1:40,19:24)=
[          0            0            0            0            0            0
 3.9144e-003 -5.0287e-004 -4.6856e-004  2.2607e-003  1.5318e-001  2.4218e-001
 4.3004e-005  9.9591e-006  3.0429e-005  2.3602e-004  2.8824e-003  7.0054e-004
           0            0            0            0            0            0
 7.0923e-001  3.2532e-001  9.3426e-002 -1.0427e+000 -4.5887e+001  1.4255e+001
-2.5007e+000 -1.2653e+000 -9.1116e-001  6.6316e-001 -7.5591e-001 -1.1757e+002
-9.2733e-001 -4.4447e-001 -5.5180e-001 -7.3003e-001 -6.9061e+000 -1.9639e+001
 6.3945e-001  4.2155e-001  3.5022e-001 -2.2878e-001 -4.7699e+000 -1.4896e+001
 2.2425e-002 -5.5960e-002 -4.2034e-002  2.2056e-002 -3.8646e+000 -1.4564e+001
 3.9123e-001  3.0292e-001  1.3110e-001 -3.5147e-001 -1.1485e-001 -2.8783e+000
-5.8612e+000 -4.8912e+000 -4.3682e+000  3.5749e-001  9.3683e+000  9.8347e+000
 1.3230e-001  2.0923e-001  2.3374e-001  1.7775e-001 -2.8683e-002  2.6162e+000
 2.9457e-002  7.7563e-002  1.4024e-001 -2.4428e-001  2.1328e+000  8.4555e+000
-1.9120e+000 -2.0134e+000 -2.4478e+000  3.2633e-001 -5.1161e+000 -1.6090e+001
-6.0842e-001 -3.0203e-001 -2.7903e-001  1.8577e-001  6.4608e+000  1.2075e+001
-7.8818e-001 -2.7447e-001 -4.5839e-001 -4.7344e-001 -1.2520e+000  1.1174e+001
-1.3966e+000 -9.1322e-001 -1.6565e+000 -2.6880e+000  3.9605e+000  1.6073e+001
 1.0701e-001  2.8607e-001  1.7951e-001  3.5997e-001 -1.7770e+000 -1.0885e+001
-2.1832e+000 -2.8772e-001 -2.1321e-001  3.1702e-001  2.3399e+000  1.0411e+001
-2.4569e+000 -3.2090e+000 -1.5980e+000  1.1296e+000  1.4354e+001  2.7687e+001
-4.7402e+000 -2.5774e+000 -4.4135e+000  1.2290e-001 -6.7849e-001  2.1976e+000
 4.0687e-001  2.0601e-001  9.4515e-002 -2.1130e+000  6.5233e-003 -5.6317e+000
           0            0            0            0            0            0
           0            0            0            0            0            0
           0            0            0            0            0            0
           0            0            0            0            0            0
           0            0            0            0            0            0
           0            0            0            0            0            0
           0            0            0            0            0            0
           0            0            0            0            0            0
           0            0            0            0            0            0
           0            0            0            0            0            0
           0            0            0            0            0            0
           0            0            0            0            0            0
           0            0            0            0            0            0
           0            0            0            0            0            0
 1.0000e+000            0            0            0            0            0
           0 1.0000e+000            0            0            0            0
           0            0 1.0000e+000            0            0            0
           0            0            0 1.0000e+000            0            0]

A(1:40,25:30)=
```

```
[          0          0          0          0          0          0
  3.1701e-002 -1.1833e+000 -2.4532e-001  2.9301e-001  3.3173e-001 -1.9397e-001
  3.4697e-003 -6.5039e-003 -3.7823e-003  9.0978e-003  4.2146e-003 -3.7861e-003
            0            0            0            0            0            0
 -1.1107e+001 -4.6602e+001 -7.9961e+000 -4.5206e+000  1.6635e+001 -2.4247e+000
 -9.0472e+000  1.1151e+002  3.2792e+001 -2.4707e+001 -5.6415e+001  2.8633e+001
 -2.4472e+002  5.1486e+001  2.8502e+001  2.9889e+000 -4.1026e+001  1.7946e+001
 -1.3772e+000 -2.7394e+002  1.3642e+001  3.3623e+001 -1.0792e+001 -1.7920e+000
 -1.3450e+000  4.9906e+001 -5.4996e+002  1.0513e+001 -2.1466e+001  1.0037e+001
  2.1006e+000  1.4215e+000  1.0107e+000 -6.8401e-002  7.7429e+000 -7.0115e+000
 -3.5829e+001 -3.4398e+001 -2.8674e+001  5.5190e+000 -8.1206e+002  3.7114e+001
  6.1950e-001 -6.6274e+000 -1.0993e+000 -9.9843e+000  4.7146e+000 -9.1744e+002
 -2.4958e+000 -2.0234e+001 -7.3330e+000 -2.2248e+001  8.1654e+000 -1.1842e+000
  3.4112e+000  2.8465e+000 -1.2295e+001  6.1210e+001 -2.9713e+001  8.6332e+000
  2.6426e+000 -5.2718e+001 -1.4195e+001 -3.6414e+000  1.5159e+001 -5.0585e+000
  2.9890e+000 -5.5458e+001 -1.3054e+001 -1.0947e+001  1.0826e+001 -8.2974e-001
 -1.9859e+001 -1.7517e+001 -2.0478e+001  2.9853e+001  1.3754e+000  7.4741e+000
 -7.5284e-001  4.7719e+001  9.5801e+000  3.4489e+001 -9.1537e+000  4.2096e-001
 -1.6573e-001 -3.7604e+001 -1.0975e+001 -6.2055e+000  1.1372e+001 -2.2859e+000
 -4.2200e+000 -1.0666e+002 -3.5791e+001  3.7031e+001  3.1560e+001 -1.2771e+001
 -1.0282e+001 -2.0739e+001 -2.3316e+001  9.5177e+001 -1.4682e+001  1.1711e+001
  1.2303e+000  2.0921e+001  5.5153e+000  2.3745e+000 -7.5781e+000  2.4293e+000
            0            0            0            0            0            0
            0            0            0            0            0            0
            0            0            0            0            0            0
            0            0            0            0            0            0
            0            0            0            0            0            0
            0            0            0            0            0            0
            0            0            0            0            0            0
            0            0            0            0            0            0
            0            0            0            0            0            0
            0            0            0            0            0            0
            0            0            0            0            0            0
            0            0            0            0            0            0
            0            0            0            0            0            0
            0            0            0            0            0            0
            0            0            0            0            0            0
            0            0            0            0            0            0
            0            0            0            0            0            0
            0            0            0            0            0            0]

A(1:40,31:36)=
[          0          0          0          0          0          0
 -1.8146e-002  2.5710e-001  5.0403e-001  8.3999e-001  4.1467e-001 -7.3711e-001
  4.4994e-003  3.0200e-003  8.6038e-003  9.3310e-003  1.0435e-002 -7.4761e-003
            0            0            0            0            0            0
 -5.3325e+000  9.8520e+000  5.0305e+001  4.9673e-001  6.2828e+000  1.8624e+001
  3.5370e+001 -7.8461e+001 -1.2972e+002 -1.4587e+002 -8.2209e+001  5.3677e+001
 -6.5108e+000 -4.0074e+001 -1.0364e+002 -1.0814e+002 -8.1212e+001  5.1152e+001
 -1.9223e+001  9.7314e-001 -5.3706e+001 -4.8617e+001  1.5445e-002  4.9402e+001
 -2.7080e+001 -1.8488e+001 -7.8834e+001 -5.8749e+001 -2.4706e+001  2.1661e+001
 -1.5371e+001  1.3070e+001  4.4257e+001  1.3806e+001  1.1013e+001  3.0327e+001
  9.9259e+001 -1.3722e+002 -5.7861e+001 -1.9768e+002 -1.7969e+002 -4.4744e+001
 -1.5039e+000  6.4506e+000  5.8551e+000  2.0172e+001  1.4490e+001 -1.2856e+001
 -1.0254e+003 -5.5500e+000  1.6607e+001  7.3526e+000  4.4324e+000 -2.7537e+001
 -3.9455e+001 -1.1609e+003 -1.6159e+001 -1.0140e+001 -6.6601e+001  5.1067e+001
  1.8109e+001  3.7371e+000 -1.2911e+003  4.1045e+001  6.7718e+000 -4.2017e+001
  9.4688e+000  8.5641e+000  5.5376e+001 -1.3998e+003 -1.9733e+000 -4.5021e+001
  1.0335e+001 -8.2071e+000  1.4981e+001 -4.6696e+000 -1.6209e+003  9.0701e+001
 -1.8315e+001  4.2676e+000 -5.2607e+000 -2.2920e+001  6.5934e+000 -1.7998e+003
  7.5901e+000  5.2634e+000  3.6154e+001  3.5908e+001  1.0899e+001 -2.6685e+001
  1.3364e+001  9.8125e+000  1.3207e+002  5.3433e+001  8.0624e+000 -2.7699e+001
 -3.2684e+001  6.0238e+000  1.5087e+001  5.2597e+000  2.8053e-001  1.7890e+002
  3.5083e-001 -5.6201e+000 -1.6878e+001 -1.5770e+001 -2.6163e+000  1.9763e+001
            0            0            0            0            0            0
            0            0            0            0            0            0
            0            0            0            0            0            0
```

```
0             0             0             0             0             0
0             0             0             0             0             0
0             0             0             0             0             0
0             0             0             0             0             0
0             0             0             0             0             0
0             0             0             0             0             0
0             0             0             0             0             0
0             0             0             0             0             0
0             0             0             0             0             0
0             0             0             0             0             0
0             0             0             0             0             0
0             0             0             0             0             0
0             0             0             0             0             0
0             0             0             0             0             0
0             0             0             0             0             0]

A(1:40,37:40)=
        [             0             0             0             0
           7.8547e-001   3.4012e-001   2.7185e-001  -1.1751e-001
           3.2199e-003   4.9899e-003   4.3762e-003   1.3782e-002
                     0             0             0             0
           5.0462e+001   3.1896e+001   1.2695e+001  -3.7902e+001
          -1.5838e+002  -1.0037e+002  -9.3094e+001   3.7679e+001
          -9.4658e+001  -6.5578e+001  -6.0591e+001  -2.5465e+001
          -2.9541e+001   1.5017e+000   9.3790e+000   9.8458e+000
          -6.6062e+001  -2.8102e+001  -1.7972e+001   1.2775e+001
           1.5609e+001   1.7748e+001   1.3486e+001  -3.5574e+000
          -1.8119e+002  -1.8877e+002  -2.4966e+002  -3.3634e+001
           1.9496e+001   1.2286e+001   1.4926e+001   2.4666e+000
           2.9006e+001   1.1282e+001   3.8788e+000  -1.0229e+001
          -9.5785e+001  -8.2644e+001  -8.6480e+001  -1.7251e+001
           4.7052e+001   1.8392e+001   3.1963e-001   1.0417e+001
           5.1960e+001   6.8264e+000  -4.9362e+000  -3.6292e+001
           1.3964e+001  -1.7170e+001  -3.7215e+001  -2.9417e+001
          -2.4719e+001   4.2242e+000   9.6335e+000   2.1315e+001
          -1.9288e+003   1.0929e+001   3.0069e+000  -1.2032e+001
           6.2916e+001  -2.0473e+003  -2.8772e+001  -2.0882e+001
          -6.4559e+001  -7.6186e+001  -2.2274e+003   1.1202e+001
          -2.1155e+001  -7.2627e+000  -2.5178e+000  -2.2418e+003
                     0             0             0             0
                     0             0             0             0
                     0             0             0             0
                     0             0             0             0
                     0             0             0             0
                     0             0             0             0
                     0             0             0             0
                     0             0             0             0
                     0             0             0             0
                     0             0             0             0
                     0             0             0             0
                     0             0             0             0
                     0             0             0             0
                     0             0             0             0
                     0             0             0             0
                     0             0             0             0
                     0             0             0             0
                     0             0             0             0]

B=
                    [             0
                       -5.5765e+001
                       -2.8282e+000
                                  0
                        9.6358e+003
                       -4.1978e+003
                        7.1384e+003
                        1.0474e+003
```

```
-8.3028e+002
 2.0219e+003
-2.3290e+003
-1.1422e+003
 2.0501e+003
-4.8571e+003
-1.1095e+003
 3.0295e+003
 9.5259e+003
-2.2321e+003
-6.8675e+002
-3.6456e+003
-1.0075e+003
 1.5052e+003
          0
          0
          0
          0
          0
          0
          0
          0
          0
          0
          0
          0
          0
          0
          0
          0
          0
          0]
```

$C_{\phi_{:,}}$ (1:18,1:3) =

```
[ 1.845854430018215e-041   -4.625552606269263e-037    5.203473835655131e-033
 -7.764968500453305e-042    1.955239317510629e-037   -2.202199504340531e-033
  3.162890561607039e-041   -8.008225899499751e-037    9.145989529447723e-033
  2.836206186943103e-041   -6.989710688820184e-037    7.633174586691557e-033
  6.487720866118946e-042   -1.512070053197199e-037    1.574179330662035e-033
  2.795743666071298e-041   -6.213404871575763e-037    6.022413053267728e-033
 -9.290295464669621e-042    2.531562689816743e-037   -3.084440986900911e-033
 -2.297223901497647e-041    5.493697420550753e-037   -5.840043610369656e-033
 -6.859289138041469e-041    1.708950131359656e-036   -1.903460753438702e-032
  5.844017201491391e-041   -1.488112767983041e-036    1.697485039036173e-032
 -1.130781235479022e-040    2.865860269857909e-036   -3.241994485898923e-032
  2.808905038742330e-040   -6.977391692036085e-036    7.734265766426079e-032
 -9.356655277790220e-041    2.255175395518763e-036   -2.422916227880410e-032
 -2.626278447221588e-040    6.457698917078113e-036   -7.079316774900523e-032
  3.877904716321026e-041   -9.474292473591560e-037    1.034598730980783e-032
 -8.580269521611381e-041    1.991927518408438e-036   -2.044266310677952e-032
 -1.065300493355004e-040    2.782359640967953e-036   -3.256359497171619e-032
  9.720067801378796e-042   -6.880968220569615e-037    1.289672197264944e-032]
```

$C_{\phi_{:,}}$ (1:18,4:6) =

```
[ -3.469025892897730e-029    1.523880664214059e-025   -4.638629985453029e-022
   1.464693824010855e-029   -6.398163787676968e-026    1.931885986471394e-022
  -6.229173815132548e-029    2.817771257559459e-025   -8.919580719792414e-022
  -4.865480746347985e-029    2.007381925028643e-025   -5.621086987524868e-022
  -9.666569237168623e-030    3.892196884263340e-026   -1.079405582925194e-022
  -3.327021201051338e-029    1.145545450904242e-025   -2.506042284851163e-022
   2.215377588761123e-029   -1.041346203983022e-025    3.363493866611508e-022
   3.639066453502725e-029   -1.476189139457384e-025    4.095815831282154e-022
   1.250392660204771e-028   -5.381498666013458e-025    1.594216471428855e-021
  -1.144274727450275e-028    5.063932806556255e-025   -1.545890822768754e-021
   2.159239276169774e-028   -9.405108718580349e-025    2.815081775638570e-021
  -5.045677424778993e-028    2.151607621201749e-024   -6.299811636054144e-021
```

```
 1.530426454001799e-028   -6.312209525403087e-025    1.785754583988273e-021
 4.562364320088836e-028   -1.919246907279114e-024    5.534397412231955e-021
-6.665056650914293e-029    2.815880457144953e-025   -8.204365534539647e-022
 1.219884211867494e-028   -4.682630735304021e-025    1.207551533616248e-021
 2.253778578410229e-028   -1.025263123192056e-024    3.222776689967474e-021
-1.208655261102651e-028    6.834063587548092e-025   -2.530466750069284e-021]
```

$C_{\phi_{:,}}$ (1:18,7:9) =

```
[ 1.001681421344153e-018   -1.544742916900381e-015    1.689852045916644e-012
 -4.132993904071691e-019    6.317302764292000e-016   -6.867282788900322e-013
  2.026855924452456e-018   -3.335205609833507e-015    3.955919953155038e-012
  1.090198853883958e-018   -1.469081758537498e-015    1.360828053076082e-012
  2.104220081270739e-019   -2.884343062727523e-016    2.730747978767000e-013
  3.313908840353397e-019   -2.015741718469770e-016   -9.094158849934221e-014
 -7.629815122527446e-019    1.221639860262616e-015   -1.369397872696618e-012
 -7.953550635212854e-019    1.088347121530364e-015   -1.043802745219756e-012
 -3.324187957838677e-018    4.905380743634486e-015   -5.082613925521371e-012
  3.330133149364010e-018   -5.092728808647920e-015    5.490214554978910e-012
 -5.923153735519761e-018    8.814260326140563e-015   -9.211849699036751e-012
  1.295172382422382e-017   -1.880179488856628e-014    1.912799546605764e-011
 -3.543471118824388e-018    4.959129284787507e-015   -4.858043850787621e-012
 -1.118422853407941e-017    1.592530327492890e-014   -1.585719347365375e-011
  1.687708172392236e-018   -2.467459026847416e-015    2.546545325697605e-012
 -2.120091160248633e-018    2.910453581100270e-015   -1.935456803102561e-012
 -7.164222821858303e-018    1.133488119174923e-014   -1.267459483597730e-011
  6.376783518783437e-018   -1.109631489159566e-014    1.329913779244364e-011]
```

$C_{\phi_{:,}}$ (1:18,10:12) =

```
[ -1.285246040680980e-009    6.551327991318115e-007   -2.100476316755090e-004
  5.215437968217406e-010   -2.670570905843774e-007    8.647993158905763e-005
 -3.322499100840963e-009    1.909130295543745e-006   -7.065602844788974e-004
 -8.452511151925910e-010    3.373602623608764e-007   -8.029556245274745e-005
 -1.717928541199096e-010    6.703323180727282e-008   -1.441309291567149e-005
  2.778650589812348e-010   -2.309021271284537e-007    9.720898157690318e-005
  1.052044904337343e-009   -5.333003236910223e-007    1.674114199831561e-004
  6.898237636949070e-010   -3.044218920634717e-007    8.471846648311471e-005
  3.620876676790909e-009   -1.708535077664307e-006    5.017268714422271e-004
 -4.089615665212588e-009    2.029318737374876e-006   -6.300757476706836e-004
  6.627508688216515e-009   -3.165204398847515e-006    9.431456719396494e-004
 -1.336035213117592e-008    6.175105584829814e-006   -1.774840548062661e-003
  3.264056339838837e-009   -1.450928717625382e-006    4.020279479279836e-004
  1.081944692080002e-008   -4.878573098796444e-006    1.367661473622654e-003
 -1.818267520668044e-009    8.659674909527677e-007   -2.584722837225973e-004
  8.945815506335862e-010   -1.943343298455045e-007   -7.221647949073051e-006
  9.814093320990166e-009   -5.068724416502000e-006    1.636503169997243e-003
 -1.078264647638997e-008    5.705569191800256e-006   -1.850062066117508e-003]
```

$C_{\phi_{:,}}$ (1:18,13:14) =

```
[  3.672372905794030e-002   -1.599754200567957e+000
  -1.628533073880650e-002    1.895956498149917e+000
   1.511427383476877e-001   -1.472050021425262e+001
   8.602332008726440e-003    6.568631507729527e-001
   1.611879825983702e-003   -2.380382371364718e-001
  -2.184051094091767e-002    2.555861592510036e+000
  -2.938479629477497e-002    2.403740612581833e+000
  -1.308237185016208e-002    7.499000324047368e-001
  -8.269711085071024e-002    6.224519412173215e+000
   1.095503146535590e-001   -8.330329224489031e+000
  -1.570272494020409e-001    1.138235732440236e+001
   2.845916942721425e-001   -2.005009132618454e+001
  -6.282311467577181e-002    4.472734230366046e+000
  -2.140624176722228e-001    1.467636093779587e+001
   4.300054796289351e-002   -2.968176883529098e+000
   1.017011853380042e-002   -9.490693346739080e-001
  -2.923214778704590e-001    2.143636632986055e+001
   3.263480405023647e-001   -2.331935750581350e+001]
```

CURRICULUM VITA

for

ABDUL GHAFOOR AL-SHEHABI

DEGREES:

Doctor of Philosophy, Aerospace Engineering, Old Dominion University, Norfolk, Virginia, August 2001

Master of Science, Aerospace Engineering, Cairo University, Cairo, Egypt, December 1995

Bachelor of Science, Mechanical Engineering, Aleppo University, Aleppo, Syria, 1986

PROFESSIONAL CHRONOLOGY:

Department of Aerospace Engineering, Old Dominion University, Norfolk, VA, USA, Research Assistant, Jan. 97 - Aug. 2001

Faculty of Mechanical Engineering, Aleppo University, Aleppo, Syria, Teaching Assistant, Jan. 95 - Dec. 96

Department of Aerospace Engineering, Cairo University, Cairo, Egypt, Scholarship, Feb. 93 - Dec. 95

Faculty of Mechanical Engineering, Aleppo University, Aleppo, Syria, Teaching Assistant, Jan. 87 - Feb. 93

PROFESSIONAL SOCIETIES MEMBERSHIP:

Member of American Institute of Aeronautics and Astronautics, USA

Member of Syrian Engineers Syndicate, Aleppo, Syria

Member of Virginia Academy of Science, Virgina, USA